Integrated Modeling and Dynamics Simulation for the Next Generation Space Telescope

by

Olivier Ladislas de Weck
Betriebs- und Produktionsingenieur mit Auszeichnung (1993)
Swiss Federal Institute of Technology, Zurich, Switzerland

Submitted to the Department of Aeronautics and Astronautics
in Partial Fulfillment of the Requirements for the Degree of
Master of Science in Aeronautics and Astronautics

at the

Massachusetts Institute of Technology
June 1999

Signature of Author...
Department of Aeronautics and Astronautics
May 7, 1999

Certified by ....
David W. Miller
Assistant Professor of Aeronautics and Astronautics
Thesis Supervisor

Accepted by ....
Jaime Peraire
Chairman, Department Committee on Graduate Studies

INTEGRATED MODELING AND DYNAMICS SIMULATION FOR THE NEXT GENERATION SPACE TELESCOPE

by

OLIVIER L. DE WECK

Submitted to the Department of Aeronautics and Astronautics
on May 7, 1999 in partial fulfillment of the requirements for the
Degree of Master of Science in Aeronautics and Astronautics

ABSTRACT

The Next Generation Space Telescope (NGST) represents a challenging problem from the point of view of maintaining a milli-arcsecond level pointing accuracy and diffraction limited wavefront performance in the presence of dynamic onboard disturbances during science observations. This is due to the fact that NGST will make extensive use of deployable, inflatable and lightweight components, which leads to high modal density and light damping of the structural plant. An integrated model comprising multiple disturbance sources, structures, optics and control systems was developed in order to predict the expected dynamic performance of the observatory in terms of wavefront error and line-of-sight jitter. A simple three degree-of-freedom system is used to motivate the analysis and to develop the equations before applying them to the full order observatory.

An initial performance assessment showed that the conceptual design model based on the NASA Goddard "Yardstick" concept for NGST cannot meet performance assuming a set of nominal design parameters stipulated by the author. This performance assessment is carried out using time domain, frequency domain and Lyapunov techniques. Two strategies for dealing with large order models using numerical conditioning and singular value decomposition of the optics linear sensitivity matrices have been demonstrated. A sensitivity analysis revealed which parameters contribute significantly to the root-mean-square errors. This information was subsequently used to recommend performance improvements including stiffening the secondary mirror tower, isolating reaction wheel disturbances and adding passive damping treatments. A repeated performance analysis and time simulations using NASA's non-linear simulation model of NGST showed that performance can be met with comfortable design margins by applying a combination of the suggested redesign actions on the nominal design. This research is motivated by the fact that it will not be possible to test the fully deployed observatory in a 1g environment before launch.

Dedicated to Lynn Marie and Gabrielle Christine

TABLE OF CONTENTS

Acknowledgments

This research has been supported by NASA's Goddard Space Flight Center under RTOP grant No. NAG5-6079 and under research grant NAG5-7839. The following individuals at GSFC have contributed to this work through their technical suggestions and support: Gary Mosier, Bill Hayden, Mike Femiano, Kong Ha, Richard Burg and Ed James. The following individuals at the Jet Propulsion Laboratory (JPL) were helpful in answering specific questions relating to IMOS, structural modeling, optical modeling and MACOS: Andy Kissil and Dave Redding. I am indebted to Rebecca Masterson, Greg Mallory, Sean Kenny, Scott Uebelhart and Brett de Blonk and especially to Homero Gutierrez for their precious support and friendship at the M.I.T. Space Systems Laboratory.

Special thanks go to Gary Mosier at the NASA Goddard Space Flight Center for his technical monitoring, numerous constructive suggestions and for hosting me during ten weeks at the Goddard Space Flight Center during the summer of 1998. Without his support and technical expertise this research would not have been possible. Professor David Miller guided me through this work with his experience and knowledge in the areas of spacecraft systems, controlled structures technology and dynamics modeling and his unwavering support and patience even during difficult times.

Chapter 1

Introduction

1.1 Background

The need for a new infrared (IR) space observatory to replace the Hubble Space Telescope after the end of its useful life in that spectral region was identified in the "HST and Beyond" report [1]. In 1996 it identified three main recommendations for NASA's space science mission at the beginning of the new millennium. (1) The Hubble Space Telescope (HST) should be operated beyond its currently scheduled termination date of 2005. (2) NASA should develop a space observatory of aperture 4m or larger, optimized for imaging and spectroscopy over the 1-5 μm regime, and (3) NASA should develop the capability for space interferometry. The development of the Next Generation Space Telescope (NGST) has been started based on recommendation (2) as part of NASA's ORIGINS program. It became clear that a specialization in the new generation of space telescopes would become necessary in order to meet the scientific objectives of the ORIGINS program. It would be impossible to cost-effectively design a single observatory featuring excellent angular resolution, spectral coverage and sensitivity in the UV, visible and infrared regions without some significant compromises in science capabilities. Three of the major observatories that are in various phases of planning are SIM (Space Interferometry Mission), NGST (Next Generation Space Telescope) and TPF (Terrestrial Planet Finder). This thesis focuses on integrated analysis methods, dynamics simulations and results for NGST. The objective of this research is broader in the sense that the methods and tools developed in this study shall be useful for and applicable to a broad variety of space-based observatory projects.

1.2 Scientific Objectives of NGST

The development of NGST is embedded in fundamental questions that have been posed to NASA's Space Science program. It is from these key questions that the scientific objectives and ultimately the engineering requirements flow in a top-down fashion. The five key questions are:

1. What is the origin and shape of the universe?
2. How are galaxies born and how do they evolve?
3. How do stars and planetary systems form and interact?
4. What are the life cycles of matter in the universe?
5. What is dark matter and how much of it exists in the known universe?

Answers to most of these questions involve objects formed extremely early in the history of the universe (see Figure 1.1 below). Such objects have their radiation greatly redshifted when observed in the current epoch, meaning that observations are best performed in the infrared portion of the spectrum. Our knowledge of the history of the universe is constrained to very early (t_{univ} < 300,000 years) and relatively late ($t_{univ} > 5 \cdot 10^9$ years.) stages of its evolution [2]. Observations by the Cosmic Background Explorer (COBE) give us a good picture of the state of the universe at the time matter decoupled from radiation based on small fluctuations in the amount of microwave background radiation over the celestial sphere. Current ground and space based telescopes have probed the universe up to redshifts around $z = 5$. The redshift is due to the Doppler effect and is mathematically defined with help of the redshift parameter z as the ratio $\Delta\lambda/\lambda$, where $\Delta\lambda$ is the observed increase in wavelength of the radiation and λ is the wavelength of the spectral line at the time of emission from the source. Due to the large recessional velocities of extragalactic sources (the region of main interest for NGST), the relativistic expression for the redshift must be used:

$$z = \left[\frac{(c+v)}{(c-v)} \right]^{1/2} - 1 \tag{1.1}$$

where v is the relative radial velocity and c is the speed of light [3]. For example a redshift of z = 5 that would be typical for a faint galaxy observed by NGST corresponds to a recessional velocity of $0.997c$. From Hubble's law it becomes clear that higher redshift objects are receding faster, they are further away from an earthbound observer and the radiation received has left the object a longer time ago.

The intermediate epoch between 300,000 years < t_{univ} <$5\text{x}10^9$ years was a decisive one, because this is exactly the time when the first large-scale structures such as primordial galaxies and the first stars began to form. This corresponds to the redshift range from z=3 ~20 [2]. It is however also the regime, where there currently is a lack of significant amounts of astronomical data. This is due to the fact that even a sensitive observatory in LEO would be disturbed by earth's black body radiation. To probe the universe as it was between a few million and a few billion years of age requires a new type of observatory. Such an observatory must be capable of collecting the very faint IR radiation of early objects with sufficient spatial resolution to distinguish the large-scale structures mentioned before. This intermediate epoch has been termed the "Dark Ages" and it is the principal target for NGST observations.

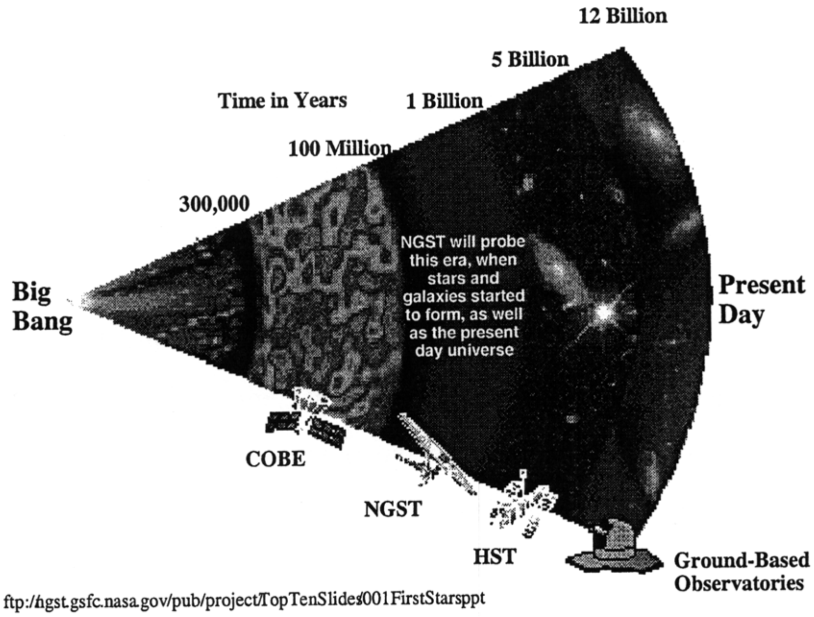

Source: ftp://ngst.gsfc.nasa.gov/pub/project/TopTenSlides/001FirstStarsppt

Figure 1.1: The scientific window for NGST observations [2]

NGST will be capable of detecting radiation whose wavelength λ lies in the range 0.6 to 20 μm (and be optimized for the 1 to 5 μm region). Furthermore NGST must be able to see objects 400 times fainter than those currently studied with large ground-based infrared telescopes (such as the Keck Observatory [1]) or the current generation of space-based infrared telescopes (e.g. SIRTF). It must do so with a spatial resolution ("image sharpness") comparable to the Hubble Space Telescope (HST) [2]. It can be shown in a rough order calculation what that particular requirement implies for the primary optics of NGST. If we first assume that the main wavelength of interest for HST is roughly $\lambda = 733$ nm, corresponding to red light in the visual regime, and knowing that the primary mirror has a diameter D_{HST} = 2.4 m, we can estimate the angular resolution of this circular aperture by applying the Rayleigh criterion for resolution [1][4] as:

$$\theta_{res} \cong 1.22 \cdot \frac{\lambda}{D} \tag{1.2}$$

For HST this corresponds to an angular resolution of ~ $3.05 \cdot 10^{-7}$ radians or roughly 63 milli-arcseconds. In order to achieve the same angular resolution at a wavelength that is 3 times as long, i.e. at λ = 2200 nm = 2.2 μm (NIR) it is evident that NGST will require a primary mirror that is three times as large in order to maintain the same ratio in Equation 1.2. Thus the primary mirror diameter for NGST is calculated as D_{NGST} = 7.2 m. It is this primary mirror dimension that poses one of the main challenges for the program in designing, building and launching this observatory, since this diameter exceeds the maximum dimensions of available payload fairings. Generally it can be said that high angular resolution and excellent IR sensitivity are the most critical components of design affecting NGST.

The top-science questions to be answered by NGST have been translated into the so-called Design Reference Mission (DRM). The DRM represents a suite of potential astronomical programs and targets along with their expected physical properties (e.g., number density and brightness) and desired observation modes. This broad science program is being used to drive the observatory design in a way as fundamental as traditional engineering parameters (power, mass, etc.) [5]. It is the total time which is required to complete the DRM that is currently used as the main metric with which to compare competing observatory design. In conclusion it can be said that the key scientific requirements that drive the NGST observatory design are:

- large aperture primary mirror for HST-like resolution at 2.2 μm
- cold optics and detectors for NIR sensitivity of ~ 1 nJy in the regime 1-5 μm
- 2-D NIR spectroscopy with R ~ 1000 (spectral resolution) and a wide field-of-view (4' x 4')
- diffraction limited optics performance at λ = 2.2 μm

---

[1] Rayleigh's criterion states that two equally bright point sources can just be resolved by an optical system if the central maximum of the diffraction pattern of one source coincides with the first minimum of the other [4].

1.2 Dynamic Performance Requirements

Whereas the previous section laid out the scientific objectives of NGST, there are a number of engineering requirements that directly flow down from the top-level science requirements. It is one of the most challenging tasks in observatory design to relate the science to the appropriate technology requirements. The following table summarizes the requirements that have been levied on the system that relate directly to the dynamics of NGST. We define dynamics in this context as the discipline that analyzes the time varying quantities, which affect the performance in terms of image quality and settling times due to the interaction of disturbances, structures, controls and optics. These requirements are the basis for the calculations in this thesis. The left column of Table 1.1 contains a specific science requirement for NGST, whereas the right column shows the corresponding engineering requirement. A RMS quantity refers to the zero-mean root-mean-square values.

Scientific Requirement	**Engineering Requirement**
4 nJy sensitivity in the near infrared region	Optimized for 1-5 μm (NIR)
OTA diffraction limited at $\lambda = 2.2$ μm	RMS WFE errors below $\lambda/14$
Excellent inertial pointing accuracy	RMS LOS jitter < 4.8 mas
All observations according to DRM completed in 5 years	slewing: π radians in 100 min minimize settling times to 5% of slew

Table 1.1: Dynamic requirements for NGST based on science objectives [2]

The main operational mode that is analyzed in this study is the fine pointing mode during scientific observations[2]. During science observations NGST requires line-of-sight (LOS) stabilization to 4.8 milli-arcseconds (mas), 1σ, and a RMS wavefront error (WFE) of less than $\lambda/14$, which corresponds to 0.157 μm at a wavelength of 2.2 μm. The slew mode for the acquisition of new science targets was analyzed in a preliminary study, whose results are shown in reference [52]. The slew requirement is a slew capability of 180° in 100 minutes with 5% settling time included. These requirements form the basis for the subsequent analyses.

---

[2] Does not include the observation of Kuiper-belt objects with significant LOS rates.

1.3 Description of NGST Yardstick Design

The present study is based on the NGST "Yardstick" design that was proposed by the GSFC-led study team in 1996 [6]. The purpose of the Yardstick mission is to establish a robust reference design with excellent scientific capability against which alternate designs can be compared [7]. The methodology developed in this thesis shall also be general enough in order to be applied to competing designs for a quantitative comparison. Figure 1.2 depicts the NASA proposed "Yardstick" design with the major observatory components. The spacecraft is shown in the deployed configuration and can be roughly subdivided into a "warm" and a "cold" section that are separated from each other by an isolation truss. The appearance of NGST is radically different from the tube-shaped configuration of the Hubble Space Telescope. Another major difference with HST is the lack of on-orbit maintenance capability since the planned operational orbit is not LEO but rather L2[3].

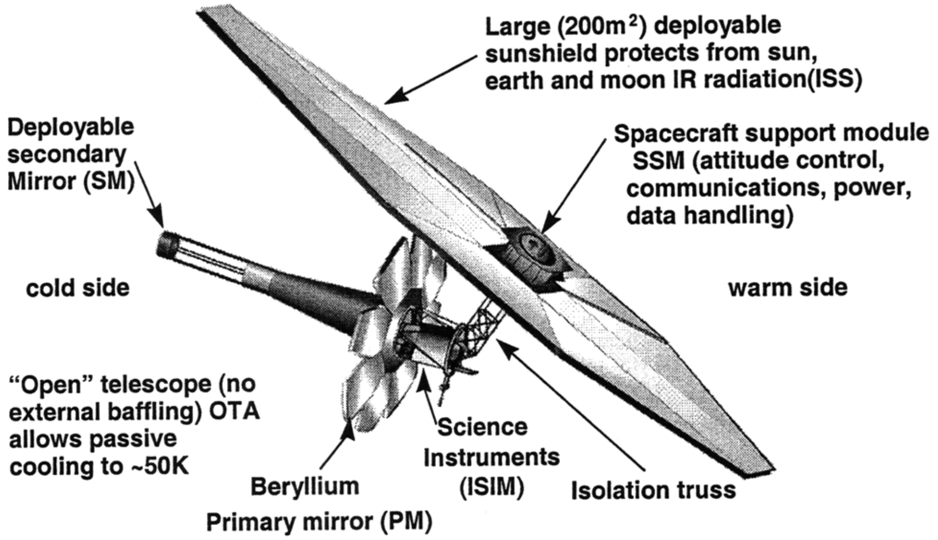

Fig. 1.2: GSFC Yardstick concept of the Next Generation Space Telescope

The Spacecraft Support Module (SSM) contains the essential subsystems for operating the spacecraft, maintaining attitude and for communicating telemetry and science data back to Earth.

---

[3] Refers to Lagrange point 2 of the Earth-Sun system [8]

The large inflatable sunshield (ISS) protects the optical telescope assembly (OTA) from direct electromagnetic radiation from the Sun and from Earth albedo. The optical design is based on a Cassegrain optical train with primary and secondary mirrors. The integrated science instrument module (ISIM) comprises all the detectors, cameras, cryocoolers, the deformable mirror (DM), a fast steering mirror (FSM) for LOS stabilization and all other optical elements.

The large primary mirror (7.2-m effective diameter) and sunshield would not fit into present-day launch vehicle fairings. Thus it is expected that NGST will make extensive use of deployable, lightweight and inflatable components, which inevitably leads to a low fundamental frequency and high modal density of the structure. Figure 1.3 depicts the NGST Yardstick in the stowed launch configuration (left) and in the deployed configuration (right). The choice of launch vehicle is still open, but an Atlas II-AS/ELV with a fairing diameter of 12’ and 33.8’ length has been used as placeholder for the yardstick mission. With this choice the allowable launch mass to an L2-orbit is 2567-kg [6]. The planned launch date is 2007 with an expected mission lifetime of 5-10 years.

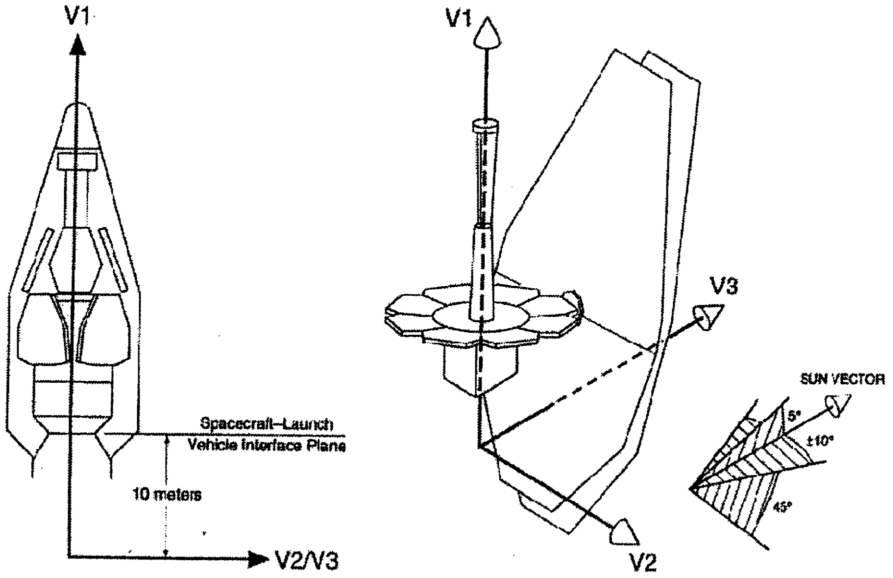

Stowed Configuration **Deployed Configuration**

Fig. 1.3: NGST “Yardstick” design in the stowed and deployed configuration [6]

An overview of more detailed information on the Yardstick design is presented in table 1.2.

Table 1.2: Technical overview of NGST yardstick design [7]

Item	Value
Scientific performance	
Wavelength coverage	0.6 to 30 microns
Aperture	8 meter, quasi-filled
Sensitivity	4 nJy in 10,000s at 2 microns, S/N=10, BP20%
Resolution	0.050'' (diffraction limited at 2.2 microns)
Science instruments	cameras, multi-object spectrograph
Field	NIR: 4'x4' (camera) 3'x3' (spectrograph) MIR: 2'x2' (camera)
Sky coverage	Yearly: full sky Instantaneous: 17%
Technical features	
Optics configuration	3-mirror anastigmat with accessible exit pupil
Aperture diameter	8 meters OD, 7.2 m effective diameter
Wavefront control	image-based wavefront sensing with 5 DOF mirror actuation + DM
Optics temperature	<70 K (50 K nominal)
Mirror material	Light weighted beryllium
System f ratio	f/24
Fine pointing	4.8 mas
Data rate	1.6 MB/s
Mission aspects	
Mass	<3300 kg
Spacecraft pointing accuracy	2'' rms.
Power	800W
Mission lifetime	5 years nominal- 10 years goal
Orbit	Sun-earth Lagrange 2 Halo orbit
Launcher	Atlas II ARS
Programmatic aspects	
Cost of manufacture	$564M (1996 $)
Development duration	48 months
Launch date	June 2007

The area of line-of-sight (LOS) stabilization is a major difference for NGST compared to previous space telescopes in the area of pointing control. Spacecraft like HST perform the telescope pointing using exclusively the spacecraft attitude determination and control system (ADCS). This requires a very stiff spacecraft and telescope structure, the use of precise gyroscopes, star trackers and/or fine guidance sensors, low-noise reaction wheels and a relatively high bandwidth attitude control system (ACS). According to current planning NGST will employ a very different approach, using the ADCS for coarse pointing only. The remaining pointing error will be sensed using the NIR science camera itself. The fine pointing subsystem uses a fast steering mirror to meet the LOS jitter specification. The result is a much-relaxed spacecraft pointing tolerance (on the order of 2 arcsec), leading to a much lower control bandwidth of about 0.025 Hz. The lower bandwidth and the low disturbance environment make it possible to use a more flexible, lighter-weight telescope structure [7].

The preliminary design of this fine pointing control and image stabilization subsystem features two controls loops [9]. The first is a low bandwidth ACS loop including star trackers, gyros, reaction wheels, and a digital PID controller. The second is a high bandwidth servo loop controlling a two-axis gimbaled, reactionless fast steering mirror (FSM) that tracks the image centroid using guide stars from the NIR science camera. The details of this subsystem have been modeled by NASA and will be explained in section 2.4 for our purposes. It is expected that the internal mechanical disturbances stem mainly from the conventional ball-bearing reaction wheels in the spacecraft support module (SSM) and from a linear action cryocooler located in the integrated science instrument module (ISIM). A block diagram of this architecture has been implemented in NASA's non-linear end-to-end time simulation model as shown in figure 1.4.

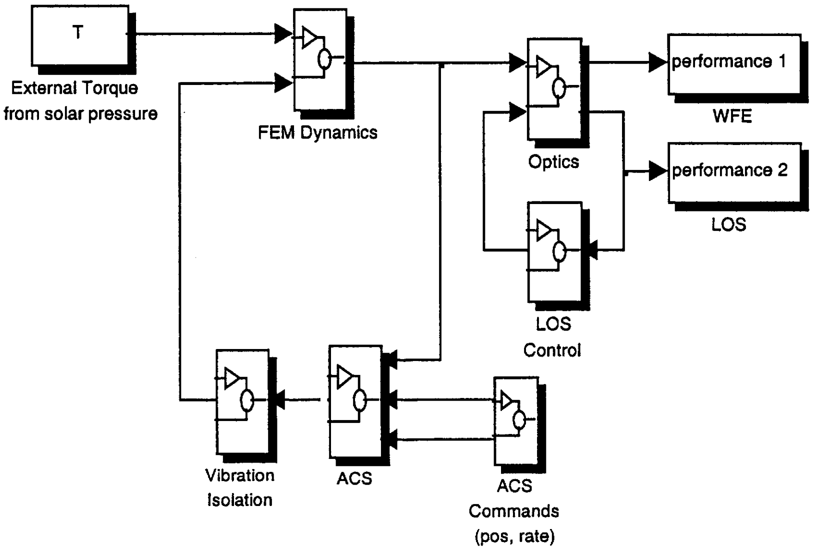

Fig. 1.4: NGST Pointing Control and Dynamics Block Diagram

In summary it can be said that NGST poses a challenging problem because the pointing accuracy of 4.8 mas (1 σ) for the LOS and the wavefront error (WFE) budget of $\lambda/14$ at $\lambda = 2.2$ μm has to be maintained for a deployable, large and flexible structure with low expected damping in a cryogenic environment. These requirements have to be met in the presence of significant dynamic and mostly uncorrelated disturbances from rotating and linearly acting machinery such as reaction wheels and cryocoolers, sensor noise such as guide star noise as well as external disturbances such as solar radiation pressure.

1.4 Thesis Objective and Methodology

1.4.1 Thesis Objective

The main objective of this thesis is to apply proven controlled structures technology (CST) modeling and analysis techniques to NGST and to extend those analysis capabilities in selected areas of interest. Specifically the thesis addresses the challenges of integrated modeling of structural dynamics, optics and controls and discusses concerns about the effects of mechanical and sensor noise on the pointing and wavefront error performance of the future observatory. Another objective of this thesis is to identify the methodologies, tools and approaches that will be critical in answering these complex questions beyond the conceptual design phase. This will be accomplished by combining previous NGST modeling work done by GSFC and JPL with disturbance and sensitivity analysis tools developed at M.I.T. Those analysis capabilities and models are then extended in selected areas that appeared to be critical to cost-effective and accurate performance predictions at the conceptual level. The ultimate objective of the research program that this thesis is embedded in is to find the best mix of actuator and sensor bandwidth, control authority, isolation requirements and optics as well as structural redesign options that will guarantee robust performance at a minimal cost. The hope is that the tools and methods demonstrated here for NGST will ultimately be applicable to other science missions such as SIM, TPF and also with some limitations to ground-based observatories.

1.4.2 Previous work

A thorough review and understanding of previous studies was critical in solidly grounding the research presented in this thesis. The previous work is roughly subdivided into two categories. The first category comprises early studies of potential architectures and conceptual designs of the Next Generation Space Telescope itself. A key document in this respect is the report entitled "Next Generation Space Telescope – Visiting a Time when Galaxies were Young" edited by H.S. Stockman [2]. An important paper on wavefront sensing and control for NGST was published by Redding, Bely, Burg, Mosier et alteri at the 1998 SPIE conference in Kona [10]. Further important literature are papers by Mosier, Femiano and Ha on integrated modeling for NGST [11], derivation of an optimal control law for spacecraft slews [12], and fine pointing control for NGST [9]. Kissil prepared a number of internal memos on the various finite element models of the yardstick design [13] that are currently available. The second category comprises literature that was essential on a more generic level. Important references in structural dynamics are attributed to Craig [14] and Blevins [15]. The fundamental work that allows formulating the linearized models of complex optical systems in state space form was performed by Redding, Breckenridge and coworkers [16] and is based on geometrical ray tracing techniques. The theory of random stochastic processes is presented in a modern and concise manner by Brown and Hwang [17]. Bialke published a series of useful papers on the sources of reaction wheel disturbances [18]. Cryocooler disturbances were analyzed by Castles and James [19], as well as Collins [20]. A very useful reference for understanding and analyzing random vibrations is the textbook "Random Vibrations" by Wirsching, Paez and Ortiz. [21]. A good review of classical and modern control is provided by Dorf and Bishop [22] and by Bélanger [23]. Finally the Ph.D. thesis of Homero Gutierrez [24] was an invaluable resource for understanding and applying the disturbance and sensitivity analysis framework.

1.4.3 Thesis Methodology Roadmap

The performance assessment and enhancement analysis process for NGST follows a number of logical steps such as integrated modeling, performance assessment, sensitivity analysis and so forth. This process is complex and difficult to follow if we consider a full order system from the onset. Before analyzing the full order model of NGST a three degree-of-freedom (3DOF) sample problem was therefore developed and solved. The purpose of this sample problem is threefold:

- To develop and demonstrate the equations using a simplified but complete model
- To confirm the accuracy of the performance assessment and enhancement framework
- To gain insight into system-level trades including disturbance, plant and control parameters

The following block diagram (Figure 1.5) provides the methodology roadmap for this thesis. Each block is labeled with the corresponding chapter or section number Going from left to right in Figure 1.5 we see that the sub-models of structural dynamics, disturbance sources, optics and controls are first merged into an integrated model. Subsequently an initial performance assessment of the system is carried out. Model reduction and singular value decomposition of the optics matrices can help in reducing the computational burden as long as no significant loss of performance prediction is incurred.

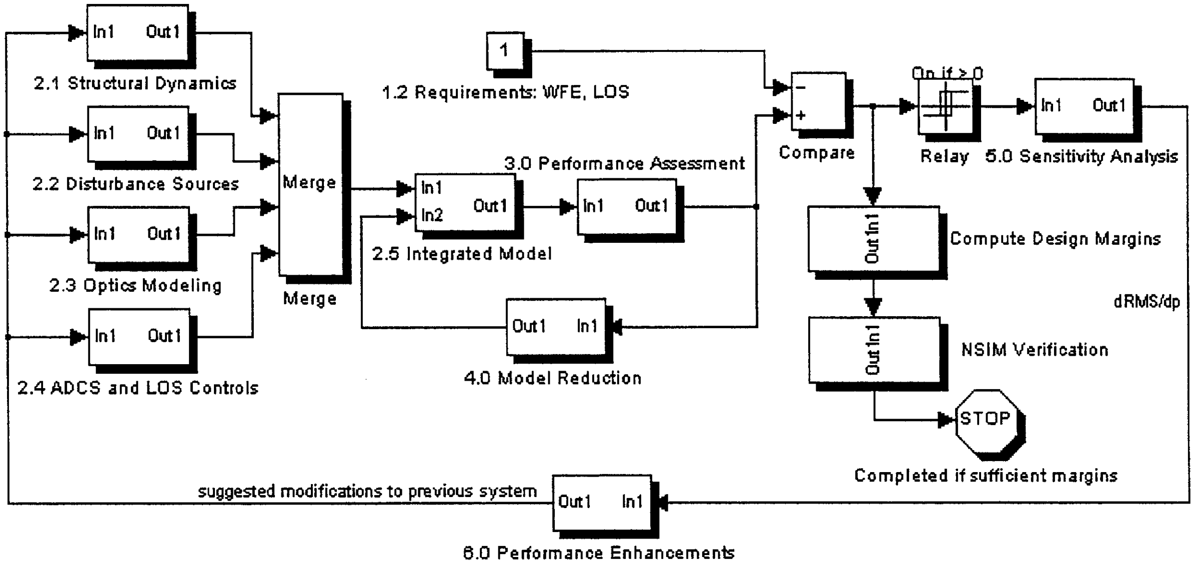

Figure 1.5: Block diagram representing the thesis roadmap

The performance in terms of RMS WFE and RMS LOS is subsequently compared with the engineering requirements for the system. If the requirements are met and the design margins appear to be sufficient a non-linear time domain simulation with NASA's NSIM model can be used to corroborate the results. If the requirements are not met a sensitivity analysis is initiated (relay box). The resulting sensitivities $\partial\sigma_z/\partial p_i$ represent the slope of the performance RMS σ_z with respect to the i-th parameter p_i. Sensitivities can be computed with respect to modal or physical parameters of the plant. This sensitivity information can be used to guide a performance enhancement or redesign effort, which results in a new and updated integrated model. The process is repeated until all requirements are met with sufficient design margin. This thesis demonstrates the process for a one-time iteration of the loop presented in figure 1.5 and only for selected system parameters that were deemed to be critical for the system's performance.

1.4.4 Thesis Contributions

As mentioned in the thesis objective section, this study focuses on applying proven controlled structures technology (CST) analysis and modeling methods to a new and challenging problem such as NGST. In selected areas new ideas and tools were developed, where this appeared to add value to existing capabilities. The following list contains some of the specific contributions of this research effort to integrated modeling and NGST.

- Applied steady-state disturbance analysis, sensitivity analysis and performance enhancement framework developed by H. Gutierrez to the Next Generation Space Telescope
- Proved the accuracy and applicability of the above framework and software with a simple three degree-of-freedom sample problem
- Performed system-level trade for NGST dynamics involving structural redesign, disturbance isolation and changes in the LOS control bandwidth
- Developed a methodology to obtain empirical state space models for linearly actuating Sterling cryocooler disturbances
- Performed an initial analysis of ITHACO E-Type reaction wheel spinup-test data using tools developed by R. Masterson and extended the capabilities of the RWA disturbance toolbox to accommodate several wheel models
- Performed analysis of multiple uncorrelated disturbance sources acting at the same time: reaction wheel assembly disturbances, cryocooler disturbances and guide star sensor noise and determined their relative contributions to the RMS performance metrics.

- Provided a method to compare the results of the generalized eigenvalue problem obtained from several sources such as IMOS and NASTRAN from the same finite element model
- Implemented a new application of singular value decomposition for optics linear sensitivity matrices in order so significantly speed up WFE computations in the frequency domain
- Demonstrated the potential benefits of input shaping to the slewing mode of NGST in a preliminary analysis
- Used NASA's non-linear end-to-end simulation tool NSIM to corroborate the results from the performance enhancement study

The section on future work points out recommended changes and enhancements to the integrated modeling process, including an extension of the sensitivity analysis framework.

Chapter 2

Integrated Modeling

2.1 Motivation

Definition: Integrated modeling, as presented in this thesis, is understood to be the process of assembly and analysis of an overall system model, containing realistic structures, disturbance, optics and controls models and their mutual interaction.

The traditional way of analyzing very complex dynamic systems by flowing requirements top-down and assigning clear error budgets (error budget tree method) for each subcomponent is not applicable to NGST anymore. A new understanding of integrated modeling consists in modeling each subsystem and its interaction with the other systems at once [11]. This leads to a front-to-end analysis of the disturbance to performance paths within the observatory. A truly integrated view utilizes linearized systems analysis in the frequency domain and non-linear time domain simulations in combination with each other. In order to compute the predicted performance – here defined in terms of RMS WFE and RMS LOS - and the mitigation provided by the optical, isolation and attitude controls we require a set of proven and useful tools in an integrated modeling environment. Such an environment has been described by Mosier and co-workers [11] for NGST. The tools used in this thesis are MSC/NASTRAN™ for finite element modeling and MACOS for linear optics modeling. A particularly important role is played by MATLAB™, as it is able to integrate the results from the above programs into an overall model using the controls, optimization, signal processing and other toolboxes. With progressing research we have been able to implement more and more functions, such as the eigenvalue problem solution and modeshape animation, directly in MATLAB™ without depending on commercial software packages. A crucial role is played by the IMOS toolbox [25], which has the ability to provide structural, optical, thermal and controls modeling capability for work at the conceptual and preliminary design levels.

The above tools are applied to the current NGST yardstick design to find out whether the performance specifications from section 1.2 can be met in the nominal case. If the results suggest that the performance cannot be met, we want to determine to which (modal or physical parameters) the performance is most sensitive to and use that knowledge to improve system performance enough to provide sufficient design margins. The main modeling tasks, which comprise the material of this chapter, are as follows:

- Structural dynamics modeling (section 2.2)
- Modeling of dynamic disturbance sources (section 2.3)
- Optics modeling, corresponds to performance modeling (section 2.4)
- Controls Modeling: ADCS and LOS stabilization models (section 2.5)
- Assembly and Analysis of overall system model (section 2.6)

In the context of this thesis, integrated modeling is used to predict the systems dynamics of NGST in terms of the science capability impact. Other uses of integrated models are to explore high-level design trades between competing architectures, to validate design concepts and to help guide the technology development activities of a large program [11].

2.1.1 Description of three degree-of-freedom (3DOF) sample problem

Before tackling the full order NGST model we will consider a much simpler integrated model that nevertheless contains most important aspects. A simple three-degree-of freedom (3DOF) sample problem of a precision opto-mechanical system was developed and solved. Firstly the problem is useful in the context of this thesis, since it derives the fundamental equations for integrated dynamics modeling. Secondly the problem was used to explore the advantages and disadvantages of different methods for predicting RMS (root-mean-square) performance values for an opto-mechanical system. Thirdly the solutions were used to analytically validate the accuracy of disturbance analysis and sensitivity analysis software tools previously developed by Gutierrez and Kenny [24]. Lastly the sample problem serves to pave the way for further developments such as the future implementation of sensitivity analyses with respect to disturbance filter or control parameters or the simultaneous optimization of the structures/controls/optics design

The 3DOF model can be thought of representing a large central mass containing the spacecraft bus and the science instruments to which a large aperture (represented by two smaller masses) is attached with a flexible link. The bus and aperture are modeled as concentrated masses connected by axial springs. The 3DOF sample problem is graphically shown in Figure 2.1. The path of stellar light from the apertures to the combiner is shown in gray.

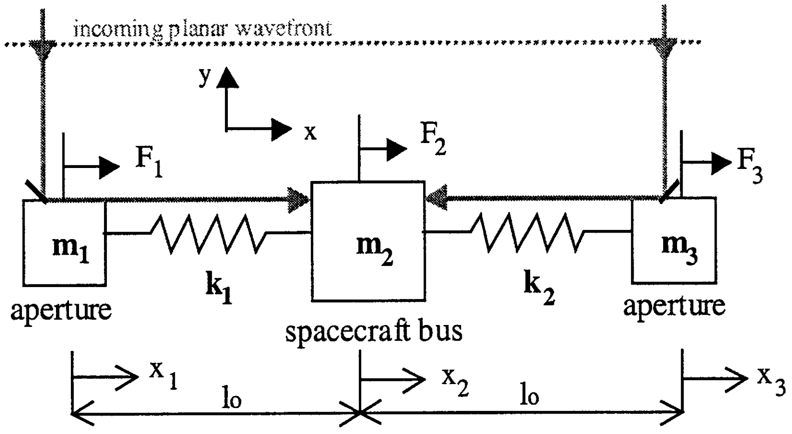

Figure 2.1: Conceptual model of opto-mechanical system with three degrees of freedom

A number of assumptions underlie the model presented in Figure 2.1. We are only interested in translational motion in the *x*-direction of the spacecraft coordinate frame. As a matter of simplification we set $m_1 = m_3 = m$. It is reasonable to assume that the bus is more massive than the apertures and we set $m_2 = 4m$. The mass of the compliant structure is neglected, the axial stiffness however is represented by identical linear springs $k_1 = k_2 = k$, that will be assigned realistic properties based on equivalent truss properties. The reference length of each arm is l_o, which will only enter into the expression for the equivalent stiffness k.

First the structural model for this sample problem is obtained by solving the generalized eigenvalue problem and assembling the corresponding state space system in 2nd order modal form. A dynamic disturbance acts at the central mass and can be characterized as a random white noise source filtered by a low-bass or alternatively by a band-pass shaping filter. The optics model consists of a linear sensitivity matrix that relates the physical displacements of the structure to the optical pathlength difference (OPD). Finally a low-impedance force actuator on one of the two springs is modeled in order to improve the performance with the help of a laser metrology sensor and a PD-controller. The integrated modeling process then consists in assembling all the sub-models into an overall state space system and analyzing its stability. The key feature of this sample problem is that it is tractable analytically (i.e. pencil and paper calculations) as well as numerically with existing MATLAB™ based analysis tools. The principles and equations derived from the sample problem are then applied to the more challenging modeling problems of the Next Generation Space Telescope (NGST). A block diagram of the integrated model for the sample problem is depicted in Figure 2.2. The disturbance w enters the system at the hub (= central mass) and is either fed through to the performance z via the $\mathbf{D}_{zw}$ matrix and/or enters the system through the disturbance influence matrix $\mathbf{B}_w$.

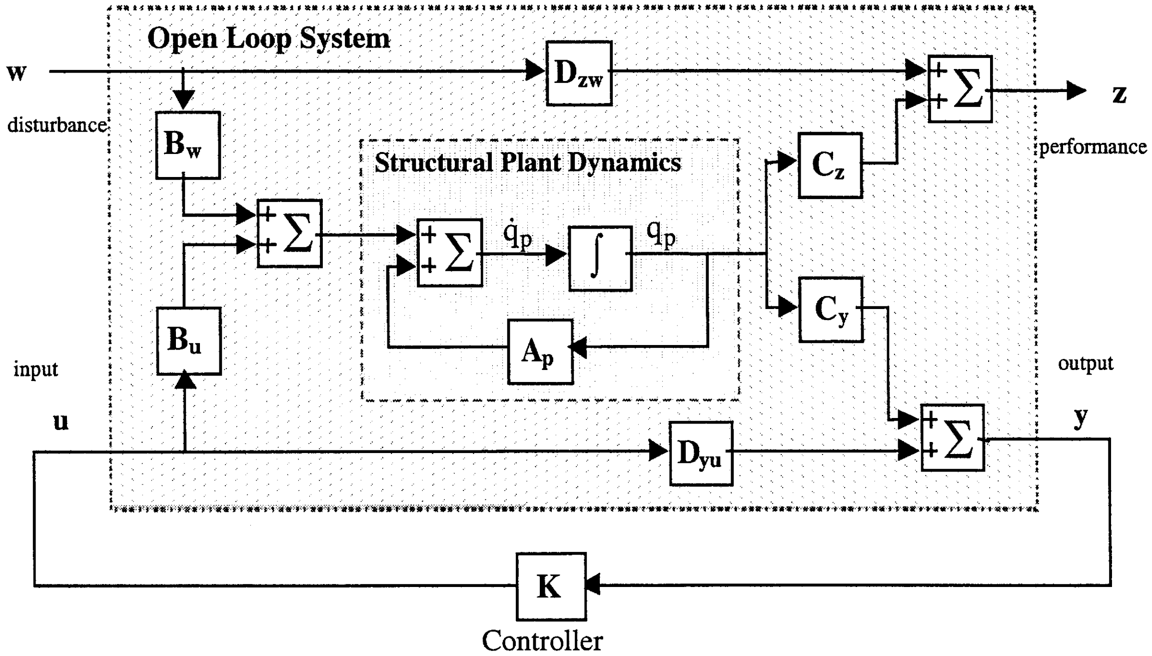

Figure 2.2: Block diagram of overall system ($\mathbf{D}_{yw}$ and $\mathbf{D}_{zu}$ not shown for simplicity)

All the outputs of the system are contained in y, which is captured by sensors, i.e. they are actually measured, whereas z contains the metrics by which we will assess the performance of the system. The matrices $\mathbf{C}_{yx}$, $\mathbf{C}_{y\dot{x}}$ and $\mathbf{C}_{zx}$, $\mathbf{C}_{z\dot{x}}$ determine the linear combination of the displacements and rates that contribute to the sensor measurements and performances. It is one of the most demanding tasks of integrated modeling to determine the **C** matrices correctly for a specific application. The determination of $\mathbf{C}_{yx}$, $\mathbf{C}_{y\dot{x}}$ will be covered in the controls modeling section, since it is a controller that ultimately uses the sensor signals. Determination of $\mathbf{C}_{zx}$, $\mathbf{C}_{z\dot{x}}$ will be covered in the optics modeling section, since the displacements of the structure affect the positions and orientations of optical elements (e.g. fast steering mirrors, primary mirror petals), which in turn affect the travel of science (and in some instances metrology) light through the system. The **D** terms are also called feedthrough terms since they feed *u* and *w* directly to the output side, while bypassing the system dynamics. Usually the feedthrough terms **D** for the structural plant are zero unless model reduction has been performed. The open loop state space system can be written in the following, very compact form,

$$\begin{bmatrix} \dot{\mathbf{q}}_p \\ \mathbf{z} \\ \mathbf{y} \end{bmatrix} = \begin{bmatrix} \mathbf{A}_p & \mathbf{B}_w & \mathbf{B}_u \\ \mathbf{C}_z & \mathbf{D}_{zw} & \mathbf{D}_{zu} \\ \mathbf{C}_y & \mathbf{D}_{yw} & \mathbf{D}_{yu} \end{bmatrix} \begin{bmatrix} \mathbf{q}_p \\ \mathbf{w} \\ \mathbf{u} \end{bmatrix} \tag{2.1}$$

where $\mathbf{q}_p$ represents the state vector of the plant dynamics. In mathematical terms the task of the disciplines in the integrated modeling process is to correctly determine the system matrices in the coefficient matrix of (2.1). This form is valid for systems of any complexity that have disturbances and controls inputs entering and performances as well as sensor outputs leaving the system. The closed form of (2.1) will be derived in section 2.6, whereby the controller matrices will have been previously determined in section 2.4. For the 3DOF problem *u, w, y* and *z* are scalars.

2.1.2 Introduction to the NGST Integrated Model

In more complex systems such as NGST the quantities **u, w, y** and **z** are vectors. The methods of MIMO controls and multivariable linear time invariant (LTI) systems are necessary to analyze these systems in a meaningful way. The systems level block diagram of NGST that is at the core of this thesis is represented in Figure 2.3. At first this diagram looks more complicated than the block diagram in Figure 1.4, which represents the NASA "NSIM" non-linear time simulation model. This is deceptive since the NSIM block diagram contains subsystems, which model the detailed behavior of the continuous-time, discrete-time and non-linear dynamics of the NGST fine pointing control system. While Figure 2.3 is partially based on this model it approximates the relevant dynamics with LTI state space systems in continuous time. It is necessary to elaborate on a number of these assumptions and simplifications in more detail. The system boundaries have been chosen such that they do not include the external environment. Specifically the RWA torques are really issued in response to external torques generated by solar radiation and the center of mass (CM) to center of pressure (CP) offset that is inevitable with a fixed sunshield configuration [26]. Also the vibration levels generated by the cryocooler are related to the thermal environment and the equilibrium temperature of the ISIM during observations. These interactions are simplified by assuming that the inputs to the system are the RWA disturbances, cryocooler vibrations and the fine guidance sensor (FGS) noise directly. The disturbance levels used in this thesis are reasonably chosen based on expected values of those environmental variables. The FGS noise level given as a noise equivalent angle (NEA) is due to the brightness magnitude of the chosen guide star, which can also be considered as an environmental variable. Additionally the integration time of the FGS between sensor updates determines the magnitude of the noise equivalent angle for a given guide star magnitude [7].

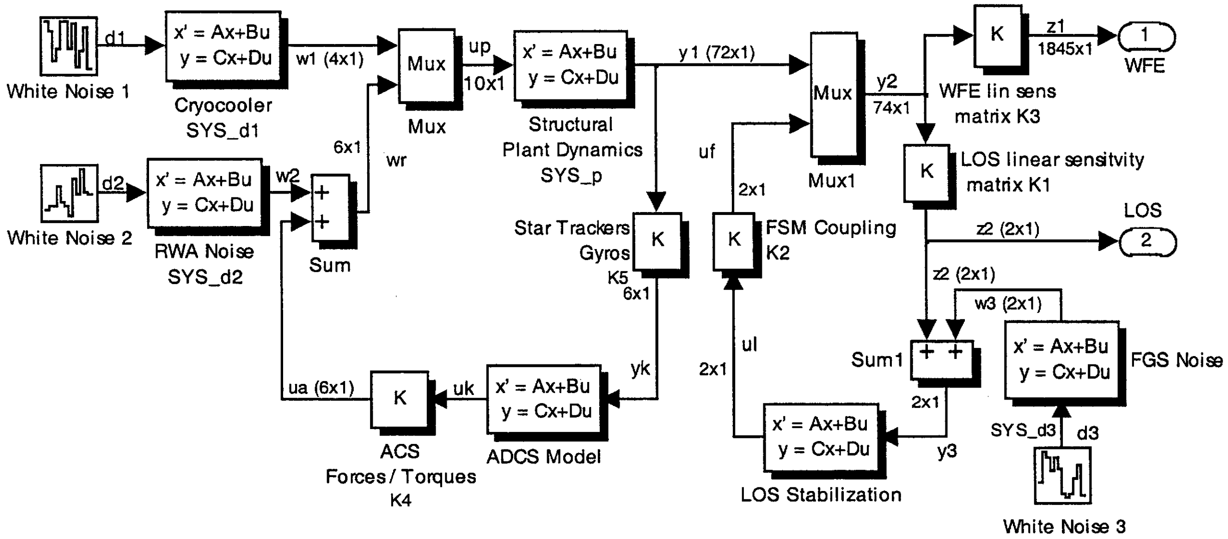

Figure 2.3: NGST continuous time LTI integrated model block diagram

Another simplification is that the coupling between the ADCS and the LOS control loops is neglected. This coupling will exist in reality since the ADCS must periodically desaturate the fast steering mirror (FSM) so that it remains close to the center of its useful range of motion. It is justified to neglect this low bandwidth coupling in the present study since the ADCS is primarily incorporated in the analysis in order to stabilize the rigid body modes. The ADCS does not significantly contribute to the performance metrics of interest since most disturbances act at frequencies well above the ADCS control bandwidth of 0.025 Hz. The subsequent sections will determine the dynamics of each component shown in Figure 2.3.

2.2 Structural Dynamics

2.2.1 Structural Dynamics Modeling for 3DOF Problem

The first step in structural dynamics modeling, regardless of the precise nature of the problem is to formulate the equations of motion of the system in an appropriate reference frame. A representation of the structure of the 3DOF problem was shown in Figure 2.1. In the present case the equations of motion can be formulated directly by looking at the freebody diagram for each mass.

$$\begin{aligned} m_1\ddot{x}_1 &= (x_2 - x_1)k_1 + F_1 \\ m_2\ddot{x}_2 &= -(x_2 - x_1)k_1 + (x_3 - x_2)k_2 + F_2 \\ m_3\ddot{x}_3 &= -(x_3 - x_2)k_2 + F_3 \end{aligned} \tag{2.2}$$

It shall be noted that these equations represent a linear system of 2nd order, coupled differential equations. The coupling makes these equations challenging to solve in the present form. These equations are then conveniently rewritten in matrix form as,

$$\underbrace{\begin{bmatrix} m_1 & 0 & 0 \\ 0 & m_2 & 0 \\ 0 & 0 & m_3 \end{bmatrix}}_{\mathbf{M}} \underbrace{\begin{bmatrix} \ddot{x}_1 \\ \ddot{x}_2 \\ \ddot{x}_3 \end{bmatrix}}_{\ddot{\mathbf{x}}} + \underbrace{\begin{bmatrix} k_1 & -k_1 & 0 \\ -k_1 & k_1 + k_2 & -k_2 \\ 0 & -k_2 & k_2 \end{bmatrix}}_{\mathbf{K}} \underbrace{\begin{bmatrix} x_1 \\ x_2 \\ x_3 \end{bmatrix}}_{\mathbf{x}} = \underbrace{\begin{bmatrix} F_1 \\ F_2 \\ F_3 \end{bmatrix}}_{\mathbf{F}} \tag{2.3}$$

$$\mathbf{M}\,\ddot{\mathbf{x}} + \mathbf{K}\,\mathbf{x} = \mathbf{F} \qquad (2.4)$$

where **M** and **K** are the global mass and stiffness matrix respectively and **F** is the vector of external forces. Note that (2.4) does not contain an explicit damping matrix **C**, as might be expected since all structures and materials experience some amount of damping due to the irreversible dissipation of mechanical energy during structural motion. Damping is typically added at a later stage of the modeling process [14]. The forces **F** arise from a superposition of disturbance and control actuator forces. We are assuming that the spring constants of both springs are equal and can be computed from the axial stiffness of an equivalent truss structure.

$$k_1 = k_2 = k = \frac{EA}{l_o} \qquad (2.5)$$

A set of initial model properties was chosen for this sample problem in Table 2.1. The values are based on related experiences from realistic programs. It will be the goal of future research to apply optimization algorithms to these nominal values in order to optimize performance within given bounds of the material properties.

Table 2.1: Sample problem nominal model properties

Mass parameter m	200 kg
Young's modulus E[4]	$71 \cdot 10^9$ N/m^2
Cross sectional area A[5]	0.001 m^2
Reference length l_o	10 m

We further reduce the number of system parameters by letting $m_1=m_3=m$ and $m_2=4m$. This together with the symmetric spring assumption leads to the following simplified equations of motion:

---

[4] Elastic modulus of aluminum [27]

[5] Corresponds to 10cm^2 cross sectional area, reasonable value for a large space truss [28]

$$\underbrace{\begin{bmatrix} m & 0 & 0 \\ 0 & 4m & 0 \\ 0 & 0 & m \end{bmatrix}}_{\mathbf{M}} \underbrace{\begin{bmatrix} \ddot{x}_1 \\ \ddot{x}_2 \\ \ddot{x}_3 \end{bmatrix}}_{\ddot{\mathbf{x}}} + \underbrace{\begin{bmatrix} k & -k & 0 \\ -k & 2k & -k \\ 0 & -k & k \end{bmatrix}}_{\mathbf{K}} \underbrace{\begin{bmatrix} x_1 \\ x_2 \\ x_3 \end{bmatrix}}_{\mathbf{x}} = \underbrace{\begin{bmatrix} F_1 \\ F_2 \\ F_3 \end{bmatrix}}_{\mathbf{F}} \tag{2.3a}$$

M:	global mass matrix	**F**:	vector of applied forces
K:	global stiffness matrix	**x**:	vector of physical displacements

A normal modes analysis is then performed, since we do not neglect the accelerations $\ddot{\mathbf{x}}$. This is done to gain insight into the dynamic behavior of the structure. We assume a periodic unforced response at each degree of freedom of the form [14]:

$$x_i = e^{j\omega t} \quad , \qquad \mathrm{i} = 1,\ 2,\ 3 \tag{2.6}$$

Substituting (2.6) in (2.3a) we can write the following expression:

$$\begin{bmatrix} mj^2\omega^2 & 0 & 0 \\ 0 & 4mj^2\omega^2 & 0 \\ 0 & 0 & mj^2\omega^2 \end{bmatrix} e^{j\omega t} + \begin{bmatrix} k & -k & 0 \\ -k & 2k & -k \\ 0 & -k & k \end{bmatrix} e^{j\omega t} = \begin{bmatrix} 0 \\ 0 \\ 0 \end{bmatrix} \tag{2.7}$$

Since we assume that $e^{j\omega t} \neq 0$ and by substituting $\lambda = \omega^2$ and $j^2 = -1$ we obtain the formulation for the generalized eigenvalue problem,

$$[\mathbf{K} - \lambda_i \mathbf{M}] \cdot \phi_i = 0 \tag{2.8}$$

where λ_i is the i-th eigenvalue of the structure (square of the natural vibration frequency in rad/sec) and ϕ_i is the i-th eigenvector. The ϕ_i's are the columns of the matrix $\mathbf{\Phi}$, that is oftentimes referred to as the modeshape matrix. First the eigenvalues are computed by setting the determinant of [$\mathbf{K}$-λ_i $\mathbf{M}$] to zero.

$$\det[\mathbf{K}-\lambda\mathbf{M}]=\det\begin{bmatrix} k-\lambda m & -k & 0 \\ -k & 2k-4\lambda m & -k \\ 0 & -k & k-\lambda m \end{bmatrix}=\mathbf{0} \tag{2.9}$$

After evaluating the determinant and some algebra we obtain a polynomial of degree n = 3, that can be solved for the eigenvalues λ.:

$$-2m^2\lambda^3+5km\lambda^2-3k^2\lambda=0 \tag{2.10}$$

We can factor out λ and multiply by (-1) so that the following expression is obtained:

$$\lambda\left(2m^2\lambda^2-5km\lambda+3k^2\right)=0 \tag{2.11}$$

It becomes immediately clear that one of the eigenvalues is $\lambda_1 = 0$. This eigenvalue corresponds to the translational rigid body mode in the x-direction as will be seen later. The remaining quadratic equation in brackets can be solved easily to yield,

$$\lambda_{2,3}=\frac{5km\pm\sqrt{25k^2m^2-24k^2m^2}}{4m^2}=\frac{5km\pm km}{4m^2}=\frac{5k\pm k}{4m} \tag{2.12}$$

so that we have three distinct and real eigenvalues, which we can evaluate by substituting the previously determined physical model properties (Table 2.1) for the stiffness k and the mass m.

$$\begin{aligned} \lambda_1 &= 0 = 0\left[\frac{rad^2}{\sec^2}\right] \\ \lambda_2 &= \frac{4km}{4m^2}=\frac{k}{m}=35500\left[\frac{rad^2}{\sec^2}\right] \\ \lambda_3 &= \frac{6km}{4m^2}=\frac{3k}{2m}=53250\left[\frac{rad^2}{\sec^2}\right] \end{aligned} \tag{2.13}$$

The natural frequencies in cycles per second [Hz] are the square root of the eigenvalues divided by 2π:

$$\begin{aligned} f_1 &= \frac{\omega_1}{2\pi} = \frac{\sqrt{\lambda_1}}{2\pi} = 0 \quad [Hz] \\ f_2 &= \frac{\omega_2}{2\pi} = \frac{\sqrt{\lambda_2}}{2\pi} = 29.99 \quad [Hz] \\ f_3 &= \frac{\omega_3}{2\pi} = \frac{\sqrt{\lambda_3}}{2\pi} = 36.73 \quad [Hz] \end{aligned} \tag{2.14}$$

It was mentioned that the first mode at 0 Hz is the rigid body mode, but the question remains what behavior the other two modes exhibit. This question can be answered by computing the corresponding eigenvectors ϕ_i.

$$[\mathbf{K}-\lambda_1\mathbf{M}]\cdot\phi_1 = 0 = \begin{bmatrix} k & -k & 0 \\ -k & 2k & -k \\ 0 & -k & k \end{bmatrix}\begin{bmatrix} \phi_{11} \\ \phi_{21} \\ \phi_{31} \end{bmatrix} = 0 \quad , \quad \text{thus } \phi_1 = \begin{bmatrix} 1 \\ 1 \\ 1 \end{bmatrix} \tag{2.15a}$$

$$[\mathbf{K}-\lambda_2\mathbf{M}]\cdot\phi_2 = 0 = \begin{bmatrix} 0 & -k & 0 \\ -k & 2k & -k \\ 0 & -k & 0 \end{bmatrix}\begin{bmatrix} \phi_{12} \\ \phi_{22} \\ \phi_{32} \end{bmatrix} = 0 \quad , \quad \text{thus } \phi_2 = \begin{bmatrix} 1 \\ 0 \\ -1 \end{bmatrix} \tag{2.15b}$$

$$[\mathbf{K}-\lambda_3\mathbf{M}]\cdot\phi_3 = 0 = \begin{bmatrix} -k/2 & -k & 0 \\ -k & -4k & -k \\ 0 & -k & -k/2 \end{bmatrix}\begin{bmatrix} \phi_{13} \\ \phi_{23} \\ \phi_{33} \end{bmatrix} = 0 \quad , \quad \text{thus } \phi_3 = \begin{bmatrix} 2 \\ -1 \\ 2 \end{bmatrix} \tag{2.15c}$$

When solving for the eigenvectors it becomes clear that $[\mathbf{K}-\lambda_i\mathbf{M}]$ is not positive definite, since the λ_i's are by definition all solutions to the characteristic equation. Thus the magnitude of the eigenvectors is not uniquely defined. If however we choose one of the entries of the eigenvector arbitrarily, then all other entries are automatically defined. We will turn to the matter of normalization of the eigenvectors later in this section. The eigenvectors are the columns of the modeshape matrix Φ.

$$\Phi = \left[\phi_1 | \phi_2 | \phi_3 \right] = \begin{bmatrix} 1 & 1 & 2 \\ 1 & 0 & -1 \\ 1 & -1 & 2 \end{bmatrix} , \quad \text{and} \quad \Phi^T = \begin{bmatrix} \phi_1^T \\ \phi_2^T \\ \phi_3^T \end{bmatrix} = \begin{bmatrix} 1 & 1 & 1 \\ 1 & 0 & -1 \\ 2 & -1 & 2 \end{bmatrix} . \qquad (2.16)$$

The physical interpretation of the eigenvectors as modeshapes is based on the underlying notion that the relative magnitudes of the components of the eigenvector correspond to the modeshape, i.e. the dynamic displacements occurring at that particular natural frequency. In the present case we can schematically depict the system behavior for the three modes of interest (Figure 2.4).

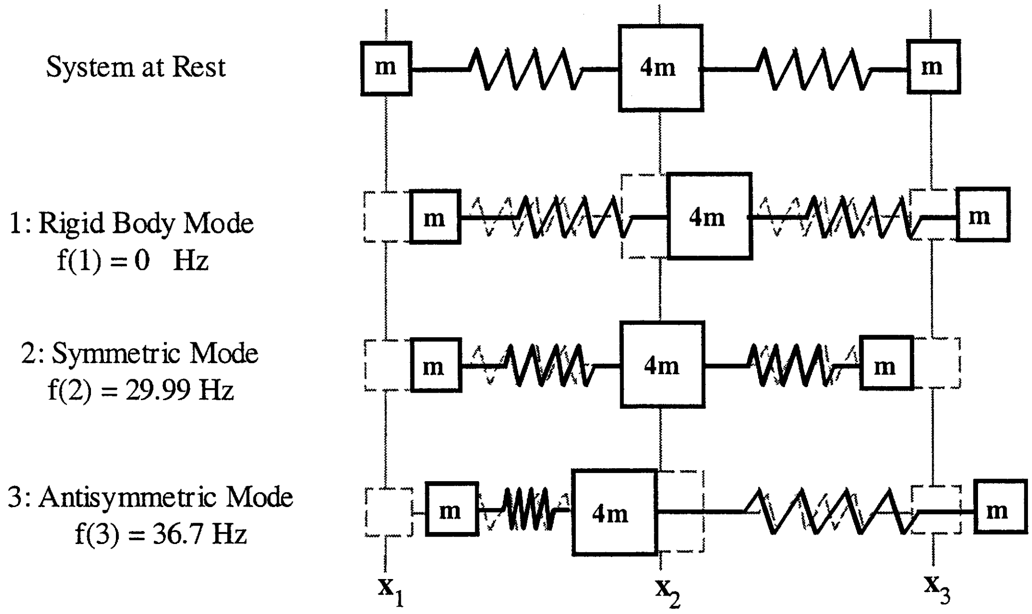

Figure 2.4: Mode shape visualization for sample 3DOF problem

It can be seen that the displacements are all equal in the rigid body mode so that every component of the structure experiences uniform translation. Since there are no relative displacements, the system contains no strain energy. For mode number 2 (the first flexible mode) we have symmetric deflections of the two aperture nodes, so that both springs are in tension or in compression at the same time. The third mode is characterized by anti-symmetric deflections of the aperture nodes, so that while one spring is in compression, the other spring will be in tension and vice versa.

For structural dynamics purposes we perform normalization of the matrix Φ using the mass matrix **M** because we will ultimately work in modal coordinates. Normal (= modal) coordinates allow to write an arbitrary motion of the system as a linear combination of the eigenvectors (=modeshapes), since these form an orthogonal set. The modal mass matrix $\tilde{\mathbf{M}}$ is obtained by pre-multiplying **M** with the transpose of Φ and by post-multiplying with Φ.

$$\Phi^T \mathbf{M} \Phi = \tilde{\mathbf{M}} = \tilde{\mathbf{M}}^{1/2} \cdot \tilde{\mathbf{M}}^{1/2} \tag{2.17}$$

Thus the normal modes of an undamped structure are orthogonal by the mass matrix. $\tilde{\mathbf{M}}$ Is the matrix containing the modal masses on the main diagonal. We can thus rewrite the right side of equation (2.17) as shown above. Pre and post-multiplication with $\tilde{\mathbf{M}}^{-1/2}$ yields,

$$\underbrace{\left(\tilde{\mathbf{M}}^{-1/2}\right)^T \Phi^T}_{{}^o\Phi^T} \mathbf{M} \underbrace{\Phi \tilde{\mathbf{M}}^{-1/2}}_{{}^o\Phi} = \left(\tilde{\mathbf{M}}^{-1/2}\right)^T \tilde{\mathbf{M}}^{1/2} \cdot \tilde{\mathbf{M}}^{1/2} \tilde{\mathbf{M}}^{-1/2} = \mathbf{I} \tag{2.18}$$

Thus we can write

$${}^o\Phi^T \mathbf{M}\, {}^o\Phi = \mathbf{I} = \begin{bmatrix} 1 & 0 & 0 \\ 0 & 1 & 0 \\ 0 & 0 & 1 \end{bmatrix} \tag{2.19}$$

${}^o\Phi$ is called the mass normalized mode shape matrix. Applying the above derivation to our sample 3DOF problem and substituting (2.3a) and (2.16) into (2.17) we get the following result:

$$\Phi^T \mathbf{M} \Phi = \begin{bmatrix} 1 & 1 & 1 \\ 1 & 0 & -1 \\ 2 & -1 & 2 \end{bmatrix} \begin{bmatrix} m & 0 & 0 \\ 0 & 4m & 0 \\ 0 & 0 & m \end{bmatrix} \begin{bmatrix} 1 & 1 & 2 \\ 1 & 0 & -1 \\ 1 & -1 & 2 \end{bmatrix} = \tilde{\mathrm{M}} = \begin{bmatrix} 6m & 0 & 0 \\ 0 & 2m & 0 \\ 0 & 0 & 12m \end{bmatrix} \tag{2.20}$$

Thus the modal masses are 1200, 400 and 2400 kg respectively. The mass normalized modeshape matrix is then given as:

$$ {}^{o}\Phi = \Phi\tilde{\mathbf{M}}^{-1/2} = \begin{bmatrix} 1 & 1 & 2 \\ 1 & 0 & -1 \\ 1 & -1 & 2 \end{bmatrix} \begin{bmatrix} \frac{1}{\sqrt{6m}} & 0 & 0 \\ 0 & \frac{1}{\sqrt{2m}} & 0 \\ 0 & 0 & \frac{1}{\sqrt{12m}} \end{bmatrix} = \begin{bmatrix} \frac{1}{\sqrt{6m}} & \frac{1}{\sqrt{2m}} & \frac{2}{\sqrt{12m}} \\ \frac{1}{\sqrt{6m}} & 0 & \frac{-1}{\sqrt{12m}} \\ \frac{1}{\sqrt{6m}} & \frac{-1}{\sqrt{2m}} & \frac{2}{\sqrt{12m}} \end{bmatrix} \tag{2.21} $$

There exists a second useful orthogonality relationship of the mode shape matrix with the stiffness matrix **K**. First the matrix of eigenvalues Λ is defined as,

$$ \Lambda = \Omega^2 = \begin{bmatrix} \omega_1^2 & 0 & 0 \\ 0 & \omega_2^2 & 0 \\ 0 & 0 & \omega_3^2 \end{bmatrix} = \begin{bmatrix} \lambda_1 & 0 & 0 \\ 0 & \lambda_2 & 0 \\ 0 & 0 & \lambda_3 \end{bmatrix} \tag{2.22} $$

where pre-multiplication of **K** with Φ^{T} and post-multiplication with Φ gives,

$$ \Phi^T \mathbf{K}\, \Phi = \tilde{\mathbf{M}}\Lambda \tag{2.23} $$

as with the mass matrix we pre- and post-multiply with $\tilde{\mathbf{M}}^{-1/2}$ and obtain

$$ \underbrace{\left(\tilde{\mathbf{M}}^{-1/2}\right)^T \Phi^T}_{{}^{o}\Phi^T} \mathbf{K} \underbrace{\Phi\, \tilde{\mathbf{M}}^{-1/2}}_{{}^{o}\Phi} = \Lambda = {}^{o}\Phi^T \mathbf{K}\ {}^{o}\Phi = \Lambda = \Omega^2 \tag{2.24} $$

We have seen that the set of eigenvectors is a linearly independent, orthogonal set of $N = 3$ vectors and can be used as a basis for the N space. This is closely related to the notion of modal expansion, where an arbitrary motion of the structure can be represented in terms of the modal contributions. We can write the following transformation from physical coordinates to modal coordinates:

$$ \mathbf{x} = {}^{o}\Phi\, \xi \tag{2.25} $$

This linear transformation through the mass normalized mode shape matrix $^{o}\Phi$ can be written componentwise as,

$$\begin{bmatrix} x_1 \\ x_2 \\ x_3 \end{bmatrix} = \underbrace{\left[\,^{o}\phi_1 \middle| ^{o}\phi_2 \middle| ^{o}\phi_3\right]}_{^{o}\Phi} \begin{bmatrix} \xi_1 \\ \xi_2 \\ \xi_3 \end{bmatrix} = {}^{o}\phi_1\xi_1 + {}^{o}\phi_2\xi_2 + {}^{o}\phi_3\xi_3 \tag{2.26}$$

where the ξ_i's are the modal (also called normal) coordinates. ξ_1 for example represents the contribution of mode 1 to the motion of the physical coordinates x_1, x_2 and x_3. By substituting (2.25) in the original equations of motion (2.4) we obtain the equations of motion in modal space

$$\mathbf{M}\ \ddot{\mathbf{x}} + \mathbf{K}\ \mathbf{x} = \mathbf{M}^{o}\Phi\ddot{\xi} + \mathbf{K}^{o}\Phi\xi = \mathbf{F} \tag{2.27}$$

and pre-multiplication with $^{o}\Phi^{T}$ along with substitution of (2.19) and (2.24) yields

$$\underbrace{^{o}\Phi^{T}\mathbf{M}^{o}\Phi}_{\mathbf{I}}\ddot{\xi} + \underbrace{^{o}\Phi^{T}\mathbf{K}^{o}\Phi}_{\Omega^2}\xi = \underbrace{^{o}\Phi^{T}\mathbf{F}}_{\mathbf{Q}} \tag{2.28}$$

Invoking the orthogonalities that were derived earlier, we can rewrite the equations of motion as a function of the modal coordinates ξ, the normal frequency matrix $\Omega^2$and the modal force matrix **Q**. The matrix **Q** represents the effective modal influence of the physical forces **F**.

$$\mathbf{Q} = {}^{o}\Phi^{T}\mathbf{F} \tag{2.29}$$

The modal force matrix **Q** is also closely related to controllability and disturbability. Specifically, if $^{o}\Phi$ contains a zero at a specific degree of freedom (row) and specific mode (column), this means that an applied control input force (controllability) or disturbance force (disturbability) will have no effect at that location for that particular mode. The modal form of the equations of motion (2.28) is especially convenient, because the coupled 2nd order differential equations from (2.4) are now decoupled, which makes them easy to solve. Now is also a good time to add damping to the system. Since damping is not easy to determine a priori, the modal damping ratios ζ_i are often determined empirically. The modal damping matrix **Z** is diagonal and is given as:

$$\mathbf{Z} = \begin{bmatrix} \zeta_1 & 0 & 0 \\ 0 & \zeta_2 & 0 \\ 0 & 0 & \zeta_3 \end{bmatrix} \tag{2.30}$$

The modal damping coefficients are in practice often different for every mode and typically vary between 0.1% and 3% for lightly damped space structures [29]. One of the largest uncertainties in spacecraft conceptual design is associated with modal damping. The damping ratios depend on a number of factors such as pre-tension, material properties, temperature and forcing levels. For this sample problem we will assume $\zeta_i = 0.005$, where i = 1,2,3. The equations of motion in modal coordinates then become,

$$\ddot{\xi} + 2\mathbf{Z}\Omega\dot{\xi} + \Omega^2\xi = \mathbf{Q} = {}^o\Phi^T\mathbf{F} \tag{2.31}$$

if we solve this equation for $\ddot{\xi}$ we obtain

$$\ddot{\xi} = -2\mathbf{Z}\Omega\dot{\xi} - \Omega^2\xi + {}^o\Phi^T\mathbf{F} \tag{2.32}$$

We can write a state vector of modal coordinates and modal velocities as follows,

$$\mathbf{q}_p = \begin{bmatrix} \xi \\ \dot{\xi} \end{bmatrix} \tag{2.33}$$

whereby the subscript *p* indicates that we are dealing with the states of the structural plant. The modal force matrix **Q** can be broken up into contributions from control inputs **u** and disturbances **w**, where $\beta_\mathbf{u}$ and $\beta_\mathbf{w}$ are the control and disturbance influence coefficient matrix respectively. The matrices $\beta_\mathbf{u}$ and $\beta_\mathbf{w}$ usually contain only ones or zeros to indicate at which degrees of freedom of the structural plant the forces act. We then obtain the following Equation:

$$\mathbf{Q}={}^{o}\Phi^{T}\mathbf{F}={}^{o}\Phi^{T}\mathbf{F}_{u}+{}^{o}\Phi^{T}\mathbf{F}_{w}={}^{o}\Phi^{T}\beta_{u}\mathbf{u}+{}^{o}\Phi^{T}\beta_{w}\mathbf{w} \tag{2.34}$$

With (2.33) and (2.34), we can write the equations of motion (the "dynamics") in 2nd order modal form, while assuming that the structure exhibits linear behavior.

$$\dot{\mathbf{q}}_{p}=\underbrace{\begin{bmatrix}\mathbf{0} & \mathbf{I}\\ -\Omega^{2} & -2\mathbf{Z}\Omega\end{bmatrix}}_{\mathbf{A}_{p}}\mathbf{q}_{p}+\underbrace{\begin{bmatrix}\mathbf{0}\\ {}^{o}\Phi^{T}\beta_{u}\end{bmatrix}}_{\mathbf{B}_{u}}\mathbf{u}+\underbrace{\begin{bmatrix}\mathbf{0}\\ {}^{o}\Phi^{T}\beta_{w}\end{bmatrix}}_{\mathbf{B}_{w}}\mathbf{w} \tag{2.35}$$

The other important relationships, that complete the state space representation, are the output **y** and the performance **z** equation. In general the outputs are given as a linear combination of the coordinates in physical space, or as a combination of states in modal space:

$$\mathbf{y}=\mathbf{C}_{yx}\mathbf{x}+\mathbf{C}_{y\dot{x}}\dot{\mathbf{x}}=\mathbf{C}_{yx}{}^{o}\Phi\xi+\mathbf{C}_{y\dot{x}}{}^{o}\Phi\dot{\xi}=\begin{bmatrix}\mathbf{C}_{yx}{}^{o}\Phi & \mathbf{C}_{y\dot{x}}{}^{o}\Phi\end{bmatrix}\mathbf{q}_{p} \tag{2.36}$$

Output equation:
$$\mathbf{y}=\underbrace{\begin{bmatrix}\mathbf{C}_{yx}{}^{o}\Phi & \mathbf{C}_{y\dot{x}}{}^{o}\Phi\end{bmatrix}}_{\mathbf{C}_{y}}\mathbf{q}_{p}+\underbrace{[\mathbf{0}]}_{\mathbf{D}_{yu}}\mathbf{u}+\underbrace{[\mathbf{0}]}_{\mathbf{D}_{yw}}\mathbf{w} \tag{2.37}$$

Performance equation:
$$\mathbf{z}=\underbrace{\begin{bmatrix}\mathbf{C}_{zx}{}^{o}\Phi & \mathbf{C}_{z\dot{x}}{}^{o}\Phi\end{bmatrix}}_{\mathbf{C}_{z}}\mathbf{q}_{p}+\underbrace{[\mathbf{0}]}_{\mathbf{D}_{zu}}\mathbf{u}+\underbrace{[\mathbf{0}]}_{\mathbf{D}_{zw}}\mathbf{w} \tag{2.38}$$

The vector **y** contains all the outputs of the system, which are captured by sensors, i.e. they are actually measured, whereas **z** contains the metrics by which we will assess the performance of the system. It is now time to compute the matrices of the structural plant for our sample problem. From (2.35) we can compute the state transition matrix of the structural plant $\mathbf{A}_{p}$ as follows:

$$\mathbf{A}_{p}=\underbrace{\begin{bmatrix}\mathbf{0} & \mathbf{I}\\ -\Omega^{2} & -2\mathbf{Z}\Omega\end{bmatrix}}_{\mathbf{A}_{p}}=\begin{bmatrix}0 & 0 & 0 & 1 & 0 & 0\\ 0 & 0 & 0 & 0 & 1 & 0\\ 0 & 0 & 0 & 0 & 0 & 1\\ -\omega_{1}^{2} & 0 & 0 & -2\zeta_{1}\omega_{1} & 0 & 0\\ 0 & -\omega_{2}^{2} & 0 & 0 & -2\zeta_{2}\omega_{2} & 0\\ 0 & 0 & -\omega_{3}^{2} & 0 & 0 & -2\zeta_{3}\omega_{3}\end{bmatrix} \tag{2.39}$$

The determination of the remaining system matrices shown in Figure 2.2 is the objective of the other disciplines of integrated modeling such as disturbance modeling, performance modeling (optics) and control design.

2.2.2 NGST Yardstick Finite Element Model

The structural modeling task for NGST is eminently important and consists in modeling the Yardstick design with its main structural members such as plates, beams, rods, concentrated masses, generalized stiffnesses and rigid body elements. According to the definition by Crawley [30] this model has to be considered a first generation model since no test data is available. The difficulty lies in correctly simplifying the structure and its mass distribution and stiffnesses so that the important dynamics are captured without creating an exceedingly large finite element model (FEM) at the conceptual level. It is difficult to obtain a solution for a model of the complexity of NGST analytically. Therefore the 3DOF model from the previous section was only used to derive the fundamental equations without claiming to accurately capture the NGST dynamics. A simplified 4 DOF model of NGST has been developed by Burg [31]. That particular model condenses the largest subsystems of NGST into lumped masses. The Sunshield, SSM, OTA and SM are represented by point masses, which are connected with flexible springs. In Burg's approach the springs are tuned, so that the expected fundamental modes for sunshield bending (0.3 Hz), isolation truss bending (8 Hz) and secondary tower bending (4.4 Hz) coincide with the natural frequencies of the connecting springs.

This approach, while very useful for first order trades, requires a priori knowledge of the fundamental system modes. Another drawback of such simplified models is that they do not provide a realistic estimate of the optical performance metrics. While a rough estimate of the WFE can be obtained via the OPD as a linear combination of the nodal displacements, the centroid location on the focal plane, which defines the LOS jitter, is more elusive for these low order models. As a consequence NASA (GSFC, MSFC and JPL) developed a series of more refined finite element models [13]. For the purposes of this thesis a simplified FEM was developed that is based on the `ngst603` model. It retains the same nodal numbering scheme but significantly reduces the number of grid points and elements to represent the NGST Yardstick design. This model is entitled `ngst810`[6] and only retains essential elements and grid points to speed up computations for the subsequent performance assessment and sensitivity analyses.

The FEM, shown in Figure 2.5, contains 109 grid points and 573 active degrees-of-freedom. Originally NASA created a detailed model of the Optical Telescope Assembly (OTA) independently of the full observatory model, to study issues such as thermal/structure interactions and optical compensation. The OTA was attached via a hexapod to the isolation truss (modeled as a single equivalent beam). This substructure was then mated with highly simplified models for the Spacecraft Support Module (SSM), Integrated Science Instrument Module (ISIM), and thermal isolation truss. On the other side of the OTA the isolation truss attaches to the spacecraft bus, containing avionics and propulsion tanks, which are modeled as a point mass with associated inertia matrix. Most of the attention for the SSM has gone into modeling of the sunshield membranes, and inflatable booms. The suggested analytical approaches are uncertain and require testing [11]. For now, the membrane mass has been distributed along the length of the beam elements that model the booms. The remainder of the SSM and ISIM consist of concentrated mass and beam elements [13]. One of the major simplifications of the `ngst810` model compared to its parent `ngst603` is that the Beryllium OTA facesheet and reaction structure have been merged together. The model nevertheless captures the essential dynamics with only 109 nodes and 573 active degrees of freedom. The model is intended for rapid turnaround trade studies and not for detailed design studies.

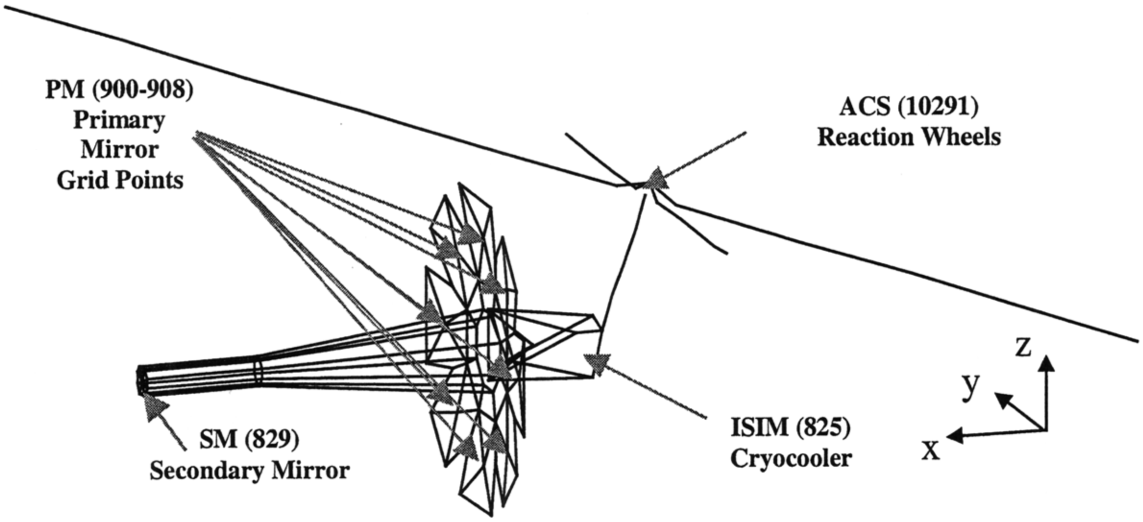

Figure 2.5: Simplified NGST finite element model (`ngst810`) of the Yardstick design

---

[6] `ngst810` was released on 10 August 1998, same numbering scheme as the other NGST models

For the dynamics analysis, a simplification is made by assuming that the mirror petals act as rigid bodies. This assumption followed preliminary analysis that indicated the mirror-petal first mode was approximately 400 Hz. Accordingly, the optics model only relies on knowledge of the motions of 11 of the 12 grid points identified in Figure 2.5. For the LTI structural plant dynamics model named *SYS_p* in Figure 2.3, the state-space system is expanded to contain the six zero frequency modes. These are the three translational and three rotational rigid body modes. Inputs are the forces and torques from the cryocooler (4 components) and from the reaction wheels (6 components). The RWA disturbances enter the system at the ACS grid point (10291), whereas the cryocooler disturbances enter at the ISIM grid point (825). Obviously the performance is distributed in nature. The simplifications of the individual petals as rigid body allows choosing one representative grid point per primary mirror petal and one for the center petal (900-908). These 9 grid points are located at the center of the primary and in a circle with radius 2.8 meters. Furthermore we pick off the displacements of the integrated science instrument module ISIM (825), which contains the FSM, DM, cryocooler and the focal plane, and the node located at the apex of the secondary mirror SM (829). It is expected that the SM lateral and axial displacements will contribute significantly to the optical performance. Thus there are a total of 11 optical grid points, which represent 66 degrees of freedom. The additional 6 degrees of freedom, which are outputs of the finite element model, are the 3 rotations and 3 angular rates of the ACS grid point (10291). In total we have 10 inputs (6 from RWA and 4 from cryocooler) and 72 outputs.

2.2.3 Normal Modes Analysis

The established method of analyzing the dynamics of the structural system is the normal modes analysis. In order to assemble the state space system in orthonormal form with modal coordinates as the states of the system as was done for the sample problem in Equation (2.35) we first need to solve the generalized eigenvalue problem. This is analogous to the procedure in the 3DOF problem. The complexity is much larger here since we merely had to solve a 3rd order polynomial for the eigenvalues in Equation (2.10). In the full order NGST model this corresponds to solving a 573rd order characteristic equation since we have 573 active degrees of freedom. We must rely on efficient numerical algorithms to extract a subset of eigenvalues and eigenvectors. This problem involves solving for the eigenvalues λ_i and the eigenvectors ϕ_i, assuming that the global stiffness and mass matrices **K** and **M** have been previously assembled in MSC/NASTRAN ™ or IMOS. In general **K** and **M** are each real symmetric and positive semi-definite. The generalized eigenvalue problem is posed as:

$$[\mathbf{K} - \lambda_i \mathbf{M}] \cdot \phi_i = 0 \tag{2.40}$$

The eigenvectors ϕ_i that are obtained from the normal modes analysis represent the flexible and rigid body modes of the structure. The eigenfrequencies ω_i can also be represented via Rayleigh's Equation [32] using the orthogonalities for **M** and **K** derived in (2.19) and (2.24) respectively:

$$\omega_i^2 = \frac{\{\phi_i\}^T [\mathbf{K}] \{\phi_i\}}{\{\phi_i\}^T [\mathbf{M}] \{\phi_i\}} \tag{2.41}$$

As a reminder the relevant orthogonalities for the mass matrix **M** are written as

$$\begin{aligned} \phi_i^T \mathbf{M} \phi_j &= 0 && \text{for all } i \neq j \text{ and} \\ \phi_j^T \mathbf{M} \phi_j &= \tilde{m}_j && \text{where } \tilde{m}_j \text{ is the j-th modal mass} \end{aligned} \tag{2.42}$$

the equivalent orthogonalities for the stiffness matrix are given as

$$\begin{aligned} \phi_i^T \mathbf{K} \phi_j &= 0 && \text{for all } i \neq j \text{ and} \\ \phi_j^T \mathbf{K} \phi_j &= k_{ij} && \text{which is the j-th generalized stiffness } = \omega_i^2 \tilde{m}_j \end{aligned} \tag{2.43}$$

A natural mode of the structure can be represented by using its generalized mass and generalized stiffness. This is very useful in formulating equivalent dynamics models and in component mode synthesis [33]. The eigenvectors are then assembled into the modeshape matrix Φ as follows:

$$\Phi = \left[\underbrace{\phi_1 \quad \phi_2 \quad \phi_3 \quad \phi_4 \quad \phi_5 \quad \phi_6}_{\text{Rigid Body Modes}} \quad \underbrace{\phi_7 \quad \cdots \quad \phi_{nm}}_{\text{Flexible Modes}} \right]$$

(2.44)

where *nm* is the number of modes retained in the model. The rigid body modes are useful in conducting dynamic analyses of unconstrained structures, such as NGST. For a routine validity check it is recommended to animate normal mode shapes ϕ_i thus providing valuable insight into the dynamic behavior of the system. Figure 2.6 shows a mosaic of four interesting modes for the `ngst810` finite element model. The first flexible mode is expected to be due to the ultra-light sunshield and is predicted to occur at 0.29 Hz. The first bending modes of the sunshields in all NGST Yardstick models up to this point are in the 0.3-0.5 Hz range [13], easily the lowest frequency of the flexible modes. According to Mosier with the membrane mass and stiffness more properly modeled, these frequencies are expected to drop by at least a factor of 2-3 [11].

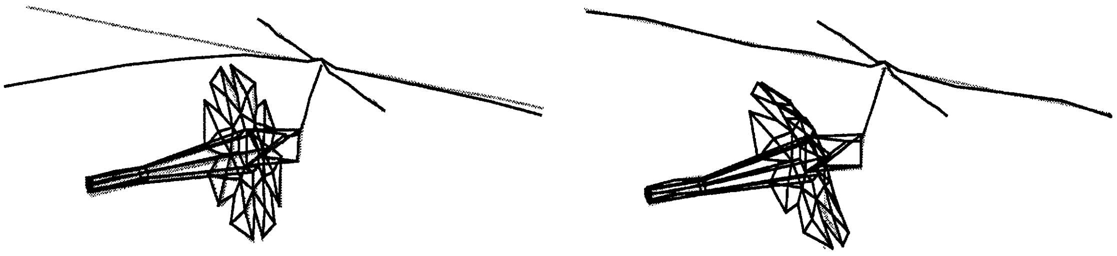

Mode 7: 0.29 Hz First Flexible Mode - Sunshield Bending

Mode 32: 7.38 Hz Global Pitch Mode - Primary Mirror Bending

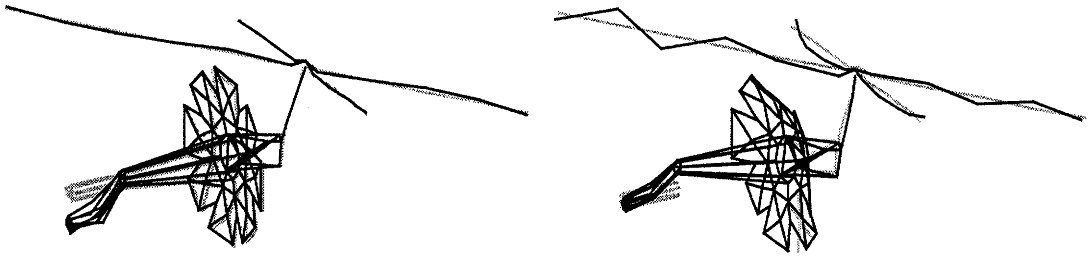

Mode 20: 3.445 Hz First Secondary Tower Bending

Mode 46: 12.07 Hz Coupled Mode - SM, PM and ISS

Figure 2.6: Selection of NGST flexible modes (`ngst810` model)

Other significant modes are the bending modes of the secondary mirror support blades at 3.4 Hz and the first global pitch mode involving the primary mirror at 7.38 Hz. Mode 46 for example involves global strain energy distribution including OTA pitch motion, secondary tower bending and higher order sunshield bending. The i-th natural frequency is obtained from the solution of (2.41) and is given as

$$\omega_i = \sqrt{\lambda_i} \tag{2.45}$$

The natural frequencies in Hertz are then obtained as:

$$f_i = \frac{\omega_i}{2\pi} \qquad i=1,2,3 \ldots nm = \# \text{ of modes} \tag{2.46}$$

Two different ways have been explored to solve for the FEM dynamics of this system. The first way involves solving the normal modes analysis (undamped) in MSC/NASTRAN™ and then converting the modal data to MATLAB format via an ASCII file reader. The second method consists in converting the NASTRAN bulk data deck to IMOS and using a sparse eigensolver to obtain the mode shapes and eigenfrequencies. These two different approaches are represented in Figure 2.7.

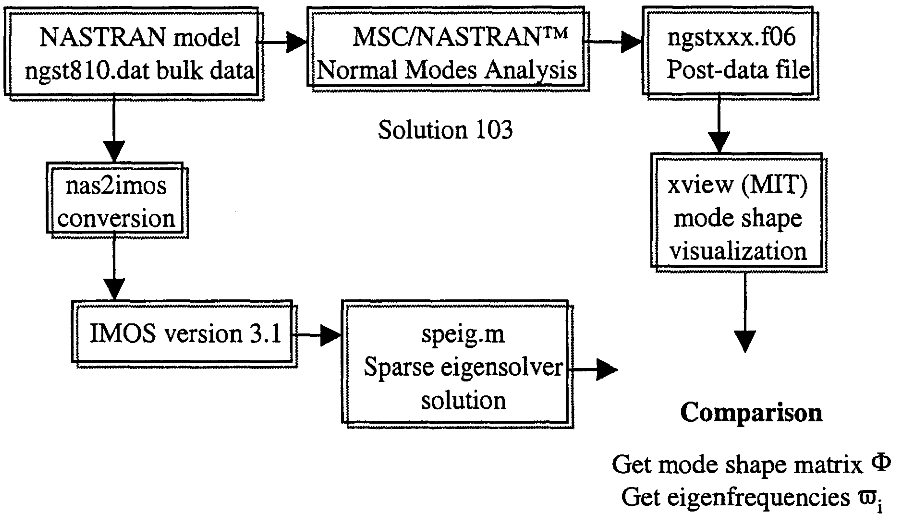

Figure 2.7: Two different methods to solve eigenvalue problem for NGST

To obtain the flexible body dynamics in IMOS, the model is converted from a NASTRAN bulk data deck into an IMOS input file using `nas2imos.m`. In MATLAB™, this IMOS model assembles the mass and stiffness matrices, and an eigenanalysis is performed to extract the desired number of modes [25]. In order to verify the consistency of the results a comparison was made between modeshapes and eigenfrequencies obtained from MSC/NASTRAN™ using the Lanzcos eigensolver and those obtained from the sparse eigensolver `speig.m` in IMOS [25] that uses the Arnoldi factorization. Figure 2.8 represents the comparison of mode numbers versus modal frequency.

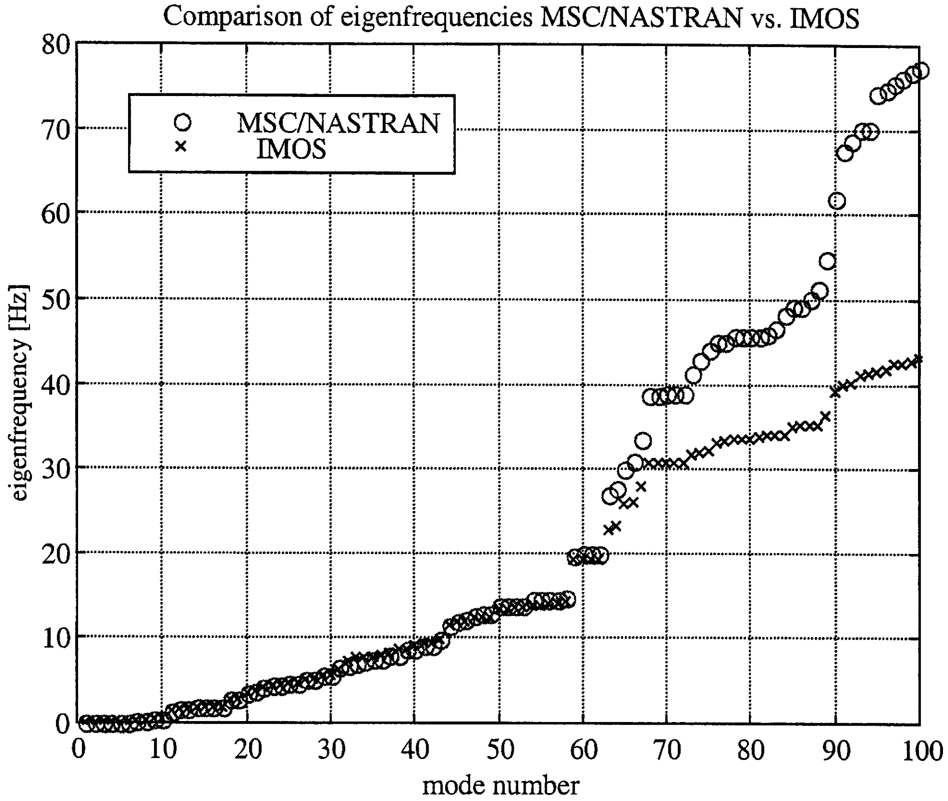

Figure 2.8: Comparison of modal frequencies MSC/NASTRAN vs. IMOS

The most important conclusion is that the natural frequencies match very well up to about mode 60. After that both curves split apart but show the same trends. It will be necessary to investigate the reasons for this discrepancy above mode 60 in future research. Possible reasons are differences in the mass matrix formulation (lumped versus consistent formulation) or numerical differences of the eigensolvers. Also the curve indicates regions of high modal density, where the mode number vs. frequency [Hz] curve is very flat. This is true in the region between 12 Hz and

15 Hz, which exhibits a large number of higher order sunshield and primary mirror modes. The MSC/NASTRAN™ model solutions will be used for this thesis, since their results have been proven to be accurate in benchmark tests. The modal assurance criterion MAC was used to verify the cross-orthogonality of modeshapes obtained from the MSC/NASTRAN™ (1) and IMOS (2) solvers respectively. A MAC value of 1.0 indicates a perfect match, whereby the MAC is defined as follows:

$$MAC_{ij} = \left| \frac{\phi_1(i)^T \cdot \phi_2(j)}{|\phi_1(i)| \cdot |\phi_2(j)|} \right| \tag{2.47}$$

where $\phi_1(i)$ is the i-th modeshape obtained from NASTRAN and $\phi_2(j)$ is the j-th modeshape obtained from IMOS. It can be seen that for a perfect match we would expect a diagonal of impulses at 1.0. The MAC is also frequently used to compare model and test data against each other.

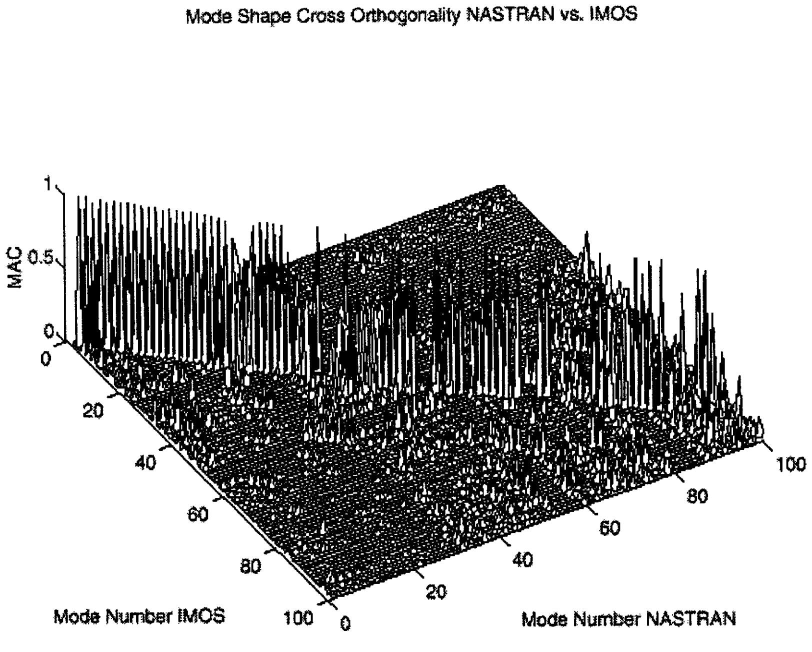

Figure 2.9: Modeshape orthogonality of MSC/NASTRAN™ vs. IMOS

The correspondence again is good up to about mode 50. The conclusion is that the results from this modal analysis can be trusted only for the lower modes. According to a structural dynamics rule-of-thumb the number of accurate modes is usually about 10% of the number of DOF's in the finite element model. Since we have 573 active degrees-of-freedom in our model we can have faith in about the first fifty modes. This corresponds exactly to the region where the NASTRAN and IMOS results match.

Based on the modeling experience gained for NGST it can be said that one of the computational bottlenecks of the modeling process is the solution of the generalized eigenvalue problem [34]. This is particularly true if it is performed with the `speig.m` eigensolver. Figure 2.10 compares the results obtained by Uebelhart for the computational cost of NASTRAN versus `speig.m`.

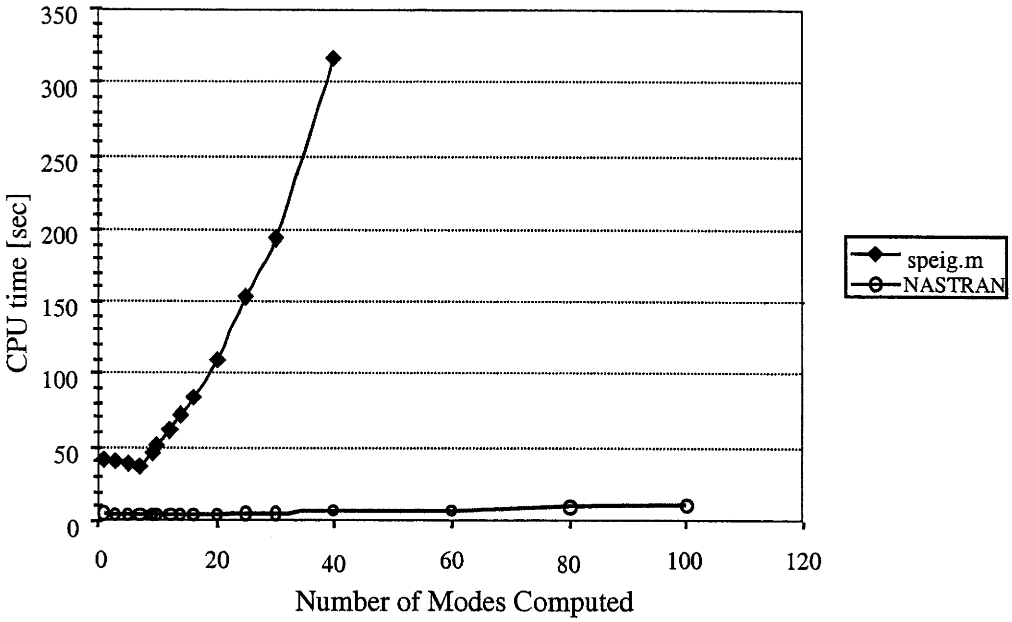

Figure 2.10: CPU time comparison for MSC/NASTRAN™ versus `speig.m` eigensolver

It is evident that the CPU time increases drastically for the `speig.m` eigensolver with an increasing number of modes and it is therefore not recommended for large problems. Currently the most efficient way of solving this problem is to perform the eigensolution in NASTRAN and to extract the eigenfrequencies and eigenvectors from the `.f06` or `.prt` file using a conversion program. The assembly of the state space system can then happen in the MATLAB™ environment. Future work will include the incorporation of Lanzcos based eigensolvers such as `lanz.m` as mex-files, which should lead to faster analysis times for a large number of extracted modes within the MATLAB environment.

2.2.4 Assembly of state space system for the structural plant

Once the natural frequencies and modeshapes are available, the input and output degrees of freedom are defined and the state-space system (A_p, B_p, C_p, D_p) matrices are assembled. This is done by assuming a modal damping ratio of $\zeta_i = 0.001$ for the entire structure. It is straightforward to modify the A_p-matrix at a later time to change the damping, even on a mode-by-mode basis. The state space equations in orthonormal modal form are then written as:

$$\begin{bmatrix} \dot{\xi} \\ \ddot{\xi} \end{bmatrix} = \underbrace{\begin{bmatrix} \mathbf{0} & \mathbf{I} \\ -\Omega^2 & -2Z\Omega \end{bmatrix}}_{\mathbf{A_p}} \begin{bmatrix} \xi \\ \dot{\xi} \end{bmatrix} + \underbrace{\begin{bmatrix} \mathbf{0} \\ {}^{o}\Phi^T \beta_u \end{bmatrix}}_{\mathbf{B_p}} \mathbf{u_p} \qquad (2.48)$$

where ξ are the modal coordinates, Ω is the matrix of natural frequencies, $\mathbf{Z}$ contains the modal damping ratios ζ on the main diagonal, ${}^{o}\Phi$ is the mass normalized mode shape matrix, β_u is the input influence coefficient matrix and $\mathbf{u_p}$ is the plant input vector. The plant input vector contains the cryocooler and the reaction wheel disturbances and can be written as follows:

$$\mathbf{u_p} = \begin{bmatrix} \underbrace{F_x^{825} \quad F_y^{825} \quad F_z^{825} \quad M_x^{825}}_{\text{Cryocooler}} \quad \underbrace{F_x^{10291} \quad F_y^{10291} \quad F_z^{10291} \quad M_x^{10291} \quad M_y^{10291} \quad M_z^{10291}}_{\text{Reaction Wheel Assembly}} \end{bmatrix} \qquad (2.49)$$

where F_i denotes a force component and M_i denotes a moment component. The right superscript refers to the FEM grid point number, where the particular disturbance component is entering the system (see Figure 2.5) and the subscript denotes the coordinate axis. In the orthonormal modal form global damping of ζ=0.001 was added to the system. This is a conservative assumption due to the uncertainties of the deployable structural components (sunshield, isolation truss and secondary tower) and the cryogenic environment. There exists evidence that the amount of damping is not uniform with frequency and that the "warm" and "cold" sections of the telescope will experience different amounts of structural damping as the dissipative mechanisms in materials and joints are themselves temperature dependent [35].

Finally the $\mathbf{C_p}$ matrix contains the output influence coefficients, which describe the outputs as a linear combination of the physical displacements of the structure. The outputs y_1 of the structural plant according to Figure 2.3 are the displacements and rotations of the 11 grid points shown in Figure 2.5 and the three angles and rates at the ACS grid point that are used by the attitude determination sensors. The output equation is written as

$$\mathbf{y}_1 = \underbrace{\begin{bmatrix} C_{yx}{}^{o}\Phi & C_{y\dot{x}}{}^{o}\Phi \end{bmatrix}}_{\mathbf{C_p}} \underbrace{\begin{bmatrix} \xi \\ \dot{\xi} \end{bmatrix}}_{\mathbf{q_p}} \tag{2.50}$$

whereby the feedthrough term $\mathbf{D_p}$ is equal to zero. The completed structural plant state space system (2.51) from the inputs $\mathbf{u_p}$ to the outputs $\mathbf{y}_1$ is then retained for the integrated modeling process:

$$\begin{aligned} \dot{\mathbf{q}}_\mathbf{p} &= \mathbf{A_p q_p} + \mathbf{B_p u_p} \\ \mathbf{y}_1 &= \mathbf{C_p q_p} \end{aligned} \tag{2.51}$$

2.3 Modeling of Dynamic Disturbance Sources

There are external and internal disturbances (generated onboard), which are expected to act on NGST. In order to quantify the effect of these dynamic disturbances on the WFE and LOS jitter it is necessary to accurately model the disturbances in the time or frequency domain. Potential disturbance sources that create vibrational mechanical energy onboard the spacecraft are all parts that contain rotating or translating machinery. On precision space structures the following components often contribute a significant amount to the micro-vibration environment:

- Reaction wheel assembly due to static and dynamic imbalances of the flywheels
- Cryocoolers due to imbalances of the compressor and expander pistons
- Fast Steering mirrors introduce reaction torques to the support structure
- Sloshing of propellants and cryogens

Based on experience from previous programs and on experimental tests, it must be determined which sources are to be modeled in detail. It shall be noted that there are also a number of other non-mechanical disturbances that enter the system as noise such as photon noise at the detectors, dark current or shot noise. In this study the main internal disturbances are due to reaction wheels, cryocooler vibration and guide star sensor noise. The only significant external disturbance at L2 is the solar torque about the spacecraft center of mass. The solar torque is not modeled in this thesis since it is assumed that the reaction wheels already counteract the solar torque. This section begins with the simple hub disturbance for the 3DOF sample problem. Subsequently the cryocooler, RWA and guide star sensor noise disturbances are modeled for NGST.

2.3.1 Sample 3DOF Disturbance

A disturbance enters the three-degree-of freedom system as w and must be characterized mathematically. There are two main tasks involved in modeling a dynamic disturbance in this context. Firstly we must determine at which physical location the disturbance is acting. Typically the disturbance source is attached to the structure at some point and the degrees of freedom of that particular grid point location must be included in the disturbance influence matrix β_w. In our sample problem the disturbance enters at the center mass m_2 as a random force F_x. The disturbance influence matrix β_w is thus given as:

$$\beta_w = \begin{bmatrix} 0 \\ 1 \\ 0 \end{bmatrix} \tag{2.52}$$

and the disturbance input matrix B_w is computed as,

$$\mathbf{B}_w = \begin{bmatrix} \mathbf{0} \\ {}^o\Phi^T \beta_w \end{bmatrix} = \begin{bmatrix} \mathbf{0}_{3x1} \\ {}^o\phi_{21} \\ {}^o\phi_{22} \\ {}^o\phi_{23} \end{bmatrix} = \begin{bmatrix} 0 & 0 & 0 & \frac{1}{\sqrt{6m}} & 0 & \frac{-1}{\sqrt{12m}} \end{bmatrix}^T \tag{2.53}$$

It is interesting to note that there are only zeros in the two states, which correspond to mode 2, the symmetric mode. This is due to the fact that the central mass is sitting at a node of the second mode and thus it is not disturbable. The second step in characterizing the disturbance is to estimate the frequency content of the disturbance energy. Representing the frequency content in power spectral density (PSD) form conveniently does this [36]. The noise energy is concentrated over a certain frequency region, whereby there is a cutoff frequency of the disturbance, i.e. the disturbance is band limited. A convenient way off thinking of this problem is to imagine a source of white noise that is filtered by a "disturbance" transfer function.

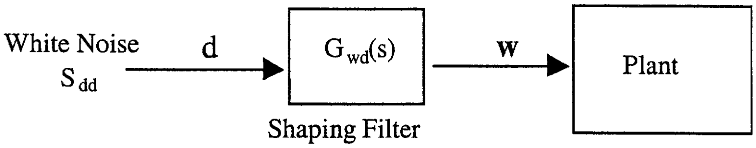

Figure 2.11: Representation of disturbance with shaping filter

The simplest such transfer function is a low-pass filter (LPF) of the form

$$^{LPF}G_{wd}(s) = \frac{w(s)}{d(s)} = \frac{\omega_{RO}}{s + \omega_{RO}} \tag{2.54}$$

where *w(s)* is the shaped disturbance, *d(s)* is the white noise, $s = j\omega$ is the complex frequency and ω_{RO} is the rolloff or corner frequency in rad/sec. The disturbance power spectral density (PSD) function can be obtained from the following relationship [21] as,

$$S_{ww}(\omega) = G_{wd}(j\omega) \cdot S_{dd} \cdot G_{wd}(j\omega)^H \tag{2.55}$$

where S_{dd} is the intensity of the white noise, $G_{wd}(j\omega)$ is the white noise to disturbance transfer function matrix and S_{ww} is the cross spectral density matrix of the disturbance w. For the low-pass filter approximation we obtain:

$$^{LPF}S_{ww}(\omega)=\frac{S_{dd}\omega_{RO}^{2}}{\omega^{2}+\omega_{RO}^{2}}=S_{ww}(2\pi f)=\frac{S_{dd}f_{RO}^{2}}{f^{2}+f_{RO}^{2}} \tag{2.56}$$

It shall be noted that the units of the PSD are N^2/Hz for force disturbances and $(Nm)^2$/Hz for moment disturbances. The LPF usually significantly overpredicts the energy content at low frequency since dynamic disturbances usually scale with the square of the wheel speed or with the actuating frequency of a particular mechanism. If accurate disturbance energy content is required at low frequency it is better to use a band-pass filter (BPF) as disturbance shaping filter. The shaping filter for a band-limited noise source is given as

$$^{BPF}G_{wd}(s)=\frac{w(s)}{d(s)}=\frac{\omega_{RO}s}{(s+\omega_{RU})(s+\omega_{RO})} \tag{2.57}$$

and the corresponding PSD is

$$^{BPF}S_{ww}(\omega)=\frac{S_{dd}\omega_{RO}^{2}\omega^{2}}{(\omega_{RO}^{2}+\omega^{2})(\omega_{RU}^{2}+\omega^{2})}=S_{ww}(2\pi f)=\frac{S_{dd}f_{RO}^{2}f^{2}}{(f_{RO}^{2}+f^{2})(f_{RU}^{2}+f^{2})} \tag{2.58}$$

Figure 2.12 plots the two power spectral densities for the disturbance F_x in the sample problem. As we will see later there are different methods to propagate this disturbance through the system in order to predict the performance z. The frequency domain approach demands PSD's in the form of equations (2.58) and (2.60) respectively. The Lyapunov approach however requires that the disturbance filter be written in state space form. Rewriting the LPF transfer function we obtain the following:

$$^{LPF}G_{wd}(s)=\frac{\omega_{RO}}{s+\omega_{RO}} \tag{2.59}$$

This can be written in canonical controller form as,

$$\begin{aligned}\dot{q}_{d1} &= [-\omega_{RO}]q_{d1} + [1]d = A_{d1}q_{d1} + B_{d1}d \\ w &= [\omega_{RO}]q_{d1} + [0]d = C_{d1}q_{d1} + D_{d1}d\end{aligned} \tag{2.60}$$

with ω_{RO}= 200π rad/sec we get the following numerical values:

$$\begin{aligned}\dot{q}_{d1} &= [-628.3]q_{d1} + [1]d = A_{d1}q_{d1} + B_{d1}d \\ w &= [628.3]q_{d1} + [0]d = C_{d1}q_{d1} + D_{d1}d\end{aligned} \tag{2.61}$$

We only need one state to describe the LPF approximation in state space. For this analysis we will assume unit intensity white noise so that S_{dd}=1. The feedthrough terms $\mathbf{D}_{zw}$ and $\mathbf{D}_{yw}$ are zero. Figure 2.12 shows a comparison of the LPF (left) and BPF (right) disturbance PSD's. We see that both PSD appear to be very smooth. This is due to the fact that we are using low order representations for the shaping filters. We will see that more complicated PSD's can also be approximated with the shaping filter approach as long as a larger number of states is used in the shaping filter equations.

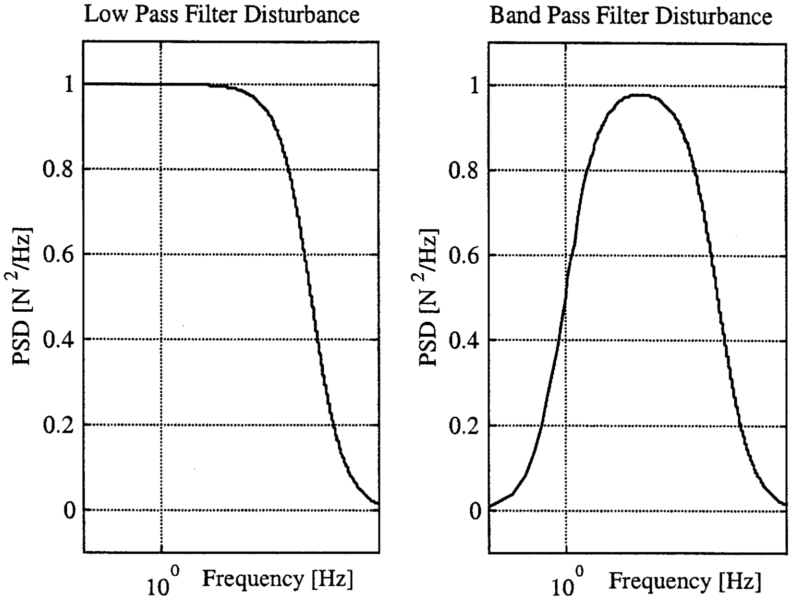

Figure 2.12: Comparison of LPF and HPF disturbance shaping filters

2.3.2 Cryocooler Disturbance Model

Many dynamics analyses focus exclusively on reaction wheel disturbances, because they are expected to be the dominant source of dynamic disturbances. They are however not the only potential source of vibration energy. The goal of this section is to explore the cryocooler assembly in the ISIM Dewar of NGST. Cryocoolers are going to have a crucial function for NGST. They are going to provide the necessary active cooling for the MIR SiAs-detectors down to about ~ 7-8 K during observations in the wavelength range from 2-16 μm [2]. Currently a reversed Brayton-cycle cooler was recommended due to its low mass (< 10 kg), long life and very low level of vibration. This particular type of cooler however is still at a very experimental stage and only a few laboratory prototypes currently exist. This analysis demonstrates the consequences of reverting to traditional Sterling cryocoolers from a dynamics perspective.

Sterling cryocoolers operate at a given drive frequency, which remains fixed during MIR observations [19], unlike the RWA spectra, where the fundamental and its harmonics occur at different frequencies as a function of wheel speed ω. Typical cryocooler drive frequencies are 20-70 Hz. The vibration levels of many cryocoolers differ by orders of magnitude, depending on the type and exact configuration as demonstrated by Castles and co-workers [37]. Major differences in experimentally measured vibration levels are due to:

- Type of cryocooler: Sterling single/dual stage, reverse-Brayton, tactical coolers
- single vs. dual arrangement (nulling of fundamental frequency)
- cooling regime depending on heat load [mW]
- Application of active vibration suppression techniques

Typical vibration levels for the axial force direction of Sterling cryocoolers are between 0.001 N and 50 N at the fundamental drive frequency. Figure 2.13 shows an overview of commercially available Sterling cryocooler technology. It is characteristic to see both the cylindrical expander and compressor housings next to each other.

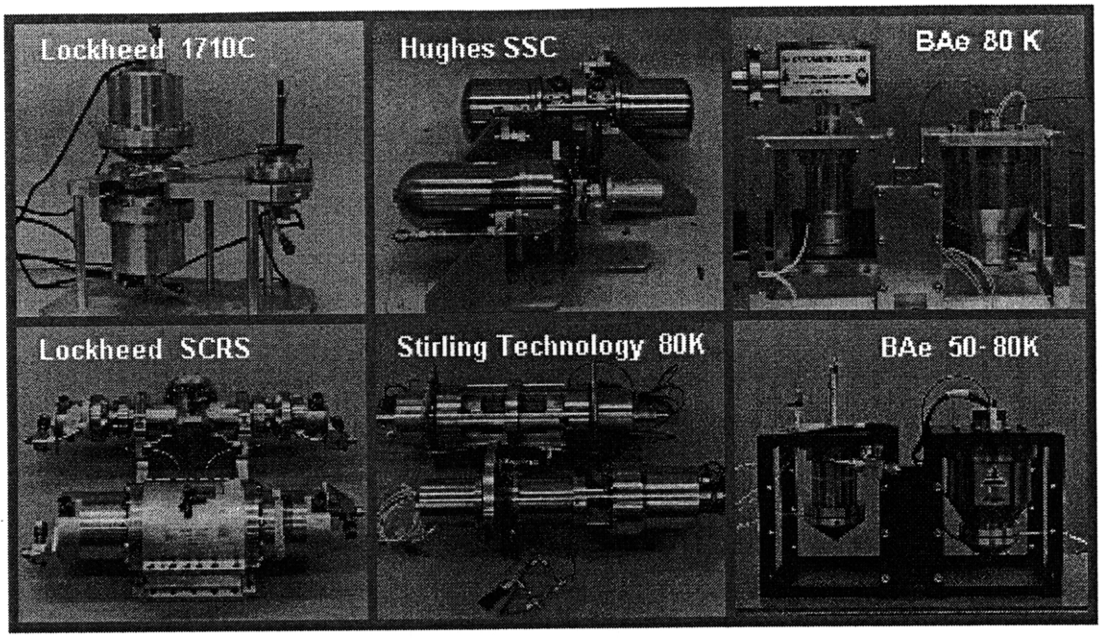

Figure 2.13: Representation of commercially available Sterling cryocoolers [38]

The cooling in the Sterling cycle is achieved through controlled motion of a piston and a displacer to compress and then expand a working fluid [19]. Sterling cryocoolers are subdivided into two main components: a compressor stage, which performs work on the cryogenic fluid /gas (NGST: He T_{crit} = 5.5 K) and an expander, which has a thermal link with the cold finger. Vibrations are generated by a momentum imbalance between the linearly reciprocating elements. The nonlinear gas spring creates the higher harmonics.

When modeling a piece of machinery that will cause vibrational energy to enter the system there are two fundamental approaches. The first approach relies on physically modeling the plant that causes the vibration and to assign realistic values to the physical parameters of the model. The second approach consists in creating an empirical model of the disturbance via the analysis of experimental test data. Both approaches were explored for the cryocooler disturbance model. The physical based model allows to predict the disturbance spectrum based on the physical design parameters of the cryocooler such as m_d the displacer mass, m_e the expander mass, stroke, drive frequency etc., whereas the empirical model relies on the extraction of harmonic frequencies and amplitudes from vibration test data. Physical cryocooler vibration modeling has previously been investigated by Collins [20]. A PSD representation is generally converted into an equivalent state space representation by approximating the harmonics with 2nd order lightly damped poles. A verification is carried out to insure that the disturbance RMS values from the PSD and the state space approach are equivalent. The disturbance analysis presented in this thesis will use an empirical cryocooler vibration model that was obtained from actual test data of the BAe 80K cryocooler at NASA GSFC. An empirical model of the cryocooler disturbance can be represented as a superposition of the fundamental frequency and higher harmonics:

$$f_k(k\Delta t) = P_o \sin(\omega k\Delta t + \phi) + \sum_{n=2}^{N} f_n \sin(n\omega k\Delta t + \phi) \tag{2.62}$$

where P_o is the force amplitude of the fundamental at the drive frequency and f_n are the coefficients of the higher harmonics. Computing F_k, which is the discrete Fourier Transform (DFT) of the time domain signal f_k we obtain

$$F_k = \sum_{r=0}^{N-1} f_r \cdot e^{\frac{-i2\pi}{N}kr} \tag{2.63}$$

The amplitude spectrum can then be defined as:

$$S_{AS}(f) = \frac{2}{N}\left|F_k(f)\right| \tag{2.64}$$

and a Power Spectral Density (PSD) function of the disturbance is obtained by taking the discrete Fourier transform of the sampled time signal $f_k(k\Delta t)$. The power spectral density (PSD) is then defined as:

$$S_{PSD}(f) = \frac{2\Delta t}{N} \cdot F_k(f) \cdot F_k^*(f) \tag{2.65}$$

where Δt is the sampling interval, N is the number of samples in the time sequence and f is the frequency in Hertz. These are essentially the three ways to mathematically characterize a cryocooler mechanical disturbance. They are also shown in Figure 2.14. The Figure shows the original BAe80K cryocooler data from [37] with an attenuation factor of 0.1 to account for vibration suppression measures as demonstrated by Collins [20].

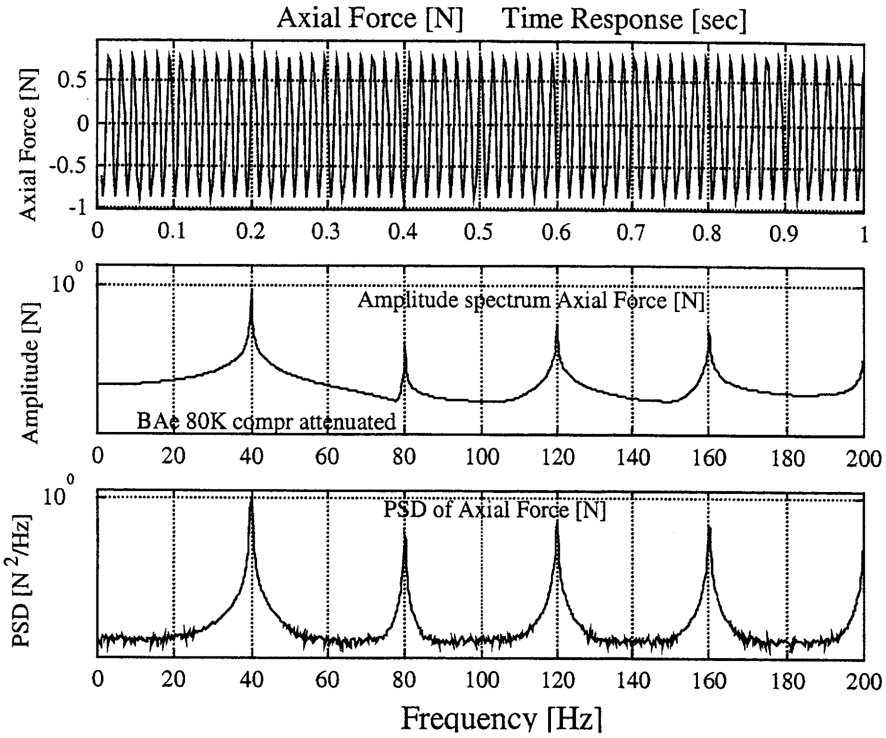

Figure 2.14: Time domain, amplitude spectrum and PSD's for BAe 80K cryocooler

In order to illustrate the effects of adding a cryocooler disturbance to NGST, we choose an empirical model based on disturbance vibration testing results [37] for the BAe 80K Sterling cryocooler. We obtain the PSD's for the F_x, F_y, F_z and M_z components for the cryocooler by reconstructing the time domain signal based on the experimental harmonics and their magnitudes. The lateral forces F_x and F_y are due to misalignment of the displacer and the housing in an axial type Sterling cryocooler [19]. The magnitude of these forces is difficult to predict analytically. Its is assumed that we have -20 dB of attenuation (factor 0.1) due to cryocooler vibration suppression techniques compared to the uncompensated cryocooler. Lateral forces are typically unaffected by cryocooler vibration suppression systems. Four PSD's in F_x, F_y, F_z and M_z are generated as shown in Figure 2.15. These PSD's will be used for the performance assessment using the frequency domain method. Experimental data shows that M_x and M_y are negligible [37].

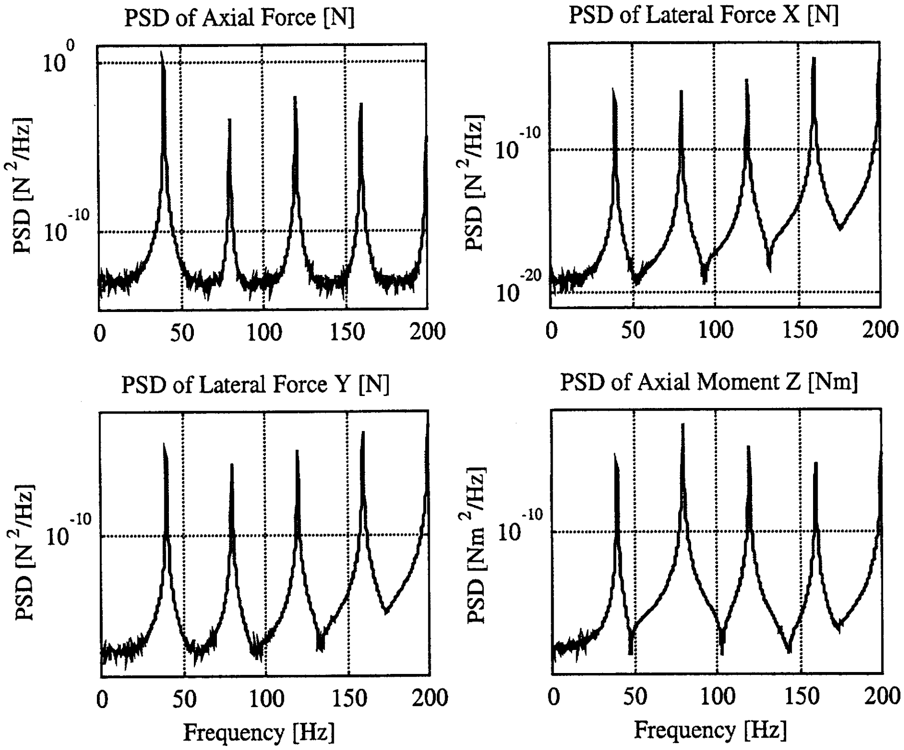

Figure 2.15: Empirical disturbance PSD's for BAe 80K cryocooler

These disturbance PSD's are included in a 4x4-spectral density matrix, which can be used for the disturbance analysis in the frequency domain. For time-domain analysis the disturbance time signals can be recreated from the amplitude spectrum with arbitrary phase (uniform probability density on [0,2π]). The 4x4 spectral density matrix is written as shown in (2.66). A simplification is made by assuming that the PSD components are uncorrelated.

$$S_{ww}^{cryo}(\omega)=\begin{bmatrix} S_{Fx}(\omega) & 0 & 0 & 0 \\ 0 & S_{Fy}(\omega) & 0 & 0 \\ 0 & 0 & S_{Fz}(\omega) & 0 \\ 0 & 0 & 0 & S_{Mz}(\omega) \end{bmatrix} \tag{2.66}$$

A transformation to state space representation for the Lyapunov and sensitivity analyses is necessary. This is achieved by modeling the harmonics shown in Figure 2.15 as second order systems, so that the power spectral density for the j-th disturbance can be written as:

$$S_j^{cryo}(\omega) = \left| G_{jww}(j\omega) \cdot G_{jww}(-j\omega) \right| \tag{2.67}$$

where the transfer function G_{jww} can be written as a superposition of second order systems as:

$$G_{jww}(s) = \sum_{n=1}^{N} \frac{k_{nj}}{s^2 + 2\zeta_{nj} n(2\pi f_d)s + n^2(2\pi f_d)^2} \tag{2.68}$$

where N is the total number of harmonics extracted from the test data, n is the integer harmonic number, k_{nj} is the residue of the n-th harmonic and j-th component, f_d is the cryocooler drive frequency in Hertz and ζ_{nj} is the damping coefficient of the n-th harmonic and j-th component. Thus it becomes clear that the problem is underdetermined since the harmonics can be thought of as delta-dirac impulse functions:

$$H_{jn}(n) = C_{jn}\delta(nf_d) \tag{2.69}$$

that are defined by the two quantities C_{jn}, the amplitude coefficient of the n-th harmonic and j-th component and by the frequency nf_d of the n-th harmonic. In the transfer function representation (2.68) we need to specify three quantities, however, we can only determine the ratio of the residue to the damping ratio. This can be seen by setting (2.68) and (2.69) equal at the n_o-th harmonic frequency:

$$H_{jn_o}(n_o) = C_{jn_o} \underbrace{\delta(n_o f_d)}_{1} = C_{jn_o} = \frac{k_{jn_o}}{2\zeta_{jn_o}\omega_{jn_o}^2} \tag{2.70}$$

We set ζ equal to 0.0015 for all harmonics after tuning so that the RMS values of the experimental PSD's and the approximation from (2.68) match. This allows to directly determine the residues k_{nj} via the following relationship

$$k_{nj} = C_{nj} \cdot 2\zeta_{nj}\omega_n^2 \tag{2.71}$$

Figure 2.16 shows a comparison of the reconstructed experimental PSD's for the axial force F_z (upper subplot) and the corresponding empirical model (lower subplot), where the harmonics are modeled as second order poles. As a check of accuracy the RMS values, which are the square root of the area under the PSD's have been compared and were found to match reasonably well.

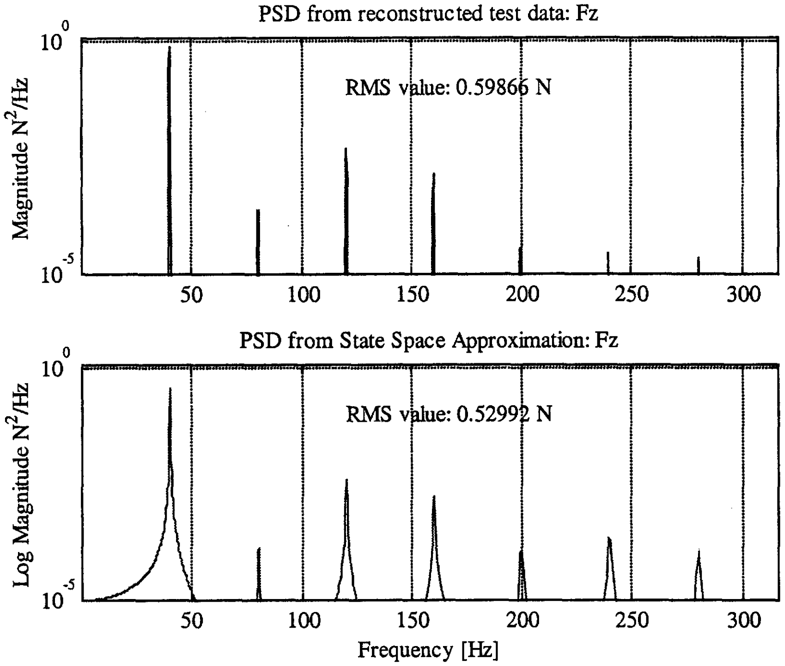

Figure 2.16: Comparison of experimental PSD's and 2nd order approximation method

A state space representation of the cryocooler disturbance is obtained, when we apply the Gauss-Jordan form. The 4 disturbance components are fed by the same white noise source. We can see that the size of the state space system is given by the fact that 2 states are needed per harmonic. Keeping 8 harmonics per components and with 4 disturbance components we obtain a 64 state system for the cryocooler disturbance as follows:

$$\begin{aligned} \dot{\mathbf{q}}_{d1} &= \mathbf{A}_{d1}\mathbf{q}_{d1} + \mathbf{B}_{d1}d_1 \\ \mathbf{w}_1 &= \mathbf{C}_{d1}\mathbf{q}_{d1} + \mathbf{D}_{d1}d_1 \end{aligned} \tag{2.72}$$

It is concluded that linear-action Sterling cryocoolers are a significant disturbance source and should be included in the integrated model. Even with vibration suppression, residual vibration at higher harmonics and in the lateral components often remains [20].

2.3.3 Reaction Wheel Disturbance Test Data Evaluation

Reaction wheels are an essential part of the Attitude Control System (ACS) of NGST. Reaction wheels exert torques by controlling the wheel speed to within a tight tolerance. A torque is only generated if the reaction wheel accelerates or decelerates. The individual reaction wheel comprises essentially the flywheel itself, the bearings, the housing and the driver electronics. Figure 2.17 shows an engineering schematic (cross section) of the ITHACO E-wheel, which is one of the candidate wheels for NGST.

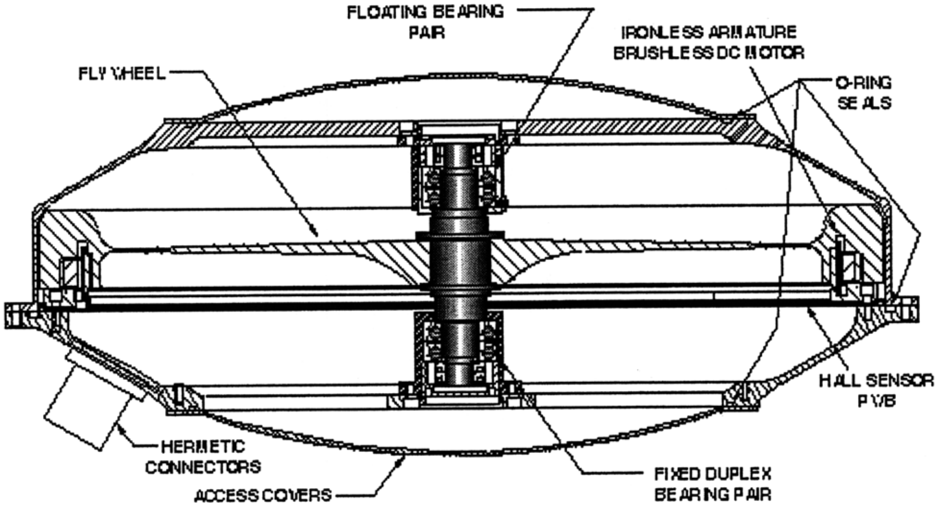

Figure 2.17: Type-E reaction wheel (ITHACO) with brushless DC motor [39]

There are essentially two criteria, which are used in dimensioning reaction wheels for spacecraft attitude control systems. Firstly the angular momentum capacity H_{max} of the reaction wheel has to be sufficient to store the angular momentum, which is constantly generated by external torques acting about the center of mass of the spacecraft. The angular momentum capacity determines the saturation time T_{sat} and thus the frequency of required momentum unloading for a given environment. Secondly the torque authority of the wheel has to be sufficient in order to meet the slewing requirement.

The relevant specifications for the ITHACO E-Wheel compared to the HST wheels are summarized in Table 2.2. It shall be noted that the specifications for static and dynamic imbalance are typically very conservative. It has been shown for various missions such as HST [40] and FUSE [41], that the actual values for the delivered wheels are significantly better than the specification level. The dynamic and static imbalance can be reduced significantly by balancing the flywheel prior to installation. It is also true however that there usually is significant scatter in the data from one wheel to another in the same model series.

Table 2.2: Reaction Wheel Specifications for NGST E-Wheel, * actual average values

Reaction Wheel Model	Speed Range [RPM]	Momentum Capacity [Nms]	Reaction Torque [mNm]	Static Imbalance [g-cm]	Dynamic Imbalance [g-cm^2]	Mass [kg]
ITHACO TW-26E300	±3850	>50	>300	<1.8	<60	<13.9
HST[7]	±3400	264	800	0.38*	4.88*	41

Even though reaction wheels are precision products and the main torque is exerted about the spin axis, there are disturbance forces and moments, which are always generated, when the flywheel is spinning. Great efforts have been undertaken to measure and minimize reaction wheel disturbances. The purpose of this section is to develop an empirical model of E-Wheel disturbances based on actual test data.

The disturbances arise mainly due to static and dynamic imbalances, which are produced by a non-uniform mass distribution within the flywheel. The other three disturbance sources of reaction wheels are bearing disturbances, motor disturbances and motor driver errors [18]. The imbalance of the flywheel however is often considered to be the most significant source of disturbance from a reaction wheel to the spacecraft. The imbalance is the sum of two errors in the symmetry of the flywheel with respect to the spin axis, known as static and dynamic imbalance.

---

[7] Honeywell P/N 5088088

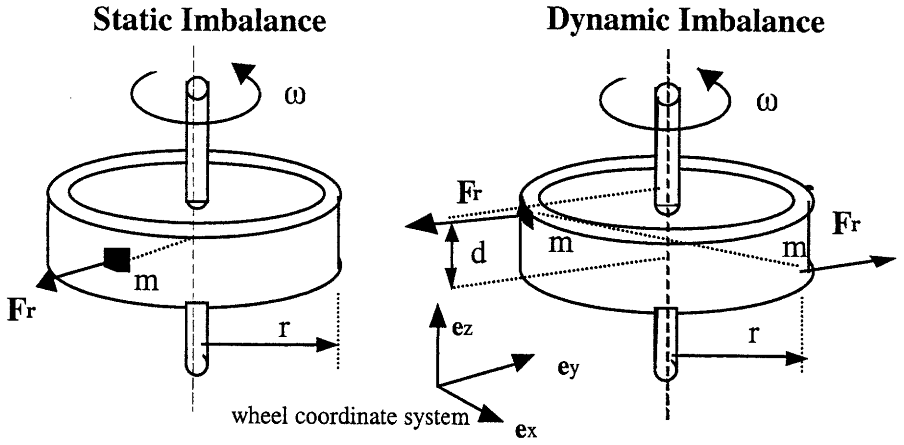

Figure 2.18: Static and Dynamic Imbalance Representation

The static imbalance represents the fact that the center of mass of the flywheel is not exactly on the spin axis. This can be interpreted as a small mass at radius *r* as shown in Figure 2.18. While the wheel is spinning, this offset mass produces a radial centripetal force, whose magnitude and vectorial components are given as:

$$F_r = m \cdot r \cdot \omega^2 = U_s \cdot \omega^2 \tag{2.73}$$

$$\vec{F}_x(t) = U_s \cdot \omega^2 \cdot \cos(\omega t + \phi) \cdot \vec{e}_x \tag{2.74}$$

$$\vec{F}_y(t) = U_s \cdot \omega^2 \cdot \sin(\omega t + \phi) \cdot \vec{e}_y \tag{2.75}$$

where *m* [kg] is the offset mass, *r* [m] is the radius of the flywheel and ω (rad/sec) is the angular velocity of the wheel. The static imbalance $U_s = mr$ is a flywheel mass property and is often given in [gcm]. The dynamic imbalance is representative of the cross product of inertia of the flywheel, which is caused by a slight angular misalignment of the principal moment of inertia with the spin axis. The two opposed masses shown in Figure 2.18 (right side) have their common center of mass on the spin axis. Nevertheless they are separated by a distance d along the rotation axis, which causes a once-per revolution rotating couple given by

$$T_r = m \cdot r \cdot d \cdot \omega^2 = U_d \cdot \omega^2 \tag{2.76}$$

$$\vec{T}_x(t) = U_d \cdot \omega^2 \cdot \cos(\omega t + \phi) \cdot \vec{e}_x \tag{2.77}$$

$$\vec{T}_y(t) = U_d \cdot \omega^2 \cdot \sin(\omega t + \phi) \cdot \vec{e}_y \tag{2.78}$$

where d is the mass offset along the spin axis. The dynamic imbalance $U_d = mrd$ is a flywheel mass property. Equations 2.73-2.78 by themselves could lead to the erroneous conclusion that the frequency normalized amplitude spectrum of the reaction wheel disturbances contains only an impulse at the fundamental frequency of rotation. Experimental measurements however show that higher harmonics contribute significantly to the disturbance spectrum [40],[41]. These harmonics occur at integer multiples of the fundamental, but also at real numbered multiples of the fundamental frequency including at sub-harmonics. The forces and torques, acting in the rotor plane, due to static and dynamic imbalance are modeled as summations of sinusoidal terms: the fundamental component at wheel speed plus harmonic plus sub-harmonic terms [42]. Equations for this model have the following form, parameterized in terms of harmonic coefficients, harmonic speed ratios and individual wheel phases.

$$m_{ijk}(t) = C_{jk} f_i^2 \sin(2\pi h_{jk} f_i t + \phi_{ijk}) \tag{2.79}$$

where,

$m =$ disturbance force ($j = 1, 2, 3$) or torque ($j = 4, 5, 6$)

$i =$ wheel number $(1, 2, \ldots, N)$; N = total number of wheels

$j =$ disturbance number $(1, 2, \ldots, 6)$

$k =$ harmonic number $(1, 2, \ldots, nj)$; nj = number of harmonics for jth disturbance component

$C_{jk} =$ amplitude coefficient for kth harmonic of jth disturbance; assumed to be the same for all wheels

$f_i =$ wheel speed of ith wheel in Hz

$h_{jk} =$ ratio of frequency of kth harmonic of jth disturbance to frequency of wheel rotation; assumed the same for all wheels

$\phi_{ijk} =$ phase angle of kth harmonic of jth disturbance of ith wheel

In this section we are looking at the test results from a single wheel, so that we can drop the index i. The parameters h_{jk} and C_{jk} are determined from test data. The objective is to determine the harmonics h_{jk} and coefficients C_{jk} for a representative ITHACO Type E-Wheel. The methods and tools developed here can however be applied to any reaction wheel in the future.

Test Description

A reaction wheel spinup and spindown test was conducted in 1997 at the NASA Goddard Space Flight Center using a single ITHACO E-Type reaction wheel [43]. The wheel started at 0 RPM and full torque voltage was applied to the motor until the wheel saturated around 2400 RPM. The wheel was integrated into a stiff cylindrical test fixture and hardmounted to a 6-axis Kistler force/torque measurement table. This allowed determination of the forces and moments generated by the reaction wheel as measured by the load cells of the Kistler table. Figure 2.19 shows a schematic representation of the measurement table. A total of 8 channels of load cell data corresponding to 12 load cell axes were sampled at 3840 Hz over at total of 390 seconds (1'500'000 data points). The high sampling rate leads to very good signal to noise ratio and prevents aliasing problems for the identification of higher harmonics.

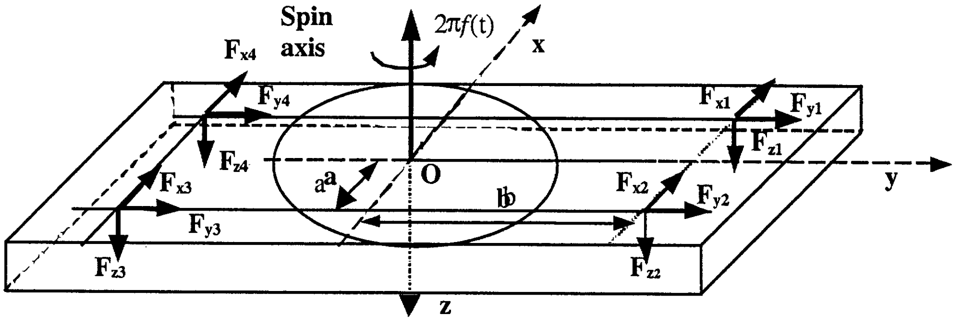

Figure 2.19: Kistler Force/Torque measurement table setup

Based on the calibrated voltages the three equivalent forces and three moments at the origin of the Kistler table can be determined based on equations (2.80-85). It shall be noted that channels F_{x1}/F_{x2} and F_{x3}/F_{x4}, as well as F_{y1}/F_{y4} and F_{y2}/F_{y3} have been permanently summed together. In this manner the number of output channels is reduced from 12 to 8 [44].

$$
\begin{aligned}
F_x &= F_{x1+2} + F_{x3+4} \\
F_y &= F_{y1+4} + F_{y2+3} \qquad\qquad (2.80\text{-}82) \\
F_z &= F_{z1} + F_{z2} + F_{z3} + F_{z4}
\end{aligned}
$$

$$
\begin{aligned}
M_x &= b \cdot \left(F_{z1} + F_{z2} - F_{z3} - F_{z4}\right) \\
M_y &= a \cdot \left(-F_{z1} + F_{z2} + F_{z3} - F_{z4}\right) \qquad\qquad (2.83\text{-}85) \\
M_z &= b \cdot \left(-F_{x1+2} + F_{x3+4}\right) + a \cdot \left(F_{y1+4} - F_{y2+3}\right)
\end{aligned}
$$

The table dimensions are a = 12cm and b = 20cm. The raw data is read from the master and slave test data files and processed according to the methodology, which is developed in the next section. Figure 2.20 shows the flow diagram for the processing of the reaction wheel data.

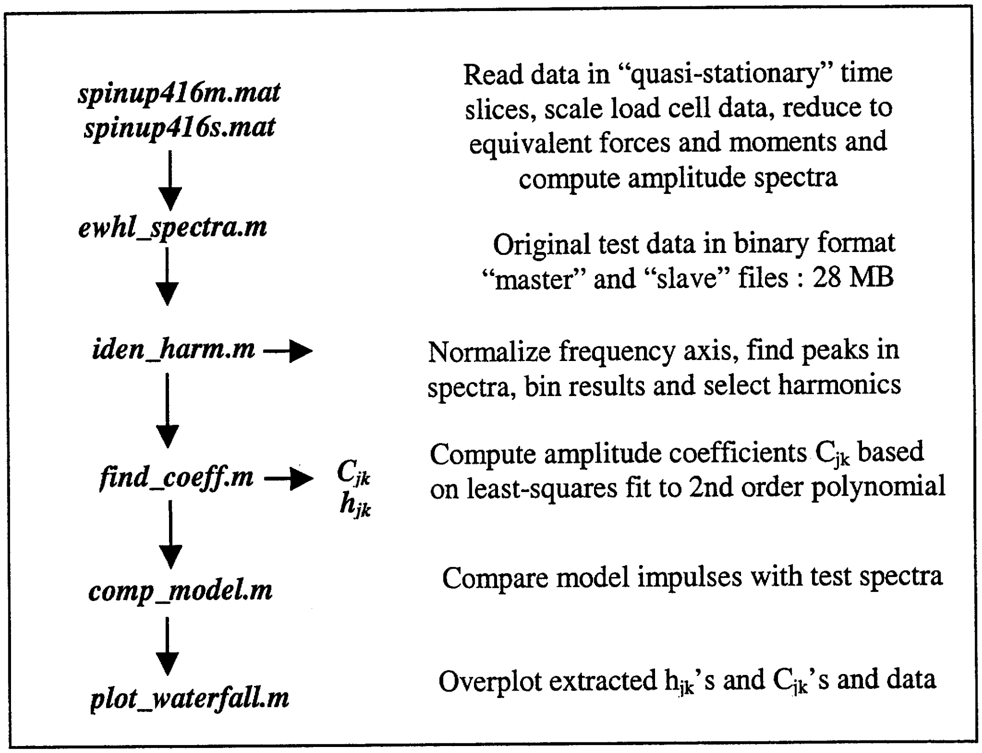

Figure 2.20: Reaction Wheel Data Evaluation flow diagram

After reading in the load cell voltages and scaling, the equivalent force and moment time histories are found with equation (2.80-85) respectively. The functions `iden_harm.m`, `find_coeff.m` and `comp_model.m` were developed by Masterson [45]. Figure 2.21 shows the time history for $F_y(t)$ for the ITHACO E-Wheel during spinup. It can be seen that the disturbance level increases as the wheel spins up and eventually reaches a quasi-steady state around 150 seconds. During the spinup there are several transients, which exceed the RMS disturbance levels, which would not be expected based on the existence of harmonics alone.

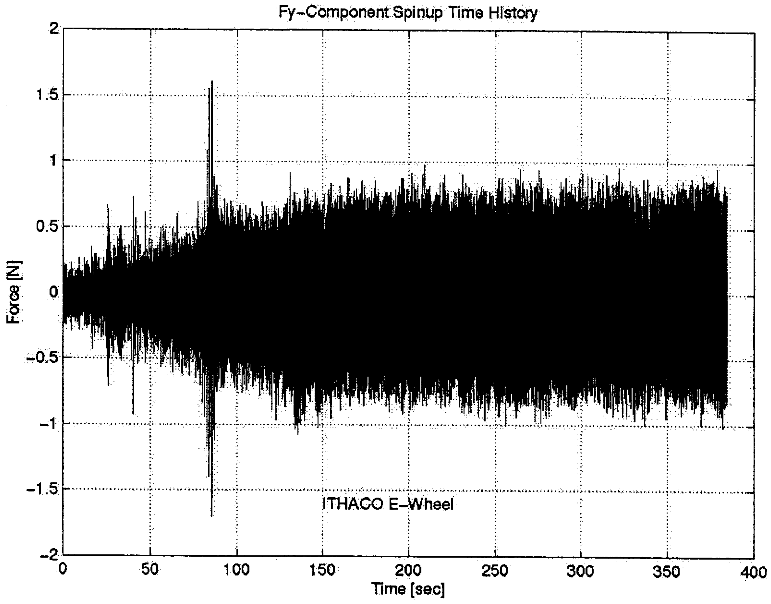

Figure 2.21: $F_y(t)$ radial force in y-direction during ITHACO E-Wheel spinup test

The next step consists in analyzing the data in time slices, which are considered to be quasi-stationary. In this test the wheel speed is not known a-priori. Therefore the data is subdivided into time slices, which consist of 8192 data points each, corresponding to a time sample length of T=2.133 seconds. The amplitude spectrum of each time sample is computed as follows:

$$M_j(f_k) = \frac{2}{N} \cdot \left| fft(m_j(k\Delta t)) \right| \tag{2.86}$$

where $M_j(f_k)$ is the amplitude spectrum of the force or moment component in units of [N] or [Nm] respectively. The corresponding frequency vector is given as:

$$f_k = \frac{k}{T} = \frac{k \cdot f_s}{N} = \frac{k}{N \cdot \Delta t} \tag{2.87}$$

where N is the number of FFT points, k is the frequency index and f_s is the sampling frequency in Hz. The frequency resolution Δf is given as the inverse of the length of the time sample. In this study the frequency resolution was obtained as:

$$\Delta f = \frac{1}{T} = 0.46Hz \tag{2.88}$$

After computing the amplitude spectra for each time sample of the entire spinup test, a waterfall plot can be generated for each of the 6-force/torque components. A waterfall plot consists of a number of amplitude spectra, which have been plotted in ascending order of time or wheel speed one behind the other. Figure 2.22 is the waterfall plot for the F_y-component from 0 to 180 seconds in the spinup test.

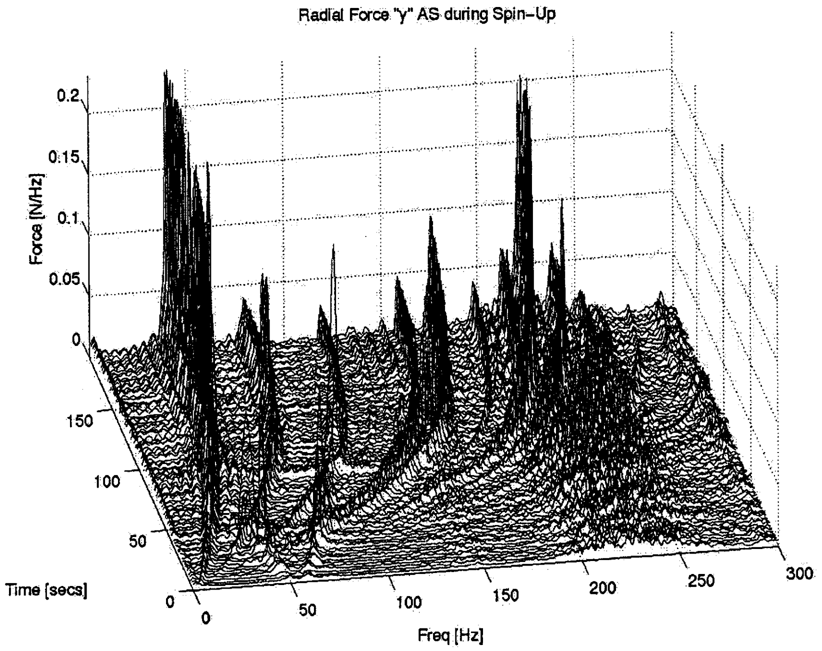

Fig. 2.22: Waterfall plot for F_y-component for ITHACO E-Wheel spinup test

The value of the waterfall plot lies in its depiction of the transient behavior of the reaction wheel disturbances in the frequency domain. The ridges, which emanate from the origin at 0 seconds and 0 Hz, represent the harmonics of the wheel speed disturbance. The first ridge, which eventually saturates at 40 Hz is the fundamental frequency of the wheel in revolutions per second [RPS]. The angular acceleration of the wheel and the saturation around 2400 RPM can clearly be seen. Also there appear to be dynamic amplifications, which cannot be explained by the existence of the flywheel harmonics alone. An algorithm was developed by the author that searches for the existence of the fundamental harmonic in the data. This is useful to reconstruct the wheel speed as a function of time in the absence of tachometer data for the test. Figure 2.23 shows the reconstructed wheel speed curve for the spinup test. The wheel speed in RPM is found by extracting the fundamental frequency $f_{h=1.0}$ at each amplitude spectrum and multiplying by 60.

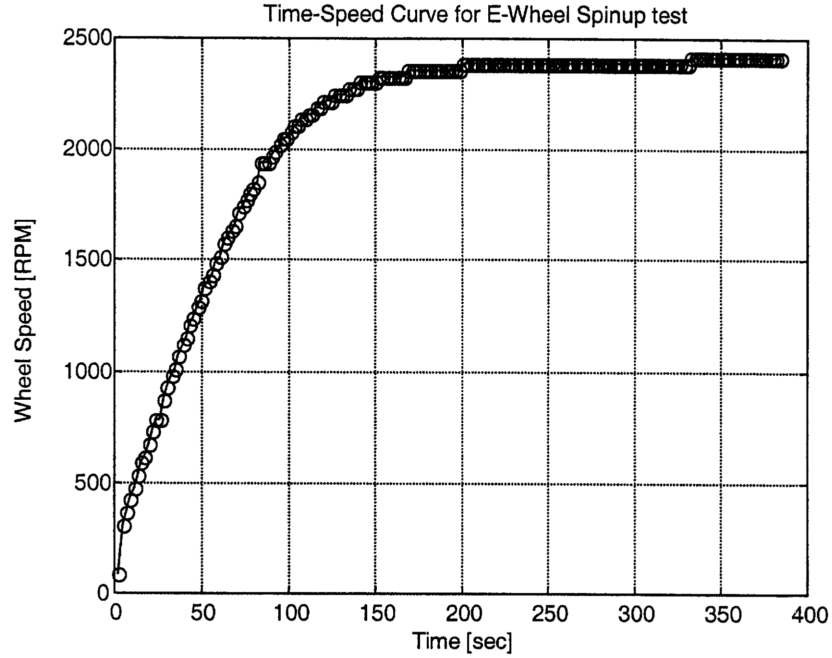

Figure 2.23: Wheel speed curve reconstructed from fundamental frequency

The wheel speed resolution is naturally limited by the frequency resolution, where the following relationship holds true:

$$\Delta RPM = 60 \cdot \Delta f = 28.125 RPM \tag{2.89}$$

The next essential step consists in identifying the harmonic coefficients h_{jk} of the reaction wheel. Figure 29 contains an example plot of the harmonics identification process. The asterisks denote the harmonics, which were identified by the algorithm. This harmonics identification is repeated for each frequency-normalized spectrum at a given wheel speed.

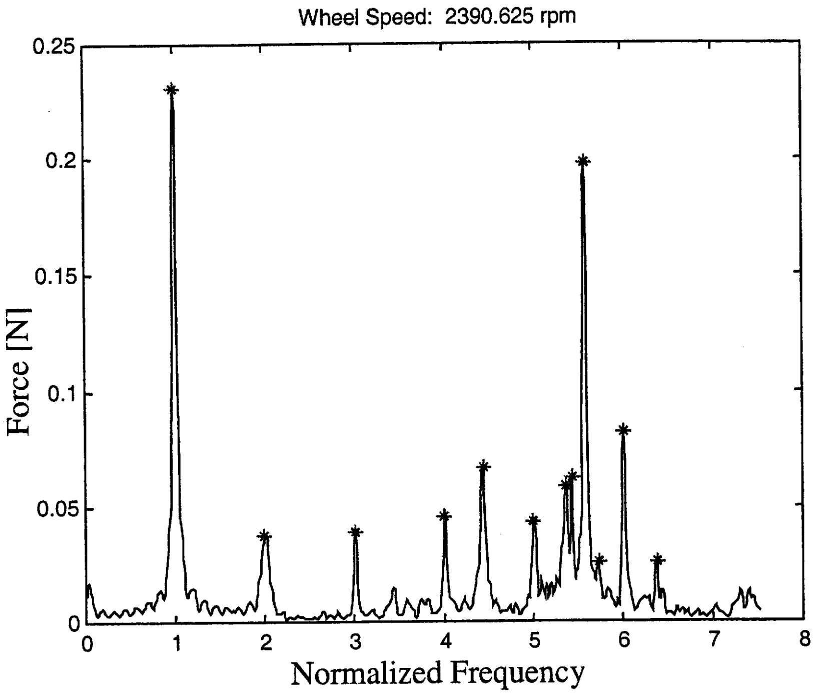

Figure 2.24: Candidate Harmonics Identification (F_y-component) and 3σ-bounds

After identification of the harmonics h_{jk} in the test data, the coefficients C_{jk} of these harmonics must be numerically determined. This is done with a least-squares fitting approach, in a similar fashion as was done for the HST wheel analysis [40]. The magnitude of the disturbance force or moment is assumed to be related to the wheel speed as follows:

$$F_i = C_i \omega^2 \tag{2.90}$$

where F_i is the force in [N], ω is the wheel speed in RPM, and C_i is the coefficient in N/RPM^2. The error between a test value at wheel speed n and the curve described by equation (2.90) is:

$$e_{i,n} = F_{i,n} - C_i \omega_n^2 \tag{2.91}$$

C_i is then calculated using the least-squares method. The square of the error is summed over all wheel speeds and minimizing that total error, results in the following equation for C_i [45]:

$$C_i = \frac{\sum_n F_{i,n}\omega_n^2}{\sum_n \omega_n^4} \tag{2.92}$$

The coefficients $C_{i,n}$ of the harmonic h_i at each wheel speed n are plotted and compared to the least-squares parabola through the origin in Figure 2.25.

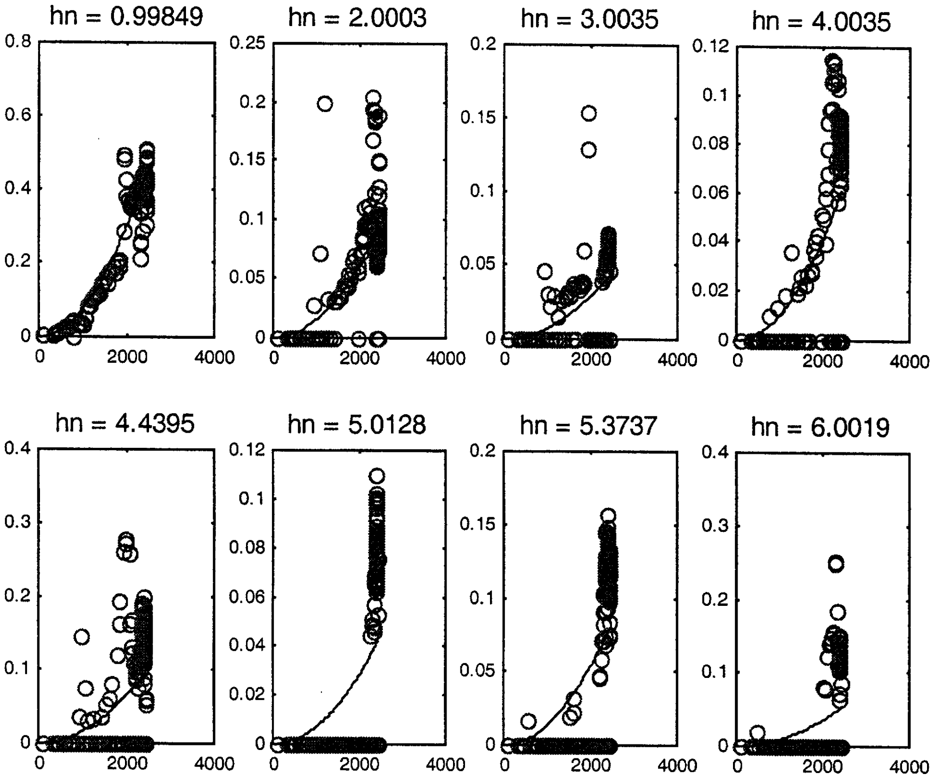

Figure 2.25: Least squares fit for amplitude coefficients of F_{rad}

It can be observed that the quadratic fit holds very well for low order harmonics. The fit degenerates for higher harmonics, which suggests that they do not follow the assumed relationship with ω^2 as closely as the fundamental. This is especially true of the non-integer harmonics, which are thought to be associated with bearing disturbances [18]. Once the harmonics h_{jk} and the coefficients C_{jk} have been determined, we can condense the results into the radial force, axial force and radial moment directions. Table 2.3 contains the resulting harmonics and coefficients, which were identified for the E-Wheel in this study.

Table 2.3: Harmonics and coefficients for ITHACO E-Wheel

Radial Force F_{rad}										
h_i	***1.0***	***2.0***	***3.0***	***4.0***	***4.43***	***5.0***	***5.38***	***5.60***	***6.0***	***6.39***
C_i	.7852	.2984	.0777	.1036	.1280	.0849	.0985	.1849	.0618	.0402

Axial Force F_{axi}									
h_i	***1.0***	***2.0***	***2.90***	***3.88***	***4.29***	***4.85***	***5.40***	***5.81***	***6.16***
C_i	.2950	.1416	.0714	.0836	.2491	.1087	.3010	.1362	.0705

Radial Moment M_{tor}											
h_i	***1.0***	***2.0***	***2.90***	***3.88***	***4.0***	***4.43***	***5.20***	***5.40***	***5.60***	***5.81***	***6.0***
C_i	.3239	.0744	.0309	.0472	.0121	.0412	.0924	.1027	.0630	.0851	.0173

Note: The coefficients C_i are in units of 10^{-7} N/RPM^2 for forces and 10^{-7} Nm/RPM^2 for moments

There is a need to increase the confidence in the harmonics h_i and corresponding coefficients C_i. For this purpose the function `comp_model.m` was designed to overplot the test data for selected spectra with the impulses defined by h_i and C_i.

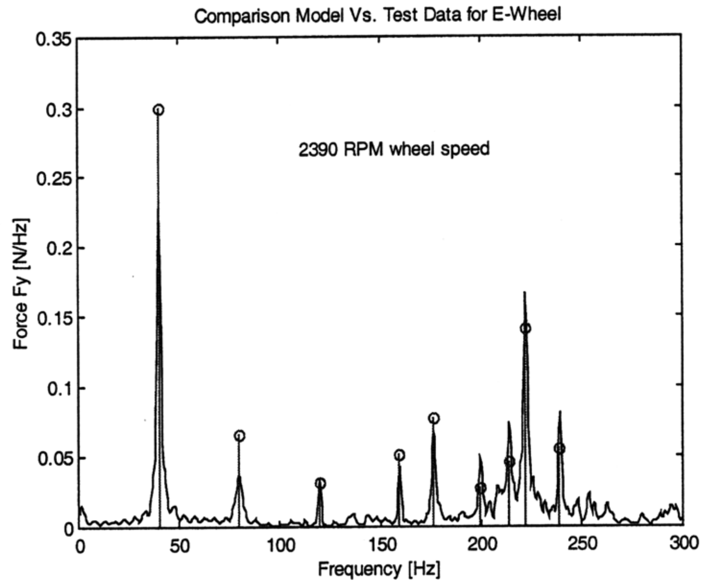

Figure 2.26: Comparison of empirical disturbance model and test data

Figure 2.26 shows such a comparison for 2390 RPM and it can be seen that the match is very good. Finally we can get a three-dimensional view by looking at the waterfall plot (Figure 2.27) of frequency versus wheel speed, which is obtained with the function `plot_waterfall.m`. We see that the harmonics have been clearly identified. There are features in the waterfall plot, which need to be further explained. These spikes are due to the structural dynamics of the wheel (whirl modes) crossing the harmonics that are caused by the wheel imbalances. More information on these phenomena can be obtained in references [46] and [47].

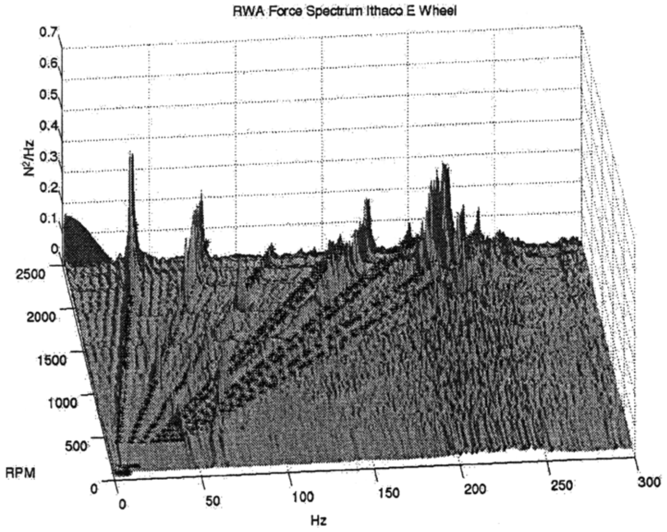

Figure 2.27: Waterfall plot comparing test data and empirical model

A result, which matters to the spacecraft designer is, whether the tested reaction wheel meets the specifications. For the E-Wheel the measured static and dynamic imbalance of the wheel can be determined from the coefficients of the fundamental. The computation of static and dynamic imbalance is as follows:

From F_{rad}:
$$U_s = C_1 \cdot \frac{1000 \cdot 60^2 \cdot 100}{(2\pi)^2} = 0.7160\, g \cdot cm \tag{2.93}$$

From M_{tor}:
$$U_d = C_1 \cdot \frac{1000 \cdot 60^2 \cdot 100^2}{(2\pi)^2} = 29.536\, g \cdot cm^2 \tag{2.94}$$

It is clear that the static and dynamic imbalances as defined above are only based on the coefficients of the harmonic radial force and moment respectively. A comparison with the specification levels is summarized in Table 2.4.

Table 2.4: Comparison of imbalance specifications with test results

Comparison	**Static Imbalance**	**Dynamic Imbalance**
E-Wheel Test data	Us = 0.7160 gcm	Ud=29.54 gcm^2
Specification E-Wheel	Us < 1.8 gcm	Ud < 60 gcm^2
HST – Wheels (avg)	Us = 0.3806 gcm	Ud = 4.88 gcm^2

The tested E-wheel satisfies the specification roughly by a margin of 2 for static and dynamic imbalance. As indicated by Bialke [18], these values can change from wheel to wheel and fine-tuning with installed bearings can reduce these values by a factor of 2-5. The HST wheels appear to be quieter in terms of imbalances. This will be further investigated in the next section.

Implementation

Identifying the harmonics and coefficients by itself does not yet allow generating disturbance input for dynamic simulations of system performance. Based on previous work by Melody [42], the results from Table 2.3 were incorporated into existing MATLAB code, which allows generating time histories of the disturbance as well as power spectral densities (PSD's). A sample case was run in order to compare the energy distribution of the empirical disturbance models for the Type-E and HST wheels. The sample case looks at the axial force component F_z for a bias wheel speed of R_o = 1000 RPM, assuming uniform probability density for the wheel speed and a variation in speed dR= 100 RPM. The results for this sample case are contained in Figure 2.28.

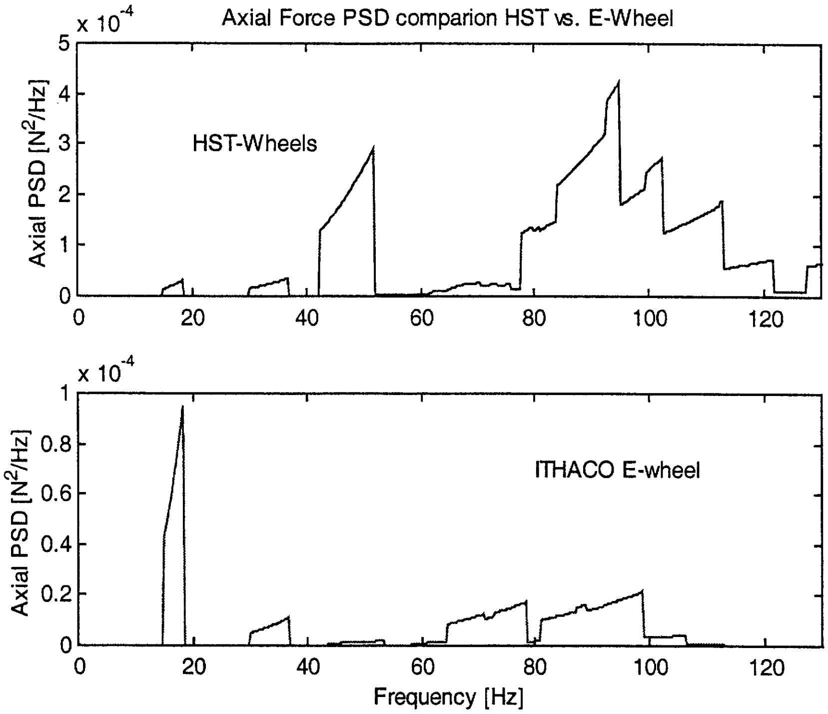

Figure 2.28: Comparison of PSD's between HST and Type-E Wheels

The results suggest that the disturbance power associated with the fundamental is higher for the E-Wheel, which is corroborated by the higher values for the static and dynamic imbalances. The HST wheels however contain significantly more disturbance power at higher frequencies. This large difference is so significant that a further investigation is warranted. Possible explanations for this difference are:

- HST wheels have been very carefully balanced[8] compared to E-Wheels
- Measurement of HST-wheels contains large contribution from test stand dynamics

The methodology and results of a reaction wheel disturbance analysis for a representative ITHACO E-Type wheel have been presented in this section. It is shown how the test data is reduced into equivalent forces and moments. Disturbance harmonics and coefficients are then evaluated based on frequency-domain based identification algorithms. It is shown that this methodology is able to correctly identify the harmonics and the corresponding magnitudes of the

---

[8] Balancing a flywheel is able to reduce the effect of the fundamental frequency, but has little effect on the higher harmonics

vibrational disturbance caused by the test specimen. The wheel meets the static and dynamic imbalance specifications by a margin of 2. The flexible dynamics of the wheel cause amplification of the disturbance, when the modes of the flywheel and the harmonics cross over. Only the harmonics and their coefficients are retained for the NGST disturbance analysis. So far we have only considered a single wheel. In reality several wheels are used concurrently in a reaction wheel assembly (RWA). This has to be taken into account in the disturbance modeling process.

2.3.4 Reaction Wheel Assembly Modeling

Because of the need to exert torque about several axes, a reaction wheel assembly (RWA) normally will contain multiple wheels whose spin axes are at different orientations. In addition, redundancy increases the number beyond that necessary for control (3) about a given set of axes [48]. It is common practice in ACS design to add a fourth wheel for redundancy and to arrange them in a square-based pyramidal configuration. This configuration has been chosen for the NGST yardstick design. The forces and torques in each wheel frame must be transformed into body frame using known coordinate transformations. It is important to take into account the offset of each wheels local coordinate frame from the RWA coordinate frame. The objective of this section is to develop of a disturbance model, which takes into account multiple wheels in a pyramidal configuration. The pyramidal configuration planned for NGST is shown in Figure 2.29.

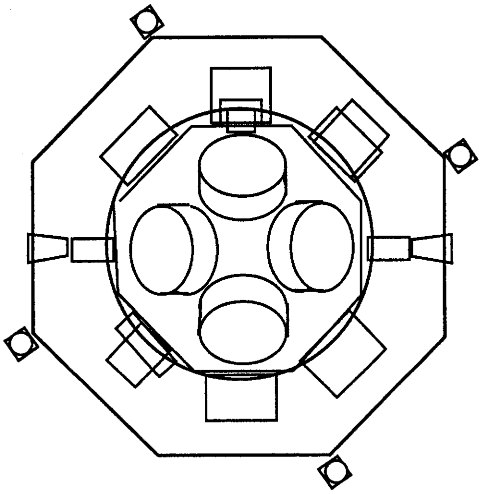

Figure 2.29:.NGST proposed RWA pyramidal arrangement

Reaction wheel disturbances are best modeled as a stochastic process. This is due to the fact that individual wheel speeds cannot be precisely predicted during an observation. Although the attitude control logic that is used to issue commands to each wheel is known a-priori, what is not known to the same level of certainty is the external torque disturbance which the wheels are counteracting [24]. Also, the initial wheel speeds at the start of an observation might be impossible to predict. For these reasons a time simulation will only represent a specific point in the disturbance envelope. In order to obtain a sense of the worst-case scenario a large number of Monte-Carlo simulations have to be run which can be very computationally expensive. The alternative explored in this thesis is to estimate the effect of reaction wheel disturbances on the WFE and LOS jitter "on average", assuming the following stochastic process:

$$m_{ijk}(t) = C_{jk} f_i^2 \sin(2\pi h_{jk} f_i t + \phi_{ijk}) \tag{2.95}$$

The key random variables are the individual wheel speeds f_i and the individual wheel phases ϕ_{ijk}. This analysis assumes a random wheel phase ϕ_{ijk} with a uniform probability density function on the interval $[0,2\pi]$. The probability density function of the wheel speeds is a much more difficult question. The following derivation is based on work done by Gutierrez [48] and applies its findings to the NGST configuration. Both f_i and ϕ_{ijk} are assumed to be independent random variables. Independent means that the joint probability density function (PDF) can be written as the product of the individual PDF's. If we use the notation $f_X(x)$ to denote the PDF of the random variable X, then independence implies $f_{H_{jk}\phi_{ijk}}(h_{jk},\phi_{ijk}) = f_{H_{jk}}(h_{jk}) f_{\phi_{ijk}}(\phi_{ijk})$.

The total disturbance of type j for the i-th wheel is simply the sum over the harmonics.

$$m_{ij}(t) = \sum_{k=1}^{n_j} m_{ijk}(t) \tag{2.96}$$

Let us now define the disturbances in the local coordinate frame of a wheel. The pre-superscript w signifies that the disturbances are expressed in the wheel frame.

$$
{}^{\omega}\mathbf{m}_i(t) = {}^{\omega}\begin{Bmatrix} m_1(t) \\ m_2(t) \\ m_3(t) \\ m_4(t) \\ m_5(t) \\ m_6(t) \end{Bmatrix}_i = {}^{\omega}\begin{Bmatrix} F_x(t) \\ F_y(t) \\ F_z(t) \\ M_x(t) \\ M_y(t) \\ M_z(t) \end{Bmatrix}_i \tag{2.97}
$$

In general a time domain representation of the RWA disturbance can be generated from equation (2.95) provided that the h_{jk}'s and C_{jk}'s are available from the previous test data analysis. Representative plots of wheel force time history for radial force, axial force and radial moment of a single wheel running at 1200 rpm (20 Hz) are shown in Figure 2.30.

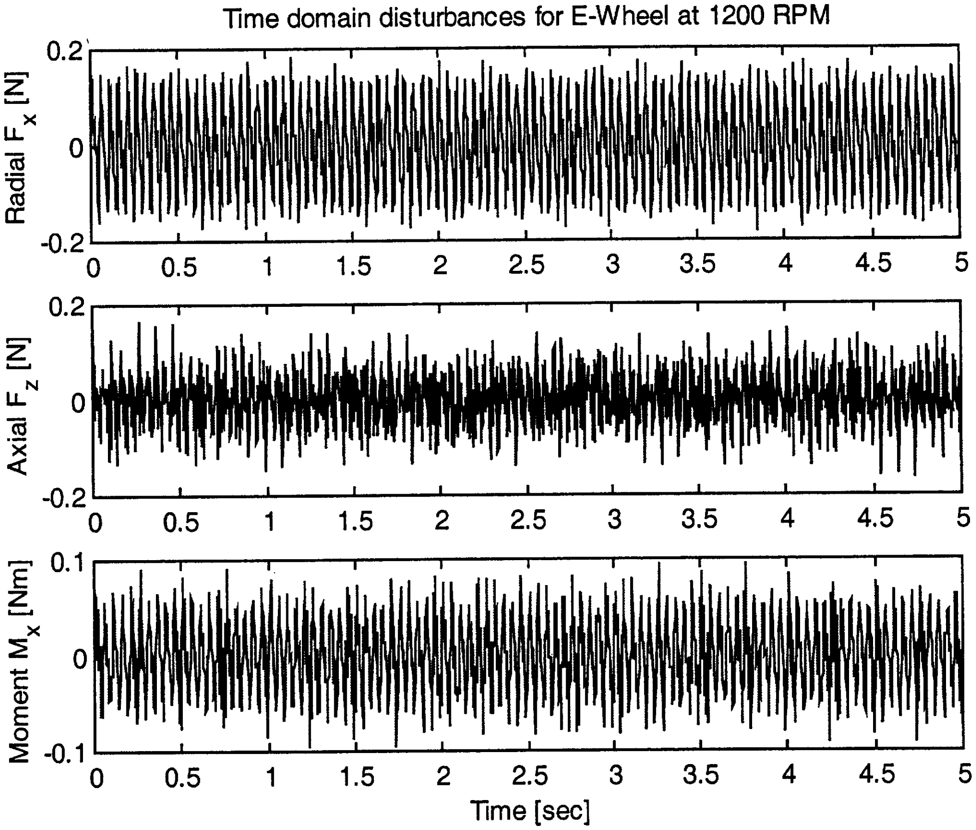

Figure 2.30: Wheel disturbance time histories for ITHACO E-Wheel at 1200 RPM

The local wheel axes are shown in Figure 2.31. These axes remain fixed in space and do not rotate as the wheel spins. F_x and F_y are the radial forces, F_z is the axial force, M_x and M_y are the radial torques, and M_z is the axial torque. One simplification that can be made (and which is supported by the experimental data) is that M_z is approximately zero. For instance, Melody in [42] states that the causes that contribute to Mz (torque ripple and motor cogging) were found to be negligible for the Hubble Space Telescope reaction wheels. Recall however that M_z provides the torque required for attitude control. This torque will not be included in the disturbance model since it is assumed that it will be accounted for in the ACS loop of the closed-loop spacecraft model.

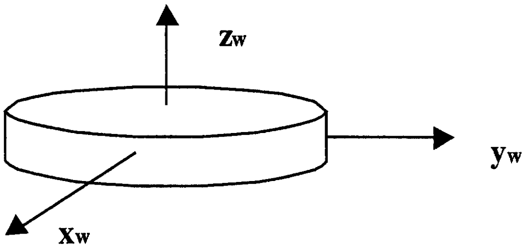

Figure 2.31: Local wheel frame (*z*-axis along spin axis)

The radial disturbances are assumed to rotate in the plane of the wheel at the frequencies of the harmonics. Hence, the disturbance forces in and the moments about the y axis are 90° out of phase with the disturbance forces in and moments about the x axis, This suggests that the following relationship holds:

$$\phi_{ijk} = \phi_{i(j-1)k} + \frac{\pi}{2}, \qquad j = 2,5 \tag{2.98}$$

The transformation of the disturbances from the local wheel frame to the global spacecraft frame requires a rotation matrix. The orientation of the wheel frame relative to the spacecraft frame can be specified by a set of Euler angles. Define the so-called *XYZ* Euler angles as follows. Begin by having the local wheel axes aligned with the spacecraft axes. Each of the three Euler angles specifies rotation about an intermediate axis. In particular, let:

α = angle of rotation about original z-axis

θ = angle of rotation about new y axis after previous rotation

γ = angle of rotation about new x axis after previous rotation

Let

$^{s/c}\mathbf{p}$ be a vector in the spacecraft axes
$^{w}\boldsymbol{p}$ be a vector in the wheel axes
R_i be the 3 x 3 rotation matrix from the *i*th wheel frame to the spacecraft frame

In this thesis, the spacecraft axes will refer to the coordinate frame whose origin is at the location at which the disturbance forces and moments are desired. With the above definitions the rotation from the wheel frame to the spacecraft frame using the rotation matrix R_i is:

$$^{s/c}p = R_i^{\,w}p \tag{2.99}$$

$$R_i = \begin{bmatrix} \cos\alpha_i\cos\theta_i & \cos\alpha_i\sin\theta_i\sin\gamma_i - \sin\alpha_i\cos\gamma_i & \cos\alpha_i\sin\theta_i\cos\gamma_i + \sin\alpha_i\sin\gamma_i \\ \sin\alpha_i\cos\theta_i & \sin\alpha_i\sin\theta_i\sin\gamma_i + \cos\alpha_i\cos\gamma_i & \sin\alpha_i\sin\theta_i\cos\gamma_i - \cos\alpha_i\sin\gamma_i \\ -\sin\theta_i & \cos\theta_i\sin\gamma_i & \cos\theta_i\cos\gamma_i \end{bmatrix} \tag{2.100}$$

The axes now need to be displaced to account for the fact that all the wheels are not at the same location. A simplifying assumption is that the spin axes (*z*-axis) of all the wheels intersect at a point, which happens to coincide with the origin of the spacecraft axes. Let the distance from this point to each of the wheel frame origins be *d*. Then the vector from the spacecraft frame origin to the origin of the *i*th wheel frame is given by

$$^{s/c}r_i = R_i^{\,w}r_i = R_i\begin{bmatrix} 0 \\ 0 \\ d \end{bmatrix} \tag{2.101}$$

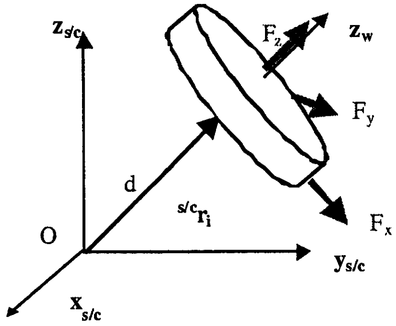

Figure 2.32: Position vector $^{s/c}\mathbf{r}_i$, which locates the *i*th wheel frame origin in spacecraft frame

The moment about 0 (in the spacecraft frame) due to the forces F_x, F_y, F_z in the wheel frame is important and cannot be neglected [49]. The moment, which generated at the RWA origin 0 due to the offset of the wheel forces, is given by the cross product

$${}^{s/c}M_i^{r\times F} = {}^{s/c}r_i \times \left(R_i \; {}^{w}\begin{Bmatrix} F_x \\ F_y \\ F_z \end{Bmatrix}_i \right) \tag{2.102}$$

We can now express in the spacecraft frame the disturbance forces and moments due to a single wheel. The disturbances can be written in terms of the rotation matrix R_i, the moment arms $\mathbf{r}_i$, and local disturbances ${}^{w}\boldsymbol{m}_i$. As a means of simplification, the cross product **r** x ( ) can be written as a matrix multiplication as follows

$$r_i \times a = \begin{bmatrix} 0 & -r_3 & r_2 \\ r_3 & 0 & -r_1 \\ -r_2 & r_1 & 0 \end{bmatrix}_i a = \Re_i a \tag{2.103}$$

The disturbance vector of the *i*-th wheel in the spacecraft frame is therefore

$${}^{s/c}m_i(t) = \begin{bmatrix} R_i & 0_{3x3} \\ r_i \times R_i & R_i \end{bmatrix} {}^{w}m_i(t) = \begin{bmatrix} R_i & 0_{3x3} \\ \Re_i R_i & R_i \end{bmatrix} {}^{w}m_i(t) = T_i \cdot {}^{w}m_i(t) \tag{2.104}$$

The individual wheel disturbances can then be summed to obtain the overall disturbance acting in the spacecraft frame.

$${}^{s/c}m(t) = \sum_{i=1}^{N} {}^{s/c}m_i(t) = {}^{s/c}\begin{Bmatrix} m_1(t) \\ m_2(t) \\ m_3(t) \\ m_4(t) \\ m_5(t) \\ m_6(t) \end{Bmatrix} = {}^{s/c}\begin{Bmatrix} F_x(t) \\ F_y(t) \\ F_z(t) \\ M_x(t) \\ M_y(t) \\ M_z(t) \end{Bmatrix} \tag{2.105}$$

The next step is the calculation of the Spectral Density Matrix. The derivation first defines the correlation matrix $R_{s/cm}(t_1,t_2)$ in spacecraft axes. Let E[ ] signify the expectation operator:

$$R_{s/c_m}(t_1,t_2) = E\left[\sum_{p=1}^{N}\sum_{q=1}^{N} T_p\, {}^{w}m_p(t_1)\, {}^{w}m_q^T(t_2)\, T_q^T\right] \tag{2.106}$$

By bringing the expectation operator inside the summation and taking the Fourier transform we can obtain the spectral density matrix. This development was performed by Gutierrez [48] and is based on a number of simplifying assumptions:

- ϕ's are independent
- ϕ's are uniform random variables over the interval $[0,2\pi]$
- f's are independent, and the probability density function of the p-th wheel is expressed as f_p. The probability density function for the wheels is either uniform or gaussian.

The spectral density functions for each of the force and moment components of a single wheel can then be written as [42]:

$$S_{{}^{w}m_{pr}\,{}^{w}m_{pr}}(\omega) = \sum_{k=1}^{n_r} \frac{\pi C_{rk}^2 \omega^4}{2(2\pi h_{rk})^5}\left[f_p\left(\frac{\omega}{2\pi h_{rk}}\right) + f_p\left(\frac{-\omega}{2\pi h_{rk}}\right)\right] \tag{2.107}$$

The cross-spectral densities are usually not zero, as there is a correlation between the F_x/F_y as well as M_x/M_y components. These cross-spectral densities are found to be equal to

$$S_{{}^{w}m_{pr}\,{}^{w}m_{ps}}(\omega) = \pm\sum_{k=1}^{n_r} \frac{j\pi C_{rk}^2 \omega^4}{2(2\pi h_{rk})^5}\left[f_p\left(\frac{\omega}{2\pi h_{rk}}\right) + f_p\left(\frac{-\omega}{2\pi h_{rk}}\right)\right] \tag{2.108}$$

where the cross spectral density is positive for r>s, negative for r<s and $j=\sqrt{-1}$. The cross-spectral density function only differs by ±j from the case where $p=q$ and $r=s$. These latter cases correspond to the diagonal terms in the cross-spectral density matrix. Finally we can write:

$$S_{s/c_m}(\omega)=\sum_{p=1}^{N}T_p\begin{bmatrix} & \vdots & \\ \cdots & S_{w_{m_{pr}}w_{m_{ps}}}(\omega) & \cdots \\ & \vdots & \end{bmatrix}T_p^T=\sum_{p=1}^{N}T_pS_{w_{m_p}}(\omega)T_p^T \tag{2.109}$$

where T_p is the transformation matrix of the p-th wheel. It can be seen that the 6x6-cross spectral density matrix in the spacecraft frame is the summation of the contributions from the N wheels. If we make the further assumption that all the wheels have the same wheel speed probability density function, namely $f_{F1}(f1)=f_{F2}(f2)=f_{FN}(fN)$, as well as the same amplitude coefficients and harmonics, then we obtain

$$S_{s/c_m}(\omega)=\sum_{p=1}^{N}T_p\begin{bmatrix} S_{m_1}(\omega) & S_{m_1m_2}(\omega) & & & & \\ S_{m_1m_2}(\omega) & S_{m_2}(\omega) & & & & \\ & & S_{m_3}(\omega) & & & \\ & & & S_{m_4}(\omega) & S_{m_4m_5}(\omega) & \\ & & & S_{m_5m_4}(\omega) & S_{m_5}(\omega) & \\ & & & & & S_{m_6}(\omega) \end{bmatrix}T_p^T \tag{2.110}$$

and elements not shown are equal to zero. For simplicity we use the notation $S_{mj}(\omega)$ to represent the PSD of the j-th disturbance of a single wheel in local wheel coordinates. $S_{mjmk}(\omega)$ represents the cross-spectral density function of the j-th and k-th disturbances of the wheel. For example, $S_{m3}(\omega)$ is the PSD of the axial force disturbance, while $S_{m4m5}(\omega)$ is the cross-spectral density function of the radial moment in the x direction and the radial moment in the y direction. Equation (2.110) is the final result that is desired. It gives the 6x6 spectral density matrix of the disturbances acting in spacecraft axes due to the contributions of all individual wheel disturbances. It requires information on the number of wheels (N), the orientation of the wheels (T_p), and the spectral density matrix of the local disturbances of a single wheel (S_{wmp}).

Application to NGST

This section applies the general derivation from above to the planned configuration of NGST. The number of wheels in the square-based pyramid is N=4. The axis of maximum solar disturbance torque is expected to be the spacecraft y-axis (normal to boresight). Thus a pyramid with a slope angle of 45° is chosen, whereby the base normal vector is collinear with the spacecraft y-axis. It shall be noted that this does not represent an "equal torque" configuration, as the torque authority about the y axis is a factor of 2 larger than the authority about the spacecraft x and z axes. Figure 2.33 schematically shows the pyramidal arrangement and the orientation of the local wheel axes in the spacecraft coordinate frame.

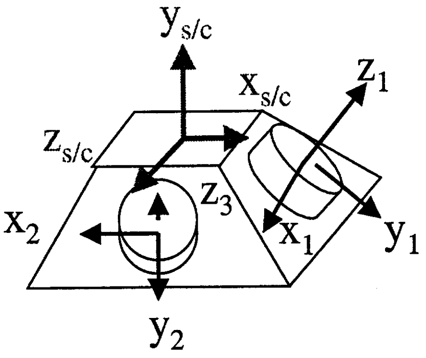

Figure 2.33: Wheel and spacecraft coordinate definition for NGST

The spin axis for each wheel is the local z-axis. The distance d from the RWA origin to the individual wheel origin can be represented by the vector $[0\ 0\ d]^T$ in the local wheel frame. All 4 wheels are oriented symmetrically about the spacecraft y-axis. The Euler angles α, θ and γ of rotation as defined earlier have to be chosen carefully. For the NGST configuration and reference wheel number 1 , we obtain the following Euler angles:

$$\alpha = -135^\circ, \quad \theta = -90^\circ, \quad \gamma = 0^\circ \tag{2.111}$$

These values can be tested by substituting into the rotation matrix equation (2.100). Thus we obtain the following rotation matrix R_1 for wheel number 1:

$$R_1 = \begin{bmatrix} 0 & \sqrt{2}/2 & \sqrt{2}/2 \\ 0 & -\sqrt{2}/2 & \sqrt{2}/2 \\ 1 & 0 & 0 \end{bmatrix} \tag{2.112}$$

An interesting question to resolve for NGST is the question of reaction wheel force offsets. So far the moments generated at the RWA origin due to wheel disturbance forces have been neglected in the NGST integrated modeling effort. This corresponds to the assumption that all wheels are physically collocated with their origins coincident with the RWA origin (i.e. no *r x F* terms are present within the RWA). The magnitude of the moments generated by the *r x F* term versus the magnitude of the radial disturbance moments can be evaluated as follows. Assuming that we are only looking at the fundamental harmonic *h=1.0* of wheel number 1 and neglecting axial forces, we can write the disturbance resultant at the wheel origin as:

$${}^{w}m_1(t) = {}^{w}\begin{Bmatrix} F_x(t) \\ F_y(t) \\ F_z(t) \\ M_x(t) \\ M_y(t) \\ M_z(t) \end{Bmatrix} = {}^{w}\begin{Bmatrix} U_s\omega^2 \sin(2\pi f_1 t + \phi_1) \\ U_s\omega^2 \cos(2\pi f_1 t + \phi_1) \\ 0 \\ U_d\omega^2 \sin(2\pi f_1 t + \phi_1) \\ U_d\omega^2 \cos(2\pi f_1 t + \phi_1) \\ 0 \end{Bmatrix} \tag{2.113}$$

The transformation from the wheel frame 1 to the RWA frame, which is assumed to be coincident with the spacecraft frame is given as:

$${}^{s/c}m_1(0) = \begin{bmatrix} R_1 & 0_{3\times3} \\ \Re_1 R_1 & R_1 \end{bmatrix} {}^{w}m_1(t) = T_1 \cdot {}^{w}m_1(t) \tag{2.114}$$

Based on engineering drawings of the TRMM [50] spacecraft and experience, the distance *d* is expected to be somewhere between 0.25 and 0.5 meters. Assuming *d*=0.5 m , F_z=0, *f*=0 and *t*=0 we obtain the disturbances from wheel 1 in RWA axes as:

$$
{}^{s/c}m_1 = \begin{bmatrix} 0 & \sqrt{2}/2 & \sqrt{2}/2 & 0 & 0 & 0 \\ 0 & -\sqrt{2}/2 & \sqrt{2}/2 & 0 & 0 & 0 \\ 1 & 0 & 0 & 0 & 0 & 0 \\ 1/2\sqrt{2} & 0 & 0 & 0 & \sqrt{2}/2 & \sqrt{2}/2 \\ -1/2\sqrt{2} & 0 & 0 & 0 & -\sqrt{2}/2 & \sqrt{2}/2 \\ 0 & -1/2 & 0 & 1 & 0 & 0 \end{bmatrix} \begin{Bmatrix} 0 \\ U_s\omega^2 \\ 0 \\ 0 \\ U_d\omega^2 \\ 0 \end{Bmatrix} = \begin{Bmatrix} (\sqrt{2}/2)U_s\omega^2 \\ -(\sqrt{2}/2)U_s\omega^2 \\ 0 \\ (\sqrt{2}/2)U_d\omega^2 \\ -(\sqrt{2}/2)U_d\omega^2 \\ -\frac{1}{2}U_s\omega^2 \end{Bmatrix} \tag{2.115}
$$

Denoting the moment due to static imbalance (forces) as M_2 and the moment due to dynamic imbalance (moments) as M_1 we can write:

$$
|M_1| = U_d\omega^2 \tag{2.116a}
$$

$$
|M_2| = d \cdot U_s\omega^2 \tag{2.116b}
$$

Taking the ratio of the magnitudes of disturbance contributions M_2/M_1 we obtain an intuitively satisfactory result. The numeric ratio was obtained assuming that d=50 cm, and for an ITHACO E-Wheel with U_s=0.716 gcm and U_d=29.54 gcm^2.

$$
c_{rxF} = \frac{|M_2|}{|M_1|} = \frac{d \cdot U_s}{U_d} = 1.21 \tag{2.117}
$$

It can be seen that the moments caused by $r \times F$ are somewhat larger, but on the same order as the moments, which are due to dynamic imbalances. For the HST wheels the above ratio is 3.896 indicating that the $r \times F$ terms are significantly larger. Thus we will retain the disturbance component due to the $r \times F$ terms in the RWA disturbance model. The key equation (2.110) has been implemented in MATLAB and can be used to generate stochastic disturbance models for subsequent performance assessments. The necessary input information, which is required to generate a realistic RWA 6x6-disturbance spectral density matrix for the NGST disturbance analysis, is shown in Table 2.5.

Table 2.5. Baseline specification of RWA disturbance parameters

Input Variables	**Values chosen**[9]
Number of wheels N	4
Euler angles reference wheel	α =-135°, θ =-90°, γ = 0°
Wheel origin offset distance	d = 0.5 m
Wheel model	ITHACO E-Wheel
Bias wheel speed	Ro= 1000 RPM
Wheel speed variation	ΔR=±1000 RPM
Wheel speed pdf	uniform

These parameters are input into a reaction wheel disturbance generation program, which incorporates the above mathematics. The result is the 6x6 spectral density matrix as indicated above except that cross spectral densities have been neglected, since they have been shown to have only minimal effects on the final results [24]. For the baseline case, using the parameters defined in Table 2.5, we obtain the following PSD's on a log-log plot:

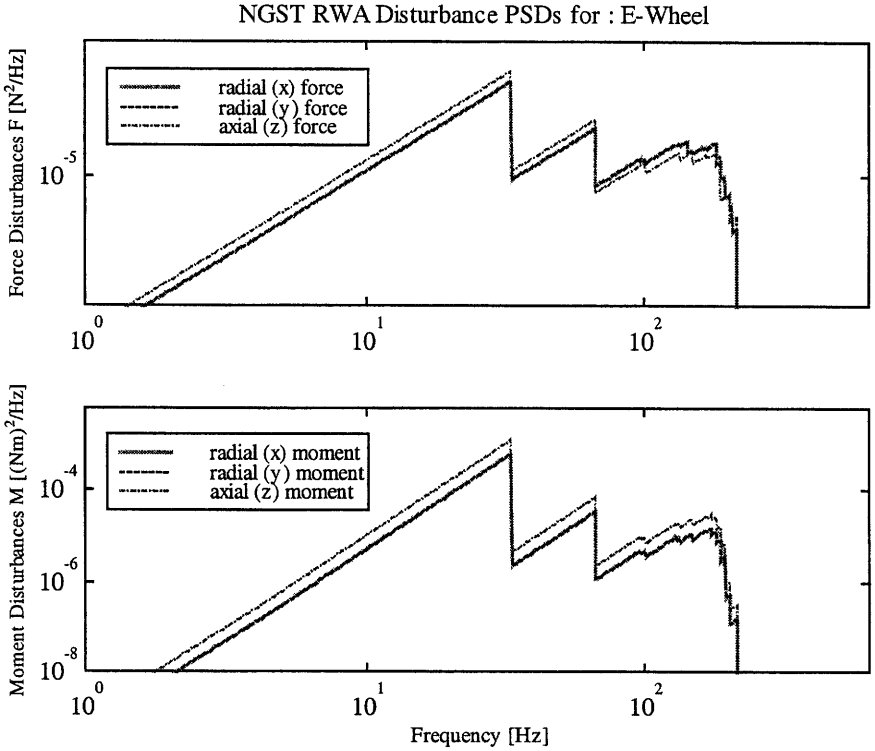

Figure 2.34: RWA disturbance PSD's for NGST baseline analysis

---

[9] These are the values chosen for the nominal case.

The resulting saw-tooth pattern is fairly typical of large RPM-variation type PSD's. The saw-tooths are due to the individual wheel harmonics and sub-harmonics sweeping across the frequency space. For smaller RPM variations there are frequency regions without any disturbance energy and for constant RPM, we would only see impulses at the frequencies of the wheel harmonics. It shall be noted that the PSD in Figure 2.34 and the ones in Figure 2.16 look very different from each other. While in the case of the cryocooler disturbance we have a narrowband disturbance, the RWA disturbances are rather broadband in nature.

2.3.5 State Space Representation of Reaction Wheel Noise

For the subsequent Lyapunov and sensitivity analyses it is necessary to recast the RWA disturbances in state space form. The stochastic RWA disturbance model, which was previously developed by Melody, Masterson and others, produces a PSD of reaction wheel disturbance assuming that the wheel speed is a random variable [47]. The output of the model is a disturbance PSD for a given wheel speed interval as shown in Figure 2.34 . However, in order to perform a disturbance analysis using Lyapunov's equation and to complete a sensitivity analysis the RWA disturbances must be in the form of linear filters. Therefore several methods have been investigated by Masterson [51]. They generally produce linear filters which, when driven by white noise, 'overbound' the PSD's, while capturing the frequency content and producing a comparable RMS value. In the case of our RWA disturbance definition in Table 2.5 we defined the wheel speed as a uniformly distributed random variable between 0 and 2000 RPM, which results in a curve covering all wheel speeds with a spike at each harmonic. The wideband overbound is successful when matching this kind of PSD. We assume a transfer function of the form:

$$G_{RWA}(s)=\frac{Ks^2}{(s+\omega_l)^2(s+\omega_h)^4} \tag{2.118}$$

is fit to the PSD. The MATLAB™ optimization toolbox is used to determine the values of the parameters, ω_l, the lower corner frequency, ω_h, the higher corner frequency and K, the gain. The optimization routine guesses values for these parameters, finds the PSD of the transfer function data using Equation (2.119), subtracts the transfer function PSD from the reference PSD and then evaluates the RMS of the resulting PSD_{diff}.

$$PSD_{TF}(\omega) = \left|G_{RWA}(\omega)\right|^2 \cdot PSD_{input} \tag{2.119}$$

where $PSD_{input} = 1$ (assuming unit intensity white noise).

The code iterates on the parameters, minimizing the RMS of PSD_{diff}. The optimization routine also contains a constraint that the first point of the PSD from the transfer function be equal to the first point of the reference PSD. As stated previously, this MATLAB function, called `wideband.m`, works relatively well when matching the wideband case as shown in Figure 2.35. It shall be noted that `wideband.m` cannot be used to match narrowband PSD's like the ones we have encountered in the cryocooler disturbance analysis.

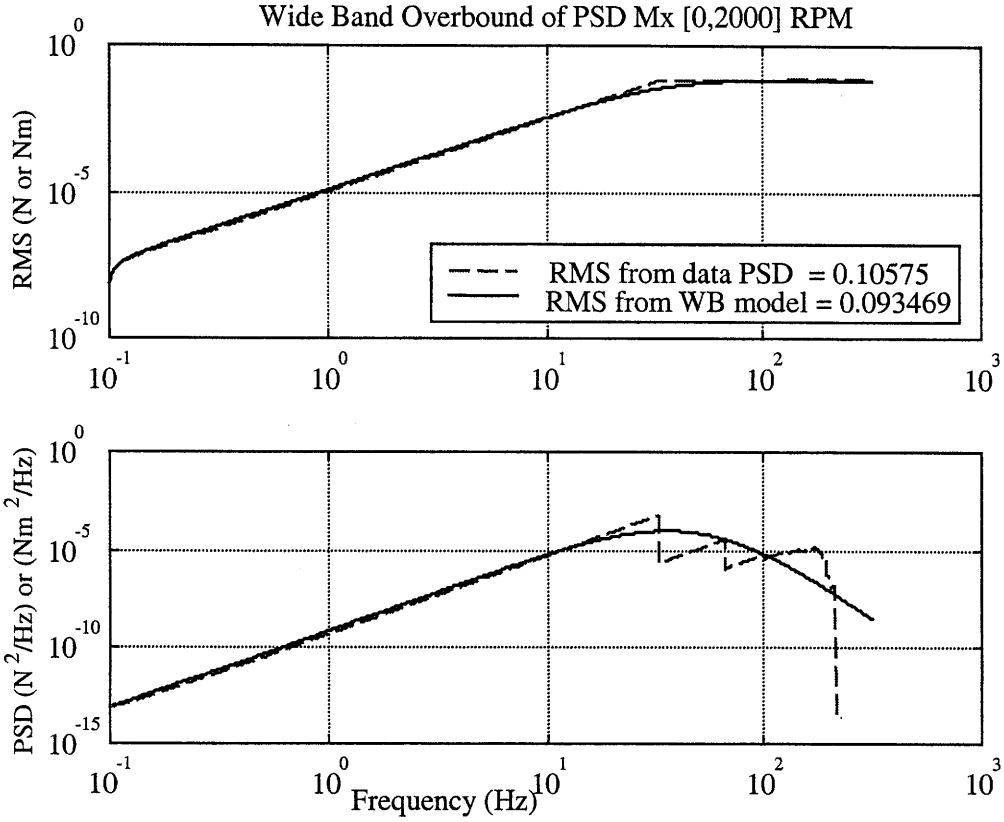

Figure 2.35: PSD overbound approximation of RWA disturbances

The 6 disturbance PSD's correspond to six outputs of the shaping filters in state space form. The optimization ensures that the RMS of the state space and the RMS of the empirical disturbance PSD are close. For the M_x component shown the RMS of the disturbance PSD is equal to 0.106 Nm , whereas the RMS for the wideband model approximation is 0.093 Nm. We can see that the energy content is similar. The state space representation uses only 6 states per component, so that the "saw-tooth" pattern of the PSD's cannot be perfectly captured. Over some frequencies the disturbance power is overpredicted (e.g. 40-100 Hz range) and over some frequencies it is underpredicted (e.g. 15-40 Hz range). Thus it is important to carry out both a frequency domain and a Lyapunov analysis in the performance assessment phase. The state space system representing the RWA disturbances can be written as:

$$\begin{aligned} \dot{\mathbf{q}}_{\mathbf{d2}} &= \mathbf{A}_{\mathbf{d2}}\mathbf{q}_{\mathbf{d2}} + \mathbf{B}_{\mathbf{d2}}d_2 \\ \mathbf{w}_2 &= \mathbf{C}_{\mathbf{d2}}\mathbf{q}_{\mathbf{d2}} \end{aligned} \tag{2.120}$$

This state space system will be appended into the overall system in the model integration section.

2.3.6 Fine Guidance Sensor Noise

It is planned to use the NIR science camera itself as the fine guidance sensor (FGS) for NGST [2]. This is a practical solution because of the large field of the cameras, and because field splitting and extensive detector mosaicing permit the use of a small portion of the field for guiding with little penalty to science. In normal operations, guide star selection can be done autonomously on-board, that is to say without prior uplink of a given guide star location. A short exposure of the desired field will first be made and the resulting image scanned for determination of the brightest star, which will then be used for guiding (thus the term "opportunistic" guide star selection). Once a guide star in the science field is identified, a small (l0x10) window of pixels surrounding the star is addressed at a relatively high frame rate (10-100 frames per second). This data is passed to a centroider, which generates commands for the FSM. The FSM control loop provides a nominal 6 Hz bandwidth. All other detector chips will be used for normal science data. To ensure a 95% probability of finding at least one guide star of a given magnitude or brighter, the average number of stars in the field available for guiding must be 3. This indicates that with a field of 4x4 arcminutes, the guiding sensor must be able to guide on stars of about 16.5 magnitude in the I band or magnitude 15.5 in the K-band. These fundamental relationships were first explored by Bely and coworkers for application to NGST [9].

Like all sensors the FGS is also subject to noise. The measuring error of a stellar guiding sensor is essentially due to photon noise and is characterized by its noise equivalent angle (NEA), which is directly dependent on the integration time. Thus a compromise between the FGS sampling rate and the resulting noise level has to be found. For a generic 4-quadrant detector (or its pixelized 2-dimensional array equivalent), the noise equivalent angle (NEA) is calculated from the equation

$$\mathrm{NEA} = \frac{1}{k\sqrt{N}} \cdot \sqrt{\left(1+\frac{R_o}{N}\right)+\varepsilon_{cent}^2} \qquad (2.121)$$

where k is the slope of the centroiding transfer function, N is the total number of detected photoelectrons, Ro is the detector readout noise, and ε_{cent} is the centroiding error. The total number of detected photoelectrons N in turn is defined by the following equation:

$$N = T_r \cdot QE \cdot A \cdot BP \cdot 10^{-0.4 \cdot M} \cdot P_H \cdot T_{INT} \qquad (2.122)$$

where T_r is the optical transmissivity, QE is the detector quantum efficiency, A is the area of sensor aperture, BP is the frequency bandpass, M is the guide star magnitude, P_H is the number of collected photons per m^2 per micron per second and T_{INT} is the integration time in seconds. The variable k is the slope of the centroiding transfer function. For a diffraction limited image, k, the slope of the positional error to error signal transfer function is given by,

$$k = \left(\frac{16}{3\pi}\right)\left(\frac{D}{\lambda}\right) \qquad (2.123)$$

where D is the diameter of the aperture in meters and λ is the electromagnetic wavelength. This finally allows to compute the noise equivalent angle as a function of the sampling time for a guide star of K-magnitude 16.5. The plot in Figure 2.36 gives the NEA as a function of integration time, assuming a read noise of 30 electrons, quantum efficiency of 0.8, an 8 meter diameter telescope, wavelength of 2.2 microns with a +/- 25% bandpass, a throughput of 0.6, and a guide star of K magnitude 16.5. To meet a requirement of 4.8 mas (1σ) and allocating no more than 50% of this error to sensor noise, we see that an integration time of at least 0.025 sec (max. 40 Hz sample rate) is required. Thus the main free variable defining the NEA is the integration time T_{INT} assuming that we will not adjust the FGS sampling rate according to the guide star magnitude. Figure 2.36 shows the guide star sensor noise in terms of NEA as a function of the sampling time T_{INT} in milliseconds:

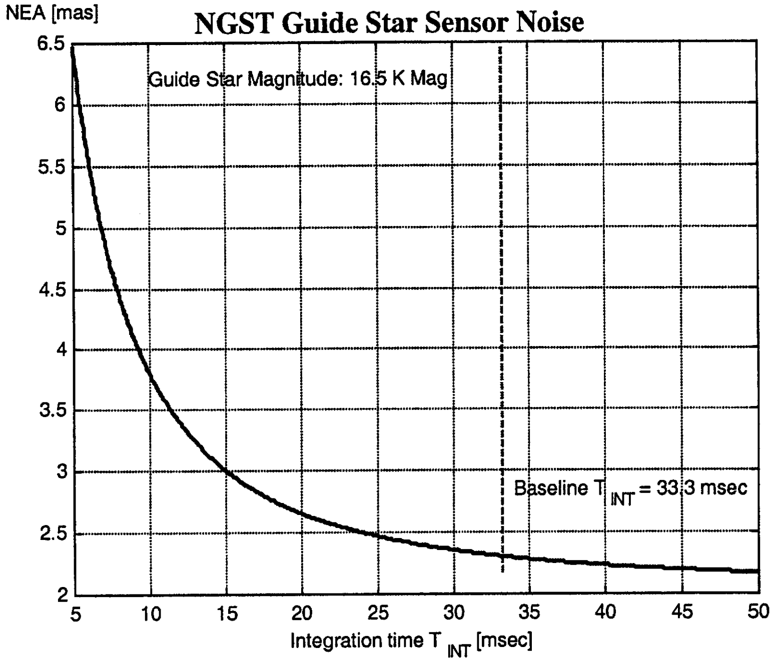

Figure 2.36: NEA [mas] versus integration time [msec] for 16.5 K magnitude star

At the nominal wavelength of 2.2 microns, at which the telescope is designed to be diffraction limited, the full width at half maximum of an image is 51 mas. Guiding errors must be less than 10% of this value (i.e. ~ 5 mas) to be practically negligible. This is the origin of the 4.8 mas pointing requirement. Guiding sensor noise is only one of the contributors to guiding errors. With a budget allocation of about 3.5 mas for sensor noise, this Figure shows that the guiding sensor could be sampled up to a rate of 100 Hz which is sufficient to correct for the internal vibrations of a deployable type observatory. The current baseline establishes an integration time of 30 msec; this is based on a guide star sampling frequency of 33 Hz. This results in a noise equivalent angle (NEA) of 2.35 mas.

In order to use the FGS noise model for the performance assessment phase in the frequency domain and Lyapunov analysis it is necessary to convert the NEA to an equivalent PSD and state space representation respectively. Since the FGS works as a discrete time system with updates every T_{int} seconds (sample-and-hold), we can approximate it with a continuos low–pass filter, whose corner frequency is equal to the update frequency. The LPF transfer function is written as:

$$G_{wd}(s) = \frac{k_{NEA}}{s + \omega_{FGS}} \tag{2.124}$$

where k_{NEA} is the noise equivalent gain and ω_{FGS} is the sampling frequency of the fine guidance sensor in rad/sec. The power spectral density of this disturbance is then computed as

$$S_{ww}(\omega) = \left| \left(\frac{k_{NEA}}{s + \omega_{FGS}} \right) \left(\frac{k_{NEA}}{\omega_{FGS} - s} \right) \right| = \frac{k_{NEA}^2}{\omega^2 + \omega_{FGS}^2} \tag{2.125}$$

The variance of the FGS noise can be computed from the area under the above PSD as

$$\begin{aligned} \sigma_{NEA}^2 &= \frac{1}{2\pi} \int_{-\infty}^{+\infty} \frac{k_{NEA}^2}{\omega^2 + \omega_{FGS}^2} d\omega = \frac{1}{\pi} \int_{0}^{+\infty} \frac{k_{NEA}^2}{\omega^2 + \omega_{FGS}^2} d\omega = \\ & \frac{k_{NEA}^2}{\pi \omega_{NEA}} \left[\underbrace{\arctan(\infty)}_{\pi/2} - \underbrace{\arctan(0)}_{0} \right] = \frac{k_{NEA}^2}{2\omega_{NEA}} \end{aligned} \tag{2.126}$$

from (2.126) we obtain the formula for k_{NEA}, since ω_{FGS} is known a priori

$$k_{NEA} = \sqrt{2\sigma_{NEA}^2 \cdot \omega_{NEA}} \tag{2.127}$$

We can transform the transfer function from white noise to FGS noise (2.124) into canonical state space form as follows:

$$\begin{aligned}\dot{q}_d &= \underbrace{\left[-\omega_{FGS}\right]}_{A_d} q_d + \underbrace{\left[1\right]}_{B_d} d_3 \\ w &= \underbrace{\left[k_{NEA}\right]}_{C_d} q_d + \underbrace{\left[0\right]}_{D_d} d_3\end{aligned} \tag{2.128}$$

This representation is valid for one axis. Since the fine guidance sensor measures the guide star position on the focal plane in the x and y channels, we have two noise signals that act in parallel. The parallel state space representation places two systems according to (2.128) in parallel:

$$\begin{aligned}\dot{\mathbf{q}}_{\mathbf{d3}} &= \underbrace{\begin{bmatrix} -\omega_{FGS} & 0 \\ 0 & -\omega_{FGS} \end{bmatrix}}_{\mathbf{A_{d3}}} \mathbf{q}_{\mathbf{d3}} + \underbrace{\begin{bmatrix} 1 \\ 1 \end{bmatrix}}_{\mathbf{B_{d3}}} d_3 \\ \mathbf{w}_3 &= \underbrace{\begin{bmatrix} k_{NEA} & 0 \\ 0 & k_{NEA} \end{bmatrix}}_{\mathbf{C_{d3}}} \mathbf{q}_{\mathbf{d3}} + \underbrace{\begin{bmatrix} 0 \\ 0 \end{bmatrix}}_{\mathbf{D_{d3}}} d_3\end{aligned} \tag{2.129}$$

It is paramount to verify that this approach indeed produces the desired noise signal. For this purpose a time simulation was created that is depicted in Figure 2.37. A band-limited white noise with a cut-off frequency that is 100 times the sampling frequency is created. This is then fed through the FGS filter state space system from (2.129).

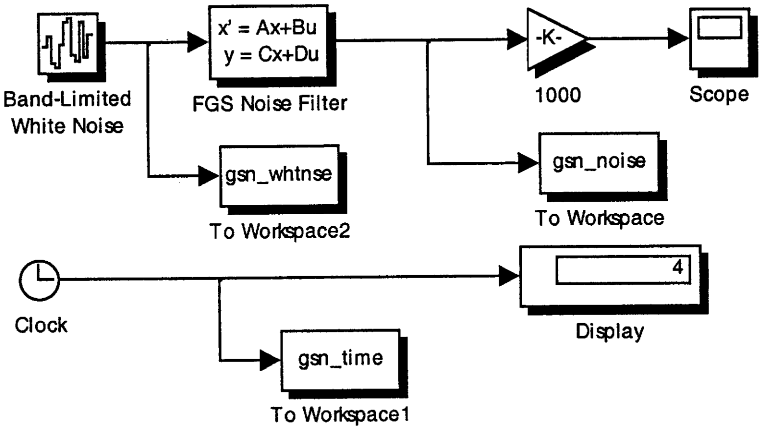

Figure 2.37: Time simulation block diagram for FGS noise

It is verified that the RMS of the noise that is generated corresponds to the NEA that we intend to simulate. By time averaging the time domain signal we obtain the desired RMS value, which is 2.36 milli-arcseconds in each channel of the guide star sensor:

$$\sigma_{d3} = \left[\frac{1}{T} \int_0^T \left(NEA(t) - \mu_{NEA} \right)^2 dt \right]^{1/2} \tag{2.130}$$

A sample realization of FGS noise is shown in Figure 2.38. This sample realization was created with a random initial seed, zero initial conditions and the state space system from (2.129).

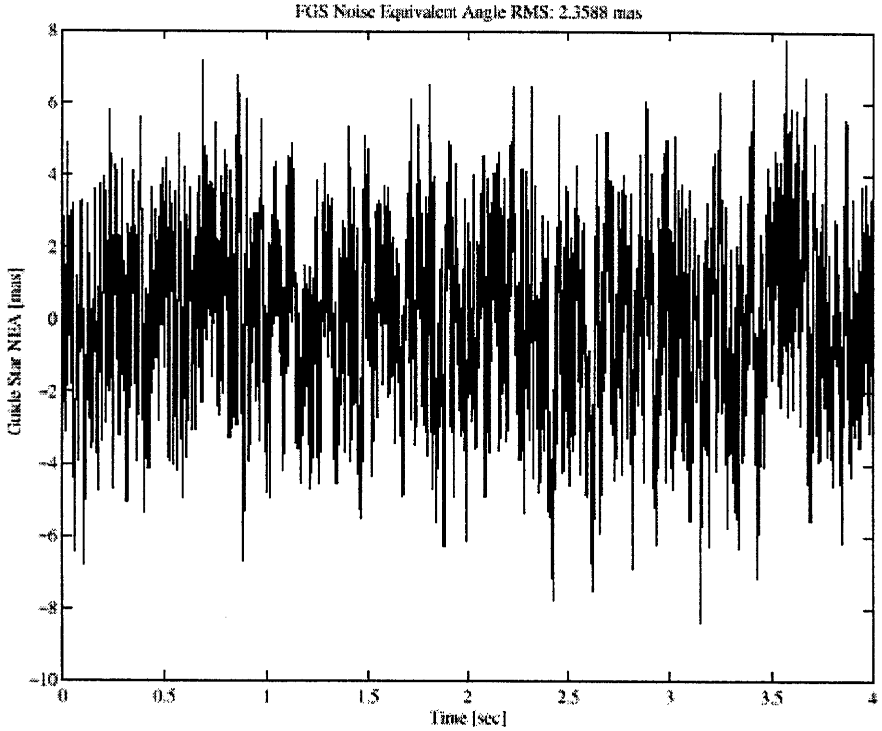

Figure 2.38: Sample realization of guide star noise expressed as NEA (only one channel shown)

Before injecting this noise into the overall state space system according to Figure 2.3 it is important to ensure that the FGS noise is in the correct units. The state space system (2.129) and specifically the matrix $\mathbf{C}_{d3}$ produces white noise in units of arcseconds. These are then converted into meters on the focal plane before being injected into the LOS stabilization loop.

2.4 Optics Modeling (= Performance Modeling)

The most challenging modeling task is doubtlessly the correct modeling of the systems performance. For space and ground based observatories optical performance metrics have to be derived from geometrical ray tracing, or if diffraction effects are of importance, Fourier optics has to be invoked. In principal the task involves first designing the optical train, i.e. the paths and elements that collect and process the science and guidance light beams from the first aperture to the detectors in the instrument module. Typical elements on the optical path are conical and flat fixed mirrors, deformable mirrors, fast steering mirrors, beam compressors, refractive lenses, beam splitters, polarization filters and the detectors themselves. The next step consists in developing an optical prescription for each of these elements, which produces the final desired result. After that the optical elements have to be placed on the structure at appropriate locations. The most difficult step is to derive the actual performance metrics and their functional dependency on the structural degrees of freedom. Two methods to accomplish this are mentioned explicitly in this thesis. The first method uses a simple ray tracing method to assess the dynamic performance of the observatory in terms of OPD and WFT using only the displacements and rotations of a few critical nodes of the system. This method is indicated only for first order trade studies and when a detailed optical prescription of the system is not available. In the second method the optics model consists of linear sensitivity matrices that are computed based on a detailed optical prescription of the system. Before discussing the optics design for NGST, we turn again to the 3DOF sample problem, which is useful for a short explanation of optics modeling in the context of LTI systems analysis.

2.4.1 Optics Modeling for 3DOF sample problem

Our sample problem shall illustrate the optics modeling process in a simplified manner. The first step consists in performing a ray trace of the science light through the system. For the sample example the science light is collected at the apertures and then redirected toward the central mass, where it is analyzed. The details of beam compressors, mirrors and the other optical elements are not modeled for this simple example. Figure 2.39 shows the two pathlengths of the light OPL1 and OPL2.

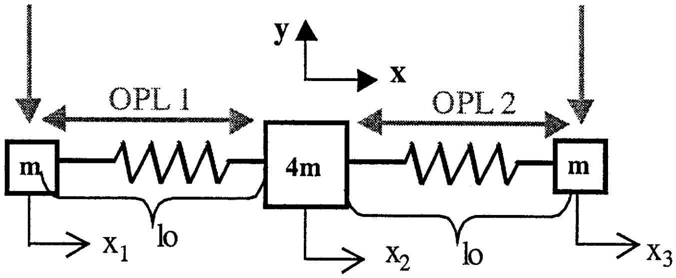

Figure 2.39: Ray Trace for sample 3-DOF problem

We choose the optical pathlength difference (OPD) as the performance metric, i.e. the optical pathlength difference is the difference in the distance between the left aperture and the right aperture from the central mass. This can be computed as:

$$OPD = OPL_1 - OPL_2 \tag{2.131}$$

The pathlengths OPL1 and OPL2 are given as

$$\begin{aligned} OPL_1 &= l_0 + (x_2 - x_1) \\ OPL_2 &= l_0 + (x_3 - x_2) \end{aligned} \tag{2.132}$$

computing the OPD gives

$$OPD = OPL_1 - OPL_2 = l_0 + x_2 - x_1 - l_o - x_3 + x_2 = -x_1 + 2x_2 - x_3 \tag{2.133}$$

and in matrix form

$$z = OPD = \underbrace{\begin{bmatrix} -1 & 2 & -1 \end{bmatrix}}_{\mathbf{C_{zx}}} \underbrace{\begin{bmatrix} x_1 \\ x_2 \\ x_3 \end{bmatrix}}_{\mathbf{X}} \tag{2.134}$$

The matrix $\mathbf{C_{zx}}$ is also called the optics linear sensitivity matrix since it relates the physical displacements of the structure to the optical performance metrics of interest. A number of simplifications have been made here since the OPD only accounts for internal pathlength differences. If rotations and *y*-displacements were allowed in the problem, we could also include the external OPD, which is due to a rigid body rotation of the entire spacecraft. This external difference is measured with respect to a reference plane of the incoming planar stellar wavefront.

At this point it is also necessary to establish a performance requirement. Typically engineering requirements are levied as a 1σ (= RMS if zero mean) requirement. For diffraction limited performance at a given wavelength λ, the OPD is constrained to be smaller than [4]

$$OPD \le \frac{\lambda}{20} \tag{2.135a}$$

Since we never want to exceed this upper bound, but we are dealing with random stochastic vibration processes, we will treat $\lambda/20$ as a 3σ upper bound, so that the following requirement for the RMS OPD emerges:

$$\sigma_{OPD} = OPD_{RMS} \le \frac{\lambda}{60} \tag{2.135b}$$

For the sample problem we will assume a wavelength of $\lambda = 7$ μm =7000 nm in the IR portion of the electromagnetic spectrum, so that the OPD RMS must be $\le$ 116 nm. For observatories working in the visual or UV regimes the requirements are tighter due to the shorter wavelength. According to (2.38) we have to compute the performance matrix $\mathbf{C_z}$ in modal space using the linear sensitivity matrix $\mathbf{C_{zx}}$ we derived above. We have only displacement and no rate dependency for the OPD such that

$$\mathbf{C_z} = \left[\mathbf{C_{zx}}{}^{o}\Phi \quad \mathbf{C_{z\dot{x}}}{}^{o}\Phi\right] = \left[\mathbf{C_{zx}}{}^{o}\Phi \quad \mathbf{0}\right] \tag{2.136}$$

Assuming we want to obtain the performance (OPD) in units of nanometers (1 nm = 10^{-9} m), we incorporate a scale factor $s_c = 10^9$ into the $\mathbf{C_z}$ matrix, which is computed as follows:

$$\mathbf{C}_{\mathbf{zx}}{}^{o}\Phi=\begin{bmatrix}-1 & 2 & -1\end{bmatrix}\begin{bmatrix}\frac{1}{\sqrt{6m}} & \frac{1}{\sqrt{2m}} & \frac{2}{\sqrt{12m}}\\ \frac{1}{\sqrt{6m}} & 0 & \frac{-1}{\sqrt{12m}}\\ \frac{1}{\sqrt{6m}} & \frac{-1}{\sqrt{2m}} & \frac{2}{\sqrt{12m}}\end{bmatrix}=\begin{bmatrix}0 & 0 & \frac{-6}{\sqrt{12m}}\end{bmatrix} \tag{2.137}$$

thus the performance matrix is given as

$$\mathbf{C}_{\mathbf{z}}=\begin{bmatrix}s_c\mathbf{C}_{\mathbf{zx}}{}^{o}\Phi & \mathbf{0}\end{bmatrix}=\begin{bmatrix}0 & 0 & -6s_c/\sqrt{12m} & 0 & 0 & 0\end{bmatrix} \tag{2.138}$$

It is interesting to note that the only non-zero entry in $\mathbf{C}_{\mathbf{z}}$ is related to the third mode. This indicates that mode 1 and mode 2 do not contribute to the OPD. Indeed this is reasonable when we consult the modeshapes on Figure 2.4. In the rigid body mode (mode 1) all masses move by the same amount simultaneously and no differential pathlength is created. In the second mode both masses move symmetrically with respect to the combiner location. Even though the optical pathlength is changing, the difference between the two paths is still zero for the second mode. Only the third mode contributes, since the masses move by different amounts, thus creating a non-zero optical pathlength difference. The feedthrough terms $\mathbf{D}_{\mathbf{zw}}$ and $\mathbf{D}_{\mathbf{zu}}$ are zero.

2.4.2 Description of NGST Optical Design

The following description of the optical design is based on reference [7]. The NGST Yardstick utilizes 9 segments in a "flower" pattern to form its primary mirror (Figure 2.40). The center segment is hard-mounted to the ISIM structure. The outer segments are folded to fit into the launch vehicle shroud. Once on orbit, they deploy, each in a single rotation. The SM is mounted on a deployed 4-strut tower, attached to a conical baffle. The mirrors and support structures are made of beryllium. The SM is followed by small tertiary and quartenary mirrors in the optical train (Figure 2.40); the latter is a deformable mirror (DM). This is followed by a fast-steering mirror (FSM). The NIR camera optics include a pyramid mirror, which feeds 4 separate channels of the NIR camera, and an Offner relay, which directs the light to the detector. More complete descriptions of the optical layout are provided in references [7] and [2].

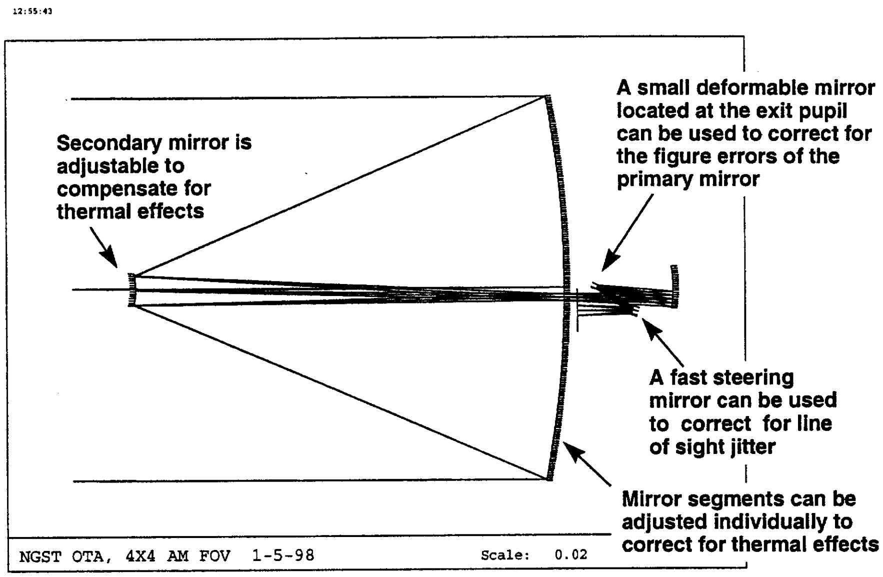

Figure 2.40: Ray trace of optical train design for NGST Yardstick

It is planned that each element in the OTA optical train can be adjusted in translation and rotation along all 6 degrees of freedom with an accuracy of about 20 nanometers. In addition, the primary mirror segments have shaping actuators, which allow for the correction of the radius of curvature.

2.4.3 Simplified Ray Tracing using critical nodes

In order to relate the performance to the science capability we need to mathematically define the performance metrics for the system. In the first approach the performance is defined in terms of the optical pathlength difference (OPD) and the wavefront tilt (WFT) in terms of only a few grid points of the system. This approach is only warranted for first order trade studies or if a detailed prescription of the optical train is not available. Figure 2.41 shows schematically how these performance metrics are defined:

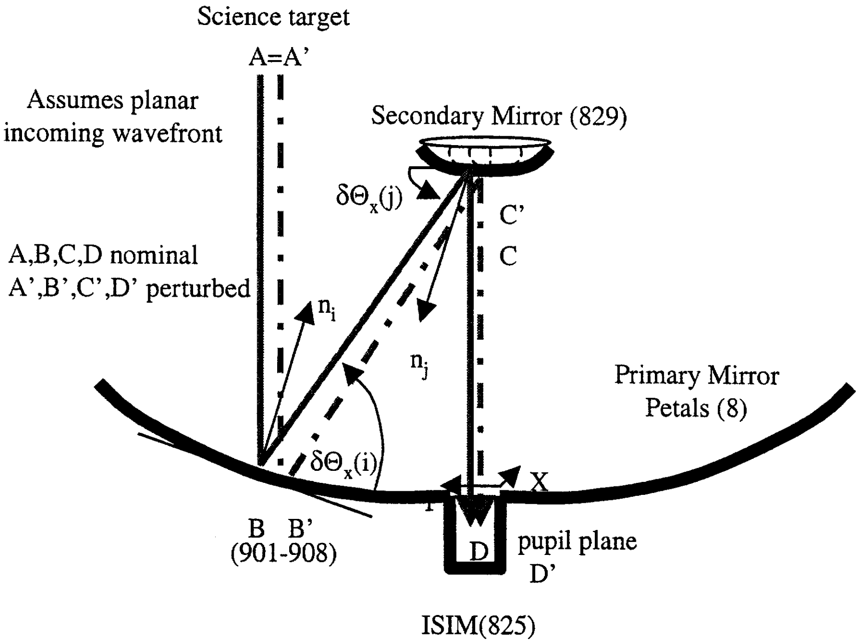

Figure 2.41: Schematic representation of linearized performance metrics

The wavefront error in terms of OPD is based on a geometric optics approach [52]. The optical pathlength difference is a measure of the phase difference of a ray, which is traced through the optical train from the primary mirror to the ISIM, compared to a ray in the unperturbed configuration. Thus the OPD is defined as:

$$\mathrm{OPD}=\overline{AB}+\overline{BC}+\overline{CD}-\overline{A'B'}-\overline{B'C'}-\overline{C'D'} \tag{2.139}$$

where the prime denotes the nodes, which are perturbed due to the flexible dynamics of the system. The wavefront tilt is the angle between the incident ray and the focal plane normal vector. In this study the wavefront tilt is determined in the x and y axes at the ISIM focal plane, which is assumed to be at the base of the secondary support tower (WFTX and WFTY). These performances are linearized and are shown schematically in Figure 2.41. The wavefront tilt is related to the angular displacements of the primary and secondary mirror nodes as:

$$\mathrm{WFTX} = 2\delta\Theta_x(i) - 2\delta\Theta_x(j) \tag{2.140}$$

The WFT in the y direction is defined accordingly. This simplified approach assumes that the only contribution to OPD and WFT comes from primary and secondary mirror and base (ISIM) displacements and rotations. Results for a preliminary analysis using this approach have been published and are shown in reference [52].

2.4.4 Full optical linear sensitivity matrices

A more appropriate method for detailed integrated modeling uses optical linear sensitivity matrices. The linear sensitivity matrices for the optics model are computed by introducing a unit perturbation to one degree of freedom at a time and computing wavefront and centroid in MACOS [53]. Fundamental work in the area of linearized optics models for dynamics and controls was carried out by Redding, Breckenridge and coworkers [16]. The matrices are formed one column at a time by numerical differentiation [11]. Mathematically, the linear optics models are given by:

$$W = W_o + \frac{\partial W}{\partial y_2} y_2 \tag{2.141}$$

$$C = C_o + \frac{\partial C}{\partial y_2} y_2 \tag{2.142}$$

where y_2 is the vector of translation and rotations of the FEM coordinates, augmented by the FSM gimbal coordinates (74xl) as shown in Figure 2.3, C is the centroid for the chief ray (2xl), W is the OPD (=WFE) vector (1845xl). We denote $K_1 = \partial C / \partial y_2$ as the centroid linear sensitivity matrix (2x74), and $K_3 = \partial W / \partial y_2$ as the wavefront linear sensitivity matrix (1845x74). Assuming that $W_o = 0$ and $C_o = 0$, equations (2.141) and (2.142) can then be rewritten as:

$$z_1 = W = \frac{\partial W}{\partial y_2} y_2 = K_3 y_2 \tag{2.143}$$

$$z_2 = C = \frac{\partial C}{\partial y_2} y_2 = K_1 y_2 \qquad (2.144)$$

Figure 2.42 plots the linear sensitivity matrix for centroid versus the degree of freedom number of the plant output vector. This is interesting, since it directly shows which displacements or rotations significantly affect the LOS performance. Analyzing this in depth, we see that the centroid is particularly sensitive to the *y* and *z* rotations of the central petal mirror node and to the primary mirror petal grid point rotations in y and z. Those grid point locations are graphically shown in Figure 2.5. At the time of this research the linear sensitivity matrices for NGST were in the process of being recalculated.

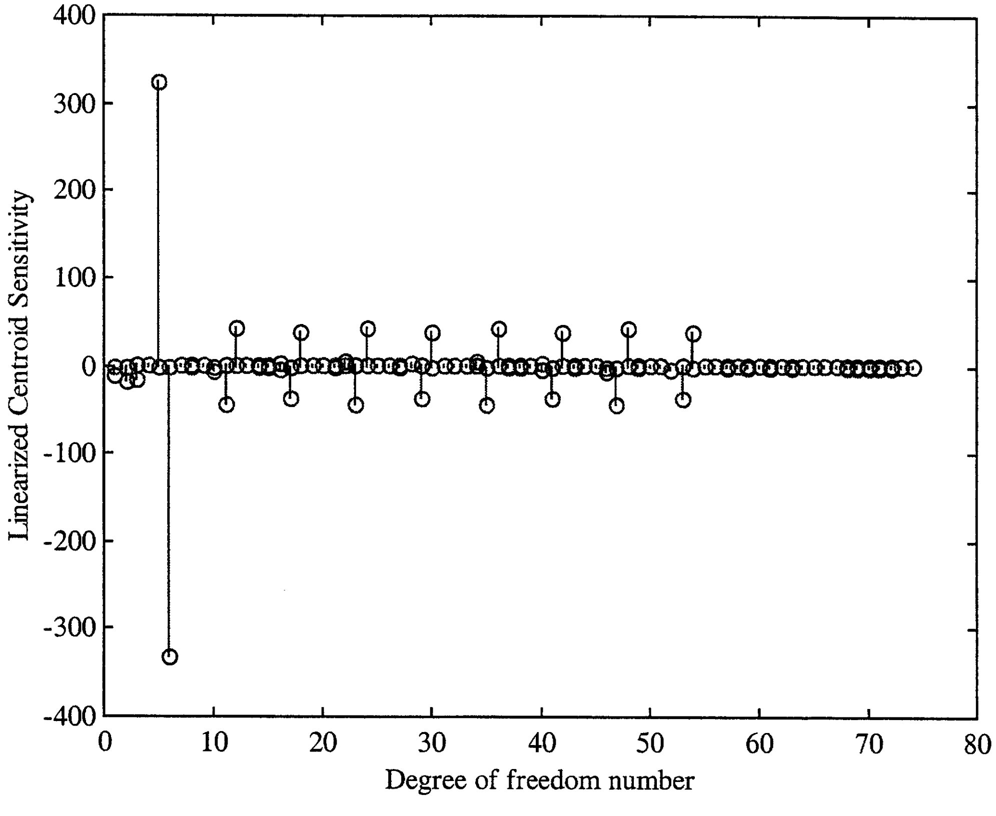

Figure 2.42: Graphical representation of centroid linear sensitivities $\partial C/\partial y_2$ versus y_2

The large number of rays used by the ray-tracing algorithm in MACOS allows a good representation of the spatial distribution of the WFE. On the other hand it requires the computation of a very large number of transfer functions. This issue is addressed in section 4.2, where singular value decomposition is demonstrated as a potential solution. Figure 2.43 shows the unperturbed spot diagram for NGST, i.e. the locus of points where the individual rays are going to pierce through a reference surface immediately before the focal plane. A total of 1845 rays are modeled in a rasterized fashion. The diameter of the spot is 6 cm, which corresponds to an optical magnification of 120, since the effective diameter of the primary mirror is 7.2 m.

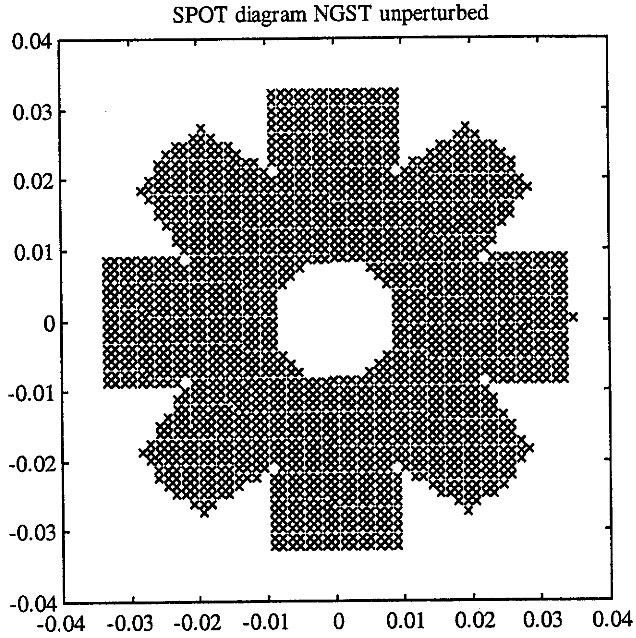

Figure 2.43: Unperturbed spot diagram for NGST (units of meters)

Ultimately, the disturbance analysis condenses the results down to only two root-mean-square numbers: RMS WFE and RMS LOS. These metrics are root-mean-square values and are obtained from the 1847 outputs in the following manner:

$$z_{WFE\ RMS} = \left(\frac{1}{n_{rays}} \left(z_1^T z_1 \right) \right)^{1/2} = \sqrt{E[z_1^2]} \tag{2.145}$$

Thus the WFE RMS value is the root mean square result of the values for each individual ray across the physical aperture of the telescope. In a similar manner the RMS LOS (line of sight) error is calculated from the centroid x and y errors:

$$z_{WFE\ LOS} = \left(\frac{1}{2} \left(z_2^T z_2 \right) \right)^{1/2} = \sqrt{E[z_2^2]} \tag{2.146}$$

The matrices $\mathbf{K}_1$, $\mathbf{K}_2$ and $\mathbf{K}_3$ are visible in the block diagram of Figure 2.3 and can be directly applied in the integrated model as will be shown in section 2.6

2.5 Controls Modeling

The last step before assembling the integrated model consists in designing a control system, which is often responsible for bringing the optical performance within the bounds set by the requirements. Due to these stringent requirements it is reasonable to predict that all future space science missions will incorporate control systems not only at the ACS level, but also for optical control. Traditionally the attitude determination and control system (ADCS) is designed to stabilize the rigid body modes of the spacecraft. In order to ensure sufficient stability margins the bandwidth of the ACS is often set to be about 1 decade below the first flexible mode of the structure. The second control system that is often modeled, as a decoupled system from the ACS, is optical control. Depending on the application the optical control incorporates deformable mirrors for wavefront control, fast steering mirrors for fine pointing control or optical delay lines for phasing control in interferometric applications. There are some key questions that need to be answered regardless of the specific goals of the optical or attitude control system:

- What is my expected control performance?
- What are my sensors, what is their resolution and sampling rate?
- What are my actuators, what is their authority, resolution and bandwidth?
- What is the control architecture to convert sensor output to control input signals?
- What are the uncertainty and delay in the system and what stability margins are expected?

Due to the complexity of these questions the control theory for flexible opto-mechanical systems has evolved dramatically over the last three decades and a number of useful tools for designing and analyzing SISO and MIMO control systems have been developed [23]. The NGST uses two control loops to provide fine pointing and slewing capability. The low-bandwidth ADCS loop uses star trackers and gyros for sensors and reaction wheels and thrusters as actuators. The fine pointing control system uses a fast steering mirror to stabilize the telescope line of sight. These two loops are modeled in a simplified way here and are described in this section. The LOS stabilization loop provides several Hz of bandwidth for fine guiding and jitter suppression. Sensing is provided by a portion of the NIR camera itself, whereby there is a fundamental limit to the sensor bandwidth due to the faintness of the guide stars used as described in the section on guide star noise. Guiding is performed continuously during initialization and observations, using opportunistic guide stars. In reality FSM displacements are fed back to the spacecraft attitude control system (ACS), which acts to desaturate them in a very low bandwidth follow-up loop. This aspect has been neglected in this analysis due to the minimal impact on the dynamic performance[10]. Before exploring the two controls systems for NGST we turn again to our sample 3DOF problem, which lays out the controls modeling steps in a simplified way.

2.5.1 Controls for sample 3DOF problem

For the sample problem we will again choose a simple approach in answering the above questions. A block diagram of the control subsystem shows which matrices have to be computed for the control design.

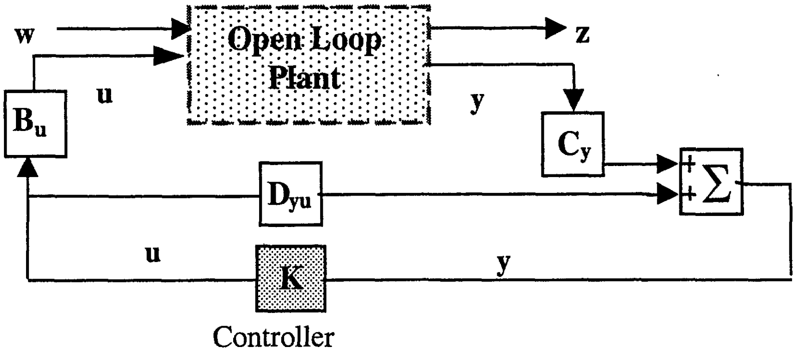

Figure 2.44: Matrices involved in control design for 3DOF sample problem

The matrix $\mathbf{C_y}$ is very similar to the matrix $\mathbf{C_z}$, as it captures the modal contributions to the sensor signals from the state space model of the plant. It contains the matrix $\mathbf{C_{yx}}$ that determines the linear combination of generalized displacement states that can be read by the sensor. In other words it maps the structural states into the ideal sensor measurements. The matrix $\mathbf{C_y}$ is

---

[10] Assuming that the FSM is continuously operating in its useful range of motion

closely related to the notion of observability. The matrix $\mathbf{B_u}$ maps the control inputs into forces and moments at the appropriate degrees of freedom of the structural model.

Optical Control: For the sample problem a laser metrology system is used as a sensor that gives a measure of the actual pathlength difference between the two apertures. The laser metrology system consists of two laser interferometers, which are located on the central mass. They bounce off a laser beam from a mirror, which is mounted, on each aperture and measure the traveled distance (which corresponds to twice the OPL for each arm). The sensor output y is then the difference between the two laser measurements.

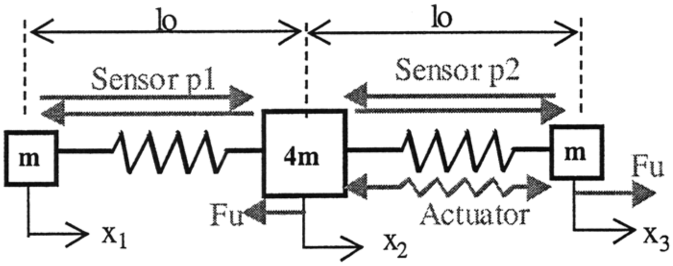

Figure 2.45: DPL measurement with laser metrology system

$$\begin{aligned} p_1 &= 2(l_0 + x_2 - x_1) \\ p_2 &= 2(l_0 + x_3 - x_2) \end{aligned} \tag{2.147}$$

the sensor output is given as

$$y = p_2 - p_1 = 2x_3 - 4x_2 + 2x_1 \tag{2.148}$$

In matrix form we obtain the output (ideal sensor measurement) as written in the following equation. It is assumed that the sensor is high quality and is able to amplify the signal, such that the sensor output is in units of nm, therefore a scale factor $s_c = 10^9$ is included in the $\mathbf{C_y}$ matrix

$$y = s_c \cdot \underbrace{\begin{bmatrix} 2 & -4 & 2 \end{bmatrix}}_{\mathbf{C_{yx}}} \underbrace{\begin{bmatrix} x_1 \\ x_2 \\ x_3 \end{bmatrix}}_{\mathbf{x}} \tag{2.149}$$

The following relationship exists between $\mathbf{C}_{\mathbf{yx}}$ and $\mathbf{C}_{\mathbf{zx}}$

$$\mathbf{C}_{\mathbf{yx}} = -2\mathbf{C}_{\mathbf{zx}} \tag{2.150a}$$

the sensor output matrix $\mathbf{C}_{\mathbf{y}}$ is computed so that $\mathbf{C}_{\mathbf{y}\dot{\mathbf{x}}} = 0$ and ensuring that the output is in nm,

$$\mathbf{C}_{\mathbf{y}} = \begin{bmatrix} s_c \mathbf{C}_{\mathbf{yx}} {}^{o}\Phi & 0 \end{bmatrix} = \begin{bmatrix} 0 & 0 & s_c\sqrt{12/m} & 0 & 0 & 0 \end{bmatrix} \tag{2.150b}$$

We assume that we are using a low impedance force actuator, such as an active strut, as represented in Figure 2.45. This actuator commands a differential force rather than differential displacement. The objective of the controller is to bring the OPD to zero, therefore only one of the observatory arms needs to be equipped with the actuator. Due to "actio=reactio" the actuator exerts a force F_u of equal magnitude but opposite sign on nodes 2 and 3. Thus we can write

$$\mathbf{u} = \begin{bmatrix} 0 \\ -F_u \\ F_u \end{bmatrix} = \underbrace{\begin{bmatrix} 0 & -1 & 1 \end{bmatrix}^T}_{\beta_{\mathbf{u}}} F_u \tag{2.151}$$

the matrix $\mathbf{B}_{\mathbf{u}}$ is obtained in an analogous fashion to $\mathbf{C}_{\mathbf{y}}$ as:

$$\mathbf{B}_{\mathbf{u}} = \begin{bmatrix} 0 \\ {}^{o}\Phi^T \beta_{\mathbf{u}} \end{bmatrix} \tag{2.152}$$

the lower half of $\mathbf{B}_{\mathbf{u}}$ is

$${}^{o}\Phi^T \beta_{\mathbf{u}} = \begin{bmatrix} \frac{1}{\sqrt{6m}} & \frac{1}{\sqrt{6m}} & \frac{1}{\sqrt{6m}} \\ \frac{1}{\sqrt{2m}} & 0 & \frac{-1}{\sqrt{2m}} \\ \frac{2}{\sqrt{12m}} & \frac{-1}{\sqrt{12m}} & \frac{2}{\sqrt{12m}} \end{bmatrix} \begin{bmatrix} 0 \\ -1 \\ 1 \end{bmatrix} = \begin{bmatrix} 0 \\ \frac{-1}{\sqrt{2m}} \\ \frac{3}{\sqrt{12m}} \end{bmatrix} \tag{2.153}$$

thus the input influence matrix $\mathbf{B}_{\mathbf{u}}$ is

$$\mathbf{B}_{\mathbf{u}} = \begin{bmatrix} 0 & 0 & 0 & 0 & -1/\sqrt{2m} & 3/\sqrt{12m} \end{bmatrix}^T \tag{2.154}$$

Since there is no feedthrough from u to y, we can set the feedthrough term $\mathbf{D_{yu}}$ to zero. The controller will be a SISO controller, which receives the y measurement from the laser metrology system and issues a force command u to the force actuator. As a simple solution we choose a PD-controller with time delay and use classical control techniques to design it. We thus apply static compensation of the OPD and provide rate feedback at the same time. The feedback equation is:

$$u = \mathbf{K}\, y \tag{2.155}$$

For PD control with negative feedback and time delay we write

$$K(s) = (-1)\left\{ K_p + \frac{K_d s}{\tau_d s + 1} \right\} \tag{2.156}$$

where K_p is the proportional gain, K_d is the derivative gain and τ_d is the time delay [22]. The controller transfer function can be rewritten as:

$$K(s) = \frac{-u(s)}{y(s)} = \frac{-\left(K_p \tau_d + K_d\right)s - Kp}{\tau_d s + 1} = \frac{a_1 s + a_o}{b_1 s + b_o} \tag{2.157}$$

The controller canonical form[11] of the controller transfer function is given as

$$\begin{aligned} \frac{dq_c}{dt} &= \left[\frac{-b_o}{b_1} \right] q_c + [1]\, y \\ u &= \left[\frac{a_o b_1 - a_1 b_0}{b_1^2} \right] q_c + \left[\frac{a_1}{b_1} \right] y \end{aligned} \tag{2.158}$$

Substituting the coefficients obtained by comparison of (2.157) and (2.158) we obtain the controller state space representation:

---

[11] This definition is also compatible with the MATLAB tf2ss.m function

$$\frac{d\dot{q}_c}{dt} = \underbrace{\left[-1/\tau_d\right]}_{\mathbf{A_c}} q_c + \underbrace{\left[1\right]}_{\mathbf{B_c}} y$$
$$u = \underbrace{\left[-K_d/\tau_d^2\right]}_{\mathbf{C_c}} q_c + \underbrace{\left[K_p + K_d/\tau_d\right]}_{\mathbf{D_c}} y \tag{2.159}$$

After some initial trials we choose $K_p = 0.01$ and $K_d = 0.05$ as initial controller gain values. This assumes that the sensor signal is provided in units of nm. It will be the goal of the performance improvement section to tune these parameters. The time delay is expected to be $\tau_d = 0.1$ sec.

ACS: This is also the point where a full attitude determination and control system design should take place. This is required in order to stabilize the rigid body mode. Instead of modeling the ACS in detail for the sample problem we represent the effect of a closed loop ACS for the sample problem by stiffening and dampening the rigid body mode. The plant dynamics matrix $\mathbf{A_p}$ is ill conditioned in the present state. The condition number c_{Ap} is given as the ratio of the largest singular value of $\mathbf{A_p}$ to the smallest singular value:

$$c_{A_p} = \frac{\sigma_{A_p}^{\max}}{\sigma_{A_p}^{\min}} = 2.53 \cdot 10^{16} \tag{2.160a}$$

A large condition number indicates that $\mathbf{A_p}$ is nearly singular. Assuming a 1 Hz bandwidth of the ACS controller and critical damping we set:

$$\omega_1 = 2\pi \left[\frac{\text{rad}}{\text{sec}}\right], \quad \zeta_1 = .707 \tag{2.161}$$

so that the $\mathbf{A_p}$ matrix with the stabilized rigid body mode and all the numerical values substituted in looks as follows:

$$\mathbf{A_p} = \begin{bmatrix} 0 & 0 & 0 & 1 & 0 & 0 \\ 0 & 0 & 0 & 0 & 1 & 0 \\ 0 & 0 & 0 & 0 & 0 & 1 \\ -39.47 & 0 & 0 & -8.8844 & 0 & 0 \\ 0 & -35500 & 0 & 0 & -1.884 & 0 \\ 0 & 0 & -53250 & 0 & 0 & -2.308 \end{bmatrix} \tag{2.162}$$

The condition number of the stabilized $\mathbf{A_p}$ matrix is now significantly lower

$$c_{A_p} = \frac{\sigma_{A_p}^{\max}}{\sigma_{A_p}^{\min}} = 5.4583 \cdot 10^4 \tag{2.160b}$$

Numerical conditioning for the full order NGST model is discussed in section 4.1. At this point we need to assemble and analyze the performance and stability of the closed loop system. This is done in the integrated modeling section.

2.5.2 NGST Attitude Control System

The following description of the NGST ADCS is based on previous work by Femiano, Ha and others [35]. The ACS block in the NGST NSIM model provides command channels for position and rate, attitude determination and control, and attitude sensor and actuator models. Attitude estimation is given by star tracker and gyro measurements, outputs of the dynamics block corrupted by sensor noise models, combined in a Kalman Filter [35]. Position and rate error signals are fed to decoupled roll/pitch/yaw PID loops. Coupling is obtained by multiplying the decoupled acceleration signals from the PID loops by the estimated inertia matrix. This is essential for NGST, as there is significant cross-axis coupling. Lowpass filters provide flexible mode suppression to meet design stability criteria of 12-dB gain and 30 degrees phase for rigid body, 10-dB gain for flexible modes. The ACS system is very low bandwidth (0.025 Hz), providing effectively no attenuation of reaction wheel disturbances, which generally are well above 1-2 Hz. The system provides base motion stable at the arc-second level. Figure 2.46 shows the top-level diagram of the ADCS model that was developed by Femiano, Ha and co-workers [35].

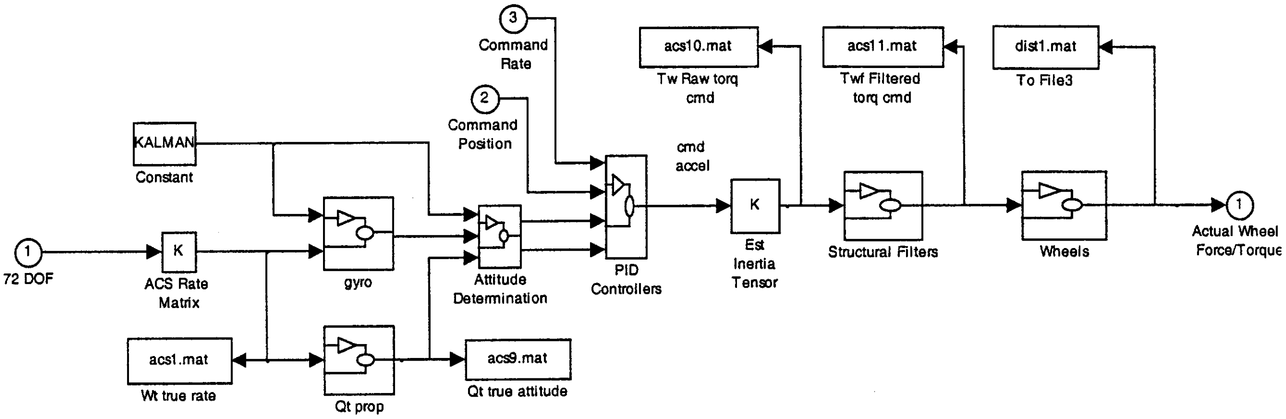

Figure 2.46 Top-Level ADCS block diagram as implemented in NSIM simulation model

For use in this analysis however we will employ a MIMO controller that is based on the LQG (Linear Quadratic Gaussian) regulator problem. A Riccati equation is solved to obtain the matrix of optimal controller gains in an H_2 sense. Frazzoli initially developed this approach for use on the conceptual TPF mission design [54]. It was shown that this method can also be applied to NGST. The inputs to the ADCS are the 3 angles and rates that are considered to be ideal sensor measurements at the ADCS grid point of NGST. The outputs of the controller are the three torques. More detailed information can be obtained in reference [54]. The ADCS controller (H_2) is cast into state space form, where the inputs are the outputs of the FEM dynamics block (3 angles and 3 rates) at the ADCS point and the outputs are the three torques that are input into the FEM dynamics together with the RWA noise:

$$\begin{aligned} \dot{\mathbf{q}}_k &= \mathbf{A}_k \mathbf{q}_k + \mathbf{B}_k \mathbf{y}_k \\ \mathbf{u}_k &= \mathbf{C}_k \mathbf{q}_k \end{aligned} \tag{2.161}$$

This state space system is integrated into the overall model in section 2.6

2.4.3 Fine Guidance System (LOS Stabilization)

One of the major technical differences between the Hubble Space Telescope (HST) and NGST is that HST relies on body pointing to achieve the desired pointing accuracy during astronomical observations. This requires that the ACS maintain the boresight axis of the spacecraft within a tight tolerance. For NGST on the other hand the pointing accuracy of the spacecraft itself and the fine pointing requirements of the optics will be decoupled within the dynamic range of the fast steering mirror (FSM). The large collecting aperture of NGST permits the sensing of line-of-sight variations at high rates using relatively faint guide stars. This sensing advantage is combined with the use of a fast steering mirror to correct the line of sight (LOS) jitter in the science instrument module itself. The OTA itself can be left to wander slightly due to SSM-induced pointing errors [7]. This approach reduces demands on the spacecraft attitude control and vibration isolation systems respectively.

The FSM is an integral part of the optical train in a feedback loop configuration, which has to maintain the centroid within the 1σ requirement. The SSM inertial reference sensors (star trackers and/or coarse sun sensors) are not suitable as a tracking reference for the FSM for two reasons. Firstly the ACS sensors are non-collocated with respect to the centroid, which can introduce non-minimum phase zeros and create stability problems for the FSM loop. Secondly the resolution of the ST and CSS's is insufficient to meet the NGST fine pointing requirements. The use of the NIR camera as the guiding sensor has already been described in section 2.3.5. Active control of the line of sight is performed by a tip-tilt mirror located at or near a pupil upstream of the science instruments. Fast steering mirrors are suspended on flexures and driven by electromagnetic actuators, which are mechanically very reliable.

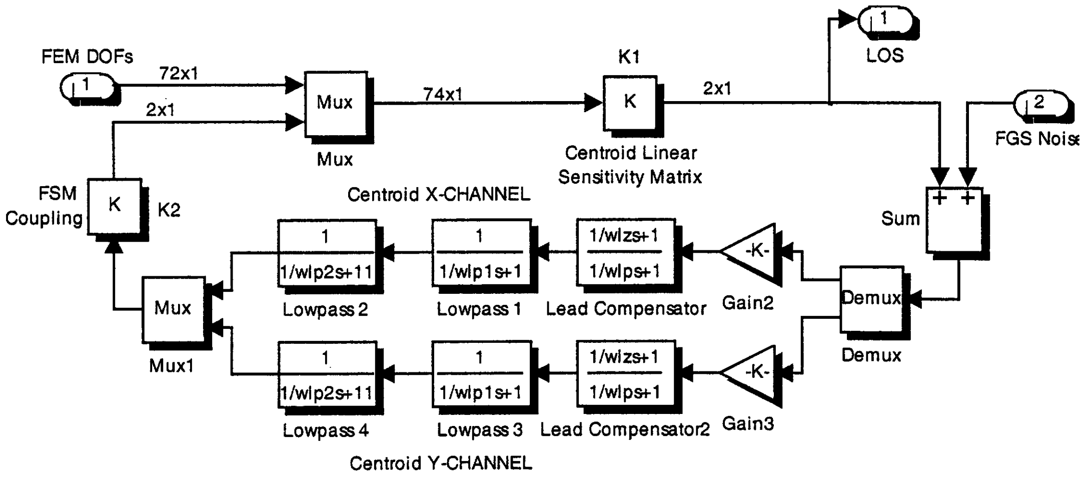

Figure 2.47: FSM controller in block diagram form (both channels)

Figure 2.47 shows the model for the FMS control, used in this thesis. We assume that the FSM plant dynamics are much higher than the plant dynamics of the spacecraft structure, so that the FSM plant itself is not modeled. The FSM model was derived from transfer function data taken from an off-the-shelf design [35]. The poles and zeros were scaled from the nominal 2200 Hz rate to the 30 Hz rate set by the guide star noise. It is seen in the transfer function plots in Figure 2.48 that the FSM acts as a low-pass filter to the mirror angle command, including guide star noise, but as a high-pass filter to the base motion. The effective bandwidth of this controller (in terms of base-motion suppression) is approximately 2 Hz. This could be raised in an attempt to use the FSM to attenuate errors due to higher structural modes, but at the expense of increasing the contribution of guide star noise to the total LOS error. A way around that would be to use brighter guide stars to reduce the sensor noise, but that, in turn, would require a larger FOV for the NIR camera – this represents a true systems-level trade according to Mosier [9]. Thus the transfer function from guide sensor noise to LOS error is given as:

$$\frac{\theta_{LOS}}{\eta_{GS}} = \frac{G_C G_P}{1 + G_C G_P} \tag{2.162}$$

and the magnitude plot is given in Figure 2.48

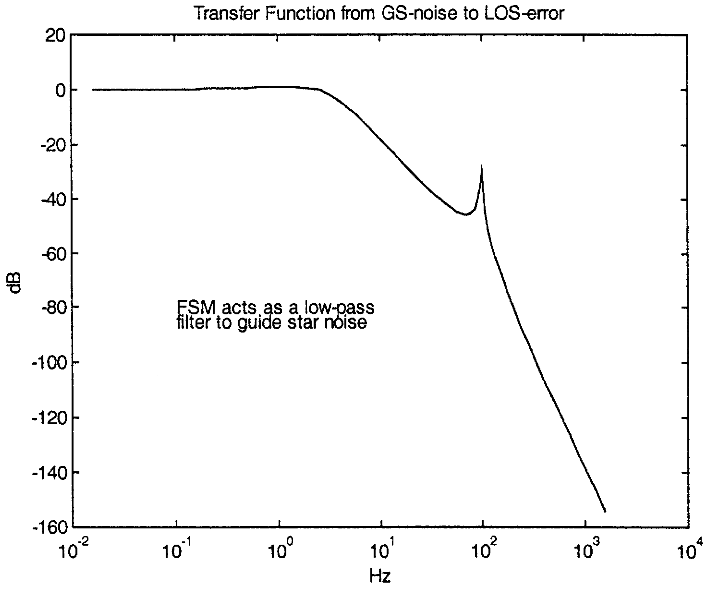

Figure 2.48: Transfer function from FGS noise to LOS error

and the transfer function from OTA angular motion to LOS error is given as:

$$\frac{\theta_{LOS}}{\theta_{OTA}} = \frac{1}{1+G_C G_P} \tag{2.163}$$

where the transfer function magnitude is shown in Figure 2.49

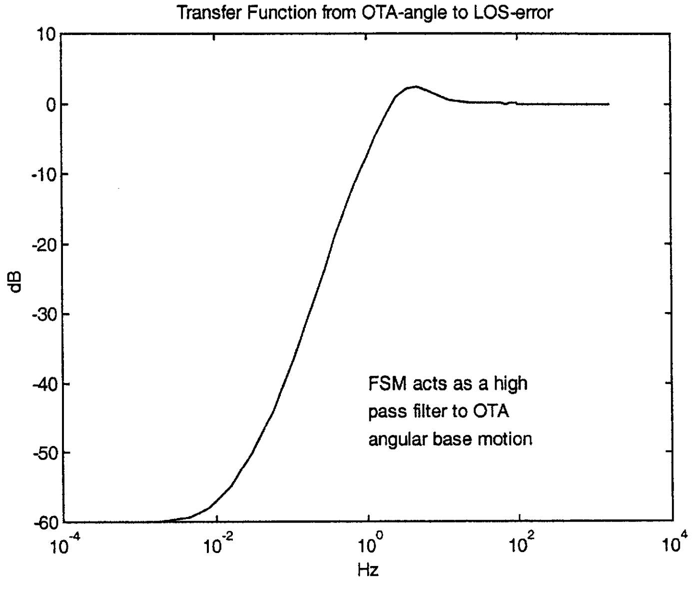

Figure 2.49:- FSM Transfer Function from OTA-angle to LOS error

The transfer function representation is transformed into a state space representation, which contains both parallel channels in the X and Y-axes. The FSM Controller state space representation is a 2x2 system and can be written as follows:

$$\begin{aligned} \mathbf{q}_1 &= \mathbf{A}_1\mathbf{q}_1 + \mathbf{B}_1\mathbf{y}_3 \\ \mathbf{u}_1 &= \mathbf{C}_1\mathbf{q}_1 + \mathbf{D}_1\mathbf{y}_3 \end{aligned} \tag{2.164}$$

This state space system will be used in the integrated modeling process as shown in the next section.

2.6 Assembly of the integrated model

This section integrates the results from the previous section into an overall linear model of the dynamics of NGST, which is subsequently used for the performance assessment analysis. There are several ways to propagate a disturbance through the closed loop system in order to estimate the performance. Gutierrez [24] suggests the following three methods as a possibility. The time-domain analysis assumes that the time history of the disturbances d is given and performs numerical integration to obtain the time history of z. The frequency-domain analysis starts with the spectral density functions of the disturbance and directly computes the PSD's of the outputs. The third option is to perform a Lyapunov analysis, which results in the covariance matrix of the performances of a linear system driven by white noise. The first and third option require that the system be written in closed loop state space form from white noise input to the performance metrics of interest. The second option is written from the shaped disturbances w to the performance metrics z of interest. The goal of the integrated modeling section is to assemble all submodels into an overall model, to check the stability of that model and to verify that all the units are correct. Before assembling the full NGST model, we will discuss the sample 3DOF problem and demonstrate the essential steps.

2.6.1 Integrated model for 3DOF sample problem

The main task of integrated modeling is to assemble the results from the previous sections, i.e. structural, disturbance, performance and controls models into one overall model. For linear systems this model is usually represented in state space form. Additionally the integrated modeler needs to analyze the closed loop system for stability, observability and controllability to ensure that no mistakes have been made previously and that the system is well conditioned for subsequent analysis. The Lyapunov analysis for example requires that the system be stable, e.g. the $\mathbf{A}_{zd}$ matrix must be non-singular. It is thus paramount that the rigid body modes of the system have either been removed or stabilized by the ADCS.

For the Lyapunov analysis it is desirable to integrate the disturbance, structural and controls models together into one system. This system describes the dynamics from a white noise source input d to the performance metrics z. The first step is to append the disturbance states $\mathbf{q}_d$, the structural plant states $\mathbf{q}_p$ and the control states $\mathbf{q}_c$ into an overall state vector:

$$\mathbf{q} = \begin{bmatrix} \mathbf{q}_d \\ \mathbf{q}_p \\ \mathbf{q}_c \end{bmatrix} \tag{2.165}$$

The overall system dynamics for the sample problem are then written by appending the system together according to the following block diagram:

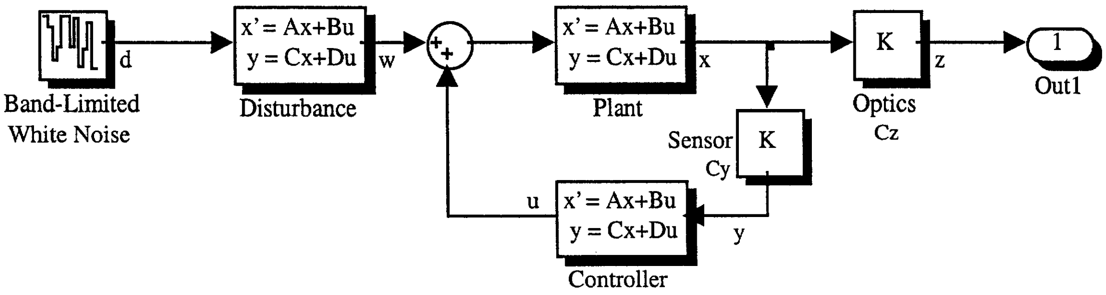

Figure 2.50: Integrated model for 3DOF sample problem

Going from left to right we can write the individual state equations and append them together. The plant state equation and the performance and output equations from (2.35) are

$$\begin{aligned} \dot{\mathbf{q}}_{\mathbf{p}} &= \mathbf{A}_{\mathbf{p}}\mathbf{q}_{\mathbf{p}} + \mathbf{B}_{\mathbf{u}}u + \mathbf{B}_{\mathbf{w}}w \\ y &= \mathbf{C}_{\mathbf{y}}\mathbf{q}_{\mathbf{p}} \\ z &= \mathbf{C}_{\mathbf{z}}\mathbf{q}_{\mathbf{p}} \end{aligned} \tag{2.166}$$

and the controller state equations from (2.159) are given as

$$\begin{aligned} \dot{q}_c &= \mathbf{A}_{\mathbf{c}}q_c + \mathbf{B}_{\mathbf{c}}y \\ u &= \mathbf{C}_{\mathbf{c}}q_c + \mathbf{D}_{\mathbf{c}}y \end{aligned} \tag{2.167}$$

Obviously here we cannot set the controller feedthrough term $\mathbf{D}_{\mathbf{c}}$ to zero, since it is not zero due to the use of proportional feedback. The plant and controller states can now be rewritten as:

$$\begin{aligned} \dot{\mathbf{q}}_{\mathbf{p}} &= \mathbf{A}_{\mathbf{p}}\mathbf{q}_{\mathbf{p}} + \mathbf{B}_{\mathbf{u}}\mathbf{C}_{\mathbf{c}}q_c + \mathbf{B}_{\mathbf{u}}\mathbf{D}_{\mathbf{c}}\mathbf{C}_{\mathbf{y}}\mathbf{q}_{\mathbf{p}} + \mathbf{B}_{\mathbf{w}}\mathbf{C}_{\mathbf{d}}q_d \\ \mathbf{q}_{\mathbf{c}} &= \mathbf{A}_{\mathbf{c}}q_c + \mathbf{B}_{\mathbf{c}}\mathbf{C}_{\mathbf{y}}\mathbf{q}_{\mathbf{p}} \end{aligned} \tag{2.168}$$

There are altogether four systems we can write, depending if we look at the open loop versus closed loop system and whether we append the disturbance filter into the state equations or not. Table 2.5 shows the four possibilities in an overview.

Table 2.5: Possibilities for assembling the integrated state space model

State Space Representations	open loop (u = 0)	closed loop (u = Ky)
disturbance states excluded	1: SYS_ozw	3:SYS_czw
disturbance states included	2:SYS_ozd	4:SYS_czd

The four systems are obtained as follows:

1) SYS_ozw:

$$\begin{aligned}
\left[\dot{\mathbf{q}}_{\mathbf{p}}\right] &= \underbrace{\left[\mathbf{A}_{\mathbf{p}}\right]}_{\mathbf{A}_{\mathbf{ozw}}}\mathbf{q}_{\mathbf{p}} + \underbrace{\left[\mathbf{B}_{\mathbf{w}}\right]}_{\mathbf{B}_{\mathbf{ozw}}} w \\
z &= \underbrace{\left[\mathbf{C}_{\mathbf{z}}\right]}_{\mathbf{C}_{\mathbf{ozw}}}\mathbf{q}_{\mathbf{p}} + \underbrace{\left[\mathbf{D}_{\mathbf{zw}}\right]}_{\mathbf{D}_{\mathbf{ozw}}} w
\end{aligned} \tag{2.169}$$

2) SYS_ozd

$$\begin{aligned}
\begin{bmatrix} \dot{\mathbf{q}}_{\mathbf{d}} \\ \dot{\mathbf{q}}_{\mathbf{p}} \end{bmatrix} &= \underbrace{\begin{bmatrix} \mathbf{A}_{\mathbf{d}} & \mathbf{0} \\ \mathbf{B}_{\mathbf{w}}\mathbf{C}_{\mathbf{d}} & \mathbf{A}_{\mathbf{p}} \end{bmatrix}}_{\mathbf{A}_{\mathbf{ozd}}} \begin{bmatrix} \mathbf{q}_{\mathbf{d}} \\ \mathbf{q}_{\mathbf{p}} \end{bmatrix} + \underbrace{\begin{bmatrix} \mathbf{B}_{\mathbf{d}} \\ \mathbf{0} \end{bmatrix}}_{\mathbf{B}_{\mathbf{ozd}}} d \\
z &= \underbrace{\begin{bmatrix} \mathbf{0} & \mathbf{C}_{\mathbf{z}} \end{bmatrix}}_{\mathbf{C}_{\mathbf{ozd}}} \begin{bmatrix} \mathbf{q}_{\mathbf{d}} \\ \mathbf{q}_{\mathbf{p}} \end{bmatrix} + \underbrace{\left[\mathbf{0}\right]}_{\mathbf{D}_{\mathbf{ozd}}} d
\end{aligned} \tag{2.170}$$

3) SYS_czw

$$\begin{aligned}
\begin{bmatrix} \dot{\mathbf{q}}_{\mathbf{p}} \\ \dot{\mathbf{q}}_{\mathbf{c}} \end{bmatrix} &= \underbrace{\begin{bmatrix} \mathbf{A}_{\mathbf{p}} + \mathbf{B}_{\mathbf{u}}\mathbf{D}_{\mathbf{c}}\mathbf{C}_{\mathbf{y}} & \mathbf{B}_{\mathbf{u}}\mathbf{C}_{\mathbf{c}} \\ \mathbf{B}_{\mathbf{c}}\mathbf{C}_{\mathbf{y}} & \mathbf{A}_{\mathbf{c}} \end{bmatrix}}_{\mathbf{A}_{\mathbf{czw}}} \begin{bmatrix} \mathbf{q}_{\mathbf{p}} \\ \mathbf{q}_{\mathbf{c}} \end{bmatrix} + \underbrace{\begin{bmatrix} \mathbf{B}_{\mathbf{w}} \\ \mathbf{0} \end{bmatrix}}_{\mathbf{B}_{\mathbf{czw}}} w \\
z &= \underbrace{\begin{bmatrix} \mathbf{C}_{\mathbf{z}} & \mathbf{0} \end{bmatrix}}_{\mathbf{C}_{\mathbf{czw}}} \begin{bmatrix} \mathbf{q}_{\mathbf{p}} \\ \mathbf{q}_{\mathbf{c}} \end{bmatrix} + \underbrace{\left[\mathbf{0}\right]}_{\mathbf{D}_{\mathbf{czw}}} w
\end{aligned} \tag{2.171}$$

4) SYS_czd

$$\begin{aligned}
\begin{bmatrix} \dot{\mathbf{q}}_{\mathbf{d}} \\ \dot{\mathbf{q}}_{\mathbf{p}} \\ \dot{\mathbf{q}}_{\mathbf{c}} \end{bmatrix} &= \underbrace{\begin{bmatrix} \mathbf{A}_{\mathbf{d}} & \mathbf{0} & \mathbf{0} \\ \mathbf{B}_{\mathbf{w}}\mathbf{C}_{\mathbf{d}} & \mathbf{A}_{\mathbf{p}} + \mathbf{B}_{\mathbf{u}}\mathbf{D}_{\mathbf{c}}\mathbf{C}_{\mathbf{y}} & \mathbf{B}_{\mathbf{u}}\mathbf{C}_{\mathbf{c}} \\ \mathbf{0} & \mathbf{B}_{\mathbf{c}}\mathbf{C}_{\mathbf{y}} & \mathbf{A}_{\mathbf{c}} \end{bmatrix}}_{\mathbf{A}_{\mathbf{czd}}} \begin{bmatrix} \mathbf{q}_{\mathbf{d}} \\ \mathbf{q}_{\mathbf{p}} \\ \mathbf{q}_{\mathbf{c}} \end{bmatrix} + \underbrace{\begin{bmatrix} \mathbf{B}_{\mathbf{d}} \\ \mathbf{0} \\ \mathbf{0} \end{bmatrix}}_{\mathbf{B}_{\mathbf{czd}}} d \\
z &= \underbrace{\begin{bmatrix} \mathbf{0} & \mathbf{C}_{\mathbf{z}} & \mathbf{0} \end{bmatrix}}_{\mathbf{C}_{\mathbf{czd}}} \begin{bmatrix} \mathbf{q}_{\mathbf{d}} & \mathbf{q}_{\mathbf{p}} & \mathbf{q}_{\mathbf{c}} \end{bmatrix}^{\mathbf{T}} + \underbrace{\left[\mathbf{0}\right]}_{\mathbf{D}_{\mathbf{czd}}} d
\end{aligned} \tag{2.172}$$

Since we are dealing with a SISO system it is useful and instructive to analytically compute the transfer functions of the above system. This will be helpful in analytically computing the system performance. The open loop transfer function $G_{ozw}(s)$ can be computed based on the following relationship [23]:

$$G_{ozw}(s)=\mathbf{C_z}\left[s\mathbf{I}-\mathbf{A_p}\right]^{-1}\mathbf{B_w}+\mathbf{D_{zw}} \tag{2.173}$$

The most time consuming step in computing the transfer function is the matrix inversion involving $\mathbf{A_p}$. In our case, where the system is in modal form we can simplify this step in the analytical calculation by bringing the $\mathbf{A_p}$ matrix into Gauss-Jordan form, i.e. it will contain decoupled sub-blocks, which will contain the 2nd order dynamics for each mode.

$$\overline{\mathbf{A}}_{\mathbf{p}}=\begin{bmatrix} \begin{bmatrix} 0 & 1 \\ -\omega_1^2 & -2\zeta_1\omega_1 \end{bmatrix} & 0_{2x2} & 0_{2x2} \\ 0_{2x2} & \begin{bmatrix} 0 & 1 \\ -\omega_2^2 & -2\zeta_2\omega_2 \end{bmatrix} & 0_{2x2} \\ 0_{2x2} & 0_{2x2} & \begin{bmatrix} 0 & 1 \\ -\omega_3^2 & -2\zeta_3\omega_3 \end{bmatrix} \end{bmatrix} \tag{2.174}$$

The following matrix inversion has to be executed analytically, substituting $\omega_1=0$ we get equation (2.175):

$$\left[s\mathbf{I}-\overline{\mathbf{A}}_{\mathbf{p}}\right]^{-1}=\begin{bmatrix} \begin{matrix} s & -1 \\ 0 & s \end{matrix} & 0_{2x2} & 0_{2x2} \\ 0_{2x2} & \begin{matrix} s & -1 \\ \omega_2^2 & s+2\zeta_2\omega_2 \end{matrix} & 0_{2x2} \\ 0_{2x2} & 0_{2x2} & \begin{matrix} s & -1 \\ \omega_3^2 & s+2\zeta_3\omega_3 \end{matrix} \end{bmatrix}^{-1}$$

$$=\begin{bmatrix} \begin{matrix} 1/s & 1/s^2 \\ 0 & 1/s \end{matrix} & 0_{2x2} & 0_{2x2} \\ 0_{2x2} & \begin{matrix} \dfrac{s+2\zeta_2\omega_2}{s^2+2\zeta_2\omega_2+\omega_2^2} & \dfrac{1}{s^2+2\zeta_2\omega_2+\omega_2^2} \\ \dfrac{-\omega_2^2}{s^2+2\zeta_2\omega_2+\omega_2^2} & \dfrac{s}{s^2+2\zeta_2\omega_2+\omega_2^2} \end{matrix} & 0_{2x2} \\ 0_{2x2} & 0_{2x2} & \begin{matrix} \dfrac{s+2\zeta_3\omega_3}{s^2+2\zeta_3\omega_3+\omega_3^2} & \dfrac{1}{s^2+2\zeta_3\omega_3+\omega_3^2} \\ \dfrac{-\omega_2^2}{s^2+2\zeta_3\omega_3+\omega_3^2} & \dfrac{s}{s^2+2\zeta_3\omega_3+\omega_3^2} \end{matrix} \end{bmatrix}$$

It is important not to forget to reorder the other matrices according to the Gauss-Jordan formulation. The other matrices to be multiplied with (2.175) according to (2.174) are given as

$$\overline{\mathbf{C}}_{\mathbf{z}} = \begin{bmatrix} 0 & 0 & 0 & 0 & \frac{-6s_c}{\sqrt{12m}} & 0 \end{bmatrix} \tag{2.176}$$

$$\overline{\mathbf{B}}_{\mathbf{w}} = \begin{bmatrix} 0 & \frac{1}{\sqrt{6m}} & 0 & 0 & 0 & \frac{-1}{\sqrt{12m}} \end{bmatrix}^T \tag{2.177}$$

Since the feed through term $\mathbf{D_{zw}}$ is zero, we can compute the closed form of the open loop transfer function by matrix multiplication. This yields the following second order system:

$$G_{ozw}(s) = \frac{(s_c/2m)}{s^2 + 2\zeta_3\omega_3 s + \omega_3^2} \tag{2.178}$$

This result is not surprising since only the third mode is contributing to the system dynamics. The rigid body mode and the symmetric flexible mode do not affect the performance. In order to compute the closed loop transfer function, we recall equation (2.173) and apply it to the closed loop case, corresponding to the state space system *SYS_czw* (2.171):

$$G_{czw}(s) = \mathbf{C_{czw}}\left[s\mathbf{I} - \mathbf{A_{czw}}\right]^{-1}\mathbf{B_{czw}} + \mathbf{D_{czw}} \tag{2.179}$$

Since only mode 3 contributes to the performance, we can truncate modes 1 and 2 from $\mathbf{A_{czw}}$ to obtain $\tilde{\mathbf{A}}_{\mathbf{czw}}$. The matrix inversion can be written as:

$$\left[s\mathbf{I} - \tilde{\mathbf{A}}_{\mathbf{czw}}\right]^{-1} = \begin{bmatrix} s & -1 & 0 \\ \omega_3^2 - \frac{3s_c}{m}\left(K_p + \frac{K_d}{\tau_d}\right) & s + 2\zeta_3\omega_3 & \frac{3K_d}{\sqrt{12m}\tau_d^2} \\ -\sqrt{12/m}\cdot s_c & 0 & s + \frac{1}{\tau_d} \end{bmatrix}^{-1} \tag{2.180}$$

the other two matrices are then given as

$$\tilde{\mathbf{B}}_{czw} = \begin{bmatrix} 0 \\ -1/\sqrt{12m} \\ 0 \end{bmatrix} \quad , \quad \tilde{\mathbf{C}}_{czw} = \begin{bmatrix} \dfrac{-6s_c}{\sqrt{12m}} & 0 & 0 \end{bmatrix}, \quad \tilde{\mathbf{D}}_{czw} = [0] \qquad (2.181)$$

solving for the closed loop transfer function we get equation (2.182):

$$G_{czw}(s) = \frac{\dfrac{s_c\tau_d}{2}s + \dfrac{s_c}{2}}{m\tau_d s^3 + (2\zeta_3\omega_3 m\tau_d + m)s^2 + \left(2\zeta_3\omega_3 m + \omega_3^2\tau_d m - 3s_cK_p\tau_d - 3s_cK_d\right)s + \left(m\omega_3^2 - 3K_ps_c\right)}$$

It can be seen that the transfer function is more complicated than in the open loop case. Figure 2.51 shows the closed loop (2.182) and open loop (2.178) transfer functions. The closed loop transfer function is of third order, since the PD-controller adds one state to the system dynamics. It can be seen that the values chosen for K_p and K_d directly affect the pole locations, but not the zero locations. The third mode from the open loop case has now been stiffened (i.e. the pole is further away from the origin along the jω-axis), which should have beneficial effects due to the disturbance rolloff.

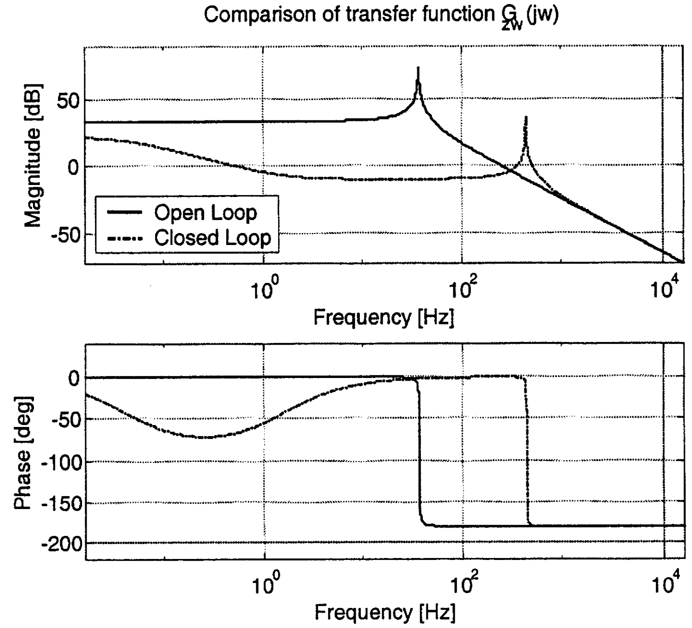

Figure 2.51: Comparison of open and closed loop $G_{zw}(j\omega)$

Next the integrated modeler must check the stability of the closed loop system. The pole-zero map here is useful, since it serves two purposes. Firstly we assure ourselves of the asymptotic stability of the open loop (top plot) and closed loop (bottom plot) of Figure 2.52. Indeed no poles ("x"s) are located in the right half-plane.

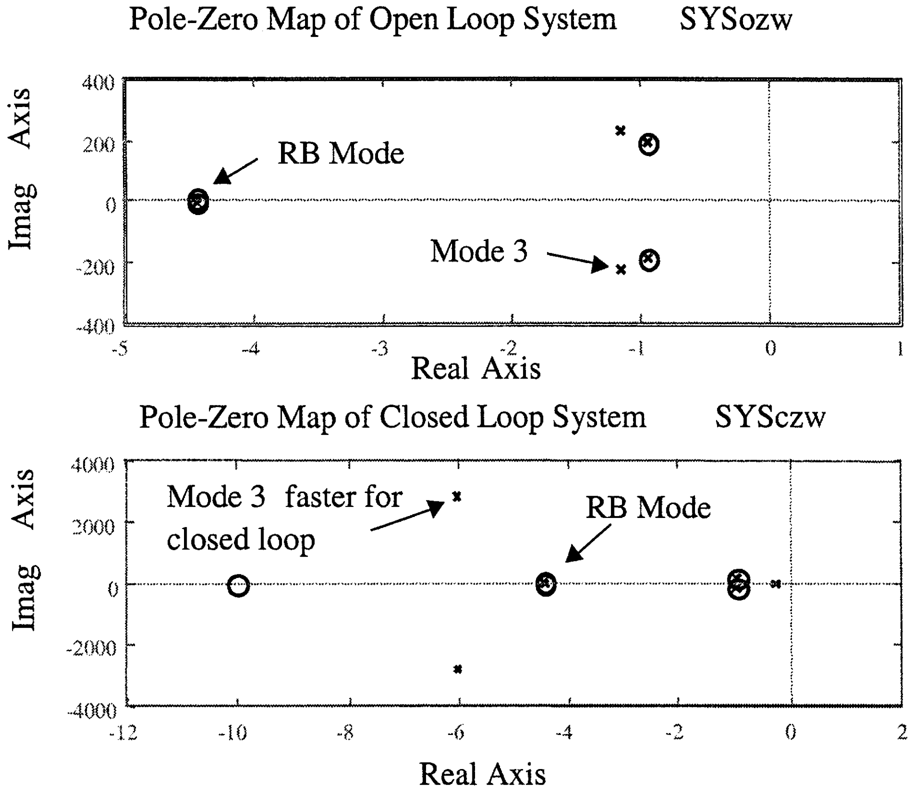

Figure 2.52: Pole-Zero map for open and closed loop system (sample 3DOF problem)

Secondly we can observe the effect of control on the pole locations. We see that for the RB-mode (artificially dampened and stiffened to simulate ACS behavior) and the symmetric mode we have perfect pole-zero cancellations, so that these modes are unobservable and uncontrollable. The third mode is significantly stiffened by the control (jω-position goes from ~ +/- 240 to roughly +/- 3000. This will undoubtedly affect performance. Also there is a pole due to the control close to the jω-axis but with some margin.

2.6.2 NGST Integrated model

The assembly process for NGST is equivalent to the process shown in the sample problem except that the matrix equations involved are more complicated. The first step is to write the overall state vector in appended form. Before doing this, we can again consult the overall block diagram with the two control loops. All elements of NGST discussed up to now are contained in this diagram.

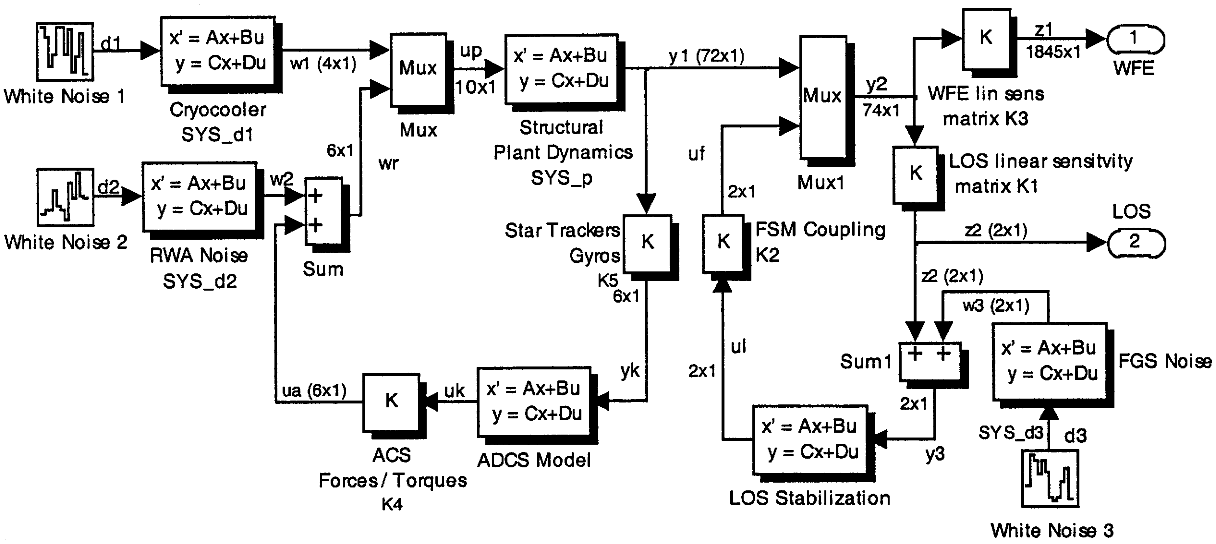

Figure 2.53: Closed loop block diagram of linear NGST fine pointing model

This model makes certain simplifications compared to the full non-linear time simulation model [55]. One simplification is that the low-frequency coupling between the LOS stabilization loop and the ACS has been neglected. It is evident that the ACS will not be able to compensate for dynamic disturbances with its bandwidth of 0.025 Hz compared to the fundamental (sunshield) frequency of 0.3 Hz. Based on the previous methodology for the sample problem we have six possibilities for the assembly of the state space system:

Table 2.6: State Space Representations for NGST Integrated Model

SS Representations	open loop (u = 0)	ACS loop only	ACS & Optics closed
disturbance states excluded	1: SYS_ozw	2:SYS_c1zw	3: SYS_c2zw
disturbance states included	4: SYS_ozd	5: SYS_c1zd	6: SYS_c2zd

Based on these possibilities the most important case is case 6, which contains all the information about the plant, disturbance, optics and controls dynamics in a single state space system. The state vector of that particular system is partitioned as follows:

$$q_6 = \begin{bmatrix} q_{d1} \\ q_{d2} \\ q_{d3} \\ q_p \\ q_k \\ q_l \end{bmatrix} = \begin{Bmatrix} \text{Cryo Disturbance states} \\ \text{RWA Disturbance states} \\ \text{FGS Disturbance states} \\ \text{Plant states} \\ \text{ADCS controller states} \\ \text{LOS Stabilization states} \end{Bmatrix} \tag{2.183}$$

In the baseline analysis case we have a total of 64+36+2+300+43+6=451 states in the appended state vector. The overall state space system from the three statistically independent white noise sources d_1, d_2 and d_3 to the performance metrics z can be written as follows (2.184):

$$\begin{bmatrix} \dot{q}_{d1} \\ \dot{q}_{d2} \\ \dot{q}_{d3} \\ \dot{q}_p \\ \dot{q}_k \\ \dot{q}_l \end{bmatrix} = \underbrace{\begin{bmatrix} A_{d1} & 0 & 0 & 0 & 0 & 0 \\ 0 & A_{d2} & 0 & 0 & 0 & 0 \\ 0 & 0 & A_{d3} & 0 & 0 & 0 \\ B_{p1}C_{d1} & B_{p2}C_{d2} & 0 & A_p & B_{p2}K_4C_k & 0 \\ 0 & 0 & 0 & B_kK_5C_p & A_k & 0 \\ 0 & 0 & B_lC_{d3} & B_lK_{11}C_p & 0 & A_l + B_lK_{12}K_2C_l \end{bmatrix}}_{A_{zd}} \begin{bmatrix} q_{d1} \\ q_{d2} \\ q_{d3} \\ q_p \\ q_k \\ q_l \end{bmatrix} + \underbrace{\begin{bmatrix} B_{d1} & 0 & 0 \\ 0 & B_{d2} & 0 \\ 0 & 0 & B_{d3} \\ 0 & 0 & 0 \\ 0 & 0 & 0 \\ 0 & 0 & 0 \end{bmatrix}}_{B_{zd}} \begin{bmatrix} d_1 \\ d_2 \\ d_3 \end{bmatrix}$$

$$\begin{bmatrix} z_1 \\ z_2 \end{bmatrix} = \underbrace{\begin{bmatrix} 0 & 0 & 0 & K_{31}C_p & 0 & K_{32}K_2C_l \\ 0 & 0 & 0 & K_{11}C_p & 0 & K_{12}K_2C_l \end{bmatrix}}_{C_{zd}} \begin{bmatrix} q_{d1} \\ q_{d2} \\ q_{d3} \\ q_p \\ q_k \\ q_l \end{bmatrix} + \underbrace{\begin{bmatrix} 0 & 0 & 0 \end{bmatrix}}_{D_{zd}} \begin{bmatrix} d_1 \\ d_2 \\ d_3 \end{bmatrix}$$

The closed loop A_{zd}-matrix is thus 451x451, the B_{zd} matrix is 451x3, the C_{zd} matrix is 1847x451 and the feedthrough matrix D_{zd} is 1847x3. Matrix algebra or alternatively the use of the `linmod` command in MATLAB™ using the block diagram representation produces this result. The two methods were found to agree. The state space representation for the initial performance assessment using the frequency domain method is from the shaped disturbances w to the performances z. The system is obtained as follows:

$$\begin{bmatrix} \dot{q}_p \\ \dot{q}_k \\ \dot{q}_l \end{bmatrix} = \underbrace{\begin{bmatrix} A_p & B_{p2}K_4C_k & 0 \\ B_kK_5C_p & A_k & 0 \\ B_lK_{11}C_p & 0 & A_l + B_lK_{12}K_2C_l \end{bmatrix}}_{A_{zw}} \begin{bmatrix} q_p \\ q_k \\ q_l \end{bmatrix} + \underbrace{\begin{bmatrix} B_{p1} & B_{p2} & 0 \\ 0 & 0 & 0 \\ 0 & 0 & B_l \end{bmatrix}}_{B_{zw}} \begin{bmatrix} w_1 \\ w_2 \\ w_3 \end{bmatrix}$$

$$z = \begin{bmatrix} z_1 \\ z_2 \end{bmatrix} = \underbrace{\begin{bmatrix} K_{31}C_p & 0 & K_{32}K_2C_l \\ K_{11}C_p & 0 & K_{12}K_2C_l \end{bmatrix}}_{C_{zw}} \begin{bmatrix} q_p \\ q_k \\ q_l \end{bmatrix} + \underbrace{\begin{bmatrix} 0 & 0 & 0 \\ 0 & 0 & 0 \end{bmatrix}}_{D_{zw}} \begin{bmatrix} w_1 \\ w_2 \\ w_3 \end{bmatrix} \tag{2.185}$$

Here we can see that the disturbance states are not appended into the system. Therefore this system has to be driven with the representative disturbance PSD's (shaping filters) or with the equivalent time domain signals in order to simulate the behavior. We can obtain a corresponding transfer function matrix by solving the following matrix equation in the s-domain:

$$G_{zw}(s) = \frac{Z(s)}{W(s)} = C_{zw}\,[sI - A_{zw}]^{-1} B_{zw} + D_{zw} \tag{2.186}$$

Figure 2.54 shows a sample transfer function from the disturbance input Mx (input component 8) at the RWA input node to the centroid x channel. Three transfer functions from w to z are plotted. The first transfer function from the top in the magnitude portion of the Bode plot corresponds to the open loop case. We can clearly see the rigid body mode behavior at low frequency. This means that the rigid body modes that have their poles on the $j\omega$-axis and are thus only neutrally stable have to be stabilized. This is achieved by closing the loop on the ADCS controller. It can be seen that the controller is low bandwidth (~ 0.025 Hz), but that it provides a first level of stabilization for the centroid x, which enters into the LOS performance metric. A second – very effective – level of attenuation is provided by the fast steering mirror loop. This is evident by looking at the third (and lowest) transfer function. It is however noticeable that the FSM loop is limited in its effective bandwidth. Above ~ 5 Hz the FSM is no longer able to attenuate the disturbances due to the limitations on the achievable guide star sampling rate. Thus the observatory will probably have to use a number of passive measures to decrease the H_{inf} or H_2 norms of these G_{zw} transfer functions. This will be the topic of the performance improvement section. The attenuation of input disturbances is effective up to a bandwidth of roughly 3 Hz. The LOS stabilization loop provides about 50dB attenuation at 0.01 Hz.

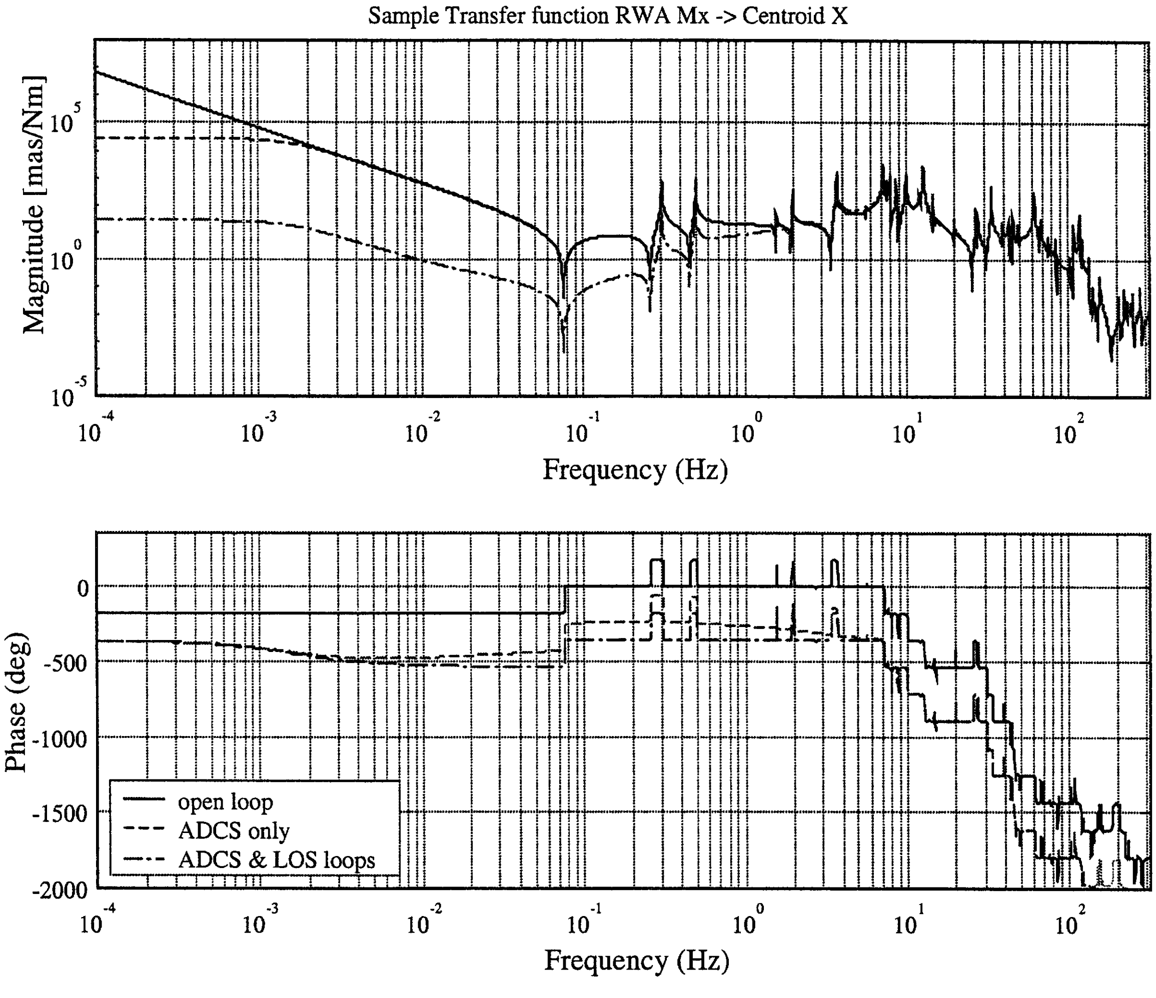

Figure 2.54: Comparison of open loop, ADCS only and closed loop transfer functions

The stability of the open and closed loop plants has been insured by analyzing the pole locations in the same way as for the sample problem. Now that the integrated modeling and assembly process has been completed, we can turn our attention to the initial performance assessment.

Chapter 3

Initial Performance Assessment

The goal of this section is to predict the dynamic performance of the observatory in terms of wavefront error (RMS WFE) and LOS jitter (RMS LOS) under the influence of three dynamic disturbance sources. For this purpose we will exercise the integrated model that was developed in the previous chapter. The goal is to apply a systematic methodology for stochastic performance prediction of the opto-structural system. In summary the goals of the analysis in this chapter are to:

1. Propagate disturbances through the closed loop NGST system
2. Predict expected performance in terms of RMS WFE and RMS LOS
3. Identify critical disturbances and modes that drive system performance

There are several ways to obtain the covariance of the stochastic performance z from the LTI models. Gutierrez [24] suggests the following three methods as a possibility: The time-domain analysis assumes that the time history of the disturbances d is given and performs numerical integration to obtain the time history of z. The frequency-domain analysis starts with the PSD's of the disturbances and computes the PSD's of the performance metrics. The covariance is obtained by computing the integral under the area of the performance PSD's. Finally the third approach solves for the exact covariance matrix by solving a steady-state Lyapunov equation on the appended closed loop system (i.e. disturbances appended) assuming that the input is white noise. All three methods are applied here and their mutual advantages and disadvantages are discussed. We turn again to our sample problem before solving the full order NGST model.

Also for each of the above methods we have investigated three different approaches for the sample case. The symbolic approach computes σ_{OPD} (= RMS OPD), which is the performance metric of interest, by carrying out all the calculations with paper and pencil or with the help of MAPLE™. The actual evaluation of the RMS OPD is done at the very end, after the analytical expression for the RMS OPD is obtained. This will give the correct answer. The numerical approach uses MATLAB™ to numerically compute the OPD RMS by substituting for the system variables before every step. Finally the third approach uses the function `dist_analysis.m`, which was developed by Gutierrez and checks its accuracy. All three methods should lead to the same prediction for the RMS performance metric, subject to numerical inaccuracies. By comparing the open loop and closed loop case, the effectiveness of the control can be evaluated.

3.1 Time domain analysis of sample problem

We will conduct a time domain analysis of the 3DOF sample problem in this section. In the time domain analysis we assume that a continuous white noise process $d(t)$ is driving the system. The "power" of the ideal white noise process is infinite, since its variance is infinite. Another difficulty comes from the fact that white noise is defined as the (non-existent) derivative of Brownian motion $B(t)$ [56]. For these reasons it is not possible to write an analytical expression for white noise $d(t)$ as an analytical function in the time domain. Therefore only two of the three approaches will be investigated here for the sample problem, since an analytical expression in the time domain for white noise cannot be found.

We can however conduct a time simulation of white noise using Simulink™. The generation of simulated white noise has been described by reference [56]. The key idea is that the white noise is naturally band-limited since we are discretizing time as Δt. Accurate results are only obtained if the sampling time t_s of the band-limited white noise generator is set to a value which allows to capture the highest frequency f_{max} of the state space system $\mathbf{A_{zd}}, \mathbf{B_{zd}}, \mathbf{C_{zd}}, \mathbf{D_{zd}}$. The rule of thumb for setting t_s is given by the following equation:

$$t_s \approx \frac{1}{100}\frac{2\pi}{f_{\max}} \tag{3.1}$$

This sampling time is a crucial parameter in the band-limited random white noise generator. In the sample problem the largest frequency is given by the third mode. A block diagram of the time simulation is shown in Figure 3.1.

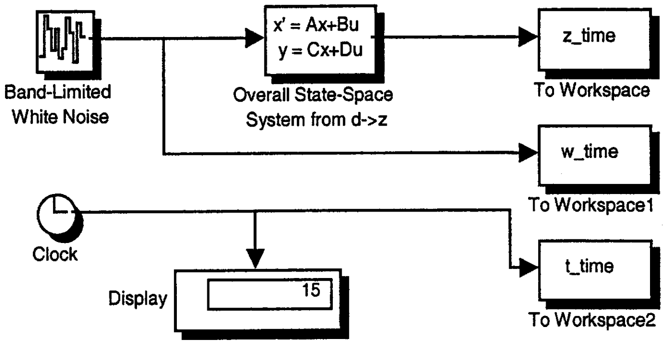

Figure 3.1: Block diagram representation for white noise time simulation

Once the simulation has been completed the resulting time history of the performance z_{time} is stored . It is then very easy to compute the standard deviation (which is equal to the RMS since we have a zero-mean stochastic process) as:

$$\sigma_{OPD} = \sqrt{E\left[(z-\mu)^2\right]} = \left\{\frac{1}{T}\int_0^T (z(t)-\mu_z)^2 dt\right\}^{1/2} = OPD_{RMS} \tag{3.2}$$

where z is the resulting performance time history, μ is the mean value and T is the length of the time sample. The resulting RMS for the sample problem in the open loop and closed loop were obtained as σ_z= 4438.096 nm (open loop) and σ_z= 41.3682 nm (closed) loop. We immediately see that control improves the performance by about 40 dB. Figure 3.2 for the 3DOF sample problem shows a sample realization of white noise and OPD.

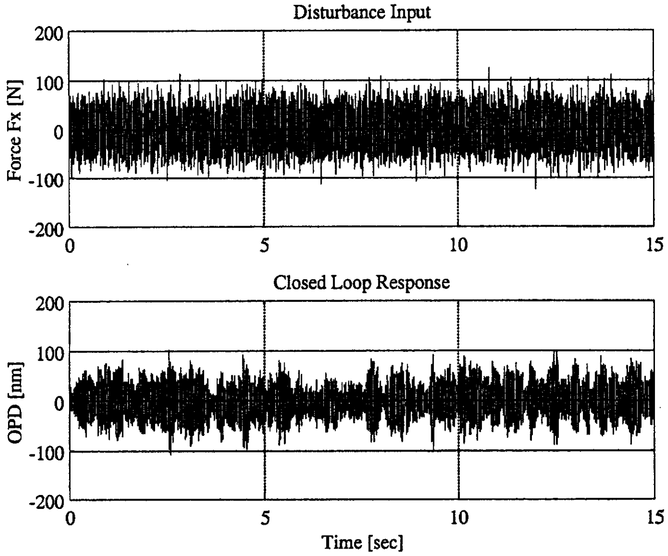

Figure 3.2: White noise input (top) and resulting OPD in the closed loop case (bottom)

The time domain analysis consists of propagating a time domain sample realization of the white noise disturbance *d(t)* through the open or closed loop system dynamics $\mathbf{A_{zd}},\mathbf{B_{zd}},\mathbf{C_{zd}},\mathbf{D_{zd}}$. This requires a time integration for each step, which is done by the `ode45` solver in this case. It is necessary to set the sampling time t_s of the white noise source fast enough, so that the fastest dynamics of the system are well captured. For a sample realization of white noise to exist it must be band-limited. However, as long as that bandwidth is larger than the fastest mode of the dynamic system, the noise source acts on the system as if it were truly white noise (i.e. infinite bandwidth). After the Simulink time domain simulation, the sample realization of the white noise was input into `dist_analysis.m` [24] along with the open and closed loop dynamics, respectively, in order to check the consistency of the results. Figure 3.3 depicts the resulting time history of OPD in the open loop case.

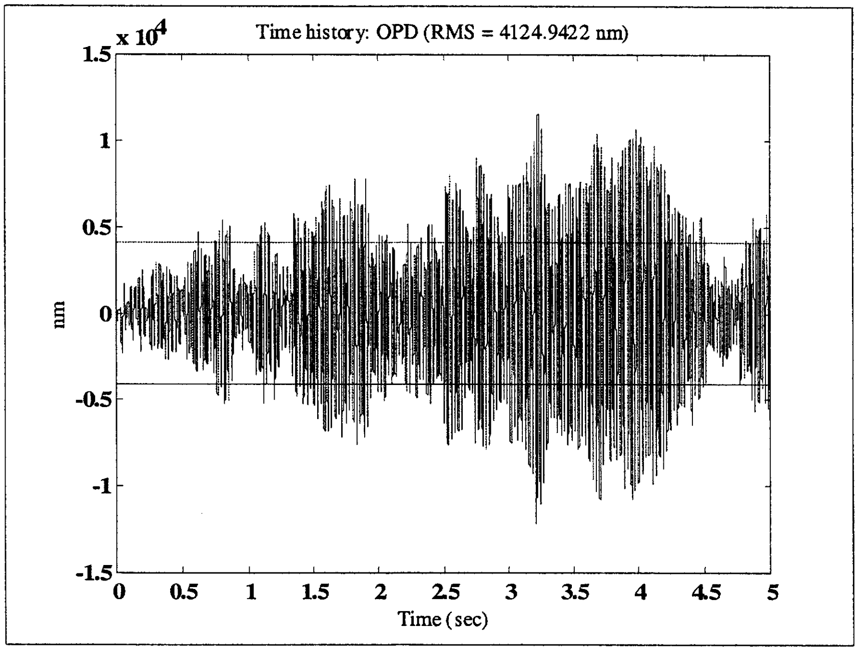

Figure 3.3: Time history of OPD in the open loop case (3DOF sample problem)

It can be seen that it is important that the length of the time sample T be sufficient that the response reaches the steady state from the zero initial conditions. Furthermore, a large T will provide good frequency resolution if we would choose to compute the frequency spectrum of this response. The results obtained from `dist_analysis.m` are identical as in the previous case: σ_z= 4438.096 nm in the open loop and σ_z= 41.3682 nm in the closed loop case.

3.2 Frequency domain analysis

The ability to precisely predict the speed of each wheel for the reaction wheel assembly (and hence the resulting disturbances) during the course of an observation is difficult. Although the attitude control logic that is used to issue commands to each wheel is known *a priori,* what is not known to the same level of certainty is the external torque disturbance which the wheels are counteracting [24]. Also, the initial wheel speeds at the start of an observation might be impossible to predict. It is for these reasons that conducting a time simulation might not be desirable. What is more useful is a sense of how the performance metrics of interest (*e.g.,* RMS WFE) are affected by disturbances arising from all possible combinations of wheel speed variations. Running countless time simulations to try numerous combinations is prohibitive due to the computational expense. A possible alternative is to estimate what the disturbances are "on average." These disturbances can then be used in a first-cut performance assessment. The "on-average" disturbance approach motivates the treatment of wheel speed as a random variable and their representation with power spectral density functions. This can then be used in a frequency-domain disturbance analysis, which can be less computationally intensive than a time-domain simulation. Another advantage to the "on-average" approach is that external torque models and initial wheel speeds are not required. Thus it is recommended to first perform frequency domain analyses and quick trades using frequency domain methods and subsequently confirm the results using well-defined non-linear time-simulations in a narrowly defined region of the parameter space. This is the logic we will follow here and we subsequently focus our attention on the frequency domain analysis. Again we analyze the sample 3DOF problem before conducting the analysis for the full order NGST model.

3.2.1 Frequency domain analysis for sample 3DOF problem

The frequency domain approach makes use of the fact that a convolution in the time domain becomes a multiplication in the frequency domain (here specifically the *s*-domain). It can be shown through linear systems theory that the performance PSD is given as:

$$S_{zz}(\omega)=G_{zw}(j\omega)S_{ww}(\omega)G_{zw}^{H}(j\omega) \tag{3.3}$$

When the performance PSD should be computed with the disturbance filters included in the transfer function matrix, we obtain the following expression:

$$\begin{aligned} S_{zz}(\omega) &= G_{zw}(j\omega)\cdot S_{ww}(\omega)\cdot G_{zw}^{H}(j\omega) = \\ &\underbrace{G_{zw}(j\omega)G_{wd}(j\omega)}_{G_{zd}(j\omega)}\cdot G_{wd}^{H}(j\omega)G_{zw}^{H}(j\omega) \end{aligned} \tag{3.4}$$

The RMS of the performance z is then the square root of the area under S_{zz} divided by 2π. Care needs to be taken to scale by a factor of 2π, when the PSD's are expressed in Hertz.

$$z_{RMS}=\left\{\frac{1}{\pi}\int_{0}^{+\infty}S_{zz}(\omega)d\omega\right\}^{1/2} \tag{3.5}$$

This can be written in terms of the white noise d to performance z transfer function matrix

$$\sigma_z=\frac{1}{2\pi}\int_{-\infty}^{+\infty}S_{zz}(\omega)d\omega=\frac{1}{2\pi}\int_{-\infty}^{+\infty}\left|G_{zd}(\omega)\right|d\omega \tag{3.6}$$

The symbolic approach can become challenging depending on the order of the transfer function from d to z. For the open loop sample problem, the transfer function from white noise to the performance OPD is written as

$$G_{zd}(s) = \frac{s_c \omega_{RO}/2m}{s^3 + (2\zeta_3\omega_3 + \omega_{RO})s^2 + (\omega_3^2 + 2\zeta_3\omega_3\omega_{RO})s + \omega_{RO}\omega_3^2} = \frac{B_2 s^2 + B_1 s + B_o}{A_3 s^3 + A_2 s^2 + A_1 s + A_o} \qquad (3.7)$$

As expected this is a third order transfer function since we have a second order plant (recall that only mode 3 was observable in the performance metric) and that the third state comes from appending the lowpass filter that describes the disturbance shaping filter. Now we substitute Equation 3.7 into Equation3.6 in order to obtain the performance RMS value. It is not trivial to directly integrate an arbitrary transfer function and to evaluate it from $-\infty$ to $+\infty$ over all frequencies. Fortunately this is a very frequently arising problem so that formulas exist for transfer functions up to about 8th order, after which the algebra becomes non-tractable. The formulas for the integrals of the square of transfer function magnitudes I_n, where n is the order of the denominator polynomial were presented by Wirsching and co-workers [21] and were derived using complex integration. Equation 3.7 shows that the coefficients of the numerator and denominator polynomials can be written as B_2, B_1, B_o and as A_3, A_2, A_1 and A_o respectively. The expression for I_3 is given as:

$$I_3 = \pi \frac{A_o A_3 (2B_o B_2 - B_1^2) - A_o A_1 B_2^2 + A_2 A_3 B_o^2}{A_o A_3 (A_o A_3 - A_1 A_2)} \qquad n = 3 \qquad (3.8)$$

We notice that B_2 and B_1 in or transfer function according to Equation 3.7 are zero. This allows simplifying the expression for I_3. These remaining coefficients are substituted in the following expression:

$$I_3 = \int_{-\infty}^{+\infty} \left|G_{zd}(\omega)\right|^2 d\omega = \pi \frac{A_2 A_3 B_o^2}{A_o A_3 (A_o A_3 - A_1 A_3)} \qquad (3.9)$$

The resulting I_3 is then used to obtain a closed form expression for the variance of the OPD.

$$\sigma_z^2 = \frac{1}{2\pi} I_3 = \frac{s_c^2\left(2\zeta_3\omega_3\omega_{RO} + \omega_{RO}^2\right)}{16\zeta_3 m^2\omega_3^2\left(\omega_3^2 + 2\zeta_3\omega_3^2\omega_{RO} + \omega_{RO}^2\right)} \tag{3.10}$$

The RMS is simply the square root of the expression above. The symbolic derivation for the closed loop performance RMS OPD is significantly more complicated than in the open loop case. This is due to the fact that also the denominator of the closed loop transfer function $G_{zw}(s)$ is more complicated with control. We see that all system parameters with the exception of those for the first and second structural mode appear in the closed form expression of the RMS OPD: m, ω_3, ω_{RO}, ζ_3, K_p, K_d, τ_d, and s_c. The stiffness k is contained implicitly in the third natural frequency ω_3. Equation 3.11 gives the expression for the closed loop variance of the OPD:

$$\sigma_z^2 = \frac{s_c^2\omega_{RO}^2\left(\Gamma_2 m\tau_d - \Gamma_3\Gamma_1 - \tau_d^2\Gamma_4\Gamma_1\right)}{8\Gamma_4\left(\Gamma_4\Gamma_1^2 + \Gamma_2^2 m\tau_d - \Gamma_3\Gamma_2\Gamma_1\right)} \tag{3.11}$$

where

$$\Gamma_1 = m\tau_d\omega_{RO} + 2\zeta_3\omega_3 m\tau_d + m \tag{3.11a}$$

$$\Gamma_2 = 2\zeta_3\omega_3 m\omega_{RO} + \omega_3^2\tau_d m\omega_{RO} - 3K_p\tau_d\omega_{RO}s_c - 3K_d\omega_{RO}s_c + m\omega_3^2 - 3K_p s_c \tag{3.11b}$$

$$\Gamma_3 = 2\zeta_3\omega_3 m\tau_d\omega_{RO} + m\omega_{RO} + 2\zeta_3\omega_3 m - \omega_3^2\tau_d m - 3K_p\tau_d s_c - 3K_d s_c \tag{3.11c}$$

$$\Gamma_4 = m\omega_3^2\omega_{RO} - 3K_p\omega_{RO}s_c \tag{3.11d}$$

This expression is significant, since we will be able to use it directly to take parameter derivatives in the sensitivity analysis. We can now substitute the nominal parameters for our sample problem into this expression and we obtain a value of $\sigma_z = 41.1332$ nm for the RMS OPD. We expect these answers from the symbolic math approach to be exact. This will be confirmed by looking at the results from the Lyapunov analysis. Based on this premise we see that the control gives us about 40dB of theoretical performance improvement (broadband), which is certainly quite optimistic compared to real life systems. This is due to the fact that we have neglected any imperfections and subtleties associated with the physical implementation of such a system (e.g. sensor noise, actuator authority limitations, quantization etc…).

The second approach consists of numerically computing the RMS values by applying 3.5 and substituting the numerical values upfront. Figure 3.4 shows the results generated by the numerical approach. The upper left plot shows the disturbance PSD entering the system. The lower left plot shows the G_{zw} transfer function and the upper right plot shows the performance PSD. The frequency domain analysis is conducted by first evaluating the disturbance S_{ww} as a function of ω. Then the open and closed loop transfer functions $G_{zw}(j\omega)$ are evaluated and finally they are multiplied together to obtain $S_{zz}(\omega)$.

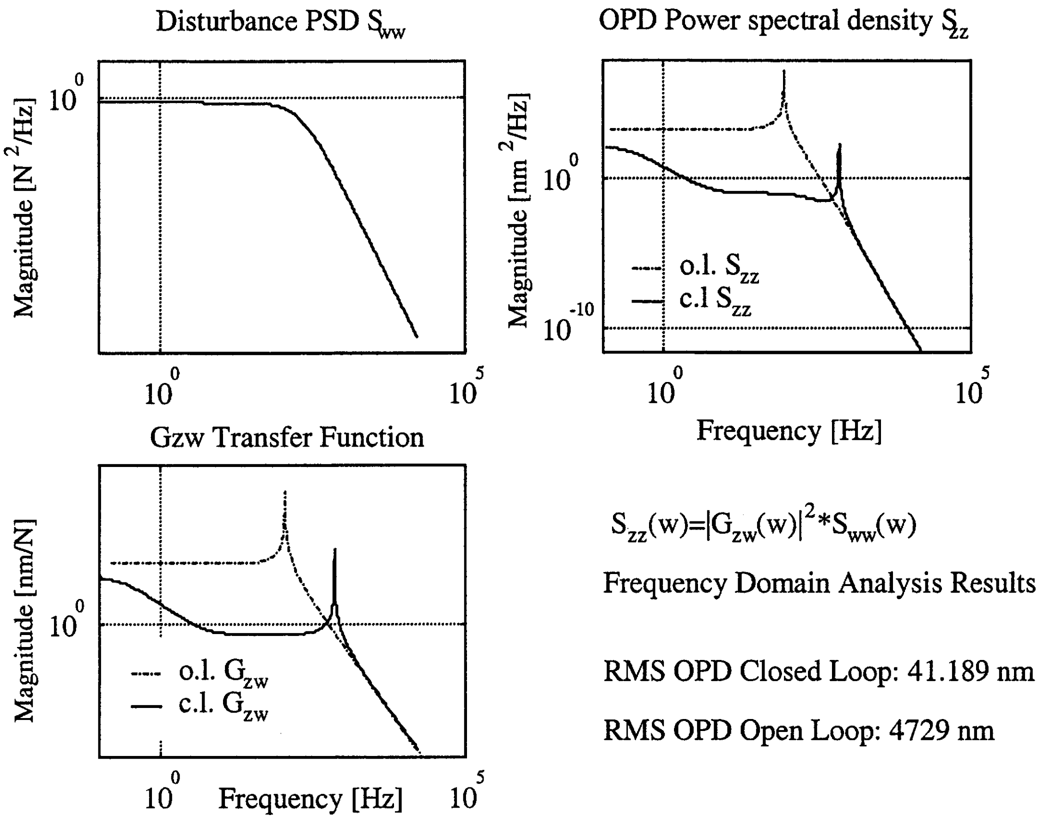

Figure 3.4: Results of frequency domain analysis (sample problem, numerical approach)

The RMS OPD is then obtained as the square root of the area under $S_{zz}(\omega)$ divided by 2π. The precision of results with this method depends strongly on the adequate resolution of the frequency vector, especially around the lightly damped resonance. This issue was already mentioned in the cryocooler disturbance modeling section. Only a high resolution of frequency points around the cryocooler disturbance harmonics was able to correctly capture the peaks in the PSD. The same effect is applicable here, since inadequate frequency resolution will produce inaccurate results that would tend to suggest significant damping in the system, when in fact the frequency resolution was insufficient to capture the resonant peaks of the lightly damped plant.

Finally we perform the frequency domain analysis on the sample problem using the function `dist_analysis.m`. The advantage of this method developed by Gutierrez [24], is the option to determine the RMS contributions by the inputs and/or critical modes as a function of frequency. In other words large steps in the cumulative RMS plot (left top plot of Figure 3.5) show which modes are critical to the system performance. This information is very useful in order to target specific modes for active control or entire modal regions for isolation or tuned damping. The right hand plot in Figure 3.5 shows the normalized cumulative area, i.e. the plot corresponds to the cumulative RMS plot on the left normalized by the RMS value, so that the maximum value is always 1.0. The user then has the option to interactively select the steps that contribute significantly to the RMS. The height of the step automatically indicates the percent contribution if multiplied by 100. Attempts have been made to automate this function, but have been unsuccessful due to the large variety of cumulative RMS curve shapes from one model to the next.

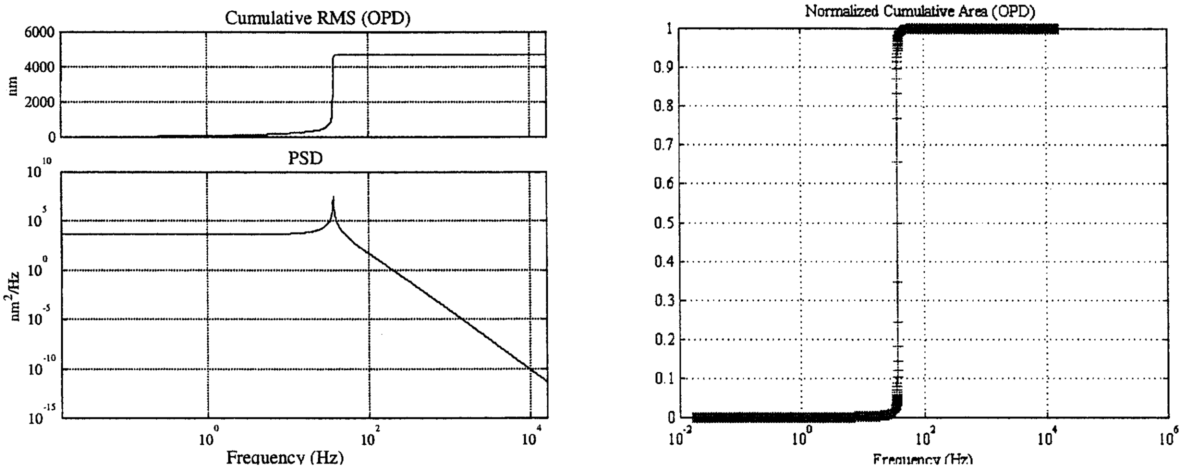

Figure 3.5: Performance PSD (bottom left) and cum. RMS plot (top left) in the open loop case Normalized cumulative area plot (OPD) for sample problem in the open loop (right)

Another useful piece of information from the right plot is related to the density of frequency points around the lightly damped modes. Each crosshair corresponds to a frequency point and we see that there are about five frequency points in the immediate vicinity of the mode (vicinity here means within +/- 20% of the resonance on the normalized area plot). The results for the open loop frequency domain analysis is a σ_{OPD} = 4728.915 nm, which is very close to the value obtained by the time domain analysis. It is interesting that only the third mode contributes to the RMS, as seen in Figure 3.5 by the large single step in the normalized cumulative area plot. In the case of NGST we will see that many modes contribute to the RMS but that a small number of them are responsible for a large percentage of the RMS. It will be our objective to find these modes. We repeat the analysis for the closed loop case of the sample problem and obtain the following results. The OPD RMS value (closed loop) is computed as σ_{OPD} = 41.1887 nm. Again this result is consistent with the results from before. We can now see that the improvement in performance is due to the fact that the resonance of mode 3 has been pushed to a higher frequency, which brings it into the rolloff region of the low-pass filter (LPF) that was assumed for the disturbance. Figure 3.6 shows the performance PSD, cumulative RMS and cumulative area plots for the closed loop case.

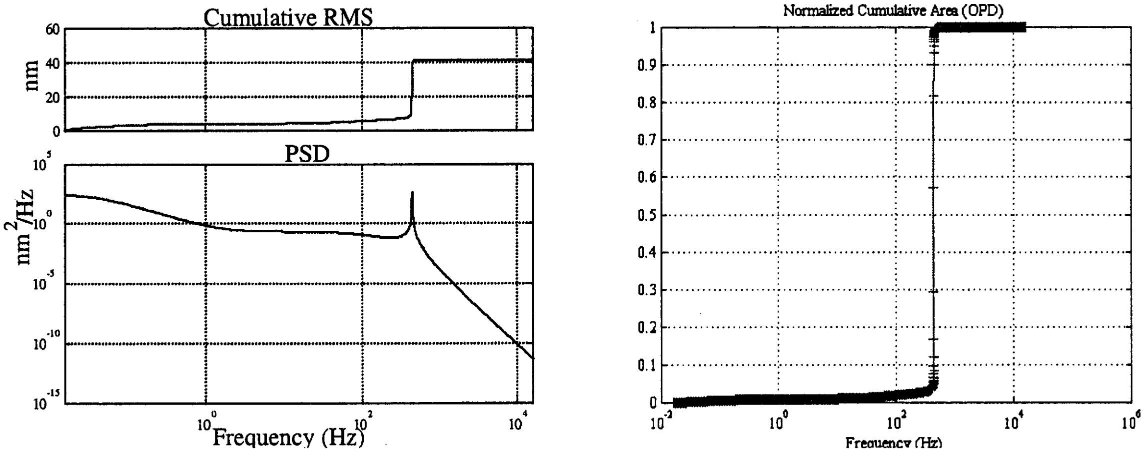

Figure 3.6: OPD performance PSD and cum. RMS plot (left) in the closed loop case Normalized cumulative area plot (OPD) for sample problem in the closed loop (right)

This chart is identical to the one before, except that we are looking at the closed loop case. Again a single mode dominates as seen by the sharp step in the cumulative RMS plot. We can see however that this mode is at a significantly higher frequency due to the control. This frequency is around 440 Hz, well within the rolloff region of the disturbance filter. This is why the performance is improved by a factor of ~ 100 (i.e. about 40 dB) compared to the open loop case.

3.2.2 Frequency domain analysis for NGST

The frequency domain analysis (initial performance assessment) for NGST is carried out with the model *SYS_c2zw*. This model was obtained from Section 2.6 and represents the closed loop system with the ADCS and LOS stabilization system included. This system is then injected with the dynamics from the 12 components of shaped noise (4 cryocooler, 6 reaction wheel assembly and 2 FGS noise components) in order to obtain the two performance metrics of interest: RMS LOS and RMS WFE. The definition of these performance metrics was given in Equations 2.145 and 2.146, respectively. Due to the large order of the closed loop system we revert to a numerical solution and use the function `dist_analysis.m` to obtain the PSD's of the performances. Figure 3.7 shows the PSD's of the disturbance sources that are injected into the system. We can clearly recognize the sawtooth pattern of the RWA PSD's, the discrete harmonic-like behavior of the cryocooler disturbance and the low-pass filter nature of the FGS noise.

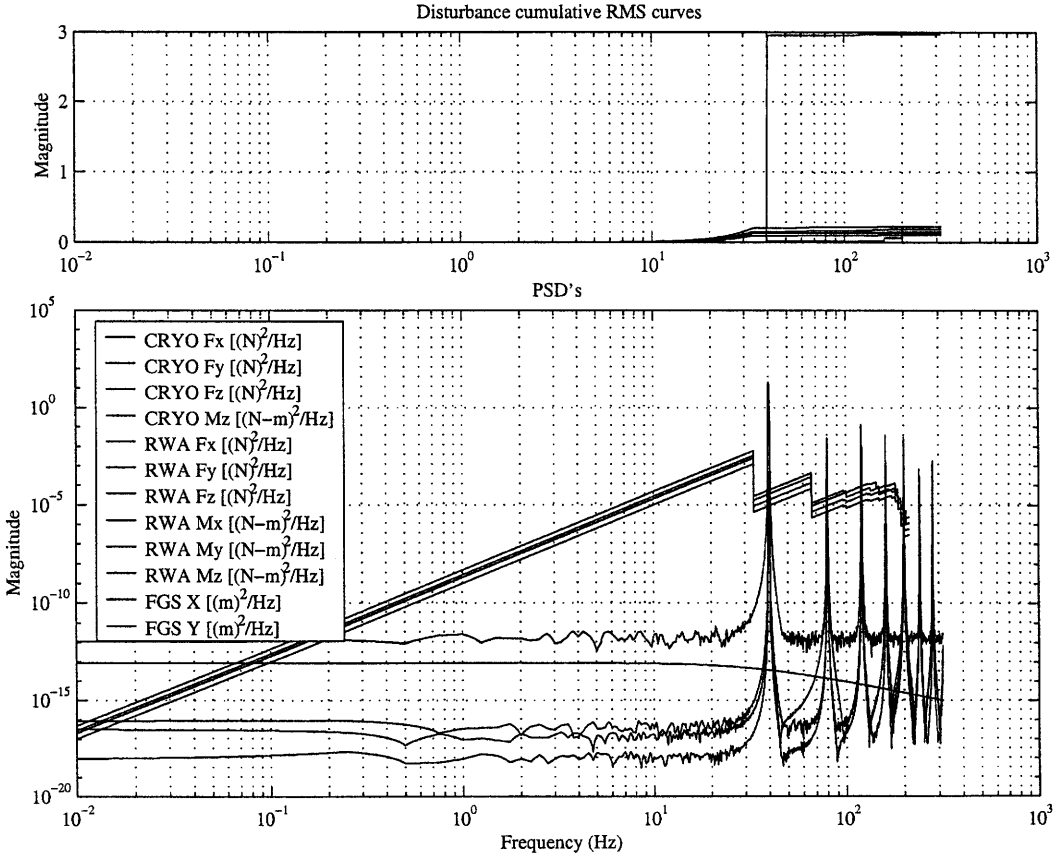

Figure 3.7: Power spectral densities of NGST disturbance sources

The first performance metric of interest is the wavefront error (WFE). The wavefront error is representative of the optical pathlength difference of each ray with respect to the unperturbed configuration. The RMS WFE is calculated by computing the spatial average of the RMS WFE over the light bundle at the exit pupil:

$$z_{WFE\ RMS} = \left(\frac{1}{n_{rays}} \left(z_1^T z_1 \right) \right)^{1/2} = \sqrt{E[z_1^2]} \tag{3.12}$$

where n_{rays} is the number of rays modeled in the system (1845 in our case) and z_1 is the performance vector containing the WFE for each individual ray. The results for the frequency domain analysis for RMS WFE are shown in Figure 3.8, whereby the middle plot shows the performance PSD for WFE, the top plot shows the cumulative RMS curve and the bottom plot shows the contributions of the different noise sources. The darkness of the line in the disturbance contribution plot indicates how strongly a disturbance contributes at a given frequency.

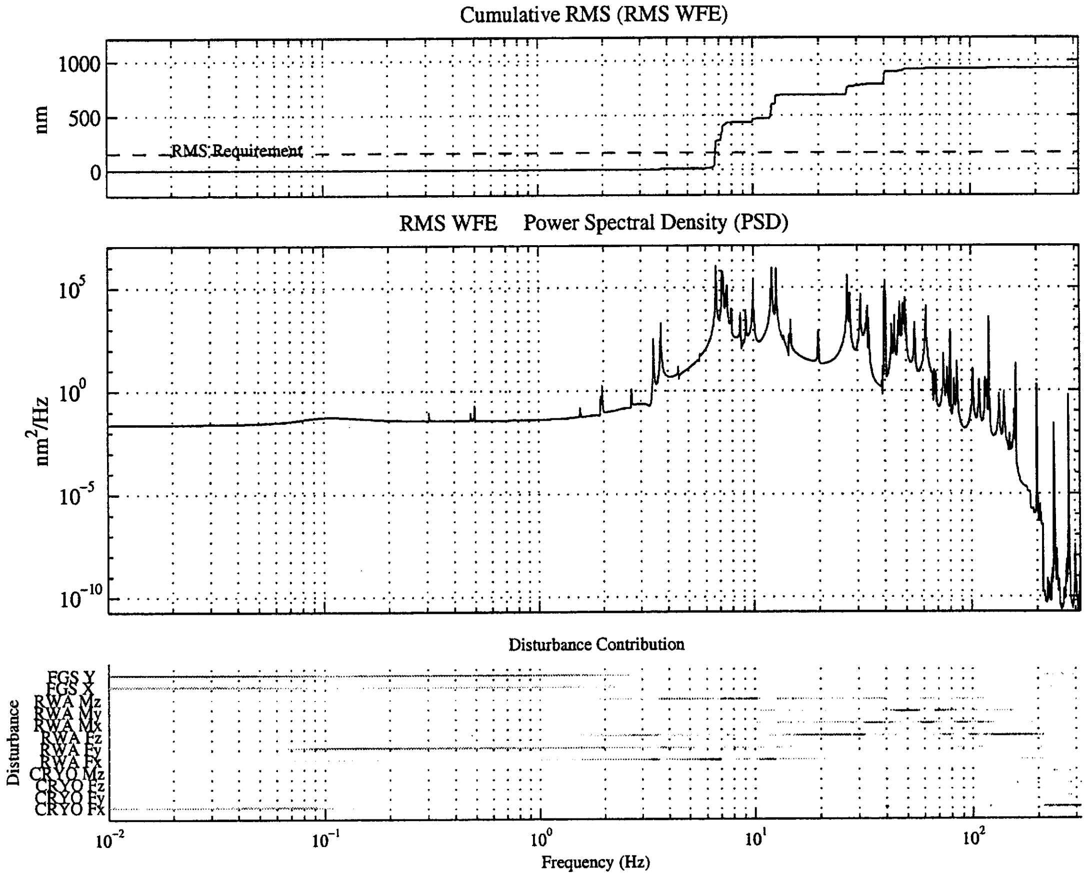

Figure 3.8: PSD Analysis nominal results for WFE

The PSD clearly shows the first flexible sunshield modes around 0.3-0.5 Hz. The power spectral density for the WFE shows lightly damped modes, which are excited in the 5-50 Hz range. It is interesting that the FGS noise is the dominant noise source at low frequency, but that it contributes little to the RMS at high frequencies. The RWA disturbances dominate the region from 5-100 Hz and the cryocooler harmonics are the most important disturbance sources above 100 Hz. The first question we must ask is whether or not we meet performance. This can be answered by consulting the cumulated RMS value at the high frequency end of the top subplot in Figure 3.8. We can see that the RMS WFE asymptotes to a RMS value of 933 nm, where the requirement (157 nm) is indicated by the dashed line on the top plot. The wavefront error (WFE) requirement is not met in this nominal case by a factor of 5.94. This error is accumulated in a relatively narrow frequency region from 5-50 Hz as the normalized area plot in Figure 3.9 shows.

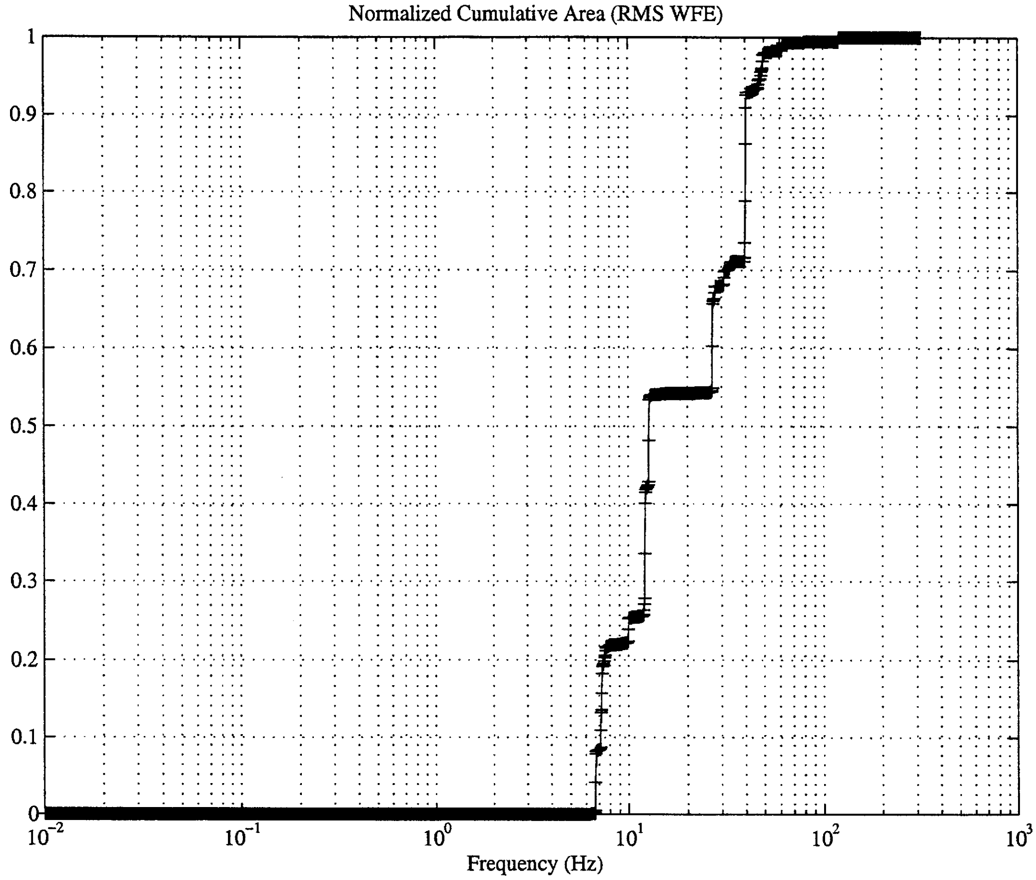

Figure 3.9: Cumulative area plot for WFE

The steps in the cumulative RMS curve can help us to identify the critical frequencies. This is done interactively by the analyst as described in reference [24]. Figure 3.9 depicts the normalized area plot for the WFE. The critical frequencies are then extracted and represented in the following bar chart. This chart shows the % contribution of each critical mode.

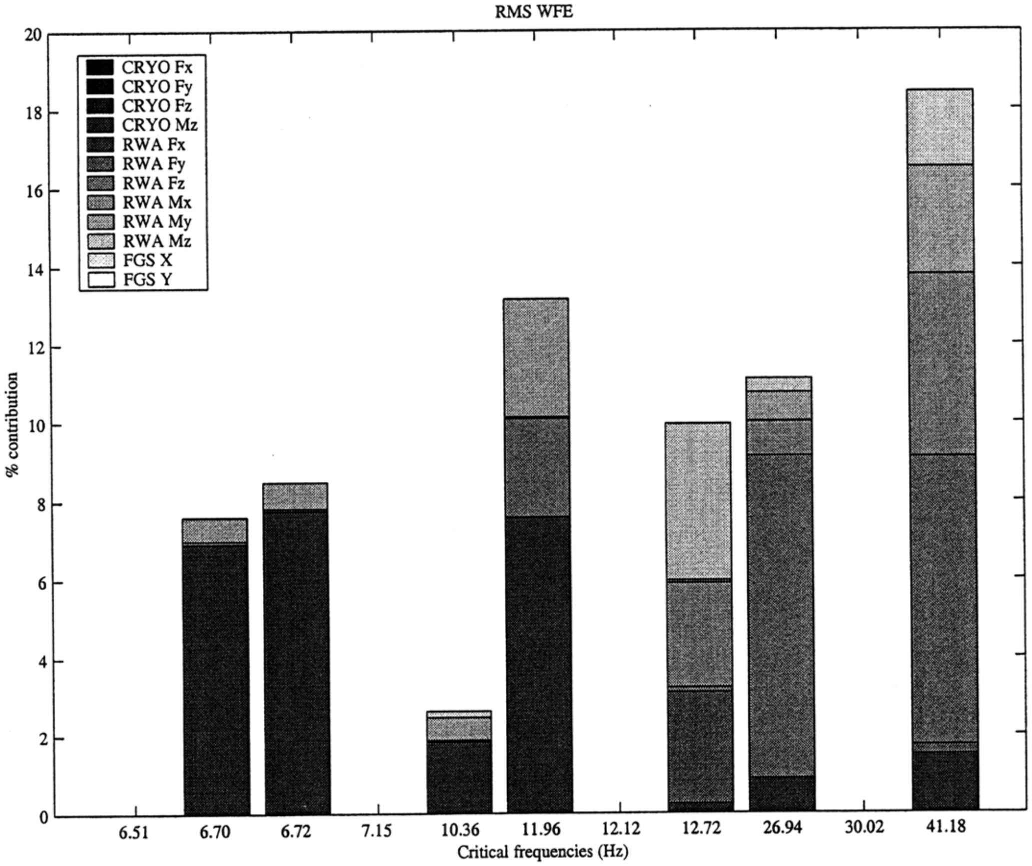

Figure 3.10: Modal significance chart for WFE (nominal case).

We can see immediately that the modes at 11.96 Hz, 12.72 Hz, 26.94 Hz and 41.18 Hz together contribute over 50% to the total RMS WFE. The relative contribution of the disturbance components at each mode to the performance is indicated by the stacked bar chart (Figure 3.10). The numerical results suggest that the RWA components are the dominant noise source in the nominal design case. It is possible to sum all the disturbance contributions to the critical frequencies found in Figure 3.10 and to look at their relative contributions as shown in Figure 3.11. We see that RWA disturbances make up over 99% of the total contribution. The FGS and Cryocooler contributions are not shown in the pie chart, since they make up less than 1 %.

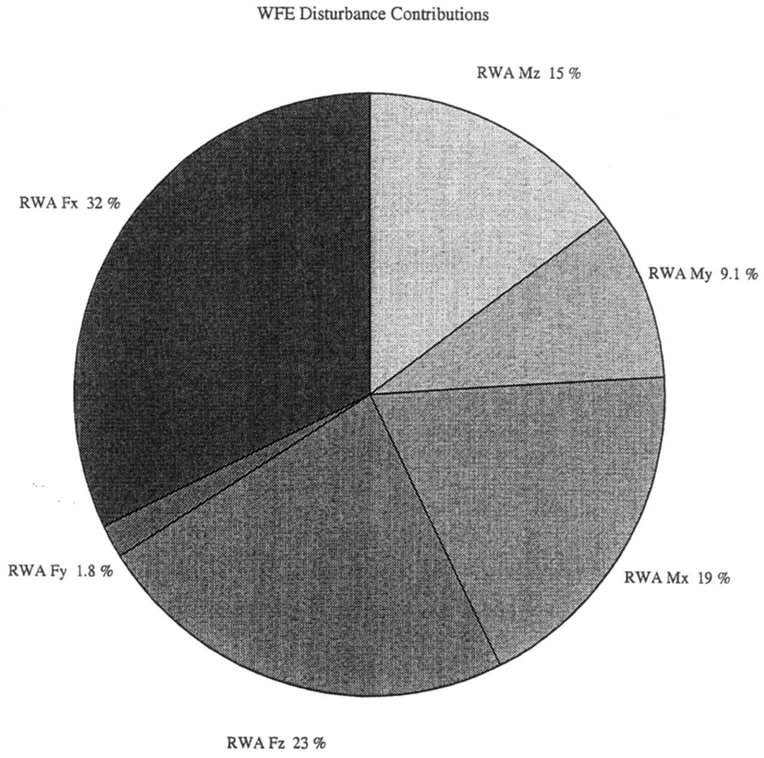

Figure 3.11: Contribution of noise sources to RMS WFE critical frequencies

This can be explained as follows. At low frequency the FSM and ADCS loops create substantial noise attenuation and the FGS noise with an RMS value of 2.35 mas (as derived in section 2.3) is negligible compared to the mechanical noise (RWA and cryocooler noise combined). At high frequencies the cryocoolers contain significant disturbance power, but the disturbance to performance transfer function is rapidly rolling off after 50 Hz, so that the high frequency noise contributes very little to the RMS WFE.

The second performance metric of interest is the LOS jitter metric that we have designated as RMS LOS. The LOS jitter is critical during science operations and is the main performance metric of the observatory fine pointing mode. The RMS LOS was previously defined as:

$$z_{WFE\ LOS} = \left(\frac{1}{2}\left(z_2^T z_2\right)\right)^{1/2} = \sqrt{E[z_2^2]} \tag{3.13}$$

It is defined as the average deviation of the image centroid in the *x* and *y* direction on the focal plane. Again we obtain the same information for the LOS that was obtained for the WFE frequency domain analysis. Figure 3.12 summarizes the frequency domain analysis results for the LOS jitter.

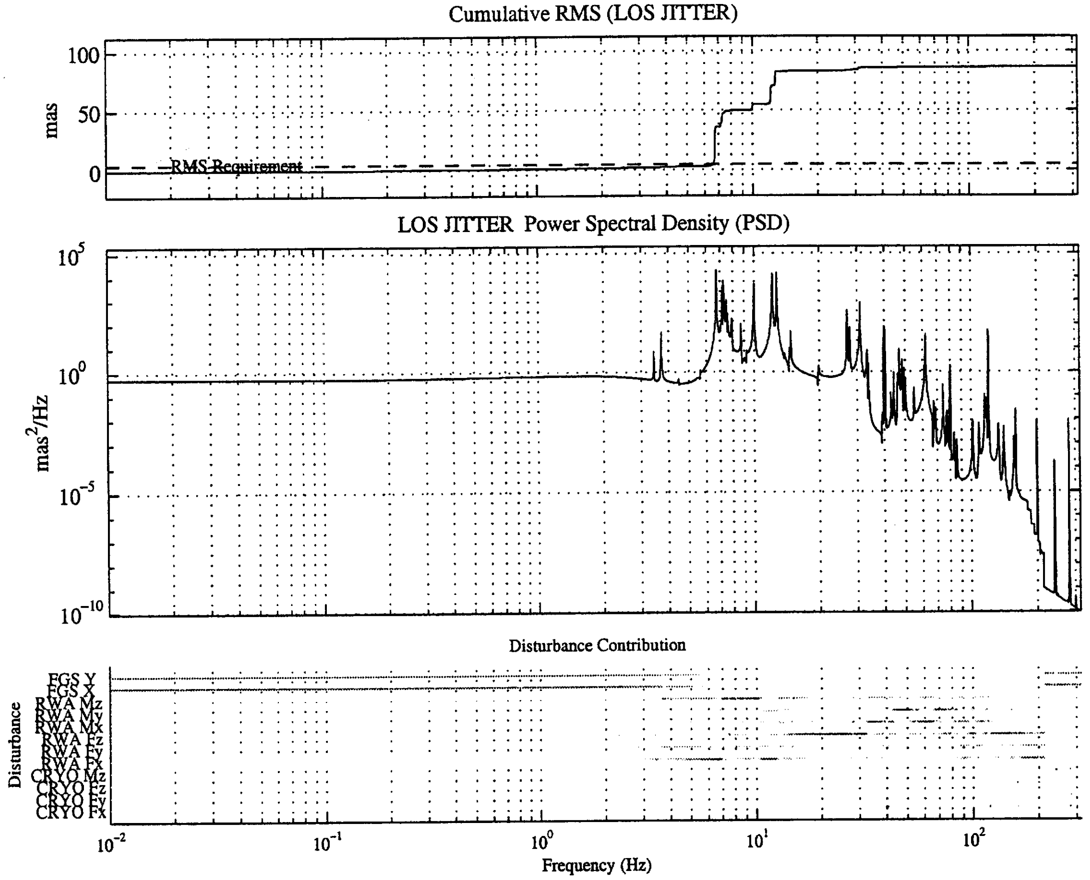

Figure 3.12: Baseline case PSD analysis results for LOS Jitter

The results in Figure 3.12 are shown in three subplots. The middle subplot shows the power spectral density $S_{zz2}(\omega)$ of the LOS as a function of frequency in units of mas^2/Hz. The upper plot shows the cumulative RMS curve, which is obtained by integrating under the PSD and taking the square root. The RMS error is accumulated over increasing frequency and tends towards a value of σ_{LOS}= 86.4 milli-arcseconds and represents the LOS jitter performance of the modeled system. It can be seen that the requirement of 4.8 mas is not met by a factor of 18 in the nominal case. The cumulative RMS curve helps to identify the modes which contribute the most to the performance. This is done by normalizing the cumulative area under the PSD and by identifying the large steps in Figure 3.13. These steps are extracted through user interaction and indicate the critical frequencies, i.e. the modes of the system that contribute significantly to the total RMS value and their % contribution to the total RMS. We notice again that most of the RMS is accumulated in the frequency range between 5 and 50 Hertz. This result confirms the findings from our preliminary study [52].

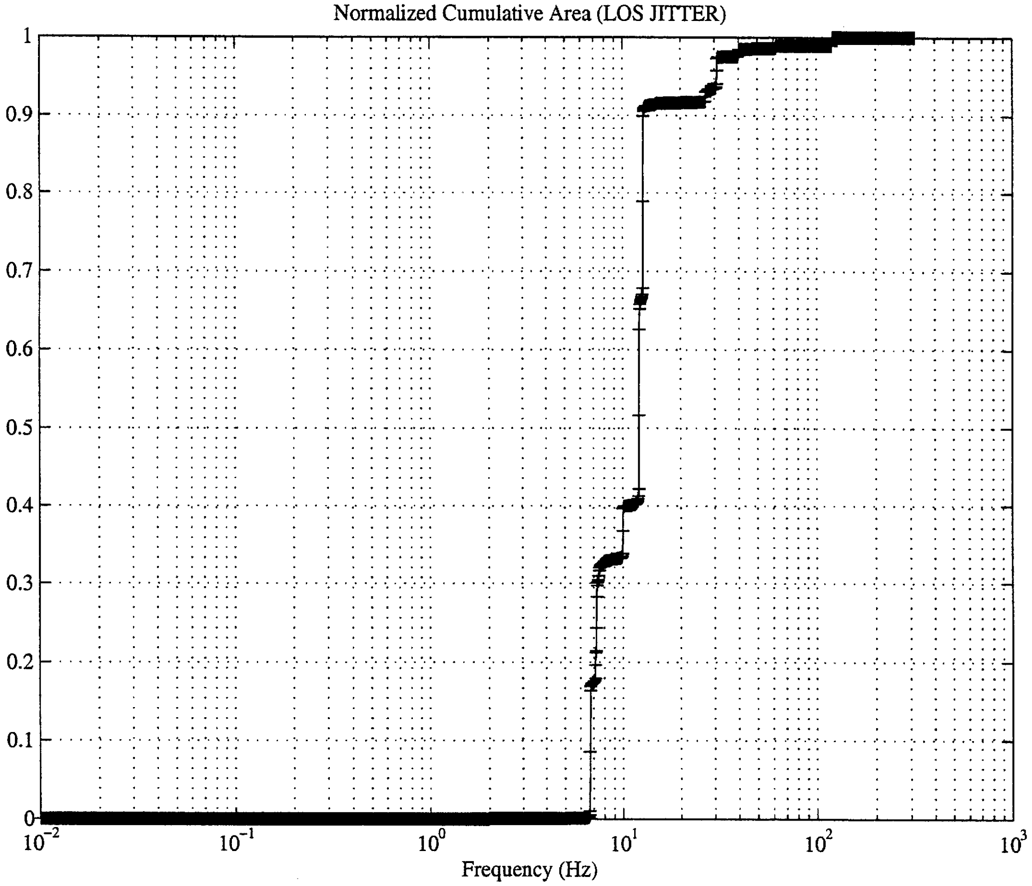

Figure 3.13: Normalized cumulative area plot for LOS jitter (nominal case)

The steps in the cumulative RMS curve are used to determine the critical modes of the system. These critical modes are subsequently extracted and plotted in increasing order of frequency (Figure 3.14). This information is an advantage of the frequency domain analysis over the other methods. Neither the time domain analysis, nor the Lyapunov analysis is able to provide this level of insight into the system dynamics. From Figure 3.14 we see that only three modes at 6.51, 11.96 and 12.12 Hz contribute about 60% to the total LOS jitter. This is a significant result, since it will allow us to focus on these few modes in order to improve system performance.

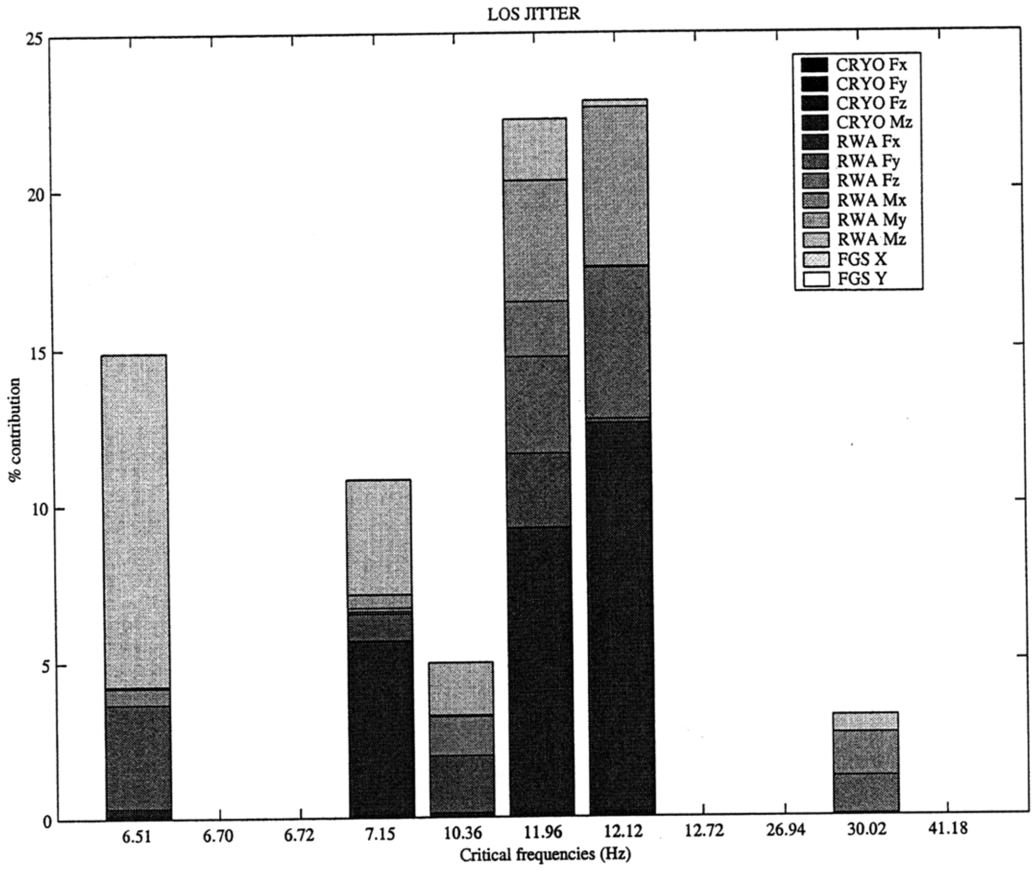

Figure 3.14: Modal significance chart for LOS Jitter (nominal case)

It shall be noted that these modes dominate under the assumption of the cryocooler, RWA and FGS power spectral density functions as defined in Chapter 2. For other disturbances such as thruster firings or thermal snap that have not been included in this analysis, it is possible that other modes would be dominant. However it is not expected that thermal snap events will occur during quasi-steady-state observations due to the thermal stability of the L2 orbit. Thruster firings in order to desaturate the stored angular momentum of the RWA are also not tolerated during science observations. Under the assumption that all disturbance sources are uncorrelated and that the critical frequencies capture the essential contributions to the total RMS (over 75%) we can compare the relative contributions of the various onboard disturbance sources with respect to each other for the LOS jitter. This was attempted in Figure 3.15. We can see that the

RWA disturbances are dominant as they were for the RMS WFE and that the FGS and cryocooler noise combined make up less than 1% contribution to the total RMS. Contributions of less than 1% are not plotted in the chart below. It is possible that a different cryocooler drive frequency will change these answers.

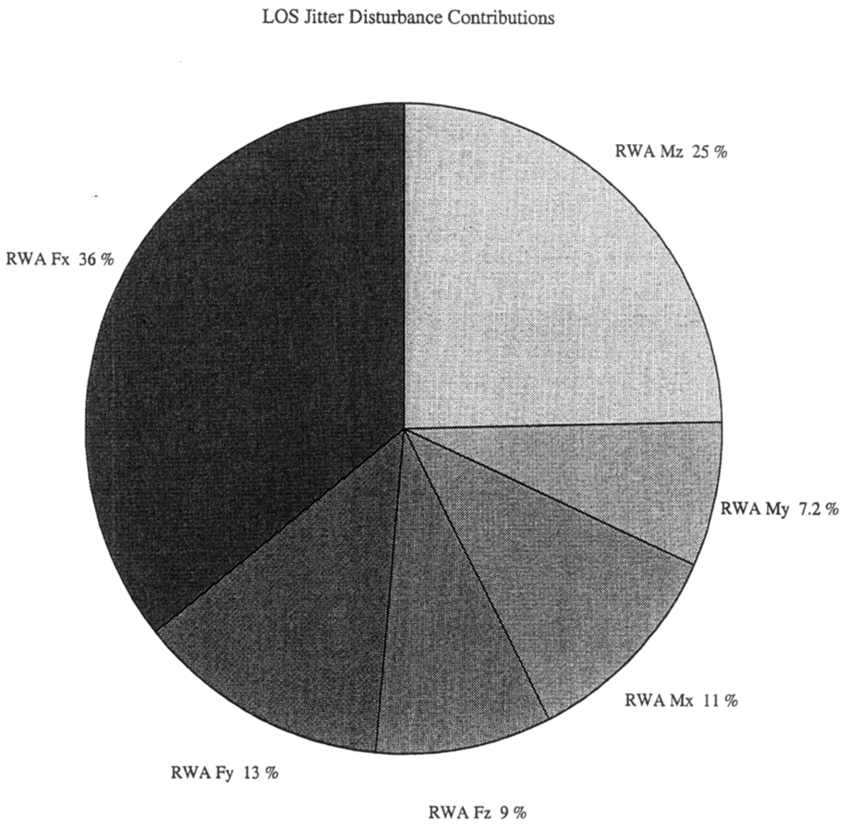

Figure 3.15 Relative contribution of noise sources to RMS LOS

This information is useful since it tells us that we must concentrate our efforts in the performance improvement phase (Chapter 6) on reducing the contribution of RWA disturbances. In the sensitivity analysis section we will try and obtain the slope of the performance with respect to modal parameters of the plant in order to find performance improvement options.

3.3 Lyapunov Analysis

The Lyapunov analysis is also based on linear systems theory. The state covariance matrix Σ_q of a linear system, driven by white noise, can be obtained by solving a steady-state Lyapunov equation as follows:

$$A_{zd}\Sigma_q + \Sigma_q A_{zd}^T + B_{zd}B_{zd}^T = 0 \qquad (3.14)$$

where $\mathbf{A_{zd}}$ and $\mathbf{B_{zd}}$ are the system matrices of the white noise d to performance z state space system. An important property is the symmetry of the state covariance matrix: $\Sigma_q = \Sigma_q^T$. The performance covariance matrix Σ_z is obtained by pre-multiplying Σ_q with the $\mathbf{C_{zd}}$ matrix and by post-multiplying with the transpose of $\mathbf{C_{zd}}$:

$$\Sigma_z = C_{zd}\Sigma_q C_{zd}^T \qquad (3.15)$$

The performance RMS value is then the square root of the performance covariance matrix Σ_z. In the multivariable case the variances are contained on the main diagonal of Σ_z.

$$\sigma_{z,i} = \left[diag\{\Sigma_z\}\right]^{1/2} \qquad (3.16)$$

The advantage of the Lyapunov solution is that it provides the exact analytical answer and is immune to frequency vector resolution issues. The disadvantage is that no information about the important modal contributions can be obtained directly. If Σ_q is in modal coordinates however, its diagonal entries give such information. Also the Lyapunov solution times increase rapidly with an increasing number of states, $\mathbf{q}$. The increase in computation time goes with n(n+1)/2 if n is the number of states. The number of states can be high if we retain many flexible modes of the plant dynamics. This is sometimes necessary if the dynamics of interest are at a significantly higher frequency than the fundamental flexible frequency of the system. Another reason for a large number of states is if the disturbance-shaping filter is of high order when the disturbance source has a complicated PSD-shape. This is often the case when the disturbance is neither really narrow-band nor wideband. Also a control system, which has many states, such as output feedback with state estimation can add a large number of states and thus make the Lyapunov solution more computationally demanding.

3.3.1 Lyapunov solution of 3DOF problem

Finding the Lyapunov solution for the 3DOF problem analytically and comparing the answers given by the `dist_analysis.m` framework motivates this section. The first Lyapunov solution of the sample 3DOF problem can be obtained analytically. This section shows how the steady-state Lyapunov equation is written and solved in the symbolic mathematics case. It can be seen that we first write out the Lyapunov equation 3.17 in terms of the entries of the covariance matrix. We also take advantage of the fact that the state covariance matrix Σ_q is symmetric. On the right hand side we have a 3x3 zero matrix.

$$\begin{aligned}
&\begin{bmatrix} -\omega_{RO} & 0 & 0 \\ 0 & 0 & 1 \\ \frac{-\omega_{RO}}{\sqrt{12m}} & -\omega_3^2 & -2\zeta_3\omega_3 \end{bmatrix}\begin{bmatrix} \sigma_{q11} & \sigma_{q12} & \sigma_{q13} \\ \sigma_{q12} & \sigma_{q22} & \sigma_{q23} \\ \sigma_{q13} & \sigma_{q23} & \sigma_{q33} \end{bmatrix}+ \\
&\begin{bmatrix} \sigma_{q11} & \sigma_{q12} & \sigma_{q13} \\ \sigma_{q12} & \sigma_{q22} & \sigma_{q23} \\ \sigma_{q13} & \sigma_{q23} & \sigma_{q33} \end{bmatrix}\begin{bmatrix} -\omega_{RO} & 0 & \frac{-\omega_{RO}}{\sqrt{12m}} \\ 0 & 0 & -\omega_3^2 \\ 0 & 1 & -2\zeta_3\omega_3 \end{bmatrix}+\begin{bmatrix} 1 \\ 0 \\ 0 \end{bmatrix}\begin{bmatrix} 1 & 0 & 0 \end{bmatrix}=\mathbf{0}
\end{aligned} \tag{3.17}$$

The second step then consists in solving the n*(n+1)/2 linear equations for the unknown entries of the state covariance matrix Σ_q. This system of linear equations can be solved by Gauss-Jordan triangularization or other methods. At this point it is also easy to understand why the system including the $\mathbf{A}_{zd}$ and $\mathbf{B}_{zd}$ matrices has to be well defined. Specifically the $\mathbf{A}_{zd}$ matrix must be full rank, so that rigid body modes must have been stabilized or removed; otherwise the system of equations in 3.17 for the entries of Σ_q cannot be solved. This is because neutrally stable modes have infinite energy under persistent excitation. The solution for the state covariance matrix Σ_q in the open loop case is obtained as (3.18):

$$\Sigma_q = \begin{bmatrix} \frac{1}{2\omega_{RO}} & \frac{-1}{2\sqrt{12m}\left(\omega_3^2+2\zeta_3\omega_3\omega_{RO}+\omega_{RO}^2\right)} & \frac{-\omega_{RO}}{2\sqrt{12m}\left(\omega_3^2+2\zeta_3\omega_3\omega_{RO}+\omega_{RO}^2\right)} \\ \frac{-1}{2\sqrt{12m}\left(\omega_3^2+2\zeta_3\omega_3\omega_{RO}+\omega_{RO}^2\right)} & \frac{\omega_{RO}^2+2\zeta_3\omega_3\omega_{RO}}{48m\zeta_3\omega_3^3\left(\omega_3^2+2\zeta_3\omega_3\omega_{RO}+\omega_{RO}^2\right)} & 0 \\ \frac{-\omega_{RO}}{2\sqrt{12m}\left(\omega_3^2+2\zeta_3\omega_3\omega_{RO}+\omega_{RO}^2\right)} & 0 & \frac{\omega_{RO}^2}{48m\zeta_3\omega_3\left(\omega_3^2+2\zeta_3\omega_3\omega_{RO}+\omega_{RO}^2\right)} \end{bmatrix}$$

After solving for the variance σ_z and substituting the correct values for the parameters we obtain the results as: open loop OPD RMS: σ_z= 4734.826 nm and closed loop OPD RMS: σ_z= 41.1332 nm. The second approach consists of solving the Lyapunov equation analytically in MATLAB™ using the `lyap.m` command. The following very simple sequence of commands yields the desired result in the open loop case:

```
Sq_oa = lyap(Aozd,Bozd*Bozd');
Sz_oa = Cozd*Sq_oa*Cozd';
sigmaz_o_la = sqrt(Sz_oa);
```

The numerical results are computed as σ_z= 4734.826 nm in the open loop case and σ_z= 41.1332 nm in the closed loop case. Again the results are consistent with the ones obtained earlier. Lastly we will look at the third option for solving the Lyapunov equation for the sample problem. The function `dist_analysis.m` also allows the use of the Lyapunov approach. This requires that the important flag dist_type be set to a value of 3, when calling the function. If dist_type = 3, then the state-space matrices for the filter (driven by unit-intensity white noise) that models the disturbance should be provided as $\mathbf{A_d}$, $\mathbf{B_d}$, $\mathbf{C_d}$, and $\mathbf{D_d}$. The results using dist_analysis.m for the Lyapunov analysis in the sample case are identical as before: RMS OPD = 4730 nm (open loop) and RMS OPD: 41.1 nm (closed loop).

The advantages and disadvantages of the Lyapunov approach are now discussed in more detail. The advantages of the Lyapunov approach are the computational speed for systems with a small or moderate number of states. Furthermore the results for the performance covariance matrix are exact and do not suffer from frequency vector or time sample realization issues. Thirdly the appended system $\mathbf{A_{zd}}$, $\mathbf{B_{zd}}$, $\mathbf{C_{zd}}$ and $\mathbf{D_{zd}}$ is already in the correct form that is needed for the subsequent sensitivity analysis. This is important since the sensitivity computations require the partial derivatives of the $\mathbf{A_{zd}}$ matrix with respect to model parameters. The disadvantages of the Lyapunov analysis are that no "visual" information is provided and that it becomes slow for a large number of system states. Additionally no information on what the critical system modes are or which disturbance components contribute the most to the RMS result can be obtained. The only output generated is the performance covariance matrix Σ_z, which we can compare to the requirements.

3.3.2 Lyapunov analysis for NGST

We perform the Lyapunov analysis using the function `dist_analysis.m`. and use the system *SYS_c2zd* as shown in Table 2.6. This is the overall system that contains all the disturbance, plant and controller states appended together. Contrary to the PSD analysis, the Lyapunov analysis computation times are not driven by the number of inputs and outputs of the system. Rather the computational effort lies in solving the Lyapunov equation itself 3.17 for the state covariance matrix Σ_q. It is the number of states in the appended overall state vector that determines the computational expense. The performance covariance matrix Σ_z is then obtained from Equation 3.18 via a matrix multiplication with $\mathbf{C_{zd}}$, which is not an expensive operation. The results from a Lyapunov solution of the baseline case are:

Table 3.1. Initial performance results from Lyapunov approach

Nominal Case	**RMS WFE**	**RMS LOS**
Results (Lyapunov)	727.98 nm	74.42 mas
Results (PSD Analysis)	933 nm	86.4 mas

We notice that the results do not exactly match the results from the PSD analysis. There are essentially two explanations for this. First, we have had to approximate the disturbance energy with low order filter functions for the RWA, cryocooler and FGS noises. Even though our shaping filters might produce the same RMS values as the corresponding disturbance PSD this does no guarantee that we will obtain the same final result due to the fact that some frequency regions are underpredicted, while others are overpredicted. This was illustrated in Figure 2.35 for the RWA overbounds. Secondly differences arise due to frequency vector resolution issues in the frequency domain. Figure 3.13 shows that only a few frequency points capture the amplification of the structural resonances that drive the system performance. The Lyapunov solution escapes this problem by solving for the performance covariance matrix Σ_z directly.

Even though the Lyapunov analysis does not give us the modal information we obtain from the PSD analysis, it has the advantage that we can cheaply compute the RMS value of the WFE for each individual ray, even if a large number of them (1845) are modeled by MACOS. Because the σ_{WFE} only represents the spatial RMS value of all rays combined, we can now also look at the spatial distribution of the RMS WFE across the light bundle at the exit pupil. The nominal location of each individual ray was given by the spot diagram presented in Figure 2.43. The WFE map (sometimes called OPD map) for NGST is shown in Figure 3.16.

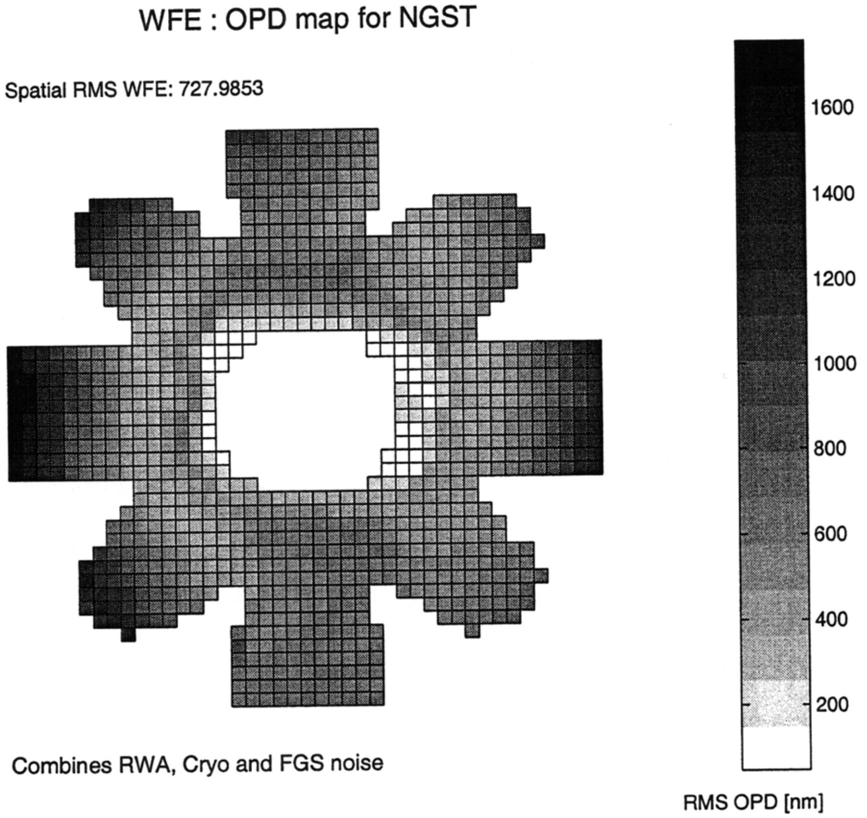

Figure 3.16: Spatial RMS WFE distribution across the pupil plane

The spatial RMS WFE can be plotted by using the nominal spot diagram, which was obtained from optical modeling with MACOS. The image is obtained in raster fashion by pairing each ray location in x and y on the spot diagram with the corresponding RMS WFE value for that particular ray. It shall be noted that this image does not represent a wavefront error distribution, which can be decomposed in its Zernike coefficients, because the RMS WFE represents the root-mean-square value of the OPD of each particular ray, thus characterizing the wavefront error as a stochastic metric. Zernike polynomial coefficients as utilized in wavefront control are based on the OPD's being deterministic quantities. Figure 3.16 shows that the WFE distribution is not uniform across the aperture. The center segment exhibits the lowest RMS WFE due to its very stiff attachment to the hexapod and backup structure. The WFE is larger at the gaps between the center segment and the eight folding segments and increases as we go out in a radial direction.

3.4.Performance Assessment results interpretation

We have computed the open loop and closed loop performance for the 3DOF sample problem in a number of different ways. Table 3.2 shows a comparison of the RMS OPD results and the computational times required for each solution.

Table 3.2: Performance Analysis results comparison for sample 3DOF problem[*]

Method of Analysis	Open Loop RMS OPD	Closed Loop RMS OPD	CPU time seconds
Time Domain Simulink	4124.942162 nm	43.18093187 nm	116.8 sec*
Time Domain dist_analysis.m	4124.942163 nm	43.18093499 nm	4.496 sec
Frequency Domain symbolic	4734.826372 nm	41.13325712 nm	1.152 sec
Frequency Domain numerical	4728.960055 nm	41.18875906 nm	1.422 sec
Frequency Domain dist_analysis.m	4728.960055 nm	41.18875906 nm	11.1 sec*
Lyapunov Analysis symbolic	4734.826372 nm	41.13325712 nm	4.036 sec
Lyapunov Analysis numerical	4728.915228 nm	41.13073179 nm	0.03 sec
Lyapunov Analysis dist_analysis.m	4728.915228 nm	41.13073179 nm	0.01 sec

---

[*] Indicates that CPU times are not relevant since user interaction was required during this particular analysis

The above table compares the open loop and closed loop answers for the time domain, frequency domain and Lyapunov methods. Within each approach we distinguish between the symbolic, the numerical and the `dist_analysis.m` approaches. For the time domain case we cannot derive a closed form analytical result (symbolic) due to the nature of white noise. Firstly we see that all answers match very closely with the exception of the time domain results. The RMS OPD requirement was determined to be 116 nm. We see that in the open loop we do not meet requirements (~ 4000 nm RMS OPD). We do however meet requirements in the closed loop case (~ 40 nm) thanks to about 40 dB of attenuation.

The exact answer is given for the symbolic approaches, since no numerical inaccuracies can influence the result. The answers for the frequency domain and Lyapunov approach match exactly with the symbolic approach. The numerical frequency domain approach suffers from frequency vector resolution issues, whereas the numerical Lyapunov solution is also prone to inaccuracies due to the solution of the steady state Lyapunov equation. The time domain answers could become more precise by increasing the sample time length T, shortening the sample time t_s of the white noise source or by varying the seed for the random number generator and averaging the results of several runs. As far as CPU time is concerned, the Lyapunov approach is the fastest for this low order model, followed by the frequency domain approach. The slowest method is the use of time simulations in SIMULINK™.

The results for the full order NGST model suggest that the performance in terms of RMS WFE and RMS LOS is not met in the baseline case. This conclusion however has to be carefully considered. There are several assumptions, which have been made in order to arrive to this result. The most important modeling uncertainties are in the RWA wheel speed distribution and the amount of global damping. Chapter 5 will analyze how sensitive the performance is to changes in these parameters. It is also interesting to note that in almost all cases the same modes that drive the RMS WFE are also responsible for causing LOS errors. The sensitivity analysis chapter will try to achieve a better understanding of these modes in order to come up with redesign and performance improvement recommendations.

Chapter 4

Challenges of large order models

The transition from a simple problem containing only a few degrees of freedoms to a full order simulation such as NGST entails a number of challenges. These challenges are related to the large size of the system matrices, numerical conditioning issues and the fact that the input-output space can be very large if we choose to model the optical system with a large number of rays.

4.1 Numerical conditioning issues

Numerical conditioning issues can have a fundamental effect on the results of a disturbance analysis. This is especially true if the analysis is carried out with a state space system such as the one used in the Lyapunov analysis (Chapter 3). This section illustrates this problem with the PSD overbounds that were developed in Section 2.3 for the reaction wheel disturbance model. The wideband overbound was successful in matching the RWA disturbance PSD's using a transfer function of the form:

$$G(s)=\frac{Ks^2}{(s+\omega_l)^2(s+\omega_h)^4} \tag{4.1}$$

The MATLAB™ optimization toolbox is used to determine the values of the lower corner frequency ω_l, the higher corner frequency ω_h and the gain K. The numerator and denominator polynomials are returned for each component. Looking at a specific example (RWA F_x) the optimization routine returns the following transfer function:

$$G_{\text{RWA Fx}}(s)=\frac{\text{num(s)}}{\text{den(s)}}=\frac{a_2s^2}{b_6s^6+b_5s^5+b_4s^4+b_3s^3+b_2s^2+b_1s+b_o} \tag{4.2}$$

$$=\frac{5.11\cdot 10^{12}s^2}{s^6+1.38\cdot 10^4s^5+7.25\cdot 10^7s^4+1.77\cdot 10^{11}s^3+1.89\cdot 10^{14}s^2+5.85\cdot 10^{16}s+5.44\cdot 10^{18}}$$

We see immediately that the magnitude of the denominator polynomial coefficients vary by orders of magnitude. This is bound to lead to numerical conditioning problems. Using the function `tf2ss.m` in MATLAB transforms the transfer function in Equation 4.2 to canonical state space form as shown in Equation 4.3. We can compute the condition number of the **A** matrix, which is defined as the ratio of the maximum to the minimum singular value of **A**. For the canonical representation in Equation 4.3 we obtain a condition number of $5.44 \cdot 10^{18}$, which indicates that the "shaping filter" state space system is very ill conditioned. This will inevitably lead to problems when the disturbance states are appended into the overall system according to Equation 2.183.

$$\dot{q} = \underbrace{\begin{bmatrix} -1.38\cdot 10^{4} & -7.25\cdot 10^{7} & -1.77\cdot 10^{11} & -1.89\cdot 10^{14} & -5.85\cdot 10^{16} & -5.44\cdot 10^{18} \\ 1 & 0 & 0 & 0 & 0 & 0 \\ 0 & 1 & 0 & 0 & 0 & 0 \\ 0 & 0 & 1 & 0 & 0 & 0 \\ 0 & 0 & 0 & 1 & 0 & 0 \\ 0 & 0 & 0 & 0 & 1 & 0 \end{bmatrix}}_{A} q + \underbrace{\begin{bmatrix} 1 \\ 0 \\ 0 \\ 0 \\ 0 \\ 0 \end{bmatrix}}_{B} d \qquad (4.3)$$

$$w = \underbrace{\begin{bmatrix} 0 & 0 & 0 & 5.11\cdot 10^{12} & 0 & 0 \end{bmatrix}}_{C} q + \underbrace{\begin{bmatrix} 0 \end{bmatrix}}_{D} d$$

A possible remedy is to balance the state space system according to Moore [57], which should dramatically improve the ill conditioning of the above state space system. Unfortunately the system is already too ill conditioned for this method to work, since a Lyapunov equation must be solved in order to obtain the gramians for balancing. The remedy applied in this case was to decompose the transfer function in Equation 4.2 as follows:

$$G(s) = \frac{Ks^2}{(s+\omega_l)^2 (s+\omega_h)^4} = \frac{\sqrt{K}s}{(s+\omega_l)(s+\omega_h)^2} \cdot \frac{\sqrt{K}s}{(s+\omega_l)(s+\omega_h)^2} \qquad (4.4)$$

Then each of the elements of the product on the right side of Equation 4.4 can be transformed into state space form individually. Finally the two systems are put in series and the new state space system representing the RWA overbound is written as:

$$\dot{q} = \underbrace{\begin{bmatrix} -1.11\cdot10^{3} & -3.92\cdot10^{5} & -4.27\cdot10^{7} & 0 & -4.14\cdot10^{4} & 0 \\ 1 & 0 & 0 & 0 & 0 & 0 \\ 0 & 1 & 0 & 0 & 0 & 0 \\ 0 & 0 & 0 & -1.11\cdot10^{3} & -3.92\cdot10^{5} & -4.27\cdot10^{7} \\ 0 & 0 & 0 & 1 & 0 & 0 \\ 0 & 0 & 0 & 0 & 1 & 0 \end{bmatrix}}_{A} q + \underbrace{\begin{bmatrix} 0 \\ 0 \\ 0 \\ 1 \\ 0 \\ 0 \end{bmatrix}}_{B} d \tag{4.5}$$

$$w = \underbrace{\begin{bmatrix} 0 & 4.14\cdot10^{4} & 0 & 0 & 0 & 0 \end{bmatrix}}_{C} q + \underbrace{\begin{bmatrix} 0 \end{bmatrix}}_{D} d$$

The condition number of **A** is now $4.27\cdot10^{7}$ compared to $5.85\cdot10^{18}$ in the previous case. Another important aspect of numerical conditioning affects the Lyapunov analysis. It is paramount that the rigid body translation modes be removed from the system, since they are not controlled in this system. The rigid body translational modes do not affect the performance since we are just sampling a different portion of the incoming wavefront. The rigid body modes do, however, lead to numerical conditioning problems in the closed loop $\mathbf{A}_{\mathbf{zd}}$ matrix. It is thus recommended to either remove or stabilize these rigid body modes.

4.2 Singular Value Decomposition of Linear Sensitivity Optics Matrices

The optical train of the NGST Yardstick design is modeled with analytical tools such as MACOS and uses a large number of rays (several thousand) to represent the propagation of the science light through the system. This has been shown in Section 2.4. The effects of the physical displacements and of the FSM gimbal angles on the performance metrics such as LOS jitter and RMS wavefront error can be approximated by linearizing the optics model. This is captured by the linear sensitivity matrices, which relate the generalized coordinates to the optical performance metrics. Due to the large number of rays, a disturbance analysis requires the computation of a large number of transfer functions. This number increases linearly with the number of rays, which are used by the ray-tracing algorithm. The linear sensitivity matrices are generally rectangular, non-full rank and also non-invertible. Singular value decomposition has been identified as a technique which allows the introduction of "surrogate" linear sensitivity matrices. These surrogate matrices are smaller and significantly reduce the number of transfer functions to be computed. This speeds up the computation of the RMS WFE and RMS LOS by a factor which is roughly equal to the ratio of the number of rays to the number of input degrees of freedom. The theory of singular value decomposition (SVD) is presented, applied to NGST integrated dynamics modeling and a sample comparison is computed. This section demonstrates that identical RMS results can be achieved with the SVD-technique, while achieving a factor 30 savings in computation time.

The block diagram in Figure 4.1 is a simplified version of the full system diagram presented in Figure 2.3. It shows the block diagram of the NGST integrated model for a RWA disturbance analysis (Cryocooler and FGS noise is neglected), while only taking into account the FSM control loop.

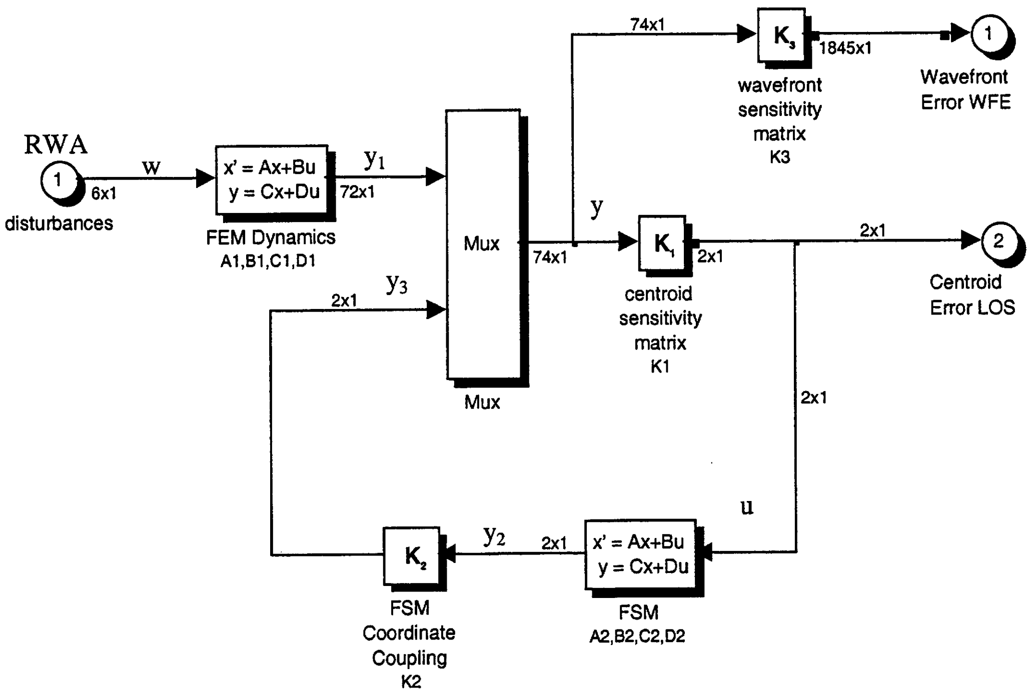

Figure 4.1: NGST block diagram for RWA disturbance analysis

The state equations for this model can be computed as follows. The RWA disturbances are represented by the vector *w* (6x1), which contains the three disturbance forces and three moments and enters the system at the ACS grid point in the FEM. The FEM state space model is in 2^{nd} order modal form and can be written as follows:

$$\frac{dx_1}{dt} = A_1 x_1 + B_1 w = \begin{bmatrix} 0 & I \\ -\Omega^2 & -2Z\Omega \end{bmatrix} x_1 + \begin{bmatrix} 0 \\ \Phi^T \beta_w \end{bmatrix} w \tag{4.6}$$

$$y_1 = C_1 x_1 + D_1 w = \begin{bmatrix} C_{yx}\Phi & C_{y\dot{x}}\Phi \end{bmatrix} x_1 + [0] w \tag{4.7}$$

where Ω is the modal frequency matrix, Z is the modal damping matrix, Φ is the matrix containing the eigenvectors (modeshapes) of the structure, β_w represents the input influence coefficients and $C_{yx}, C_{y\dot{x}}$ are the output influence coefficient matrices that determine which structural degrees of freedom affect the outputs of the state space system. The second system included in the block diagram in Figure 4.1 is the state space representation of the FSM controller, which contains two independent channels in x and y:

$$\frac{dx_2}{dt} = A_2 x_2 + B_2 u \tag{4.8}$$

$$y_2 = C_2 x_2 + D_2 u \tag{4.9}$$

Here the inputs *u* are the *X* and *Y* position of the centroid as measured on the focal plane by the FGS. These inputs are processed by the FSM controller and converted into the two gimbal angles, which control the FSM. The two gimbal angles are obtained by transforming the output vector $\mathbf{y_2}$ into $\mathbf{y_3}$ with the inverse of the centroid linear sensitivity matrix:

$$y_3 = K_2 y_2 = -k_{opt} \cdot K_{12}^{-1} y_2 \tag{4.10}$$

where $\mathbf{K_2}$ is the inverse of the FSM-to-Centroid matrix $\mathbf{K_{12}}$, multiplied by (-1) and the optical magnification of the telescope ($k_{opt} = 120$). The two systems are connected via a MUX block which stacks the vectors y_1 (FEM generalized displacements – 72x1) and y_3 (FSM angles – 2x1) to the vector *y* of generalized coordinates. This vector in the baseline NGST model is of dimension 74x1:

$$y = \begin{bmatrix} y_1 \\ y_3 \end{bmatrix} = \begin{bmatrix} y_1 \\ K_2 y_2 \end{bmatrix} = \begin{bmatrix} C_1 x_1 \\ K_2 C_2 x_2 \end{bmatrix} \tag{4.11}$$

If we represent the MUX block by partitioning the centroid linear sensitivity matrix $\mathbf{K_1}$ (of dimension 2x74 in the NGST baseline) and the WFE linear sensitivity matrix $\mathbf{K_3}$ (of dimension 1845x74 in the NGST baseline case) as follows:

Centroid Linear Sensitivity: $$K_1 = \left[{}_{2x72}K_{11} \quad {}_{2x2}K_{12} \right] \qquad (4.12)$$

WFE Linear Sensitivity: $$K_3 = \left[{}_{1845x72}K_{31} \quad {}_{1845x2}K_{32} \right] \qquad (4.13)$$

Then assuming that $\mathbf{D_1}$=0 and $\mathbf{D_2}$=0 (no feedthrough terms) we can write the closed loop state equations in matrix form:

$$\frac{dx}{dt} = \begin{bmatrix} A_1 & 0 \\ B_2K_{11}C_1 & A_2 + B_2K_{12}K_2C_2 \end{bmatrix} \begin{bmatrix} x_1 \\ x_2 \end{bmatrix} + \begin{bmatrix} B_1 \\ 0 \end{bmatrix} w = A_{cl}x + B_{cl}w \qquad (4.14)$$

the output equations are derived in a similar fashion. The two performance metrics of interest are z_1, which is the WFE error vector (1845x1), which assigns a WFE to each ray and z_2 which is a 2x1 vector and represents the LOS error in x and y, respectively. The performances z_1 and z_2 can be computed as follows:

WFE: $$\begin{aligned} z_1 = K_3y = \left[K_{31} \quad K_{32}\right]\left[y_1 \quad K_2y_2\right]^T = K_{31}y_1 + K_{32}K_2y_2 = \\ K_{31}C_1x_1 + K_{32}K_2C_2x_2 = \left[K_{31}C_1 \quad K_{32}K_2C_2\right]\cdot\left[x_1 \quad x_2\right]^T \end{aligned} \qquad (4.15)$$

LOS: $$z_2 = K_1y = K_{11}y_1 + K_{12}K_2y_2 = \left[K_{11}C_1 \quad K_{12}K_2C_2\right]\left[x_1 \quad x_2\right]^T \qquad (4.16)$$

Therefore the output equations can be formulated in matrix form:

$$z = \begin{bmatrix} z_1 \\ z_2 \end{bmatrix} = \begin{bmatrix} K_{31}C_1 & K_{32}K_2C_2 \\ K_{11}C_1 & K_{12}K_2C_2 \end{bmatrix} \begin{bmatrix} x_1 \\ x_2 \end{bmatrix} + [0]w = C_{cl}x + D_{cl}w \qquad (4.17)$$

Appending the two state space systems together as shown above and solving for the closed loop state equations finally yields the following MIMO system, which is obtained from Equations 4.14 and 4.17:

$$\begin{aligned} \dot{x} &= A_{cl}x + B_{cl}w \\ z &= C_{cl}x + D_{cl}w \end{aligned} \tag{4.18}$$

For the NGST yardstick baseline analysis, the closed loop A_{cl}-matrix is 206x206, the B_{cl} matrix is 206x6, the C_{cl} matrix is 1847x206 and the feedthrough matrix D_{cl} is 1847x6. We can obtain the closed loop transfer function matrix $G_{zw}(j\omega) = G_{zw}(s)$ by solving the following matrix equation in the s-domain:

$$G_{zw}(s) = C_{cl}\left[sI - A_{cl}\right]^{-1} B_{cl} + D_{cl} \tag{4.19}$$

The final goal of the disturbance analysis is to obtain the RMS (root mean square) values for the performances z_1 = WFE and z_2 = LOS under the influence of dynamic RWA disturbances. The first step after computing the closed loop transfer function matrix in Equation 4.19 is to obtain the output PSD's of the performances [21]:

$$S_{zz}(\omega) = G_{zw}(j\omega)S_{ww}(\omega)G_{zw}^{H}(j\omega) \tag{4.20}$$

where $S_{ww}(\omega)$ is the 6x6 spectral density matrix of the disturbance and $G_{zw}(j\omega)$ is the transfer function matrix as computed in Equation 4.19. The covariance of the performance z can be obtained by integrating the output spectral density matrix $S_{zz}(\omega)$ across all frequencies. The vector of root-mean-square values z_{RMS} is obtained by taking the square root of the covariances.

$$z_{RMS} = \left(2\int_{0}^{+\infty} S_{zz}(\omega)d\omega \right)^{1/2} \tag{4.21}$$

The linear sensitivity matrices for the optics model are computed by introducing a unit perturbation to one degree of freedom at a time and computing wavefront and centroid in MACOS. The matrices are thus formed one column at a time by numerical differentiation [16]. Mathematically, the linear optics models are given by:

$$W = W_o + \frac{\partial W}{\partial y} y \tag{4.22}$$

$$C = C_o + \frac{\partial C}{\partial y} y \tag{4.23}$$

where y is the vector of translations and rotations of the FEM coordinates, augmented by the FSM gimbal coordinates (74xl), C is the centroid for the chief ray (2xl), W is the OPD (=WFE) vector (1845xl), $K_1=\frac{\partial C}{\partial y}$ is the centroid linear sensitivity matrix (2x74), and $K_3=\frac{\partial W}{\partial y}$ is the wavefront linear sensitivity matrix (1845x74). Assuming that $W_o = 0$ and $C_o = 0$, Equations 4.22 and 4.23 are rewritten as:

$$z_1 = W = \frac{\partial W}{\partial y} y = K_3 y \tag{4.24}$$

$$z_2 = C = \frac{\partial C}{\partial y} y = K_1 y \tag{4.25}$$

The large number of rays used by the ray-tracing algorithm in MACOS allows a good representation of the spatial distribution of the WFE. On the other hand it requires the computation of a very large number of transfer functions according to equation (1.18). This number increases linearly with the number of rays, which are used by the ray-tracing algorithm. The number of frequency response points, which have to be computed in the closed loop transfer function matrix $G_{zw}(j\omega)$ is equal to:

$$N_{pts} = n_{rays} \cdot n_{inp} \cdot n_{freq} \tag{4.26}$$

where n_{rays} is the number of rays used, n_{inp} is the number of input (noise) source components and n_{freq} is the number of frequency points used in the Bode computations. A high frequency resolution ($\Delta j\omega$ small) is desired in order to capture the effects of the lightly damped resonant modes. For the NGST baseline analysis this number is equal to:

$$N_{pts} = (1845+2)\cdot(6)\cdot 1000 = 11{,}082{,}000 \qquad (4.27)$$

Thus a significant amount of CPU time is spent computing the transfer function matrix. Ultimately, however, the disturbance analysis in the frequency domain yields only two scalar numbers as a result: RMS WFE and RMS LOS. These metrics are root-mean-square values and are obtained from the 1847 outputs in the following manner:

$$z_{WFE\ RMS} = \left(\frac{1}{n_{rays}}\left(z_1^T z_1\right)\right)^{1/2} = \sqrt{E[z_1^2]} \qquad (4.28)$$

Thus the WFE RMS value is the root mean square result of the values which are obtained from Equation 4.24 for each individual ray across the physical aperture of the telescope. In a similar manner the RMS LOS (line of sight) error is calculated from the centroid x and y errors (=LOS when combined together):

$$z_{WFE\ LOS} = \left(\frac{1}{2}\left(z_2^T z_2\right)\right)^{1/2} = \sqrt{E[z_2^2]} \qquad (4.29)$$

It shall be noted that these RMS values are *not* equal to the standard deviation of WFE and LOS due to the following relationship:

$$Var[z] = \sigma_z^2 = E[z^2] - \mu^2 \qquad (4.30)$$

In the general case the mean value μ for wavefront error and centroid is not zero. The question, which is discussed in this Section is whether or not there exists a more efficient method to compute the RMS performances in the frequency domain, while preserving the high number of rays used to approximate the science light and guaranteeing identical results at the same time. The next section introduces the singular value decomposition as a potential remedy, if the number of rays (output metrics) significantly exceeds the number of input degrees of freedom.

The singular value decomposition (SVD) for a general matrix **A** allows a decomposition of **A** into three matrices **U**, Σ and **V**. First we assume that the matrix **A** is m by n , of rank r and contains only real elements[12]. Then the "singular values" are the square roots of the r positive eigenvalues of A^TA [58]. These square roots $\sigma_1, \sigma_2, \ldots, \sigma_r$ are also the square roots of the eigenvalues of AA^T and are the only nonzero entries in the *m* by *n* diagonal matrix Σ. U and V are orthogonal, unitary, square matrices of orders m and n, and their columns contain the eigenvectors of AA^T and A^TA respectively. The singular value decomposition is written as:

$$A = U \cdot \Sigma \cdot V^T \tag{4.31}$$

For general rectangular matrices the SVD is very useful. Among other things it can be used to approximate the original matrix A by a matrix of smaller rank or determine the "maximum gain" of a matrix by looking at the largest singular value σ_1 [58]. The singular values are contained on the main diagonal of Σ and are ordered in descending order of magnitude. Thus we can write:

$$_{mxn}\Sigma = \begin{bmatrix} \sigma_1 & 0 & 0 \\ 0 & \ldots & 0 \\ 0 & 0 & \sigma_n \\ 0 & 0 & 0 \\ 0 & 0 & 0 \\ 0 & 0 & 0 \end{bmatrix} = \begin{bmatrix} _{nxn}\Sigma_1 \\ _{(m-n)xn}\Sigma_0 \end{bmatrix} \tag{4.32}$$

where the submatrix Σ_1 contains all the singular values and Σ_0 contains only zeros. If the rank of the matrix A is r = n, there will be n nonzero singular values. The column space and left nullspace are displayed in U and the row space and right nullspace are contained in V^T. The singular value decomposition can also be applied to the linear sensitivity matrices for NGST, which are rectangular, non-full rank, real matrices. In general we can write the singular value decomposition for the linear wavefront sensitivity matrix K_3 and the linear centroid sensitivity matrix K_1 as:

---

[12] SVD is also feasible for complex matrices. The transpose operator T has to be replaced with *, which indicates the complex conjugate transpose operator.

$$K_3 = U_3 \Sigma_3 V_3^T \tag{4.33}$$

$$K_1 = U_1 \Sigma_1 V_1^T \tag{4.34}$$

If we substitute these results from the SVD in the expression for the output performances for WFE and LOS we obtain:

$$z_1 = K_3 y = U_3 \Sigma_3 V_3^T y \tag{4.35}$$

$$z_2 = K_1 y = U_1 \Sigma_1 V_1^T y \tag{4.36}$$

The RMS WFE and RMS LOS can now be computed by using the above expressions and substituting them into equations 4.28 and 4.29:

$$z_{WFE\ RMS} = \left(\frac{1}{n_{rays}} \left(z_1^T z_1 \right) \right)^{1/2} = \left(\frac{1}{n_{rays}} \left(y^T V_3 \Sigma_3^T U_3^T U_3 \Sigma_3 V^T y \right) \right)^{1/2} \tag{4.37}$$

$$z_{WFE\ LOS} = \left(\frac{1}{2} \left(z_2^T z_2 \right) \right)^{1/2} = \left(\frac{1}{2} \left(y^T V_1 \Sigma_1^T U_1^T U_1 \Sigma_1 V_1^T y \right) \right)^{1/2} \tag{4.38}$$

because U is a unitary matrix, the following relationships hold true:

$$\begin{aligned} U_3^T U_3 &= I \\ U_1^T U_1 &= I \end{aligned} \tag{4.39}$$

The expressions in brackets in (4.5) and (4.6) can be simplified to:

$$z_{WFE\ RMS} = \left(\frac{1}{n_{rays}} \left(y^T V_3 \Sigma_3^T \Sigma_3 V^T y \right) \right)^{1/2} = \left(\frac{1}{n_{rays}} \left(y^T \tilde{K}_3^T \tilde{K}_3 y \right) \right)^{1/2} \tag{4.40}$$

$$z_{WFE\ LOS} = \left(\frac{1}{2} \left(y^T V_1 \Sigma_1^T \Sigma_1 V_1^T y \right) \right)^{1/2} = \left(\frac{1}{2} \left(y^T \tilde{K}_1^T \tilde{K}_1 y \right) \right)^{1/2} \tag{4.41}$$

where we have introduced the notion of "surrogate" linear sensitivity matrices $\tilde{K}_3$ and $\tilde{K}_1$, which are defined as follows:

$$\begin{aligned} \tilde{K}_3 &= \Sigma_3 V_3^T \\ \tilde{K}_1 &= \Sigma_1 V_1^T \end{aligned} \tag{4.42}$$

According to this definition the dimensionality of the surrogate linear sensitivity matrices is still (mxn)=(mxn)x(nxn). The advantage is gained when we realize that the submatrix Σ_0 of the singular value matrix Σ, see equation (3.2), contains only zeros and does not contribute to the result. Thus we substitute $\Sigma_{1,i}$ for Σ_ι (i = 1,3) in the above Equations and obtain:

$$\begin{aligned} \overline{K}_3 &= \Sigma_{1,3} V_3^T \\ \overline{K}_1 &= \Sigma_{1,1} V_1^T \end{aligned} \tag{4.43}$$

these are the "surrogate" linear sensitivity matrices, which we will use for our disturbance analysis. A distinction has to be made between K_3 and K_1. In the baseline case of K_3 (WFE linear sensitivities), we have reduced a 1845x74 matrix K_3 to a 74x74 matrix $\overline{K}_3$, which will lead to a significant improvement in computation time. The matrix $\overline{K}_1$ however is still 2x74, like the original matrix. The reason for this is that the number of outputs (m=2) in this case is smaller than the number of inputs (n=74). Therefore the advantages of the SVD will only come into effect if m > n. It shall be noted that the results for the "non-RMS" quantities according to 4.12 are not identical to the ones computed in 4.24 and 4.25:

$$z_1 = K_3 y \neq \overline{z}_1 = \overline{K}_3 y \tag{4.44}$$

The following transcript of a MATLAB session is intended to support the above development with a specific example:

```
% Start of MATLAB 5.2 diary session
load linoptpp  % Load linear optics model
K1=dcdu; % define linear sensitivity matrix for centroid
K3=dwdu; % define linear sensitivity matrix for wavefront
```

```
whos
  Name       Size          Bytes  Class
  K1         2x74           1184  double array
  K3      1845x74        1092240  double array

Grand total is 136678 elements using 1093424 bytes
%(Note: all other variables have been cleared from workspace)

% Do singular value decompositions

[U1,S1,V1]=svd(K1);
[U3,S3,V3]=svd(K3);

S1_1=S1 (1:2,1:74);    % Extract the nonzero submatrix of S1
S1_3=S3(1:74,1:74);    % Extract the nonzero submatrix of S3
K1_bar=S1_1*V1';       % Define surrogate matrix for K1
K3_bar=S1_3*V3';       % Define surrogate matrix for K3

clear S1 S3 U1 U3 V1 V3 S1_1 S1_3

whos

  Name           Size          Bytes  Class

  K1             2x74           1184  double array
  K1_bar         2x74           1184  double array
  K3          1845x74        1092240  double array
  K3_bar        74x74          43808  double array

Grand total is 142302 elements using 1138416 bytes
(Note: It is seen that K3_bar is significantly smaller than K3)

y=randn(74,1);   % create a random displacement vector
nrays=length(K3)
nrays = 1845          % determine the number of rays used by MACOS
% Compute RMS values both ways and compare results
%
RMS_WFE_old=sqrt((1/nrays)*(y'*K3'*K3*y))
RMS_WFE_old =  6.6580e+000
RMS_WFE_svd=sqrt((1/nrays)*(y'*K3_bar'*K3_bar*y))
RMS_WFE_svd =  6.6580e+000


RMS_LOS_old=sqrt((1/2)*(y'*K1'*K1*y))
RMS_LOS_old =  3.2031e+002
RMS_LOS_svd=sqrt((1/2)*(y'*K1_bar'*K1_bar*y))
RMS_LOS_svd =  3.2031e+002

diary off
```

The above session demonstrates the benefits by showing that the surrogate linear sensitivity matrix $\overline{K}_3$ is only 74x74, which is significantly smaller than K3. The time to compute (74+2)*6 transfer functions versus (1845+2)*6 transfer functions in the baseline case should be shorter by a factor of roughly 25. There is however an overhead, which is introduced due to the computation of the SVD for the sensitivity matrices. The next section is intended to corroborate these claims for the baseline NGST frequency domain analysis.

The benefits of SVD for linear optics matrices are proven with a sample case. The sample case assumes that a 6x6 spectral disturbance matrix $S_{ww}(\omega)$ for the RWA disturbances has been computed previously. Furthermore the system is modeled according to the block diagram in Figure 4.1, whereby the closed loop state equations as defined in Equation 4.14 are applicable. *Case A* is defined to be the baseline analysis with the full linear sensitivity matrices (K_1=2x74, K_3=1845x74), where *Case B* uses the surrogate matrices ($\overline{K}_1$=2x74, $\overline{K}_3$=74x74), which are substituted into the closed loop equations in the following manner:

$$\begin{aligned} \overline{K}_1 &= \left[\overline{K}_{11} \quad \overline{K}_{12} \right] \\ \overline{K}_3 &= \left[\overline{K}_{31} \quad \overline{K}_{32} \right] \end{aligned} \tag{4.45}$$

From the two expressions above, we actually only substituted $\overline{K}_{31}$ and $\overline{K}_{32}$ into the equations for K_{31} and K_{32}, because erroneous results were obtained if $\overline{K}_{11}$ and $\overline{K}_{12}$ were substituted in equation 4.12. This has to do with the fact that $\overline{K}_1$ is utilized in the FSM loop and the substitution for K_1 is only legal, when "RMS" quantities are computed, but not within the feedback loop. The resulting closed loop "surrogate" system has only 76 outputs and 74 inputs. The RMS WFE power spectral density and cumulative RMS curve for *Case B* are shown in Figure 4.2. The RMS LOS power spectral density and cumulative RMS curve for Case B are shown in Figure 4.3.

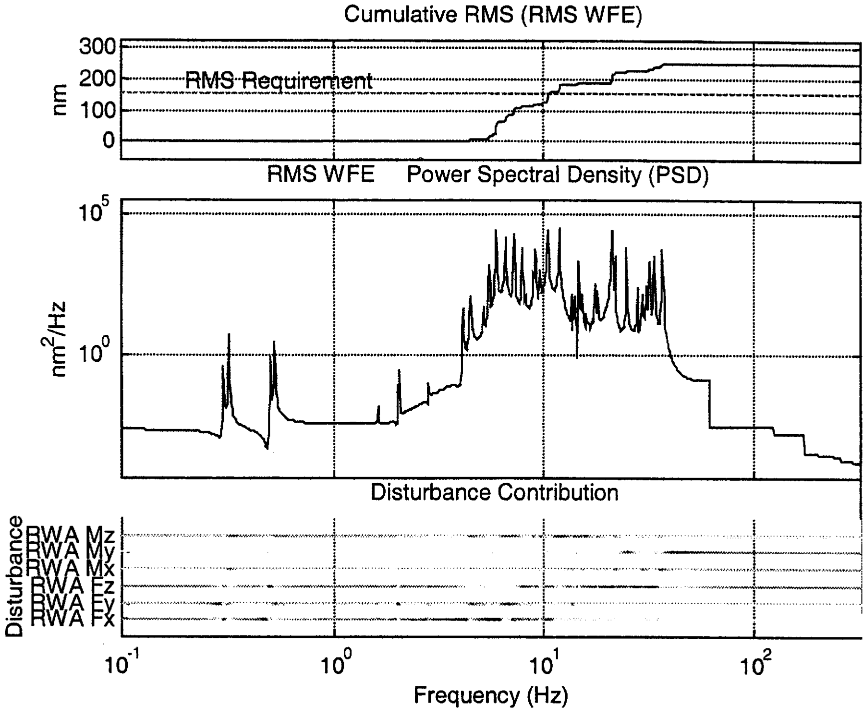

Figure 4.2: RMS WFE power spectral density (middle) and cum. RMS plot (top) for Case B

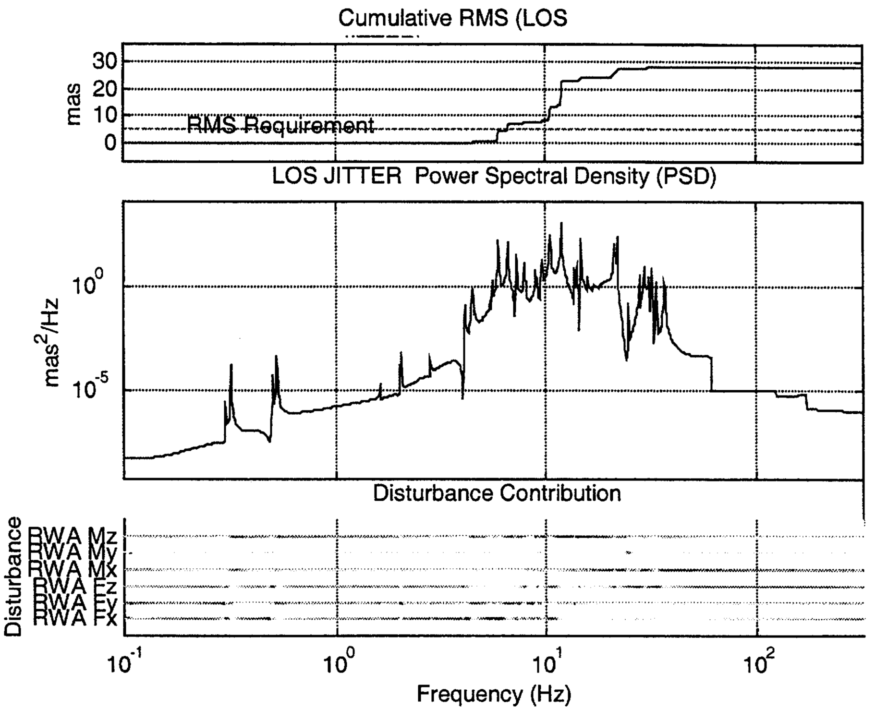

Figure 4.3: RMS LOS power spectral density (middle) and cum. RMS plot (top) for Case B

The RMS WFE and RMS LOS results for Case A and Case B are summarized in Table 4.1. It can be seen that the RMS WFE and RMS LOS results are identical, as expected. This disturbance analysis was carried out with the function `dist_analysis.m`, which is described in [24]. The big difference between Cases A and B becomes apparent, when considering the CPU times necessary for both solutions. The CPU times for Case B with singular value decomposition is significantly faster. The CPU time savings is roughly equivalent to a factor r

$$r = \frac{n_{rays}}{n_{inp}} \tag{4.46}$$

where n_{rays} is the number of rays used to model the optics and n_{inp} is the number of input degrees of freedom into the closed loop system. In our case the savings should be roughly equivalent to a factor of r = 1845/74 = **25**.

Table 4.1: Comparison of PSD analysis for NGST between Case A and B

Case	RMS WFE	RMS LOS	CPU time[13]	SVD time	Total time
A (Full K_3)	250 nm	28.2 mas	3951.72 sec	0 sec	3951.72 sec
B (SVD $\bar{K}_3$)	250 nm	28.2 mas	113.16 sec	19.04 sec	132.2 sec

The actual savings are slightly different than the factor r may suggest. The reasons are the overhead of computations, which are common to both cases - regardless of the size of the K's, the CPU time to perform the SVD in Case B and losses in Case A if swapping is necessary due to a shortage of RAM. The actual CPU timesaving, as determined from Table 4.1, is on the order of a factor 29.9. The accuracy of the RMS results has also been demonstrated: both Case A and B yield the same performance values.

This section has demonstrated that the theory of singular value decomposition (SVD) can be applied to the linear sensitivity matrices of the NGST optics. This allows the introduction of "surrogate" sensitivity matrices, which are of smaller dimension than the full sensitivity matrices

---

[13] Computations were executed on snipe.gsfc.nasa.gov

from MACOS. The maximum dimension of a surrogate matrix $\overline{K}_i$ is nxn, where n is the number of input degrees of freedom from the FEM and the FSM. As a consequence a significant savings in CPU time can be achieved when computing RMS values. Caution has to be applied if values other than RMS are computed or when the product of a multiplication with a K_i matrix is used in a feedback loop. In the future this methodology will support the frequency domain analysis, even if the number of rays modeled increases rapidly (e.g. over 10,000) with increasing fidelity of the NGST design. It will allow avoiding "out-of-memory" conditions and permit the incorporation of WFE computations in the Simulink-based time domain simulations. For those time simulations, the WFE had to be post-processed up to now due to the large computational effort.

Chapter 5

Sensitivity Analysis

The goal of the sensitivity analysis in a broad sense is to understand which parameters of the integrated model most influence the performance metrics computed in Chapter 3. We hope to derive useful information for the performance improvement step from this. In a narrow sense the sensitivity analysis seeks to compute the slope of the RMS metrics with respect to modal or physical parameters of the system. In Chapter 3 we computed the nominal RMS performance of the system. In this chapter we are trying to understand the internal parameters of the model that drive the performance. This is the key step in gaining the necessary knowledge in order to improve system performance. Again we illustrate the process with the sample 3DOF problem before analyzing the full order NGST model. This chapter also creates the link between the critical frequencies of the system and a physical understanding of the modes that are involved.

5.1 Sensitivity Analysis for 3 DOF sample problem

The purpose of the sensitivity analysis is to determine the sensitivity of the RMS performance with respect to parameters of the integrated model, i.e. $\partial\sigma_z/\partial p_i$. We are looking for the first order partial derivative of the RMS with respect to a parameter of the system. The magnitude and sign of this sensitivity gives useful information for an uncertainty analysis or to point the systems engineer toward promising performance enhancement options. Currently, modal parameters (frequency, damping ratio and modal mass) or physical parameters (masses, stiffnesses) of the structural plant are implemented in the sensitivity analysis framework. In order to compare sensitivities of different parameters to various performance metrics, it is necessary to normalize the sensitivities as follows:

$$ns_{p_i} = \frac{p_i^{nom}}{\sigma_z^{nom}} \cdot \frac{\partial \sigma_z}{\partial p_i} \tag{5.1}$$

where p_i^{nom} is the nominal value of the i-th parameter, σ_z^{nom} is the RMS performance of the performance z and $\partial\sigma_z/\partial p_i$ is the partial derivative of the RMS performance of z with respect to the i-th parameter. The resulting normalized sensitivity ns_{p_i} can be interpreted as the % change in the RMS for a 1 % change in the parameter at the nominal RMS level. This interpretation is only valid for a small % change of the parameter. For the 3DOF sample problem, three different methods for obtaining the sensitivities are analyzed. The first method is also conceptually the easiest to understand. If a closed-form symbolic expression for the RMS as a function of all desired parameters is available, we can simply compute the first partial derivative of the RMS with respect to the desired parameter p_i.

$$\frac{\partial\sigma_z}{\partial p_i}=\frac{\partial\sigma_z(p_i)}{\partial p_i} \tag{5.2}$$

Alternatively, if such an expression is not available we may compute the Lagrangian of the variance (RMS squared).

$$\left(\sigma_z^2\right)^* = C_z\Sigma_q C_z^T + tr\left\{L\left(A_{zd}\Sigma_q + \Sigma_q A_{zd}^T + B_{zd}B_{zd}^T\right)\right\} \tag{5.3}$$

where σ_z is the RMS of the performance z, ( )* denotes the Lagrangian, $\mathbf{C_z}$ is the performance **C** matrix, $\Sigma_\mathbf{q}$ is the state covariance matrix, tr { } denotes the trace operator, $\mathbf{A_{zd}}$ and $\mathbf{B_{zd}}$ are the closed loop appended state space system matrices and **L** is the Lagrange multiplier matrix. The Lagrangian contains the expression $\mathbf{C}\Sigma_\mathbf{q}\mathbf{C}^\mathbf{T}$ that we are trying to take the derivative of, subject to a constraint, which corresponds to the Lyapunov equation for the state covariance matrix $\Sigma_\mathbf{q}$. Thus two Lyapunov equations have to be solved: one for the state covariance matrix $\Sigma_\mathbf{q}$ and one for the Lagrange multiplier matrix **L** according to Gutierrez [24]:

$$A_{zd}\Sigma_q + \Sigma_q A_{zd}^T + B_{zd}B_{zd}^T = 0 \tag{5.4}$$

$$LA_{zd} + A_{zd}^T L + C_z^T C_z = 0 \tag{5.5}$$

These results are then substituted into the governing sensitivity equation. This is the key equation for the sensitivity analysis, since it is applicable regardless of whether we are trying to compute sensitivities with respect to modal or physical parameters:

$$\frac{\partial \sigma_z^2}{\partial p} = tr\left[\Sigma_q \frac{\partial \left(C_z^T C_z\right)}{\partial p}\right] + tr\left[L\left\{\frac{\partial A_{zd}}{\partial p}\Sigma_q + \Sigma_q \frac{\partial A_{zd}^T}{\partial p} + \frac{\partial \left(B_{zd} B_{zd}^T\right)}{\partial p}\right\}\right] \tag{5.6}$$

Also we see that the partial derivatives of the system matrices $\mathbf{A}_{zd}$, $\mathbf{B}_{zd}$ and $\mathbf{C}_{zd}$ need to be computed before getting the final answer for the RMS sensitivity. This is where the fundamental difference in the difficulty level between modal and physical parameter sensitivity lies. If the parameters of interest appear explicitly in $\mathbf{A}_{zd}$, $\mathbf{B}_{zd}$ and $\mathbf{C}_{z}$, then we can directly obtain the partial derivatives of those matrices. This is the case for modal parameters. If they only appear implicitly additional steps are necessary. The third method for the sample problem is to proceed numerically and to use the existing `sens_analysis.m` and `sens_analysis_phys.m` framework. We will first focus on the modal sensitivity analysis.

The main characteristic of the modal parameter sensitivity analysis is that the modal parameters ω, ζ and m all appear explicitly in the state space system matrices $\mathbf{A}_{zd}$, $\mathbf{B}_{zd}$, $\mathbf{C}_{zd}$ and $\mathbf{D}_{zd}$, so that the partial derivatives can be taken directly,

$$p_1 = \omega_3, \quad p_2 = \zeta_3, \quad p_3 = \tilde{m}_3 \tag{5.7}$$

where p_1 is the modal frequency of mode 3, p_2 is the modal damping ratio of mode 3 and p_3 is the modal mass of mode 3. Experience shows that modes that show a large sensitivity with respect to the modal frequency are usually also the modes that contribute the most to the RMS [24]. In other words, these are also the modes that exhibit large steps in the corresponding cumulative RMS curves as shown in Chapter 3.

The most convenient method is direct partial differentiation if a closed form expression for the RMS value of the corresponding variance (= square of RMS) is available. The starting point is the closed form expression for the variance. Equation (5.8) gives the expression for the open loop variance of the OPD in the sample problem:

$$\sigma_z^2 = \frac{s_c^2\left(2\zeta_3\omega_3\omega_{RO} + \omega_{RO}^2\right)}{16\zeta_3 m^2\omega_3^2\left(\omega_3^2 + 2\zeta_3\omega_3^2\omega_{RO} + \omega_{RO}^2\right)} \tag{5.8}$$

Then the partial derivative with respect to ω_3 is taken as follows:

$$\frac{\partial\sigma_z^2}{\partial\omega_3} = \frac{\omega_{RO}}{8m^2\omega_3^2\Gamma} - \frac{3\left(\omega_{RO}^2 + 2\zeta_3\omega_3\omega_{RO}\right)}{m^2\zeta_3\omega_3^4\Gamma} - \frac{\left(\omega_{RO}^2 + 2\zeta_3\omega_3\omega_{RO}\right)\left(\omega_3 + \zeta_3\omega_{RO}\right)}{8m^2\zeta_3\omega_3^3\Gamma^2} \tag{5.9}$$

where the expression Γ stands for

$$\Gamma = \left(\omega_3^2 + 2\zeta_3\omega_3\omega_{RO} + \omega_{RO}^2\right) \tag{5.10}$$

Now we have obtained the partial derivative with respect to the variance σ_z^2, but we wish to obtain the partial derivative with respect to the RMS value σ_z. With the help of the calculus rule for the derivative of the square of a function we obtain the derivative of the RMS with respect to the parameter p_1,

$$\frac{\partial\sigma_z}{\partial\omega_3} = \frac{1}{2\sigma_z}\frac{\partial\sigma_z^2}{\partial\omega_3} \tag{5.11}$$

The last step involves the normalization with respect to the nominal parameter and RMS values,

$$ns_{\omega_3} = \frac{\omega_3}{\sigma_z}\cdot\frac{\partial\sigma_z}{\partial\omega_3} \tag{5.12}$$

Substituting the numerical values of the sample problem parameters into Equation (5.12), we compute a normalized sensitivity of the RMS OPD with respect to the third modal frequency ω_3

of $ns_{\omega 3} = -1.62$. This means that in the vicinity of the nominal modal frequency, a 1% increase in that frequency will lead to a 1.62% decrease of the RMS OPD, which is desirable. How can we explain this sensitivity based on the physics of the problem? Increasing the modal frequency ω_3 has a similar effect than what the controller is doing to the poles of the third mode. By increasing ω_3 we push the resonant peak further into the rolloff region of the LPF disturbance, which reduces the total RMS and also reduces its static response. The sensitivity with respect to the damping ratio of the third mode is obtained in an analogous fashion and results in a normalized sensitivity of $ns_{\zeta 3} = -0.4998$, which is not surprising either. It is expected that damping ratios will always have negative sensitivities, since increasing damping should always reduce the resulting RMS value. This effect however is less pronounced if the plant is already heavily damped. Another method for obtaining the modal sensitivities is the function `sens_analysis.m` that was developed by Gutierrez [24]. The plot in Figure 5.1 shows the normalized sensitivities with respect to the modal parameters of the sample problem.

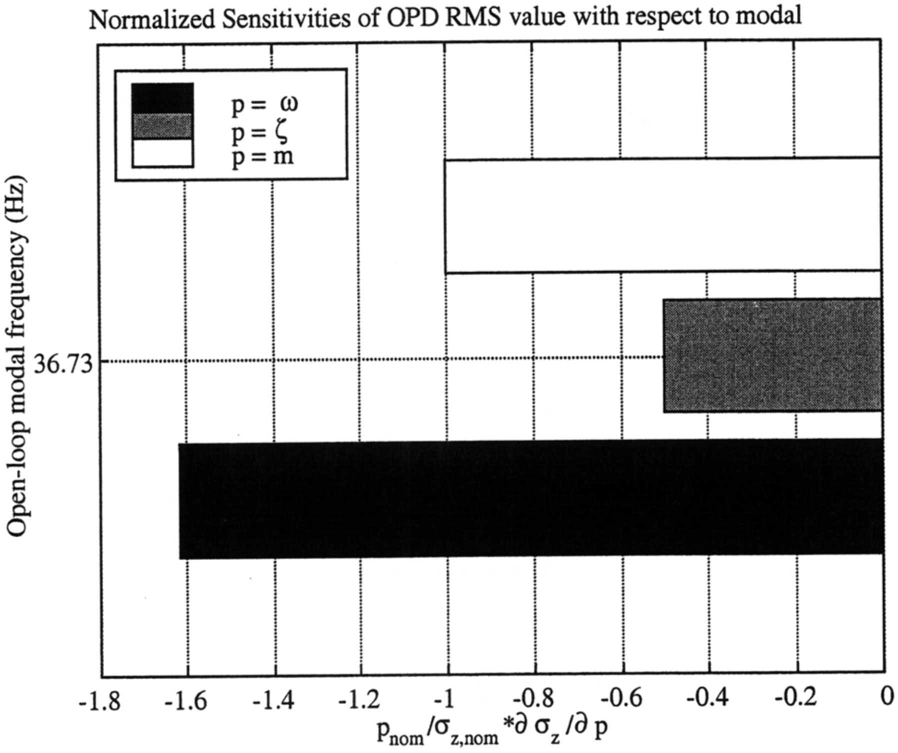

Figure 5.1: Normalized sensitivities with respect to modal parameters (sample problem)

The use of the function `sens_analysis.m` is intended for the modal parameter sensitivity only. We need to give the state space representation of the open or closed loop plant with the disturbance dynamics appended as an input to the function. Additionally we specify which modes we are interested in, since it would be very time-consuming to compute the sensitivities for every mode in a large order model. In our sample problem the only mode of interest is mode 3 since the other modes are not observable. The general idea is that the modes that are critical to the RMS performance have been previously computed in the frequency domain disturbance analysis (Chapter 3). Thus we can compute the sensitivities only with respect to the critical frequencies. In the sample problem we know that only mode 3 at 36.73 Hz contributes to the RMS.

The sensitivities with respect to modal frequency, damping ratio and modal mass are returned and plotted on a bar chart like the one in Figure 5.1. A negative sensitivity means that an increase in the modal parameter value will lower the RMS, which is usually desired. It is expected that the sensitivities for modal damping will always be negative. As a mode becomes more and more damped (and approaches the backbone of a given transfer function) the sensitivity will become smaller and smaller in magnitude. It is also possible to compute the modal sensitivities with finite differencing. This simply means recomputing the RMS with the modified parameters and computing the slope as the secant from the nominal to the changed value. This is only valid for small perturbations. According to Gutierrez the finite difference method is also not reliable for large order models [24]. A comparison of results obtained with the different methods is shown in Table 5.1:

Table 5.1: Comparison of modal sensitivity results (sample 3DOF problem)

Parameter / Method used	Open Loop System	Closed Loop System
$\partial \sigma_z / \partial \omega_3$ symbolically	-1.62027522	-0.10406083
$\partial \sigma_z / \partial \omega_3$ finite difference	-1.598337842	*-1.491337273*
$\partial \sigma_z / \partial \omega_3$ sens_analysis.m	-1.618252405	*-1.694645285*
$\partial \sigma_z / \partial \zeta_3$ symbolically	-0.500407977	-0.0929866636
$\partial \sigma_z / \partial \zeta_3$ finite difference	-0.49606531	-0.09542462121
$\partial \sigma_z / \partial \zeta_3$ sens_analysis.m	-0.499783248	-0.09298343267

This table shows a comparison of the modal sensitivity analysis for our 3DOF sample problem. We see that the RMS performance has a strong negative sensitivity with respect to the open-loop structural frequency, ω_3. This is not surprising since the frequency is at 36.73 Hz and the disturbance rolloff frequency ω_{RO} is 100 Hz. Increasing the frequency ω_3 will thus lower the RMS because the resonance is then pushed further into the rolloff region of the disturbance. The open loop results for modal frequency and damping match well for all three methods. The finite difference result was computed with a perturbation of 1% of the parameters. In the closed loop case we have a good match for the closed loop modal damping. There is however a discrepancy in the modal frequency sensitivity. The correct expected sensitivity is given by the direct differentiation method (-0.104). We see that the closed loop RMS is much less sensitive to ω_3 than in the open loop case. The answers from `sens_analysis.m` did however not match. An investigation revealed that `sens_analysis.m` indeed works correctly, but that it expects the compensator state space model to be in " strictly proper, linear form" [24]. Hence the detected discrepancy is due to the presence of the feedthrough term $\mathbf{D_c}$ (due to the PD-controller), which is not allowed by the `sens_analysis.m` framework. This problem could be resolved by adding a high frequency pole to the controller to ensure rolloff and a strictly proper controller transfer function. This would however add one more state to the controller and make paper and pencil computations more cumbersome.

5.2 Physical parameter sensitivities for sample problem

The physical parameter sensitivity is somewhat more useful and intuitive than the modal parameter sensitivity. This is due to the fact that the parameters are directly related to the finite element model or the entries of the mass and stiffness matrix in the case of our sample problem. It must be noted that this feature also complicates the computation of the physical parameter sensitivities, since the system matrices $\mathbf{A_{zd}}$, $\mathbf{B_{zd}}$ and $\mathbf{C_{zd}}$ only contain the physical parameters implicitly through the natural frequencies, modeshapes and modal masses. Therefore the eigenderivatives, i.e. derivatives of natural frequencies, modeshapes and modal masses with respect to the physical parameters of interest have to be computed:

$$\frac{\partial \omega}{\partial k}, \quad \frac{\partial \Phi}{\partial k}, \quad \frac{\partial \tilde{m}}{\partial k} \tag{5.13}$$

Again we start by invoking the governing sensitivity equation:

$$\frac{\partial \sigma_z^2}{\partial p} = tr\left[\Sigma_q \frac{\partial\left(C_z^T C_z\right)}{\partial p}\right] + tr\left[L\left\{\frac{\partial A_{zd}}{\partial p}\Sigma_q + \Sigma_q \frac{\partial A_{zd}^T}{\partial p} + \frac{\partial\left(B_{zd} B_{zd}^T\right)}{\partial p}\right\}\right] \tag{5.14}$$

Let us assume we choose the stiffness parameter k as the physical parameter of interest. Applying the chain rule in this case we obtain:

$$\frac{\partial A_{zd}}{\partial k} = \frac{\partial A_{zd}}{\partial \omega_3} \cdot \frac{\partial \omega_3}{\partial k} \tag{5.15}$$

Since the modal frequency derivatives have been previously computed, the physical parameter sensitivity can build on the modal sensitivities by applying the chain rule as shown above. In the sample case the eigenderivatives are not difficult to compute, since closed form expressions for the ω's, ϕ's and modal masses exist. Again the simplest method to find physical parameter sensitivities is to write the modal frequencies as a function of the physical parameters k and m. These are the only two physical parameters of the plant in our sample problem. Figure 5.2 depicts our 3DOF sample problem and shows that we only have two physical parameters: p_1 the stiffness and p_2 the mass parameter.

$p_1 = k$ spring stiffness [N/m]
$p_2 = m$ mass parameter [kg]

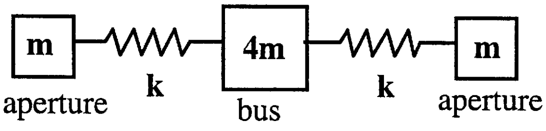

Figure 5.2: Physical parameters of the 3DOF sample problem

In the case of the RMS sensitivity to the stiffness k we can take the previously computed sensitivity of the RMS with respect to the natural frequency ω_3 (5.15):

$$\frac{\partial \sigma_z^2}{\partial \omega_3} = \frac{\omega_{RO}}{8m^2\omega_3^2\Gamma} - \frac{3\left(\omega_{RO}^2 + 2\zeta_3\omega_3\omega_{RO}\right)}{m^2\zeta_3\omega_3^4\Gamma} - \frac{\left(\omega_{RO}^2 + 2\zeta_3\omega_3\omega_{RO}\right)\left(\omega_3 + \zeta_3\omega_{RO}\right)}{8m^2\zeta_3\omega_3^3\Gamma^2} \tag{5.16}$$

where

$$\Gamma = \left(\omega_3^2 + 2\zeta_3\omega_3\omega_{RO} + \omega_{RO}^2\right) \tag{5.17}$$

Then we apply the chain rule, since the natural frequency of the third mode was computed to be equal to (see Equation 2.12):

$$\omega_3 = \sqrt{\frac{3m}{2k}} \tag{5.18}$$

and

$$\frac{\partial \omega_3}{\partial k} = \sqrt{\frac{3}{2m}} \cdot \left(\frac{1}{2}\right) \cdot \frac{1}{\sqrt{k}} = \sqrt{\frac{3}{8mk}} \tag{5.19}$$

Thus we multiply by the partial derivative of the natural frequency ω_3 with respect to k and we normalize to obtain the normalized physical sensitivity with respect to k.

$$\frac{\partial \sigma_z}{\partial k} = \frac{1}{2\sigma_z} \cdot \frac{\partial \sigma_z^2}{\partial k} = \frac{1}{2\sigma_z} \cdot \frac{\partial \sigma_z^2}{\partial \omega_3} \cdot \frac{\partial \omega_3}{\partial k} \tag{5.20}$$

We get the final answer with normalization as follows:

$$ns_k = \frac{k_{nom}}{\sigma_z^{nom}} \cdot \frac{\partial \sigma_z}{\partial k} = -0.80913 \tag{5.21}$$

In the case of the sensitivity with respect to the mass m we have to be more careful. This is because m also appears in the closed form expression for the RMS outside of ω_3 and the same approach as for k would lead to an erroneous result. Here the procedure is to find the functional dependency of all modal parameters on *m* and to substitute into the original expression for the RMS. Then the first partial derivative with respect to *m* can be taken without applying the chain rule. This method assumes that a closed form symbolic expression for the RMS is available.

The second approach for finding the physical parameter sensitivities for the 3 DOF sample problem is the symbolic approach. The symbolic approach first solves the two Lyapunov equations for the state covariance matrix Σ_q and the Lagrange multiplier matrix **L** analytically. This involves solving a linear system of n(n+1)/2 for each Lyapunov equation, where n is the number of states in the overall state space system. These two Lyapunov equations are given as:

$$A_{zd}\Sigma_q + \Sigma_q A_{zd}^T + B_{zd}B_{zd}^T \tag{5.22}$$

$$LA_{zd} + A_{zd}^T L + C_z^T C_z = 0 \tag{5.23}$$

the analytical solution for the state covariance matrix for example is then obtained as:

$$\Sigma_q = \begin{bmatrix} \dfrac{1}{2\omega_{RO}} & \dfrac{-1}{2\sqrt{12m\Gamma}} & \dfrac{-\omega_{RO}}{2\sqrt{12m\Gamma}} \\ \dfrac{-1}{2\sqrt{12m\Gamma}} & \dfrac{\omega_{RO}^2 + 2\zeta_3\omega_3\omega_{RO}}{48m\zeta_3\omega_3^3\Gamma} & 0 \\ \dfrac{-\omega_{RO}}{2\sqrt{12m\Gamma}} & 0 & \dfrac{\omega_{RO}^2}{48m\zeta_3\omega_3\Gamma} \end{bmatrix} \tag{5.24}$$

Then the eigenderivatives are computed analytically as shown below. These are used to compute the partial derivatives of the system matrices $\mathbf{A_{zd}}$, $\mathbf{B_{zd}}$ and $\mathbf{C_{zd}}$.

$$d\Lambda = \begin{bmatrix} \dfrac{\partial\omega_1^2}{\partial p_1} & \dfrac{\partial\omega_2^2}{\partial p_1} & \dfrac{\partial\omega_3^2}{\partial p_1} \\ \dfrac{\partial\omega_1^2}{\partial p_2} & \dfrac{\partial\omega_2^2}{\partial p_2} & \dfrac{\partial\omega_3^2}{\partial p_2} \end{bmatrix} = \begin{bmatrix} 0 & \dfrac{1}{m} & \dfrac{3}{2m} \\ 0 & \dfrac{-k}{m^2} & \dfrac{-3k}{2m^2} \end{bmatrix} \tag{5.25}$$

$$dm = \begin{bmatrix} 0 & 0 & 0 \\ 0 & 0 & 0 \end{bmatrix} \tag{5.26}$$

$$d\Phi=\begin{bmatrix}\frac{\partial\phi_1}{\partial k} & \frac{\partial\phi_2}{\partial k} & \frac{\partial\phi_3}{\partial k} & \frac{\partial\phi_1}{\partial m} & \frac{\partial\phi_2}{\partial m} & \frac{\partial\phi_3}{\partial m}\end{bmatrix}=$$

$$\begin{bmatrix}0 & 0 & 0 & \frac{-1}{2\sqrt{6}m^{3/2}} & \frac{-1}{2\sqrt{2}m^{3/2}} & \frac{-2}{2\sqrt{12}m^{3/2}} \\ 0 & 0 & 0 & \frac{-1}{2\sqrt{6}m^{3/2}} & 0 & \frac{1}{2\sqrt{12}m^{3/2}} \\ 0 & 0 & 0 & \frac{-1}{2\sqrt{6}m^{3/2}} & \frac{1}{2\sqrt{2}m^{3/2}} & \frac{-2}{2\sqrt{12}m^{3/2}}\end{bmatrix} \tag{5.27}$$

Once this has been completed all the results are entered into the governing sensitivity Equation 5.14 and the physical parameter sensitivities are calculated analytically. The actual numbers for the system parameters are only substituted at the very end of this process.

As a third option the physical parameter sensitivities can be computed with the help of the function `sens_analysis_phys.m`. This requires that most system matrices that were used to define the state space system such as $\boldsymbol{\beta}_{\mathbf{u}}$, $\boldsymbol{\beta}_{\mathbf{w}}$, $\mathbf{C}_{\mathbf{yx}}$ and $\mathbf{C}_{\mathbf{zx}}$ must be available as inputs. Furthermore the eigenderivatives have to be provided to the function. These can be computed via different methods external to the `sens_analysis_phys.m` function. Tools for spring elements (celas) or beam elements (beam) have been made available [24]. These tools use Nelson's method and have been developed by Kenny and Gutierrez . The function loops over the frequencies and degrees of freedom of interest. Again there is a possibility to only include the critical modes in order to speed up computation times. The function produces bar charts to show the normalized sensitivities to physical parameters Figure 5.3

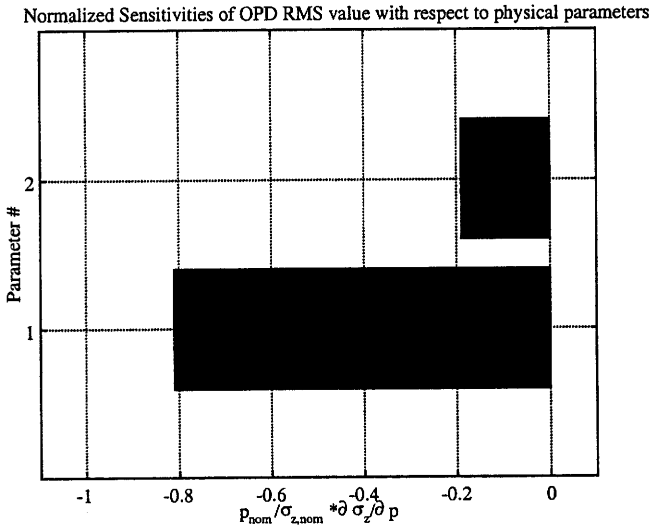

Figure 5.3: Normalized physical parameter sensitivities (p#1= k, p#2 = m)

In our sample problem we care about the spring stiffness *k* (parameter#1) and the mass parameter *m* (parameter #2). Table 5.2 shows a comparison for the physical parameter sensitivities with respect to the open loop system. The physical parameter sensitivities with respect to the closed loop system were not computed due to the existence of the feedthrough term $\mathbf{D_c}$.

Table 5.2: Physical parameter sensitivities (comparison for sample problem)

Method used	**Parameter k**	**Parameter m**
Direct differentiation	-0.8091262023	-0.1908737977
Symbolic solution (2 Lyap)	-0.8091262023	-0.1908737977
sens_analysis_phys.m	-0.8091262023	-0.1914986026

The three methods show good match for the physical parameter sensitivities in the open loop case. This analysis requires the solution of two Lyapunov equations for Σ_q and L, as well as the computation of the eigenderivatives. Note: a closed loop physical parameter comparison has not been done due to the existence of the $\mathbf{D_c}$ term. The table shows that we have nearly perfect agreement for the physical sensitivities using the three different methods. The two symbolic approaches (direct differentiation and full symbolic derivation with solution of $\mathbf{L}$ and Σ_q) yield exactly the same result as expected. This sensitivity analysis gave useful information for the performance improvement phase.

5.3 NGST Sensitivity Analysis

In Chapter 3 we have identified the critical frequencies of the system based on the modal contributions to the cumulative RMS WFE and RMS LOS. Once we have identified the critical modes of the system we first retrieve these modes and analyze the dynamic behavior using modeshape animations (`xview.m`). Along with the modeshapes, the analyst is interested in understanding the modal strain energy distribution for those critical modes. The strain energy is broken into the main structural components of NGST and we can see which group participates significantly for a given critical mode of the system. For the RMS WFE the most critical modes were at 11.96, 12.72, 26.94 and 41.18 Hz and they are shown again in Figure 5.4

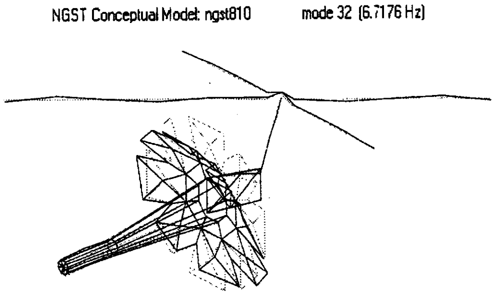

Mode 32 at **6.72 Hz**

This mode is characterized by pitch motion of the primary mirror, sunshield bending and secondary tower bending. It is a global mode.

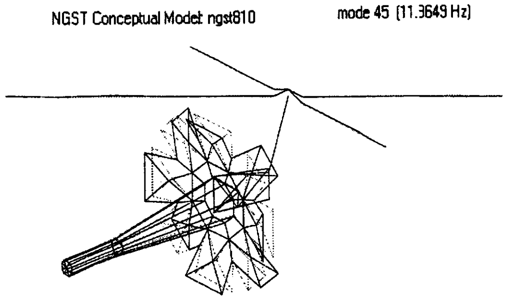

Mode 45 at **11.96 Hz**

Symmetric mode of the primary mirror with mirror petals bending forward and aft in opposite pairs.

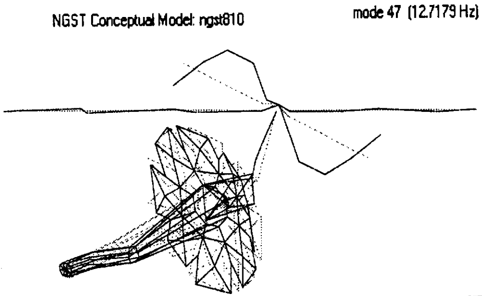

Mode 47 at **12.72 Hz**

Global pitch mode with OTA rotation about the spacecraft z-axis, secondary tower and isolation truss bending. Higher order sunshield bending.

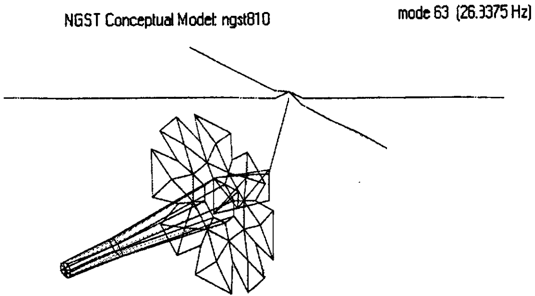

Mode 63 at **26.94 Hz**

Conic baffle mode with expansion and contraction of baffle in the radial direction. Expect high strain energy participation of baffle.

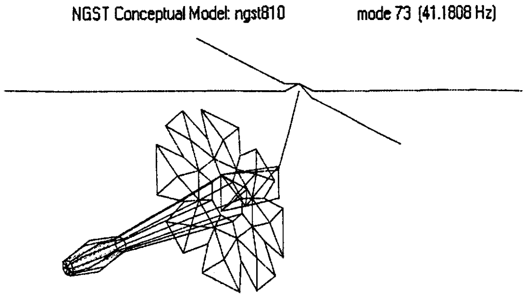

Mode 73 at **41.18 Hz**

Secondary tower higher order bending mode with the secondary tower blades bending inward and outward (radially) in a symmetric manner.

Figure 5.4: Analysis of critical modes for wavefront error

From the description of the critical modes on the right side of the above figure it is possible to deduce which element groups contribute significantly to the WFE RMS. There is however a more rigorous way to quantify this. First we define the element groups of the `ngst810` model. The groups are based on their function and structural design of the observatory; we distinguish between the element groups listed in Table 5.3.

Table 5.3: Element groups for NGST model

Element Group	Element Type	Element numbers
Primary Mirror	CQUAD4, CTRIA	1-40
Conic Baffle	CQUAD	41-48
ISIM	CBAR	49-54
Secondary Tower	CBAR	58-73
Secondary Mirror	CTRIA	74-81
Hexapod	CBAR	82-87
Isolation Truss	CBAR	91-94
Sunshield	CBAR	101-117

The relative participation of major element groups in the critical modes in terms of strain energy can give valuable information to the designer. The strain energy fraction of the *i*-th group of elements to the total strain energy of the *j*-th mode is defined as:

$$f_{i,j} = \frac{\sum_{i,j} group}{\frac{1}{2}\phi_j^T \mathbf{K} \phi_j} \tag{5.28}$$

where *group* is the group strain energy for a particular mode as computed with the MATLAB `groupse.m` function. Depending on the element type (plate, beam, rod) there will be contributions from bending, torsion, shear and tension or compression. The strain energy shown in Figure 5.5 shows the total relative contribution of each element group to a particular mode. This gives the designer useful information, since it points directly to the physical parameters in the system that need to be targeted for redesign. The strain energy distribution for the critical modes with respect to the wavefront error (WFE) is shown in Figure 5.5

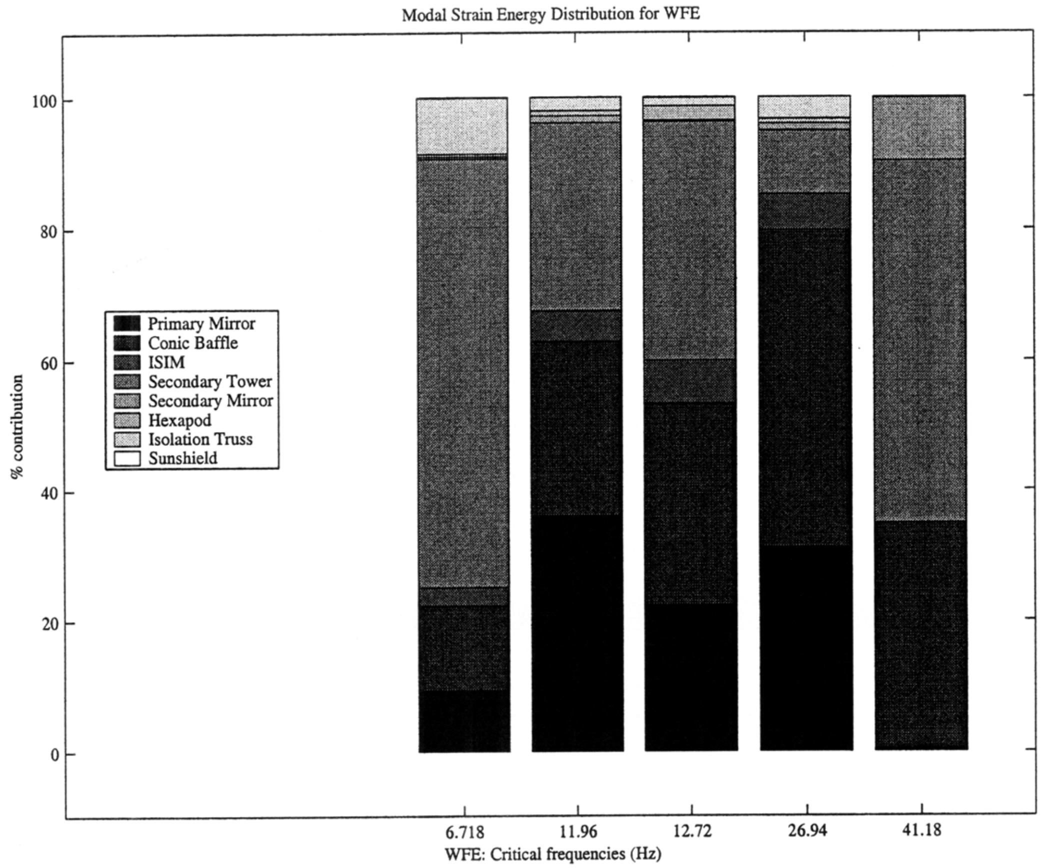

Figure 5.5: Strain energy distribution for WFE critical modes

The above figure shows that the secondary tower plays a very important role for the WFE, since it has significant strain energy contributions at virtually all modes. Also, the primary mirror petals contribute a large amount of strain energy with the exception of the mode at 6.72 Hz. This tells the system engineer that structural redesign of the secondary tower and the primary mirror petals (backup structure, latches) should be considered. It is also interesting to note that the sunshield flexibility does not significantly impact the WFE. We expect to see a larger contribution of the sunshield to the LOS error. At this point we do not yet know how to redesign the plant, since we do not know what the modal parameter sensitivities are. In an analogous way to the 3DOF sample problem, we compute the modal parameter sensitivities for the critical modes. The modal parameters are the modal frequency, damping ratio and modal mass. Figure 5.6. shows the results of the modal sensitivity analysis for the RMS WFE.

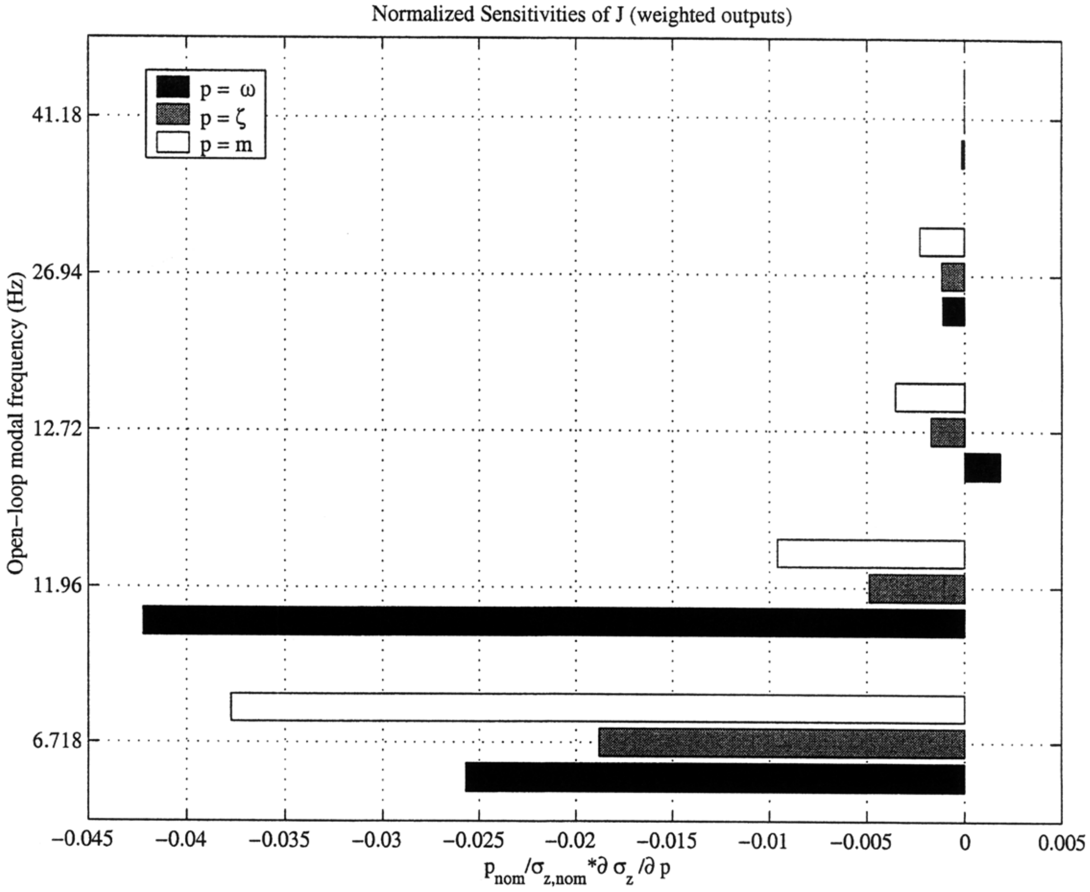

Figure 5.6: Modal Sensitivities of RMS WFE for critical modes

We can see that the performance is most sensitive to changes in the modes at 6.72 and 11.96 Hz. As expected, the sensitivity with respect to modal damping is negative. We should therefore strive to increase the amount of damping in the structure from the current value of ζ=0.001 (see Chapter 6). Furthermore we see that stiffening these two modes should lead to a decrease in the RMS WFE as well. Since the secondary tower has a significant strain energy contribution to these two modes (see Figure 5.5) this suggests that stiffening the secondary tower should improve the RMS WFE. In order to confirm this result a physical parameter sensitivity analysis on the secondary tower stiffness parameters should be conducted in the future.

The second metric of interest is the LOS jitter. Again we have already determined in Chapter 3 which of the flexible modes of the structural plant are critical to the LOS pointing performance of NGST. These modes are at 6.51, 7.15, 11.96 12.12 and 30.02 Hz, respectively. Again we analyze the modeshapes of these modes in Figure 5.7 (with exception of the mode at 12.12 Hz, since it was already discussed as a major contributor for the wavefront error).

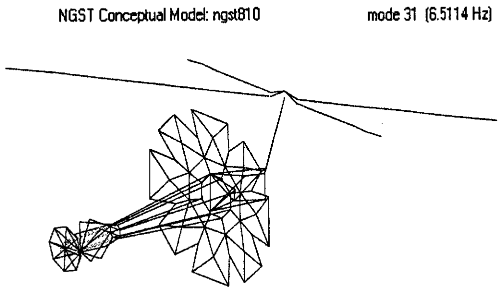

Mode 31 at **6.51 Hz**

Secondary Tower Mode including blade bending and torsion. Local mode since little participation from the rest of the structure.

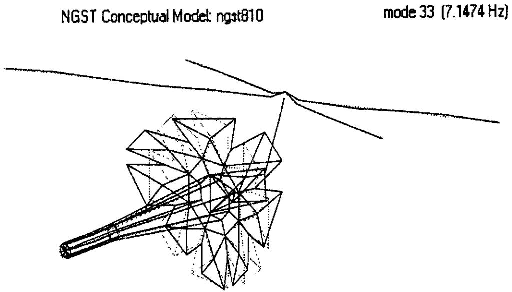

Mode 33 at **7.15 Hz**

Primary mirror asymmetric mode. Asymmetric bending of the primary mirror petals contributes to lateral centroid error.

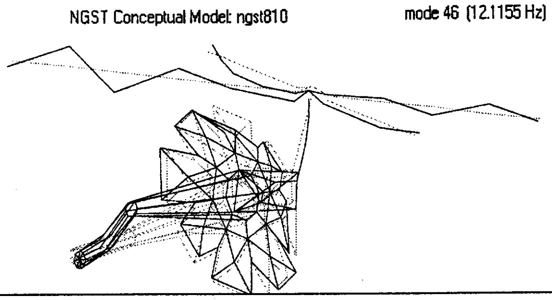

Mode 46 at **12.12 Hz**

Global pitch mode involving primary mirror pitch motion, secondary tower bending , isolation truss bending and sunshield bending. This is a mode of fundamental importance .

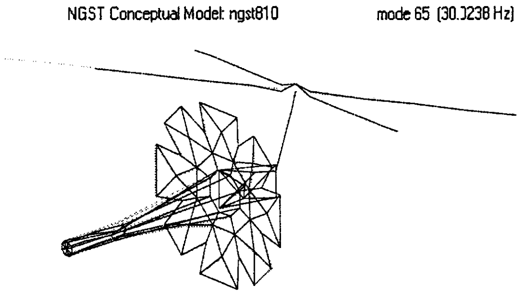

Mode 65 at **30.02 Hz**

This is a relatively indistinct mode involving baffle motion and secondary tower bending. Also there are axial contributions from the sunshield booms.

Figure 5.7: Analysis of critical modes for LOS jitter

Again we can compute the strain energy distribution for the modes that are critical for the RMS LOS in the same way as was done for the WFE. Figure 5.8 depicts the relative contribution of the element groups to the modal strain energy. It is very interesting to note that the contribution of the secondary tower is even more important for the pointing (LOS) than for the phasing (WFE). This is not surprising since we expect that even slight lateral motion of the secondary mirror will be very visible on the focal plane due to the optical magnification of the system.

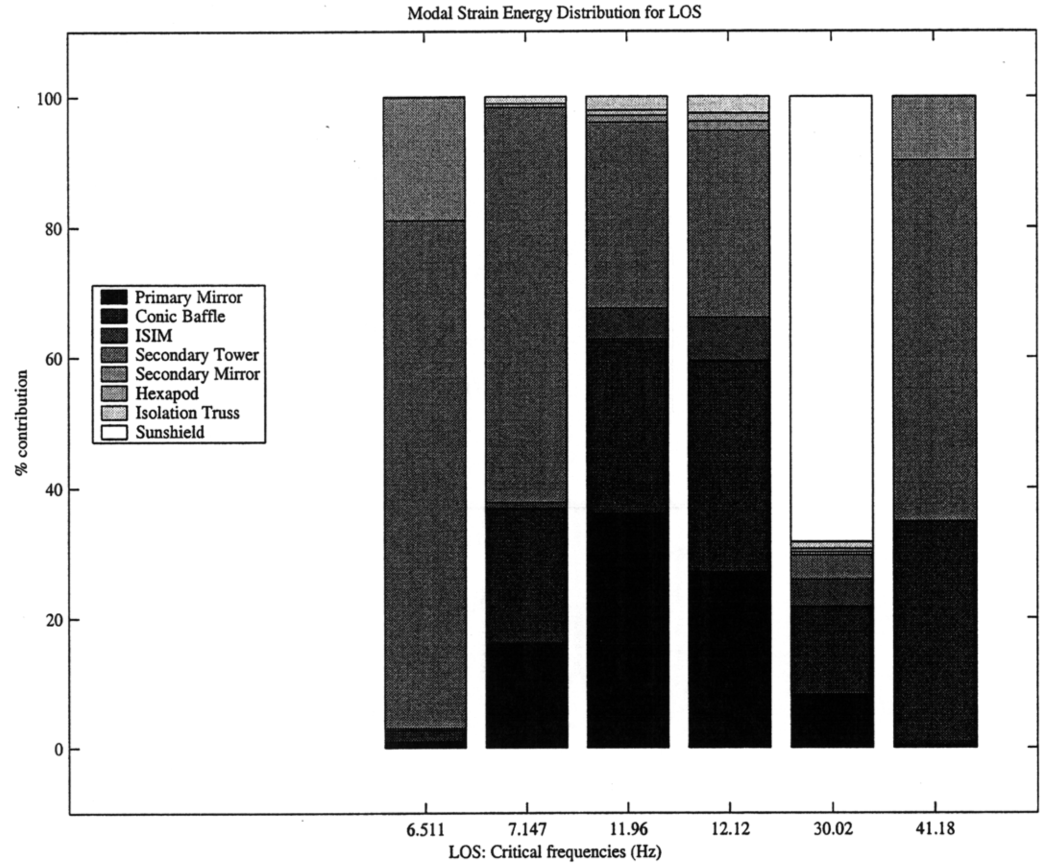

Figure 5.8: Strain energy distribution for LOS jitter critical modes

Again it is not necessarily evident what kind of redesign action should be considered based on these results. It is not always true that stiffening a structure will lead to better performance, since the critical modes could be pushed into a region with higher disturbance energy. In order to answer this question, a modal sensitivity analysis was performed for the modes that are critical to the LOS. It was found that the modal sensitivities are smaller in the closed loop case compared to the open-loop case. This is not surprising since the FSM is already compensating for the lower frequency resonances. At the higher frequencies, however, the FSM is not effective due to the limited sensor bandwidth. It was also found that the sensitivities in Figure 5.9 (LOS) are considerably smaller than those predicted for SIM by Gutierrez [24]. This should be investigated in the future.

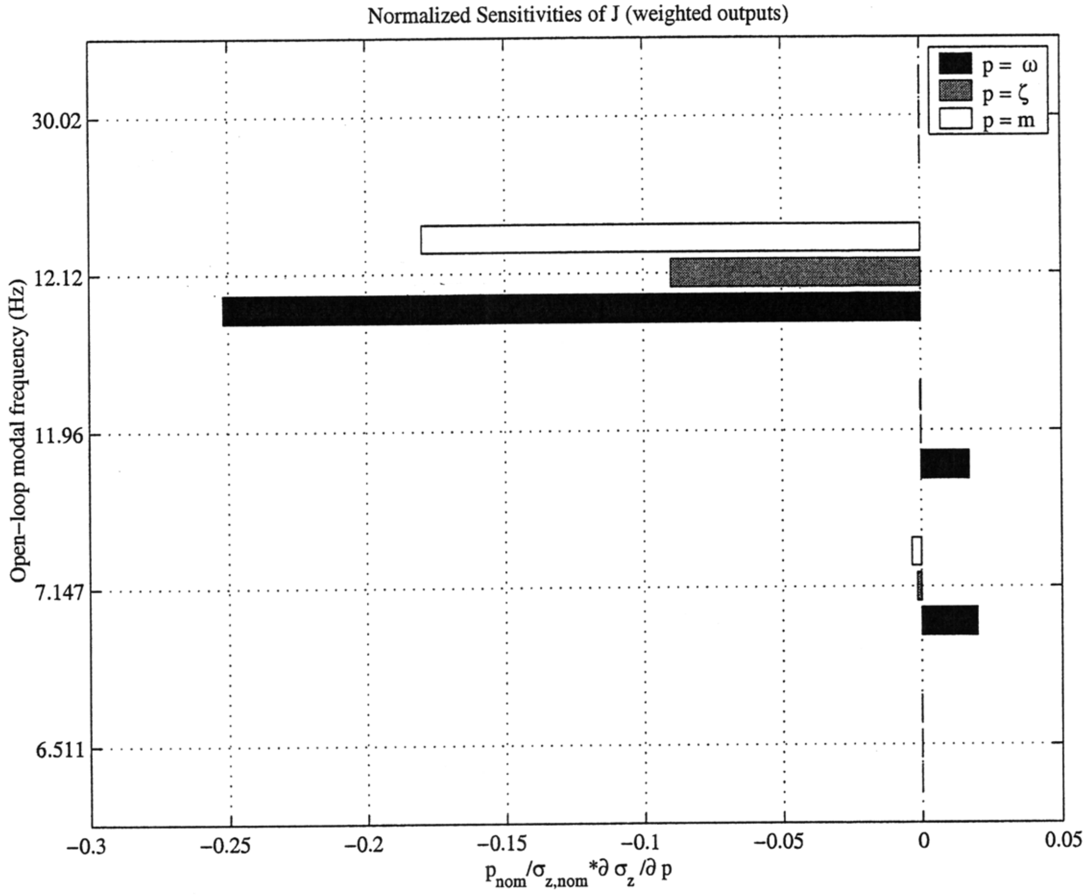

Figure 5.9: Modal Sensitivities of RMS LOS for critical modes

We observe that the mode at 12.12 Hz has the largest sensitivity with respect to frequency. This global pitch mode is of significant importance to the pointing of NGST. The results also predict that the LOS in detector y-direction (corresponds to spacecraft z-axis) is dominant (about 76 % contribution to total LOS jitter). We expect to see the centroid trace to be oval in time simulations for NGST as a consequence.

The results, which are presented for the nominal case in Chapter 3 are based on a number of disturbance and plant modeling assumptions. It is important to note that a number of these assumptions are associated with a large degree of uncertainty in the conceptual design phase. These uncertainties are associated with modeling of the disturbance source on the one hand and plant modeling uncertainties of the plant on the other hand as shown in Figure 5.10. The uncertainties are modeled as “Delta”-blocks. Gutierrez has analyzed the effects of parametric uncertainty on the nominal performance for SIM [24].

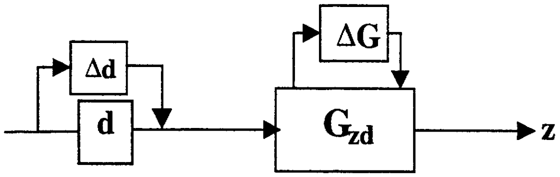

Figure 5.10: : Uncertainty in disturbance and plant modeling

Without repeating the uncertainty analysis for NGST, we want to demonstrate the effects of modeling uncertainty on the nominal performance using an important parameter. It was mentioned in section 2.2 that modal damping has a high degree of uncertainty associated with it. A reduction in the uncertainty can only be obtained from model refinement, ground testbeds, precursor missions and component tests. The approach of rerunning new disturbance analyses by changing the uncertain parameters is called the finite difference approach. This approach was used here, i.e. the modal damping $\mathbf{Z}$ was changed each time in the plant matrix $\mathbf{A}_\mathrm{p}$, and the performance analysis repeated for each step.

$$\mathbf{A}_\mathrm{p} = \underbrace{\begin{bmatrix} 0 & I \\ -\Omega^2 & -2Z\Omega \end{bmatrix}}_{\mathbf{A}_\mathrm{p}} \tag{5.29}$$

Based on experience with various spacecraft and a comprehensive study of modal damping in spacecraft [29], we recomputed the RMS WFE and RMS LOS for a modal damping ratio ζ in the interval [0.0001 , 0.1]. It has been shown experimentally that the amount of damping varies for each mode. The assumption of $\zeta = 0.0001$ (0.01 %) is a worst case scenario. Actual damping measurements on various spacecraft have given values between 0.02 and 0.005 [29]. It is also uncertain what damping differences can be expected from the “warm section” of the spacecraft on the SSM side compared to the "cold section" on the OTA side. Figure 5.11. summarizes the performance predictions for RMS WFE and RMS LOS based on modal damping uncertainty. The predictions were made using the Lyapunov method. This has the big advantage that frequency resolution issues do not enter into the problem and the RMS contributions of the lightly damped poles are always correctly captured.

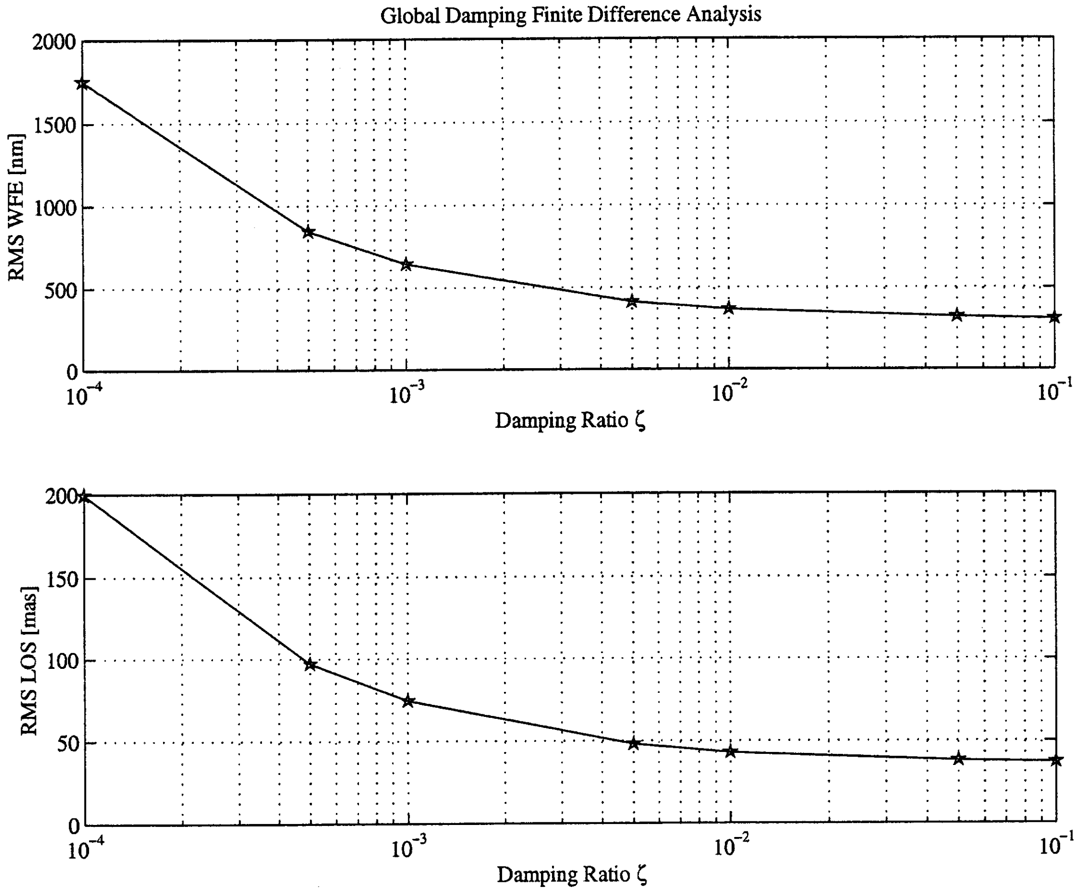

Figure 5.11: Modal damping sensitivity for NGST (finite difference approach)

We recall that we had assumed a modal damping ratio of ζ=0.001 and the results as read from the above chart are the same. As expected the RMS of the WFE and LOS increase as the modal damping decreases. We can see that this effect is non-linear. Eventually the curve flattens out as ζ tends to larger numbers. As the damping increases, the resonant peaks are more and more damped. At this end of the graph the performance curves also flatten out, which is due to the fact that the resonant peaks are already reduced and the backbone of the transfer function now determines the resulting performance. If we only provided 5% active damping to of the system, we still would not be able to meet performance, because we have not affected the backbone of the transfer function. It is interesting to see that even with 10% damping (which would require active structural control), we can only achieve values of ~ 350 nm for the RMS WFE and ~ 40 mas for the RMS LOS. Thus additional measures that affect the backbone of the disturbance to performance transfer functions will have to be considered in Chapter 6. It must be concluded that the modeling uncertainty is large and that modal damping and other modeling assumptions change the performance answers significantly. Future testing and more detailed modeling is recommended in order to reduce the modeling uncertainty for NGST.

Chapter 6

Performance Improvement Strategies

The initial performance assessment in Chapter 3 has shown that our sample problem meets performance in the closed loop ($OPD_{cl} = 41$ nm) but not in the open loop case ($OPD_{ol}=4734$ nm), whereby the requirement was set to $OPD_{req} = 116$ nm. In the full order NGST frequency domain analysis, the nominal case yielded a RMS WFE = 933 nm and RMS LOS = 86.4 mas, whereby the requirements are set to be RMS $WFE_{req} = 157$ nm and RMS $LOS_{req} = 4.8$ mas, respectively. It is thus necessary to improve the system performance such that requirements are met, and to provide for sufficient design margins. In Chapter 5 we have analyzed the sensitivities of the dynamic performance to various system parameters. We will use this information to improve the system in an intelligent way instead of randomly modifying system parameters until we find a case that meets performance. The Controlled Structures Technology (CST) framework [30] offers a systematic approach for performance improvement of an integrated system. The block diagram in Figure 6.1 summarizes the different options such as input or output isolation, passive damping, redesign and active control. Output isolation is already part of the system and is performed by the FSM loop. The first option to consider is the reduction of the disturbance levels which enter the system. Again before carrying out performance improvements on the full order NGST system we consider the 3DOF sample problem. It is our objective to first assess the effectiveness of individual improvements and subsequently to investigate the cumulative effect of combining all the previous improvements.

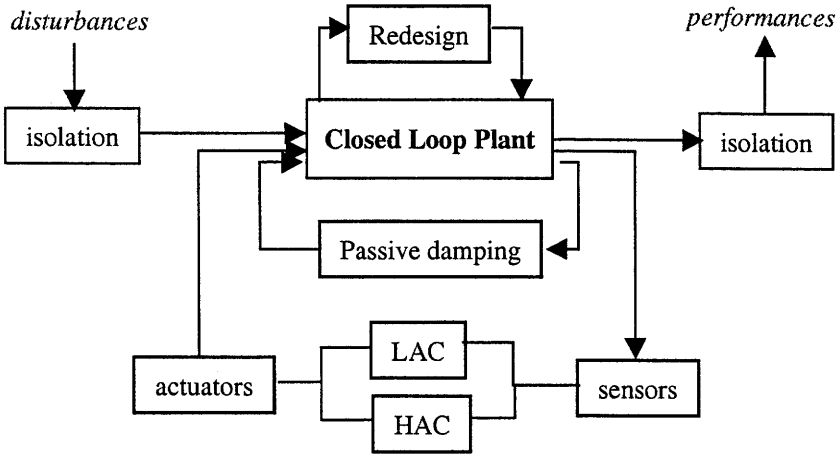

Figure 6.1: Block diagram of Controlled Structures Methodology

6.1 Performance improvement for sample 3DOF problem

Before looking at specific improvement options we consider the results from the physical parameter sensitivity analysis as shown in Table 6.1. These results directly indicate in which direction the physical parameters of a system should be changed in order to reduce the resulting RMS.

Table 6.1: Physical parameter sensitivities (comparison for sample problem)

Method used	Parameter k	Parameter m
Direct differentiation	-0.8091262023	-0.1908737977
Symbolic solution (2 Lyap)	-0.8091262023	-0.1908737977
sens_analysis_phys.m	-0.8091262023	-0.1914986026

The result tells us that increasing the stiffness *k* and mass *m* of our structural plant will both lead to a lower RMS. The physical way of how this is achieved is different however. Increasing the stiffness *k* will lead to a higher modal frequency ω_3, which in turn has been shown to lower the RMS by pushing the pole into the rolloff region of the disturbance. On the other hand increasing *m* will increase the central mass more in relation to the mass of the apertures and it will thus become “less disturbable” due to is higher inertia. Valuable insights can also be gained by considering the closed form expression for the open loop and closed loop σ_z^2:

$$\sigma_z^2 = \frac{s_c^2\left(2\zeta_3\omega_3\omega_{RO} + \omega_{RO}^2\right)}{16\zeta_3 m^2\omega_3^2\left(\omega_3^2 + 2\zeta_3\omega_3^2\omega_{RO} + \omega_{RO}^2\right)} \qquad (6.1)$$

The above equation corresponds to the open loop case and we can see that ω_3 appears to the fourth power in the denominator, but only to the first power in the numerator. Thus the performance should improve with $1/\omega_3^3$. This confirms the results for the modal sensitivity analysis from Section 5.1. Also we see that increasing the damping ζ_3 will improve performance since the square of the damping ratio appears in the denominator. We expect the performance to scale with $1/\zeta_3$. The decrease of the RMS with increasing mass (due to the higher inertia) is confirmed since the mass only appears explicitly as $1/m^2$. Finally, lowering the disturbance corner frequency ω_{RO} will lower the RMS since the expression tends to 0 in the limit as ω_{RO} tends to zero. We consult the closed loop expression of the performance σ_z^2 to assess the impact that the control parameters might have on the performance:

$$\sigma_z^2 = \frac{s_c^2\omega_{RO}^2\left(\Gamma_2 m\tau_d - \Gamma_3\Gamma_1 - \tau_d^2\Gamma_4\Gamma_1\right)}{8\Gamma_4\left(\Gamma_4\Gamma_1^2 + \Gamma_2^2 m\tau_d - \Gamma_3\Gamma_2\Gamma_1\right)} \qquad (6.2)$$

$$\Gamma_1 = m\tau_d\omega_{RO} + 2\zeta_3\omega_3 m\tau_d + m \qquad (6.2a)$$

$$\Gamma_2 = 2\zeta_3\omega_3 m\omega_{RO} + \omega_3^2\tau_d m\omega_{RO} - 3K_p\tau_d\omega_{RO}s_c - 3K_d\omega_{RO}s_c + m\omega_3^2 - 3K_p s_c \qquad (6.2b)$$

$$\Gamma_3 = 2\zeta_3\omega_3 m\tau_d\omega_{RO} + m\omega_{RO} + 2\zeta_3\omega_3 m - \omega_3^2\tau_d m - 3K_p\tau_d s_c - 3K_d s_c \qquad (6.2c)$$

$$\Gamma_4 = m\omega_3^2\omega_{RO} - 3K_p\omega_{RO}s_c \qquad (6.2d)$$

Looking at the denominator polynomial and only considering the proportional gain K_d, we see that K_d, appears to the first power in the numerator, but to the third power in the denominator. Therefore we expect that the RMS is going to scale with $1/K_d^2$ so long as the system is asymptotically stable. Now we want to consider how this information helps us in improving system performance. The performance improvement for the sample problem consists of assuming a 5% change for each of the above parameters and recomputing the performance. The closed loop and open loop performance is then recomputed for each change individually. The results are shown in Table 6.2. It is interesting to observe that a 5% change in a particular parameter does not necessarily entail a corresponding change in the RMS performance. We can see that changes to the structural parameters *k* and *m* have a significantly larger effect on the RMS in the open loop case (-3.87% and –0.81% respectively) compared to the closed loop case (-0.049% and –0.024 %). This is not surprising since the PD-controller reduces the OPD by about 40 dB. Thus an important conclusion is that there usually is little merit in spending a lot of resources on improving structural parameters of the system if aggressive control loops are already closed around the optics. The results in the table below are compared based on a frequency domain analysis for the sample problem.

Table 6.2: Effect of various parameter changes on the nominal performance

Parameter	**Nominal value**	**(±) 5 % change**	**RMS OPD open loop**	**% change**	**RMS OPD closed loop**	**% change**
Nominal	All	0	4728.96	0	41.19	0
ζ_3	0.005	+0.00025	4615.02	-2.14	40.99	-0.49
k	$7.1 \cdot 10^6$ N/m	$+3.5 \cdot 10^5$ N/m	4545.62	-3.87	41.17	-0.049
m	200 kg	+10 kg	4690.65	-0.81	41.18	-0.024
ω_{RO}	$200\pi \frac{\text{rad}}{\text{sec}}$	$-10\pi \frac{\text{rad}}{\text{sec}}$	4699.04	-0.63	39.26	-4.69
K_d	-0.05	-0.0025	4728.96	0	38.94	-5.46
Combined	N/A	all of the above	4372.92	-7.53	37.31	-9.41

In conclusion it can be said that the performance of a system such as the one presented in the 3DOF sample problem can be improved significantly through a combination of system parameter changes. Typically we first consider a reduction or change in frequency content of the disturbance PSD and structural redesign such as stiffening or softening and changes in the mass distribution of the system. Adding damping always improves performance and adds robustness to the control. If the plant is already heavily damped, however, the addition of damping will not improve the performance significantly since the backbone of the disturbance to performance transfer function doesn't change due to damping alone. Finally we see that the performance is most sensitive to the control system parameters (K_d, K_p and τ_d in our case) in the closed loop case. This means that efforts for fine tuning control parameters are likely to pay off more than any other redesign action. Figure 6.2 shows the comparison of the cumulative RMS curves for the open loop (left side) and closed loop cases(right side).

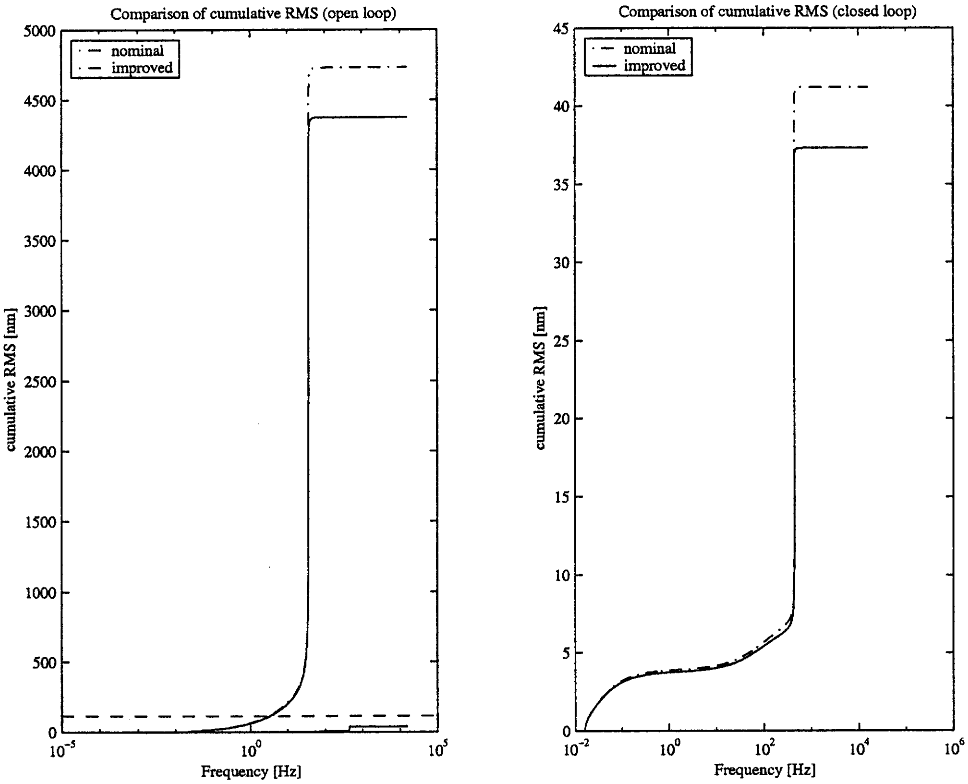

Figure 6.2: Comparison of nominal and improved design for 5% change of parameters (Sample 3DOF Problem)

6.2 Performance Improvement Strategies for NGST

The sensitivity analysis (Chapter 5) has given us a number of indications as to which performance enhancement options might be the most promising for NGST. The CST framework in Figure 6.1 also gives us a systematic framework in which to operate. We will consider a number of performance improvement steps. For steps 1 and 2 we will consider the effects individually.

1. Use quieter wheels and/or reduce imbalances for existing wheels
2. Analyze the effects of reaction wheel isolation
3. Structural redesign through stiffening of the secondary tower
4. Addition of passive damping to the system
5. Extend LOS stabilization system bandwidth

After assessing the performance impact of each of measures 1 and 2 individually, we will combine all the measures into a combined case, which will be compared with the nominal case. The hope is that the combination of performance enhancement steps will provide the required performance with sufficient margins.

6.2.1 Use of alternate wheels and imbalance reduction

Using quieter reaction wheels can reduce the disturbance levels significantly. The challenge lies in finding reaction wheels which have sufficient torque and momentum capability without producing large dynamic disturbances. This analysis shows the cumulative RMS levels when four different types of wheels are used. Table 6.3 shows the 4 wheels and the resulting RMS performances that are obtained. It shall be noted that the fourth option is the original E-Wheel, where the nominal imbalance level has been reduced by 50%. This is not unrealistic since, according to Bialke, the imbalance levels can be reduced by a factor of 2-3 by carefully balancing and installing the flywheels [18]. This would lead to additional costs, but greatly improve the dynamic performance since the RWA is expected to be the dominant source of dynamic disturbances.

Table 6.3. Comparison between four different wheel models

Wheel Model	% Imb	RMS WFE	RMS LOS
1) HST Wheel	100	828 nm	74.5 mas
2) ITHACO E-Wheel	100	933 nm	86.4 mas
3) ITHACO B-Wheel	100	549 nm	36.3 mas
4) ITHACO E-Wheel	50	604 nm	44.5 mas

Each of the above wheels has been modeled using the same input parameters as for the baseline case. The bias wheel speed R_o is 1000 RPM and the wheel speed deviation is dR = 1000 RPM with a uniform wheel speed distribution. Figure 6.3 shows the results for the four wheels using cumulative RMS curves.

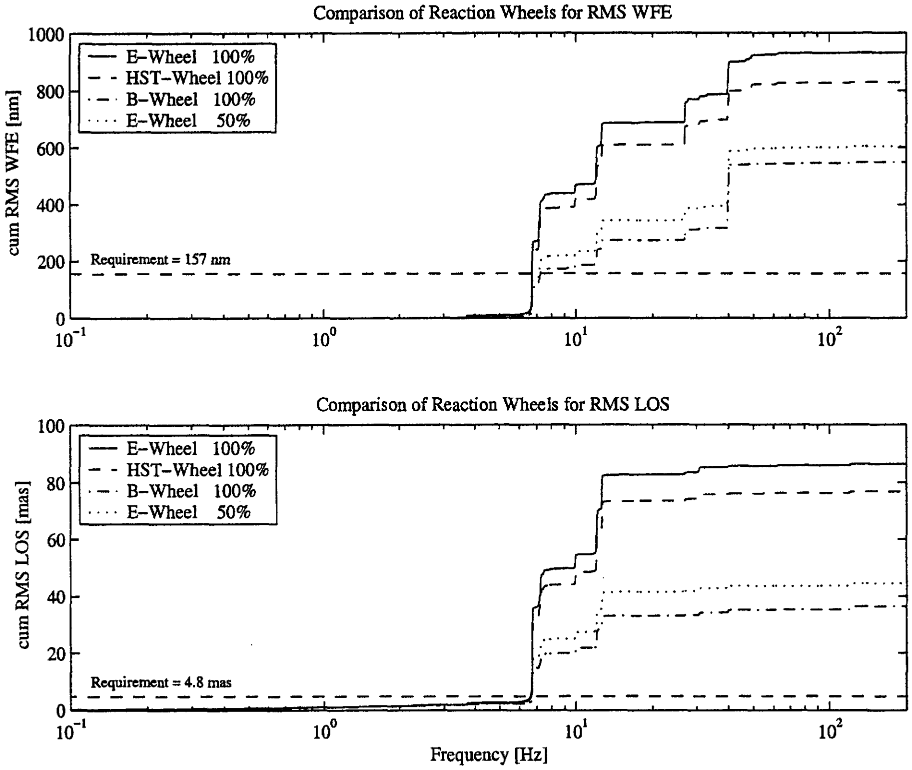

Figure 6.3: Cumulative RMS curves for four different wheel models

It can be concluded that reducing the disturbance level of reaction wheels by reducing the amount of imbalance or using quieter wheels (e.g. HST versus E-Wheel) can significantly reduce the resulting RMS. It is worthwhile to use quieter wheels, but it is insufficient by itself. The flywheel can be balanced to a very small tolerance before installation by removing small amounts of material and re-measuring the wheel. This process is very lengthy and thus costly. Also installing active magnetic bearing wheels is an attractive option. In view of the fact that using quieter wheels alone does not help meet the requirement, reasonable imbalance specifications have to be defined for the NGST reaction wheels but additional vibration mitigation measures are necessary.

6.2.2 Effects of RWA Isolation

Another effective measure is to mechanically isolate the reaction wheel assembly from the rest of the SSM. This isolation can be accomplished passively or actively, depending on the desired corner frequency and rolloff of the transmissibility function. Significant work in this area has been done by Zheng, Haynes and Lee [59] as well as Spanos, Rahman and Blackwood [60]. The second paper mentions the development of a 6-axis active vibration isolator as depticed in Figure 6.4.

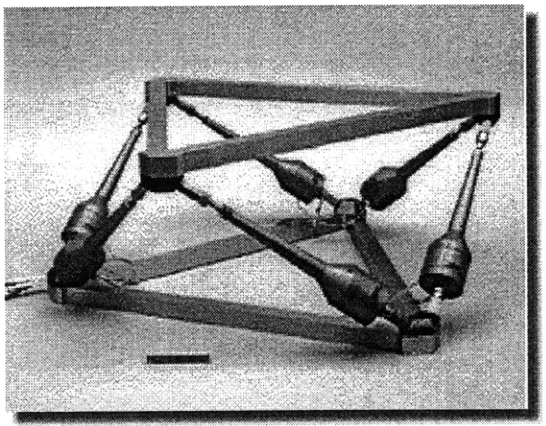

Six axis active vibration isolator

Figure 6.4: Prototype 6-axis active vibration isolator developed by JPL [60]

In this study we model the isolator as a 2^{nd} order system for each axis independently as shown in Figure 6.5. This is an approximation since there is cross-axis compliance in reality and we do not expect equal isolation performance in all axes.

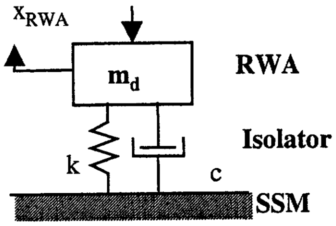

Figure 6.5: 2^{nd} order system approximation for isolator

This approximation of a RWA isolator leads to the following transfer function:

$$G_{iso}(\omega) = \frac{\omega_{iso}^2}{s^2 + 2\zeta_{iso}\omega_{iso} + \omega_{iso}^2} \tag{6.3}$$

where ζ_{iso} is the damping ratio and ω_{iso} is the isolator corner frequency. Experimental results have shown that passive isolators work well for high frequencies (above ~ 100 Hz), but that amplification can occur at lower frequencies. Active control needs to be used if we want to achieve corner frequencies below 2 Hz. The nominal case was recomputed by assuming that all six RWA noise channels as shown in Figure 2.3 are isolated and first pass through this low-pass filter. The six filters are in a parallel arrangement as shown in Figure 6.6.

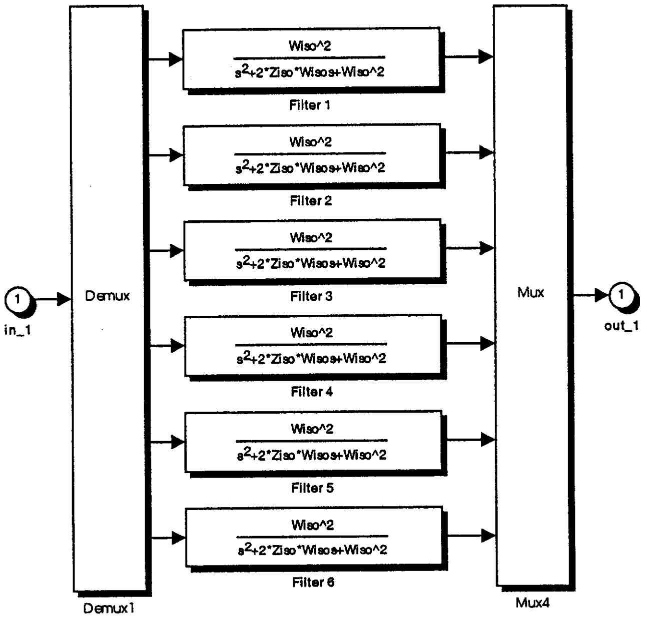

Figure 6.6: Simplified model of RWA isolator (according to Mosier)

The corner frequency ω_{iso} was varied in order to determine which corner frequency would allow to meet the system performance. This type of isolator modeling is too optimistic as it neglects cross axis stiffness and sensor noise limitations in the case of an active isolation system. Figure 6.7 summarizes the results for the vibration isolation assuming 20% damping of the RWA isolator. It is possible to isolate the RWA more about axes, where the RWA disturbance contributions have been shown to be the largest.. Figure 6.7 shows the results of the trade study involving the RWA isolator corner frequency.

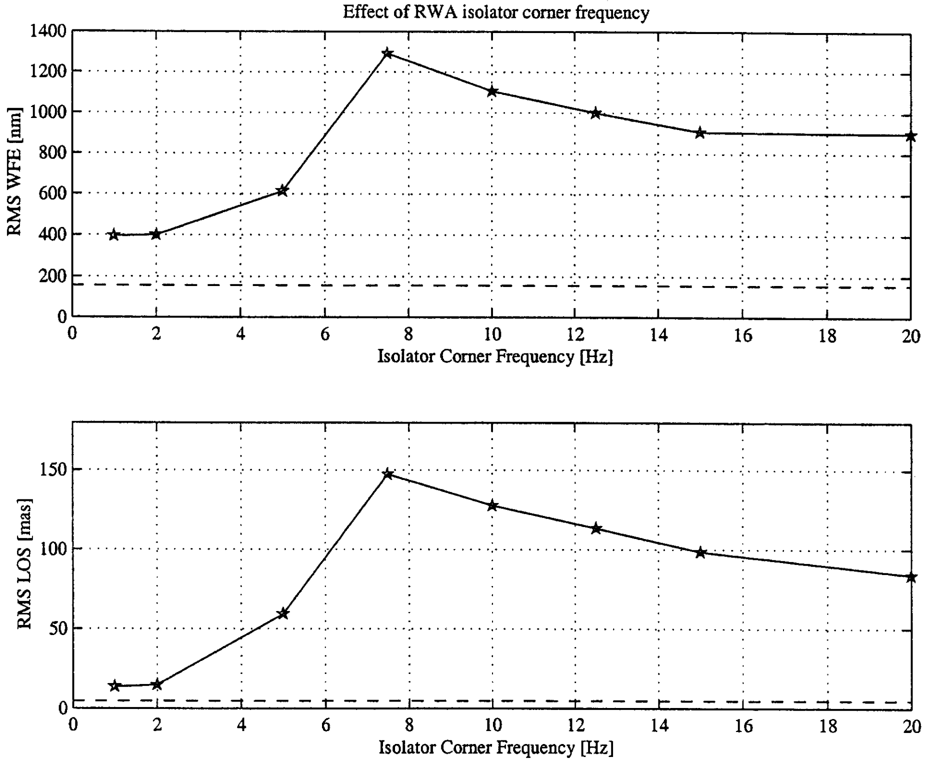

Figure 6.7: Effects of RWA isolation on performance RMS values

Two interesting effects have been discovered. On the one hand we see that an isolator corner frequency between 5 and 15 Hz does not help but worsens the performance. This can be explained by the fact that the passive (2-parameter) isolator amplifies disturbances near the corner frequency. If this amplification occurs where the disturbance to performance transfer function magnitudes have their maximum values (region between 6 and 12 Hz) we obtain poor performance. On the other hand we would expect a more significant improvement between 1 and 2 Hz, which is not the case. The explanation can be found when we consider the performance PSD for a RWA corner frequency of 2 Hz (see Figure 6.8). We see that we have indeed significantly isolated the RWA disturbances from the system. The cryocooler disturbances, specifically the fundamental at 40 Hz, have now become the dominant disturbance sources. The cryocooler disturbance by itself is sufficient to exceed the requirements for the RMS WFE and the RMS LOS. This leads to the conclusion that further mitigation of cryocooler disturbances along with RWA isolation are necessary.

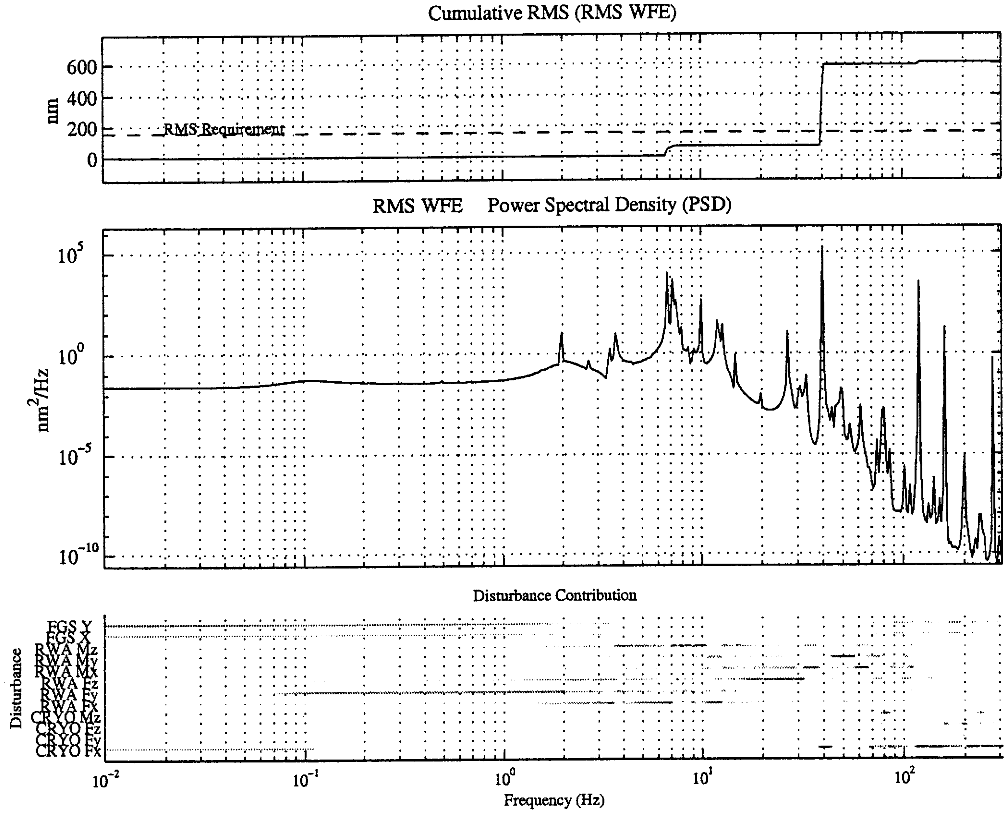

Figure 6.8 : Performance PSD (WFE) with 2 Hz RWA Isolation

We conclude that RWA isolation can significantly lower the RMS values if the corner frequency is below 5 Hz. A 1 Hz RWA isolator seems to be the ideal solution for NGST. This is also the region were current technology transitions from passive isolation to active isolation systems. The results suggest that a passive, active or hybrid isolator with a corner frequency between 1 and 2

Hz would be very effective. Additionally we will not be able to meet performance without also mitigating the cryocooler disturbance levels.

6.2.3 Combination of performance improvements

The previous results suggest that a combination of the suggested mitigation measures should provide sufficient performance. A combination case was run, where all of the above performance enhancement steps were incorporated. Table 6.4 gives a comparison of the physical disturbance, plant and controls parameters in the nominal case and the combination ("improved design") case.

Table 6.4. Comparison of nominal and improved design parameters

Parameter	Nominal Design	Improved Design
Bae80K Cryocooler attenuation	0.1	0.001
E-Wheel Imbalance Level	100%	50%
RWA Isolator Corner Frequency	N/A	2 Hz
FGS Integration time	30 msec	20 msec
Modal Damping Ratio	0.001	0.01
Tower Blade Area moment of inertia I1	2.7778e-7	5.0e-6

It would be desirable to conduct a more rigorous exploration of the trade space involving the above parameters in the future. The integrated model for the improved case is assembled the same way as in the baseline case (see Chapter 2). We then conduct a frequency domain analysis to assess the combined effect of all the performance improvements. The following figures should be compared with the results in Chapter 3. The disturbance PSD's for the improved case are shown in Figure 6.9. We can immediately see that the RWA PSD's look different compared to Figure 3.7. The magnitudes are lower and the effect of the 2 Hz isolator is clearly visible around the corner frequency. The cryocooler disturbances are the dominant disturbances at higher frequencies, while the FGS noise dominates the low frequency regime.

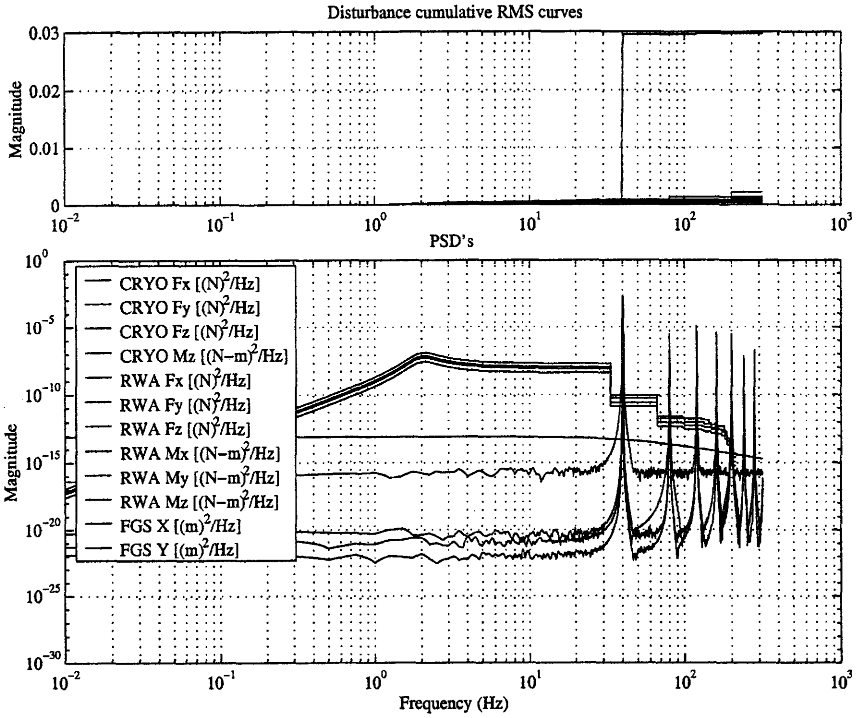

Figure 6.9: Disturbance PSD's for the improved design case

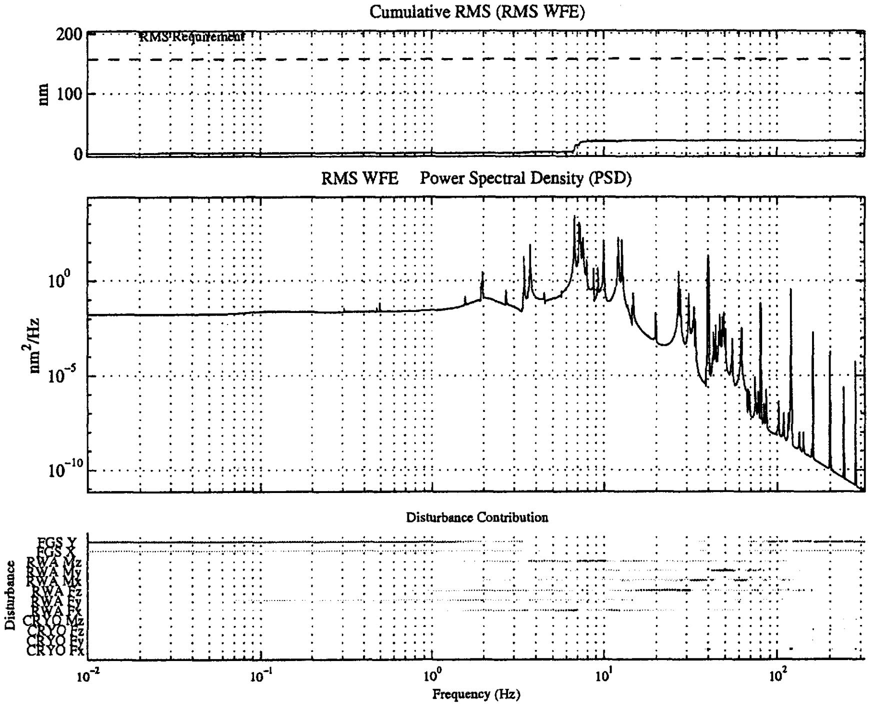

Figure 6.10: Performance PSD for WFE in the combined case

The performance PSD's, cumulative RMS curve and disturbance contributions to the RMS WFE are shown in Figure 6.10. The most important result is that we now meet performance with the cumulative RMS curve asymptoting to a value of 21.22 nm. This is well below the requirement of 157 nm. It can also be seen that the RMS is accumulated over a narrow frequency range between 5 and 10 Hz. The identification of critical frequencies allows us to find the modes that are still contributing to the remaining WFE (see Figure 6.11).

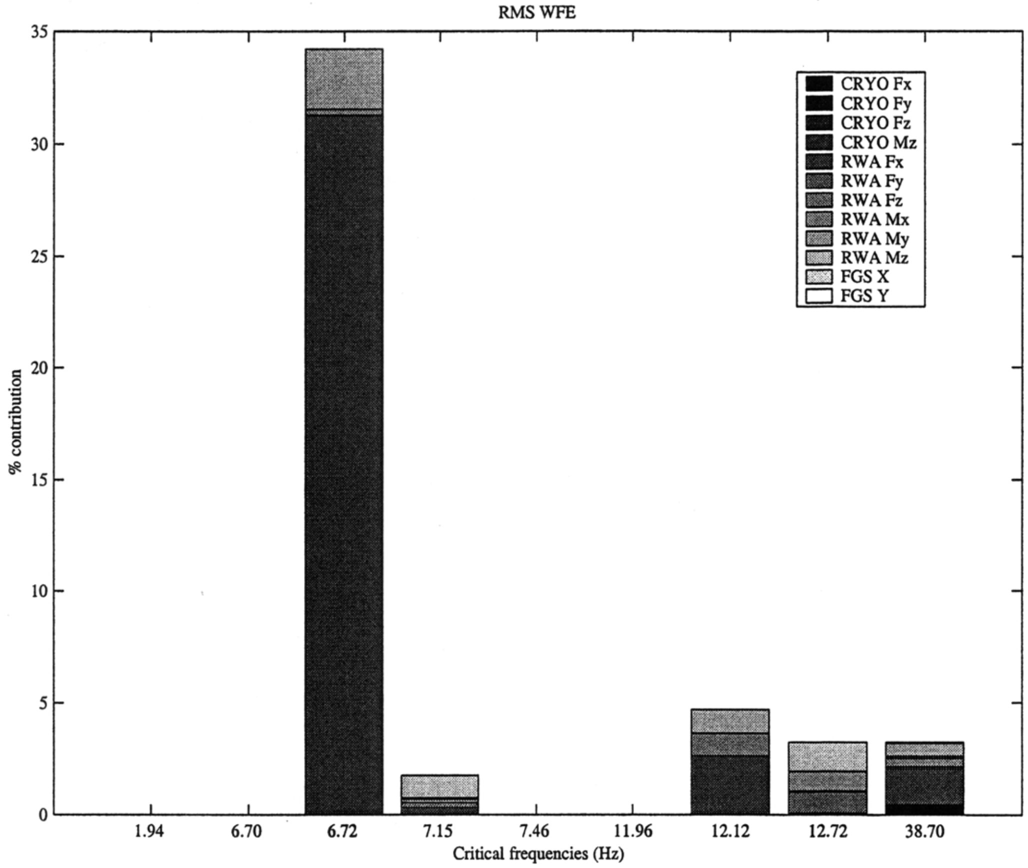

Figure 6.11: Critical frequencies for the combined case (WFE)

The dominant mode is at 6.72 Hz is excited by the remaining RWA disturbances, whereby the moment about the y-axis is dominant. This makes sense, when we consult the corresponding mode on top of Figure 5.4. The global pitch motion of the observatory is excited by precisely the disturbance torque about the spacecraft y-axis. We expect this phenomenon to also be observable in the time simulations. The second performance metric we want to analyze for the improved design is the LOS jitter. Figure 6.12. shows the performance PSD, cumulative RMS and disturbance contributions for the LOS metric. We first determine that we do indeed meet the requirements in this case. The RMS WFE is predicted to be 3.204 milli-arcseconds, which is below the requirement of 4.8 mas. It is interesting to note that the largest contributor to the RMS LOS has now become the FGS noise. This is also expected since we have shortened the integration time of the guide star sensor from 30 msec to 20 msec. None of the RWA and cryocooler disturbance mitigation measures will help to improve the FGS noise level. We have however managed to bring the mechanical vibration sources down to or below the FGS noise level. This is very desirable. It is interesting to note that most of the RMS LOS is accumulated gradually over the bandwidth of the FGS sensor as indicated by the cumulative RMS curve (top plot). We also see a contribution from RWA noise around 7 Hz.

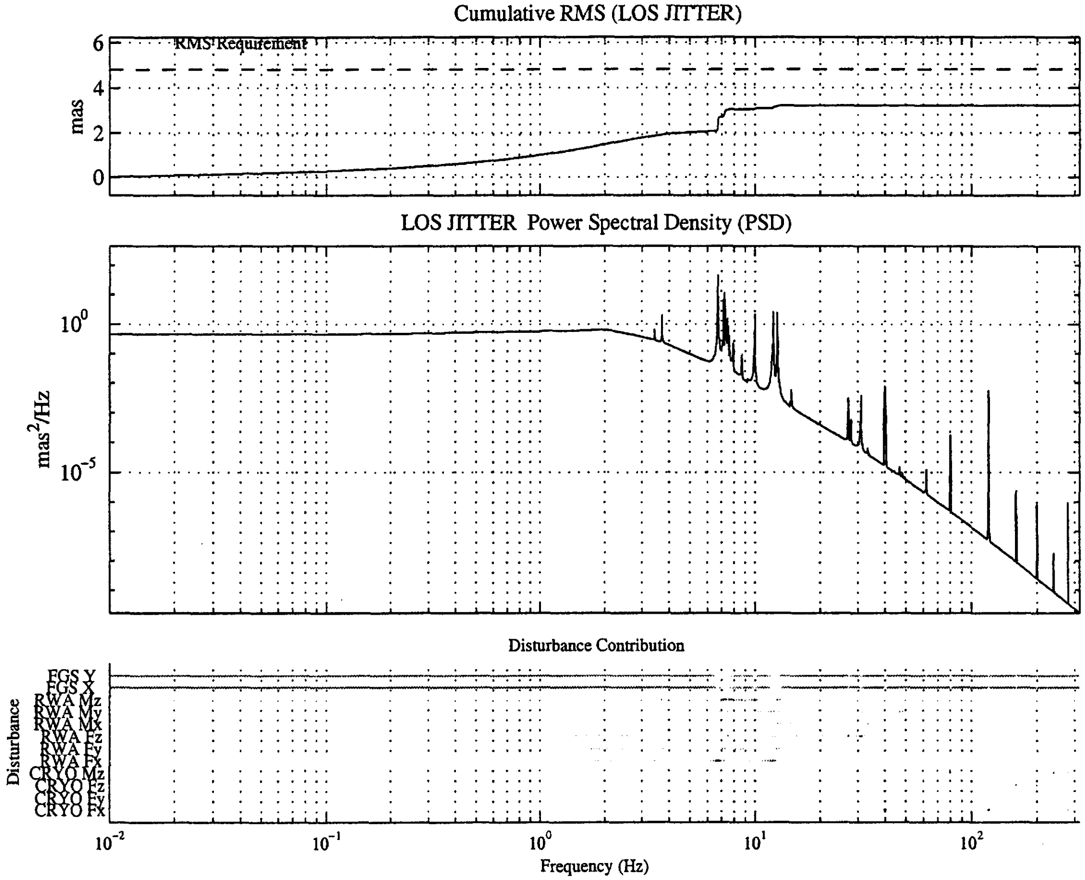

Figure 6.12: Performance PSD for LOS jitter in the combined case

We have shown that a combination of performance enhancements is able to bring the system into compliance with the dynamic performance requirements stated in Section 1.2. It is true, however, that the combination presented in this subsection is not the only possible solution. The question then arises, which of these options appears to be the most promising for NGST. There is a desire to keep the complexity of the NGST to a minimum. Passive means such as disturbance level reduction (magnetic bearing RWA, Brayton cryocoolers), RWA isolation and passive damping by themselves have been shown to be very effective.

Chapter 7

Summary and Conclusions

This chapter contains the conclusions of the thesis from the analysis of the 3DOF sample problem and from the analysis of the full order NGST model. A thesis summary and recommendations for future work are also included.

7.1 Thesis Summary

The Next Generation Space Telescope (NGST) represents a challenging problem from the point of view of integrated modeling of structural dynamics, controls and optics. This is due to the fact that NGST will make extensive use of deployable, inflatable and lightweight components, while taking into account launch weight and fairing dimensional constraints. In order to meet the scientific objectives, NGST will have to be diffraction limited at a wavelength of λ=2.2 μm and be able to point the Optical Telescope Assembly (OTA) with a precision of 4.8 milli-arcseconds (1σ) during scientific observations. The two key metrics that relate to these science requirements are the root-mean-square wavefront error (RMS WFE) and the line-of-sight jitter root-mean-square error (RMS LOS), which is representative of the motion of the image centroid on the focal plane. It is important to assess the impact of the expected micro-vibration environment on the scientific performance before design, construction and launch.

All current concepts for the NGST are innovative designs, which present unique systems-level challenges. The goals are to outperform existing observatories at a fraction of the current price/performance ratio. Standard practices for developing systems error budgets, such as the "root-sum-of-squares" error tree, are insufficient for designs of this complexity according to Mosier [11]. As a consequence, this thesis attempts to present a concise approach to integrated modeling, dynamic performance assessment, sensitivity analysis and performance improvement strategies for NGST.

The integrated modeling process consist of assembling and rigorously analyzing a system level dynamics model of the observatory including disturbances, structural dynamics, optics and controls. The basis for this work is the well-established theory of linear time-invariant (LTI) systems. A simple three degree-of-freedom example is first developed in order to lay out the mathematics and methods used in a transparent manner. These methods are then applied to a large order conceptual design model of the NASA NGST Yardstick mission. The structural dynamics model utilizes the results from the generalized eigenvalue problem to represent the plant dynamics in 2^{nd} order modal form. The noise sources of interest are reaction wheel assembly (RWA) imbalances, cryocooler vibrations and guide star sensor noise. Stochastic random signal theory is invoked in order to characterize these disturbances in the time domain, frequency domain and to describe the disturbances in state space form. A detailed optical prescription containing the primary mirror (PM), secondary mirror (SM), deformable mirror (DM), fast steering mirror (FSM) and all other elements upstream of the focal plane describes the optical train of NGST. Linear sensitivity matrices previously generated by MACOS relate the generalized coordinates of the structural plant to the optical performance metrics OPD and WFT. The control strategy comprises a conventional H_2 attitude determination and control system (ADCS) for rigid body mode stabilization and a line-of-sight (LOS) stabilization subsystem. The latter system uses the NIR science camera with its mosaic focal plane as a fine guidance sensor (FGS) and a 2-axis fast-steering mirror as an actuator in a servo-loop arrangement. Due to the large difference in bandwidth the coupling between the two control loops is not modeled. Finally the last step of the integrated modeling process consists in assembling the integrated model into an overall state space representation.

The goal of the initial performance assessment is to predict the optical performance of the system under the influence of dynamic disturbances. The predicted performance was compared with the requirements for the wavefront error and the LOS jitter. We predicted an RMS WFE of 933 nm and RMS LOS of 86.4 mas in the nominal case (using the PSD analysis), which did not meet the requirements of $\sigma_{WFE} = 157$ nm and $\sigma_{LOS} = 4.8$ mas respectively. Three different methods were used to come up with the performance predictions and their respective advantages and disadvantages: time integration, frequency domain analysis using power spectral densities

(PSD's) and Lyapunov analysis. The initial performance assessment showed that the NGST Yardstick design does not meet dynamic performance with the nominal disturbance and system parameters chosen for this study. It was also found that the RWA is the dominant noise contributor and that the critical modes for the system lie in the region between 5 and 50 Hz.

In order to compute accurate RMS values for the performance metrics of interest (WFE and LOS) it is paramount that the integrated model contains a sufficient number of normal modes. This is especially true for the frequency regions, where the disturbances have a large power density. In the case of RWA disturbances most of the disturbance power enters the system between 1 and roughly 300 Hz. The inherently high modal density of lightly damped large space structures compounds the problem and leads to numerical ill conditioning. Additionally the optical train is modeled using a geometrical ray tracing technique that utilizes up to several thousand rays. Both of these factors lead to large order state space systems already at the conceptual level in terms of input-output dimensions but also in terms of the size of the overall appended state vector. Two strategies have been presented and applied that significantly alleviate the computer memory and CPU run-time problems such large order models. The first method reduces the input-output dimensions of the system by applying a singular value decomposition technique to the optics linear sensitivity matrices. This allows the use of "surrogate" sensitivity matrices that lead to identical RMS results while significantly reducing the computational burden in the cases of the frequency domain analysis. Secondly the numerical conditioning of the overall system needs to be improved as demonstrated in Section 4.1.

The sensitivity analysis computes the local slope of the performance RMS to modal or physical parameters of the system. The modal parameter sensitivity was performed for the critical system modes and gives an indication if stiffening or softening a particular mode will improve performance. The physical parameter sensitivity was used in the sample problem to determine the dependency of the RMS on selected structural parameters. This method has numerical and conceptual advantages over a simple finite difference computation and gives important indications for the performance improvement phase of the conceptual design. The effect of modal damping uncertainty on the performance was also investigated.

The performance improvements to the nominal design include increasing the LOS stabilization bandwidth, stiffening the secondary mirror tower, using a passive 2-Hz RWA isolator, adding passive damping, using a quieter cryocooler and finally reducing the imbalances of the reaction wheels in the first place. It has been shown quantitatively that the combination of these incremental changes to the nominal design is able to bring the system into compliance with the requirements. The resulting performance for the improved design was predicted to be RMS WFE = 21.2 nm and RMS LOS = 3.204 mas. Thus a true system level improvement has been carried out, without attempting to optimize each subsystem individually.

7.2 Conclusions from the 3 degree-of-freedom sample problem

A sample problem with three degrees-of-freedom was developed that contains all the essential elements of a large space observatory model (structures, optics, disturbances and controls). The goal of the sample problem was to validate the performance assessment and improvement framework before applying it to the full order NGST model. Conclusions from this work are:

- A low order sample problem with three degrees of freedom was successfully solved. It was used to derive an integrated model that is representative of a more complex precision opto-mechanical system.
- The limit of symbolic hand calculations is achieved with a closed loop system *SYS_czd* that contains a total of about 6 states. This limit is given by the complexity of the closed form expressions for the performance RMS and the associated sensitivities.
- The three methods of computing the RMS OPD were demonstrated and comparing these results with analytical results from hand calculations validated the performance assessment and enhancement framework developed by Gutierrez [24].
- The time domain requires the longest CPU times and averaging to get a precise answer. The frequency domain method requires good frequency vector resolution but offers cumulative RMS information and the Lyapunov solution is the fastest and most accurate but only gives the RMS result, without explicit modal information.

- The sensitivity analysis code was validated (open loop only). Care needs to be taken that the eigenderivatives are computed correctly and that the $\mathbf{A}_{zd}$ matrix is in an acceptable form for the physical parameter sensitivity analysis (e.g. no $\mathbf{D}_c$ term allowed).

The most important conclusion is that we have been able to analytically validate the performance assessment and the sensitivity analysis framework. Even though the problem is seemingly trivial at first sight, the closed form calculation of the open loop and especially the closed loop expressions for the RMS OPD is challenging. For realistic large order models such as NGST, SIM or TPF we cannot expect to have closed form symbolic expressions for the RMS and the corresponding sensitivities so that we must revert to purely numerical calculations using the existing MATLAB based framework.

7.3 Conclusions for NGST

This thesis has shown that even complex systems like NGST can be modeled by first subdividing the problem into individual components. Firstly we analyzed the structural dynamics, the disturbance sources (especially RWA imbalances), the optical performances and the controls (ACS and LOS stabilization) separately. We then integrated the different sub-models into an integrated and multidisciplinary model in order to predict the RMS WFE and RMS LOS performance under the influence of dynamic disturbances.

The frequency-domain was attractive for simulations because we could treat uncertain parameters such as wheel speed as random stochastic processes which allows to run "on average" cases, thus covering a large portion of the design space. Time simulations of NGST on the other hand allow taking into account more complexity in terms of noise sources, discrete-time subsystems and non-linearities. Finally the Lyapunov solution produces the fastest and most reliable answer since it does not suffer from frequency vector resolution issues. The only information provided by the Lyapunov solution is the performance covariance matrix. The ideal solution is to use all three methods side by side. Also there is a need to expand the current framework in order to compute the expected "worst case" performance. More specific conclusions and recommendations are:

- The nominal analysis for NGST in the fine pointing mode showed that the wavefront error and LOS jitter did not meet the $\lambda/14$ and 4.8 mas requirements, respectively. A sensitivity analysis was performed to find that the performance is most sensitive to RWA noise levels and secondary tower bending modes.
- The system is brought into compliance by applying a combination of CST improvement measures. The most promising is a "combined, passive" approach using passive damping, quieter reaction wheels and reaction wheel isolation with a corner frequency of around 2 Hz.
- Because the RWA M_y axis dominates the RMS WFE response it is recommended to provide aggressive isolation for this axis since it is able to excite the global pitch mode of the observatory at 6.72 Hz.
- Based on the cumulative RMS plots it can be concluded that the performance critical modes of the system lie in the 5-12 Hz range. Thus it is also recommended not to bias the reaction wheel speeds in the 300-720 RPM range because the fundamental harmonic of the RWA disturbances would then be allowed to excite the modes in that region more frequently during observations.
- Another recommendation is to create a detailed structural model of the integrated science instrument module (ISIM), where the potential load paths from the cryocooler to the focal plane can be evaluated in detail.

7.4 Future Work

The sample problem strongly suggests that the existing sensitivity analysis framework should be extended to include disturbance filter and control parameters such as K_d, K_p, τ_d, ω_{RO}. This can be explained by looking at the closed loop state transition matrix $\mathbf{A}_{zd}$ for the sample problem as shown below. This matrix contains all the essential parameters of the closed loop system.

$$A_{zd} = \begin{bmatrix} -\omega_{RO} & 0 & 0 & 0 & 0 & 0 & 0 & 0 \\ 0 & 0 & 0 & 0 & 1 & 0 & 0 & 0 \\ 0 & 0 & 0 & 0 & 0 & 1 & 0 & 0 \\ 0 & 0 & 0 & 0 & 0 & 0 & 1 & 0 \\ \frac{\omega_{RO}}{\sqrt{6m}} & -\omega_1^2 & 0 & 0 & -2\zeta_1\omega_1 & 0 & 0 & 0 \\ 0 & 0 & -\omega_2^2 & \frac{-s_c\sqrt{6}}{m}\left(K_p + \frac{K_d}{\tau_d}\right) & 0 & -2\zeta_2\omega_2 & 0 & \frac{K_d}{\sqrt{2m}\tau_d^2} \\ \frac{-\omega_{RO}}{\sqrt{12m}} & 0 & 0 & -\omega_3^2 + \frac{3s_c}{m}\left(K_p + \frac{K_d}{\tau_d}\right) & 0 & 0 & -2\zeta_3\omega_3 & \frac{-3K_d}{\sqrt{12m}\tau_d^2} \\ 0 & 0 & 0 & s_c\sqrt{12/m} & 0 & 0 & 0 & -1/\tau_d \end{bmatrix}$$

It would be very beneficial to be able to compute the sensitivities with respect to disturbance, plant and control parameters of the system. As a specific example we could then compute the sensitivity of σ_z with respect to the derivative control gain K_d, i.e. we would be looking for $\partial\sigma_z/\partial K_d$. Since a closed form expression for σ_z is available we can obtain the normalized sensitivity by direct differentiation. We obtain a value of $ns_{Kd} = -0.9544$, which is significantly more sensitive than the sensitivity with respect to the plant natural frequency ω_3 in the closed loop case. This tells the system engineer that the merits are higher if we can increase the derivative control gain by 1% than if we increase the structural frequency ω_3 by 1 % (by stiffening the truss for example). If we could obtain the sensitivities for all parameters that appear in A_{zd}, we could rank them and only focus the performance improvements on the parameters that have a large sensitivity (e.g. increasing control gain is better than redesigning the truss). Future work should therefore include sensitivities with respect to disturbance filter parameters and control parameters in addition to the plant parameters that are currently supported. Other suggestions for future work include:

- Apply uncertainty analysis framework to NGST analysis. It was shown that model assumptions such as modal damping can have a large effect on the RMS results. An uncertainty analysis would determine which parameters are uncertain and within what bounds. This would allow to put "error bars" on the results of the performance assessment.

- Compute second derivatives (curvatures) of RMS. This would allow predicting the range of validity of the sensitivities (slope). It is expected that some parameters behave very well, but other parameters can flip signs and show non-linear behavior depending on the specific model assumptions.

- Wrap gradient-based optimization loop around the whole process depicted in Figure 1.5 in order to optimize the performance RMS, while each parameter is given an allowable bound. A cost function could include RMS, control effort, system mass, system cost and stability margins.

- Include ADCS design into the improvement process and compute sensitivities with respect to ACS bandwidth, gains and stability margins

References

[1] Dressler A.(editor) "HST and Beyond – Exploration and the Search for Origins. A Vision for Ultraviolet-Optical-Infrared Space Astronomy" – The HST and Beyond Committee report, AURA, May 15, 1996

[2] H.S. Stockman (editor) et al., "Next Generation Space Telescope – Visiting a Time when Galaxies were Young", The NGST Study Team, The Association of Universities for Research in Astronomy, Inc., June 1997

[3] Illingworth, V., The Facts dictionary of Astronomy, Third Edition, Facts on File, Infobase Holdings Company, ISBN 0-8160-3184-1, New York, 1994

[4] Fogiel M, Research Education Association, "Optics – REA's Problem Solvers", Research and Education Association, New Jersey, 1991

[5] URL: http://www.ngst.nasa.gov/science/drm.html

[6] NASA GSFC Study team, "The Next Generation Space Telescope"- A presentation to the NGST study office, NASA Goddard Space Flight Center, August 21, 1996

[7] Bely P., Burg, R. Perrygo C., "NGST Monograph No 1" NGST Yardstick Mission, NASA Goddard Space Flight Center , Draft version, 1997

[8] Battin, R. "Astrodynamics" AIAA EducationSeries, 1996

[9] Mosier, "Fine Pointing Control for NGST", SPIE conference , Kona 1998

[10] Redding D. e a. "Wavefront Sensing and Control for the Next Generation Space Telescope", SPIE conference, Kona, 1998

[11] Mosier, Gary, Mike Femiano and Kong Ha, Goddard Space Flight Center, Redding, Dave, JPL, National Aeronautics and Space Administration, "*An Integrated Modeling Environment for Systems-level Performance Analysis of the Next Generation Space Telescope*", SPIE Conference, Kona, 1998

[12] Mosier G., Ha K., Femiano M., "NGST Slew Algorithm Description", GSFC Internal Memorandum, May 28, 1998

[13] Kissil A., " Description of NGST Finite Element Models", Internal Memorandum, 1998

[14] Craig, Roy, "Structural Dynamics – An introduction to computer methods", John Wiley & Sons, New York, 1981

[15] Blevins, Robert D., "Formulas for natural frequency and Mode Shape", Krieger Publishing Company, Malabar, Florida, 1979

[16] Redding, D., Breckenridge, "Optical modeling for Dynamics and Control:

[17] Brown, R.G., Hwang, P.Y.C., "Introduction to Random Signals and Applied Kalman Filtering" , Third Edition, John Wiley & Sons, 1997

[18] Bialke, Bill, "A compilation of reaction wheel induced spacecraft disturbances", 20th Annual Annual American Astronautical Society Guidance and Control Conference, paper 97-038 Breckenridge, Colorado, February 5-9, 1997

[19] Castles S. e.a., "NASA/GSFC Cryocooler Development Program", Paper, 1996

[20] Collins, Simon A., "Multi-Axis Analog Adaptive Feedforward Cancellation of Cryocooler Vibration", Ph.D. thesis, Massachusetts Institute of Technology, 1994

[21] Wirsching P.H., Paez T.L., Ortiz K., "Random Vibrations – Theory and Practice", John Wiley & Sons Inc, First Edition, 1995

[22] Dorf R.C., Bishop, R.H. , "Modern Control Systems", 7th edition, ISBN 0-201-50174-0, Addison-Wesley Publishing Company, 1995, page 662

[23] Bélanger, P.R., " Control Engineering – A modern Approach", Saunders College Publishing, Harcourt Brace and Company, 1995

[24] Gutierrez, H.,"Performance Assessment and Improvement of Precision Structures during Conceptual Design", Ph.D. Thesis, Massachusetts Institute of Technology, February 1999

[25] JPL Publication 98-12 "Integrated Modeling of Optical Systems User's manual", Release 4.0, National Aeronautics and Space Administration, Jet Propulsion Laboratory, California Institute of Technology, Pasadena, California, September 19, 1998

[26] Mosier, G., "Analysis of Solar Pressure and C.M.-C.P. Offset on Momentum Unloading Distribution, NGST Systems Analysis Memorandum , NASA Goddard Space Flight Center, July 17, 1997

[27] DMK/DPK Formeln und Tafeln, Unterrichtswerk der deutschschweizerischen Mathematikkommission und der deutschschweizerischen Physikkommission, 3. Auflage, 1984

[28] Gross, D., Messner, D., "ADAM Technology", AEC ABLE Engineering Product Information Binder, Goleta, California, 1999

[29] Garnek M., "EOS Orbital Damping Study", EOS-Study 282, MA93-EOS-002, GE Astro Space, Astro-Space Division, March 31, 1997

[30] Crawley, E., Hall S., "Dynamics of Controlled Structures", 16.243 Course Notes, Space Engineering Research Center (SERC), Massachusetts Institute of Technology, 1991

[31] Bely P.Y., Burg, R., Femiano M., Ha K., Kissil A., Mosier G., Perrygo C., "First order determination of the main structural and dynamic parameters for NGST", Memorandum, NGST project office, June 17, 1997

[32] Blakely, K. "MSC/NASTRAN- Basic Dynamic Analysis", User's guide, Version 68, The MacNeal-Schwendler Corporation, 1993

[33] Gutierrez, H.L. " Damping formulations in substructure synthesis", M.S. thesis, Massachusetts Institute of Technology , May 1994

[34] Uebelhart, S.,"Uncertainty and Modeling Error", Presentation at the SIM contract review, Jet Propulsion laboratory, April 1999

[35] Mosier,Gary, Michael Femiano NASA/GSFC, Kong Ha, Jackson & Tull, Richard Burg JHU, "Dynamics and Controls", Presentation at Modeling Peer Review, JPL, January 22, 1998

[36] Campell, M., "Disturabnce Modeling" Chapter, 16243 Course Notes on " Dynamics of Controlled Structures", 1997

[37] Sparr L.,Boyle R., Cory R., Connors F., James E., Fink R., Arillo V., Marketon J., "NASA/GSFC Cryocooler Test Program Results", Memorandum, NASA Goddard Space Flight Center, 1993

[38] Source URL: http://www-b.jpl.nasa.gov/cryocooler/char.html

[39] ITHACO Home page Uniform Resource Locator (URL): TORQWHEEL© <u>*http://www.ithaco.com/T-wheel.html*</u>, Reference date: 28 October 1998

[40] Hasha, M.D., "Reaction Wheel Mechanical Noise Variations", Engineering Memorandum EM No. SSS-218, Space Telescope Program, 30 June 1986

[41] Orbital Sciences Corporation, Germantown, MD. ITHACO B-Wheel Reaction Wheel Tests for the FUSE Mission. Internal Memorandum, April 1997

[42] Melody, J.W., "*Discrete Frequency and Broadband Reaction Wheel Disturbance Models*", JPL Interoffice Memorandum, 3411-95-200csi, June 1, 1995

[43] Mosier G., Brown G., GSFC test data from E-Wheel spinup test and readme file, NASA Goddard Space Flight Center, delivered 26 August 1998

[44] Kistler Load table user manual excerpt, fax received from NASA Goddard Space Flight Center, Code 723, 1998

[45] Masterson, Rebecca, Memorandum to R. Grogan, "*Reaction Wheel Modeling from ITHACO test data*", SIM/MPI-MIT Program, April 9, 1998

[46] de Weck, Olivier, Memorandum MIT-SSL-NGST-98-1, " Reaction Wheel Disturbance Analysis - Test Data Evaluation of Baseline Reaction Wheel (ITHACO E-Wheel) for the Next Generation Space Telescope (NGST)", October 29, 1998

[47] Masterson R., "Development and Validation of Empirical and Analytical Reaction Wheel Disturbance Models", MS thesis, Massachusetts Institute of Technology, June 1999

[48] Gutierrez, Homero, "*Stochastic Frequency-domain Disturbance Model of Multiple Reaction Wheels of Arbitrary Orientation*", Memorandum to Jet Propulsion Laboratory, February 13, 1998

[49] de Weck, Olivier, Memorandum MIT-SSL-NGST-98-2, "*Reaction Wheel Assembly (RWA) Disturbance Modeling (Multiple Wheels) for the Next Generation Space Telescope (NGST) Program*", December 1998

[50] Femiano, Mike, Personal e-mail message regarding RWA configuration of the TRMM spacecraft, August, 1998

[51] Masterson, R., "Reaction Wheel Disturbance Models", Memorandum, Massachusetts Institute of Technology, March 11, 1998

[52] de Weck, O., Miller D.W., Gutierrez H., "Structural Dynamics and Controls for NGST – A preliminary study", presented at the 34th Liege International Astrophysics Colloquium in Liege, Belgium, 15-18 June 1998

[53] Breault Research Organization, "Modeling and Analysis for Controlled Optical Systems" , MACOS User Manual, Version 2.4, April 1, 1997

[54] Curtis A. (editor), "Terrestrial Planet Finder Architecture Design Report", 16.89 Space Systems Engineering, Massachusetts Institute of Technology, May 1999

[55] Description of NSIM simulation model, GSFC internal memorandum, 1998

[56] The Mathworks Inc. SIMULINK®, Application Note: "Simulations in SIMULINK- Use of the White Noise, Band Limited White Noise, and Random Blocks" ,Revised 2/26/97

[57] Moore B.C., "Principal component analysis of linear systems: Controllability, Observability and model reduction", IEEE Transactions on Automatic Control, AC-26 pp. 17-32, 1981

[58] Strang, Gilbert., "*Introduction to Applied Mathematics*", Chapter 1, Symmetric Linear Systems, , page 78, Singular Value Decomposition, Wellesley-Cambridge Press, 1986

[59] Zheng G., Haynes L.S. and Lee J.D., "A Stewart Platform as an Adaptive Structure – Its Application to Active Vibration Control", Paper

[60] Spanos J, Rahman Z., Blackwood G., "A Soft 6-axis Acive Vibration Isolator", American Control Conference, Seattle, WA, June 21-23, 1995